UNIVERSITÉ DE SHERBROOKE
Faculté de génie
Département de génie chimique et biotechnologique

MODÉLISATION NUMÉRIQUE, CARACTÉRISATION ET VALIDATION EXPÉRIMENTALE DU TRANSFERT THERMIQUE AU-DESSUS DE CELLULES D'ÉLECTROLYSE D’ALUMINIUM

Thèse de doctorat
Spécialité : génie chimique

François ALLARD

Sherbrooke (Québec) Canada

Décembre 2018

MEMBRES DU JURY

Pr Martin DÉSILETS

Directeur

Dr Yves CARATINI

Évaluateur externe

Pr Bernard MARCOS

Évaluateur

Pr Gervais SOUCY

Évaluateur

À tous ceux qui contribuent à l'avancement des sciences et technologies,
et plus spécialement à mon épouse Vanessa et ma famille

RÉSUMÉ

La production d'aluminium primaire par le procédé d'électrolyse est améliorée continuellement afin d'atteindre une meilleure efficacité énergétique et un meilleur bilan environnemental, tout en augmentant la production. Cette augmentation se fait en améliorant la conception des cellules d'électrolyse d'aluminium et en intensifiant le courant alimentant les technologies existantes. Pour donner un ordre de grandeur, la production d'aluminium au Canada nécessitait environ 42 500 GWh d'électricité en 2017, soit environ 24 % de la production totale d'hydroélectricité du Québec pour produire 3.2 millions de tonnes.

Dans la salle d'électrolyse, un puissant courant électrique situé entre 200 kA et 600 kA, selon la technologie, traverse chacune des cellules d'électrolyse en série pour alimenter la réaction électrochimique. L'énergie générée par effet Joule est dissipée par les différentes composantes de la cellule d'électrolyse. Dans le cadre de cette thèse, le comportement thermique de la cellule d'électrolyse est prédit par la modélisation numérique des phénomènes de transfert thermique et de conduction électrique, avec une emphase particulière sur les composantes supérieures. La prédiction est améliorée par la caractérisation des propriétés thermochimiques de matériaux et la validation expérimentale effectuée sur des cellules d'électrolyse industrielles.

Le recouvrement anodique est composé par deux éléments distincts : 1) le matériau de recouvrement anodique poudreux (*ACM*) et 2) la croûte d'anode qui est générée par la réaction entre l'*ACM* et le bain électrolytique à l'état liquide ou vapeur. La quantification des phases cristallines a démontré les gradients verticaux de $Na_5Al_3F_{14}$, Na_3AlF_6, $Na_2Ca_3Al_2F_{14}$ et Al_2O_3 dans la croûte d'anode, engendrés par la pénétration de bain liquide et de vapeur ($NaAlF_4$). Selon les analyses thermochimiques, l'*ACM* se transforme en croûte d'anode dans la plage de température variant entre 685 °C et 710 °C, tandis que la croûte se détériore à une température d'approximativement 935 °C pour former une cavité dans la cellule d'électrolyse. Les propriétés thermiques complètes (α, k, c_p, ρ, enthalpie et ε) ont été déterminées expérimentalement.

La géométrie servant à représenter le recouvrement anodique a été améliorée par des mesures de profils de l'*ACM* et de la croûte d'anode. La modélisation thermique-électrique en régime permanent a été améliorée en programmant un algorithme de prédiction de l'emplacement de la cavité et en intégrant un module de rayonnement thermique. L'augmentation de l'épaisseur du recouvrement anodique engendre une diminution de la dissipation thermique par le haut et une augmentation de celle par le côté, causant la fonte du talus sur les parois latérales. À partir des simulations, une corrélation numérique a été établie pour diagnostiquer des cellules d'électrolyse présentant une dissipation thermique atypique ou problématique.

Une nouvelle stratégie de modélisation transitoire a été développée pour résoudre deux problèmes comprenant des variations géométriques temporelles. Pour la première fois, l'évolution thermique et électrique d'un ensemble anodique durant toute sa durée de vie a été prédite et validée par des anodes instrumentées placées dans des cellules d'électrolyse industrielles. De plus, le modèle transitoire démontre que l'augmentation temporaire de l'énergie générée, en augmentant le potentiel électrique d'opération, engendre la détérioration irréversible du recouvrement anodique et génère un nouvel équilibre thermique caractérisé par une dissipation latérale plus importante.

Mots-clés : Aluminium, électrolyse, modélisation par éléments finis, transfert thermique, caractérisation des matériaux, conductivité thermique, anode, croûte.

REMERCIEMENTS

En premier lieu, l'auteur remercie l'organisation de l'Université de Sherbrooke et la compagnie Rio Tinto Aluminium pour avoir supporté le projet de recherche de doctorat. Plus précisément, les remerciements s'adressent au directeur de recherche, Pr Martin Désilets, pour sa supervision et sa contribution à ce projet de recherche. Pr Martin Désilets a su mettre à l'épreuve les techniques de caractérisation thermique et surtout les aspects concernant la modélisation numérique durant les évaluations périodiques de l'avancement des résultats de doctorat. Ensuite, l'auteur souhaite remercier Dr Alexandre Blais pour sa grande collaboration au projet de recherche, qui se résume entre autres par la planification des campagnes de mesures industrielles et par la mise à l'épreuve des techniques de mesure thermique. De plus, l'auteur aimerait remercier le Dr Marc LeBreux pour sa participation durant certaines campagnes de mesures et son support avec la modélisation numérique au début du projet de recherche.

Par la suite, l'auteur souhaite remercier le Pr Gervais Soucy pour avoir rendu disponibles les techniques de caractérisation des matériaux inorganiques et les équipements du laboratoire des technologies de l'aluminium. L'auteur remercie aussi les chercheurs Dr Jean-François Bilodeau et M. Sébastien Guérard pour leur grande contribution durant les rencontres de transfert des connaissances scientifiques qui ont été planifiées durant le projet de recherche. De plus, l'auteur aimerait remercier les techniciens du Centre de recherche et de développement Arvida (CRDA) et de l'usine Grande-Baie (UGB) de Rio Tinto pour leur participation aux campagnes de mesures industrielles. Aussi, l'auteur remercie M. André Bilodeau pour son aide avec les montages et les expérimentations. Finalement, l'auteur aimerait remercier les professionnels du Centre de caractérisation des matériaux (CCM) de l'Université de Sherbrooke pour leur aide avec les équipements de caractérisation, ainsi que les chercheurs du Laboratoire de recherche des fabrications (LRF) pour leur contribution lors de différentes rencontres.

Le support financier du Conseil de recherches en sciences naturelles et en génie du Canada (CRSNG) et de Rio Tinto Aluminium pour le projet de recherche est grandement apprécié. De plus, le support financier du Fonds de recherche du Québec - Nature et technologies (FRQNT), de l'Association francophone pour le savoir (ACFAS) et de Ressources naturelles Canada (RNCan) est aussi énormément apprécié.

TABLE DES MATIÈRES

LISTE DES FIGURES

LISTE DES TABLEAUX

LEXIQUE

Terme technique	Définition
Anode (*anode*)	L’anode de carbone est fabriquée principalement à partir du coke de pétrole et contient du brai comme liant. Elle est moulée sous la forme d’un bloc et cuite à une température d’environ 1100 °C.
Bain (*bath*)	Le bain électrolytique contient plusieurs phases cristallines à l’état solide. Ces principales sont la cryolite, la chiolite, les cryolites de calcium et les différentes phases d’alumine. À température d’opération, le bain électrolytique devient liquide et se caractérise par des espèces ioniques, entre autres $Al_2OF_6^{2-}$ et AlF_4^-.
Boue (s*ludge*)	Dépôt se formant sur le bloc cathodique. La boue est composée de bain électrolytique liquide et d’alumine solide en suspension dans des conditions d’opération.
Cadre anodique (*anode beam*)	Chaque tige d’anode est fixée au cadre anodique. Le cadre anodique se déplace afin de maintenir une certaine distance interpolaire (anode-cathode). Le cadre anodique est remonté après quelques semaines, lorsqu’il atteint sa position la plus basse.
Croûte d’anode (*anode crust*)	Matériau qui se forme par des réactions chimiques à partir du matériau de recouvrement anodique poudreux. La croûte d’anode contient de l’alumine et du bain électrolytique et c’est un matériau très solide qui demeure en place au-dessus de la cellule d’électrolyse.
Dépôt (*deposit*)	Phases solides présentes sur la surface cathodique.
Effet anodique (*anode effect*)	Interruption des conditions d’électrolyse normales qui mène à la formation de $CO_{(g)}$, $CF_{4(g)}$ et $C_2F_{6(g)}$. Le potentiel électrique peut atteindre jusqu’à 30-40 V.
Efficacité de courant (*courant efficiency*)	Quantité d’aluminium produit par la cellule d’électrolyse par rapport à la quantité théorique calculée selon la loi de Faraday.

Matériau de recouvrement anodique (*anode cover material*)	Le matériau primaire servant au recouvrement des anodes est composé d'alumine, de bain électrolytique et de croûte d'anode récupérée et broyée. Ce mélange poudreux est de granulométrie variable et il contient autant des poudres fines que des gros morceaux de croûte non broyée.
Paroi latérale (s*ide wall*)	Section située sur les côtés de la cellule d'électrolyse. Cette partie peut être composée par du carbone ou des matériaux réfractaires.
Pied de talus (l*edge toe*)	Dépôt se formant sous le talus et sur le bloc cathodique. La position horizontale du pied de talus part de la paroi latérale et s'étend jusqu'au début de la zone érodé du bloc cathodique.
Recouvrement anodique (*anode cover*)	Le recouvrement anodique comprend le matériau de recouvrement anodique primaire (poudreux) et la croûte d'anode.
Rondins (*stubs*)	Les rondins d'acier sont fixés à l'anode. Ils ont la fonction de la soutenir et d'y acheminer le courant électrique.
Superstructure (*superstructure*)	La superstructure contient le réservoir d'alumine servant à l'alimentation de la cellule d'électrolyse et divers autres équipements.
Talus (*side ledge*)	Dépôt se formant sur la paroi latérale (*side wall*). Il est constitué principalement de bain électrolytique solidifié et se forme par refroidissement sur le côté de la cellule.
Tige d'anode (*anode rod*)	La tige est fabriquée à partir d'aluminium ou de cuivre. Elle conduit le courant électrique jusqu'à l'anode de carbone.
Traverse (*yoke*)	La traverse est fabriquée en acier et elle sert de jonction entre les rondins et la tige d'anode.

LISTE DES SYMBOLES

Symbole	**Définition**
A	Aire (m^2)
c_p	Capacité thermique massique (J/kg·K)
E	Champ électrique (V/m)
F	Facteur de forme pour le rayonnement thermique
G	Irradiation thermique (W/m^2)
Gr	Nombre de Grashof
H	Hauteur (m)
h	Coefficient de transfert de chaleur par convection ($W/m^2 \cdot K$)
J	Densité de courant (A/m^2); Radiosité (W/m^2)
k	Conductivité thermique (W/m·K)
L	Longueur (m)
Nu	Nombre de Nusselt
P	Périmètre (m)
Pr	Nombre de Prandtl
Q	Transfert d'énergie (J)
q	Taux de transfert d'énergie (W)
q'	Taux de transfert d'énergie par unité de distance (W/m)
q''	Densité de flux thermique (W/m^2)
$\dot{q}$	Taux de génération d'énergie par unité de volume (W/m^3)
Re	Nombre de Reynolds
T	Température (K ou °C)
U	Énergie interne (J)
$\hat{U}$	Énergie interne spécifique (J/kg)
V	Potentiel électrique (V)
α	Diffusivité thermique (m^2/s); Absorptivité
δ	Delta de Kronecker
ε	Émissivité
ρ	Densité (kg/m^3); Réflectivité
σ	Conductivité électrique (S/m); Constante de Stefan-Boltzmann ($5.67 \cdot 10^{-8}\ W/m^2 \cdot K^4$)
τ	Transmissivité
υ	Vitesse (m/s)

gras	Vecteur
[crochet]	Matrice ou une concentration d'espèce chimique

LISTE DES ACRONYMES

Acronyme	**Définition**
ACM	Matériau de recouvrement anodique (*anode cover material*)
AEC	Cellule d’électrolyse d’aluminium (a*luminum electrolysis cell*)
CR	Ratio molaire de cryolite ou [NaF]/[AlF_3] (*cryolite ratio*)
CVD	Perte de potentiel électrique à la cathode (*cathode voltage drop*)
DRX (*XRD*)	Diffractométrie de rayons X (*X-ray diffraction*)
DSC	Calorimétrie différentielle à balayage (*differential scanning calorimetry*)
DTA	Analyse thermodifférentielle (*differential thermal analysis*)
EDS	Analyse dispersive en énergie (*energy-dispersive X-ray spectroscopy*)
LFA	Analyse à flash laser (*laser flash analysis*)
MEB (*SEM*)	Microscopie électronique à balayage (*scanning electron microscopy*)
TG (*TGA*)	Thermogravimétrie (*thermogravimetric analysis*)
XRF	Spectrométrie de fluorescence X (*X-ray fluorescence*)

CHAPITRE 1 INTRODUCTION

1.1 Mise en contexte

1.1.1 Industrie de l'aluminium

L'industrie canadienne de l'aluminium compte parmi les plus importantes à l'échelle internationale. La production d'aluminium primaire au Canada se situe à près de 3.2 millions de tonnes par année [Aluminium Association of Canada, 2017]. Cette production est principalement localisée au Québec, où les centrales hydroélectriques fournissent l'électricité aux alumineries. La production mondiale d'aluminium primaire se situe actuellement à 63.4 millions de tonnes par années et la demande suit une croissance annuelle de 4.3 % [International Aluminium Institute, 2017; Aluminium Association of Canada, 2017]. Selon les estimations de l'International Aluminium Institute, la Chine est responsable d'environ 60 % de la production mondiale d'aluminium primaire. Pour demeurer compétitive, l'industrie de l'aluminium doit constamment diminuer ses coûts de production. L'aluminium primaire est produit dans les cuves d'électrolyse, telles que celles présentées dans la Figure 1-1.

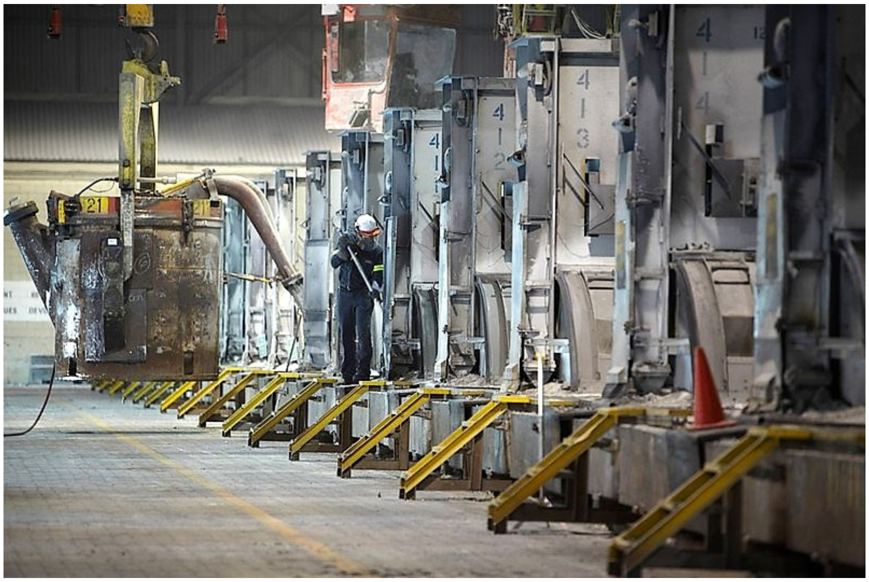

Figure 1-1 Cuves en série dans une salle d'électrolyse [Rio Tinto, 2009]

1.1.2 Procédé Hall-Héroult

Le procédé de réduction de l'alumine (Al_2O_3) en aluminium (Al) est couramment appelé « Hall-Héroult », d'après les noms de ses inventeurs. Pour effectuer l'électrolyse, l'Al_2O_3 est dissoute dans un électrolyte liquide très corrosif, principalement composé par la cryolite (Na_3AlF_6). L'électrolyte, typiquement appelé bain, peut être décrit par le système NaF-AlF_3-CaF_2-Al_2O_3 et contient des additifs ou impuretés sous la forme de fluorure de lithium (LiF), fluorure de potassium (KF) et fluorure de magnésium (MgF_2). Ces sels électrolytiques sont liquides à la température d'opération, soit typiquement autour de 965 °C, et ils se retrouvent sous leurs formes ioniques. Le procédé d'électrolyse se déroule en continu dans une cellule électrochimique composée par des anodes de carbone et des cathodes graphitisées. Un puissant courant électrique, situé entre 200 kA et 600 kA selon la technologie, entre par les anodes et traverse la cellule d'électrolyse pour alimenter la réaction électrochimique. Le courant ressort par les barres collectrices reliées aux blocs cathodiques, pour ensuite rejoindre la prochaine cuve de la série.

En plus de produire l'aluminium, le courant électrique génère de la chaleur par effet Joule en traversant la cellule d'électrolyse. La majeure partie de la chaleur est générée dans le bain liquide, à l'endroit situé entre l'anode et la cathode. Dans ce procédé, la cathode électrochimique est l'aluminium liquide, car il s'agit de l'endroit où l'aluminium est produit. Les principales composantes de la cellule d'électrolyse sont présentées dans la Figure 1-2.

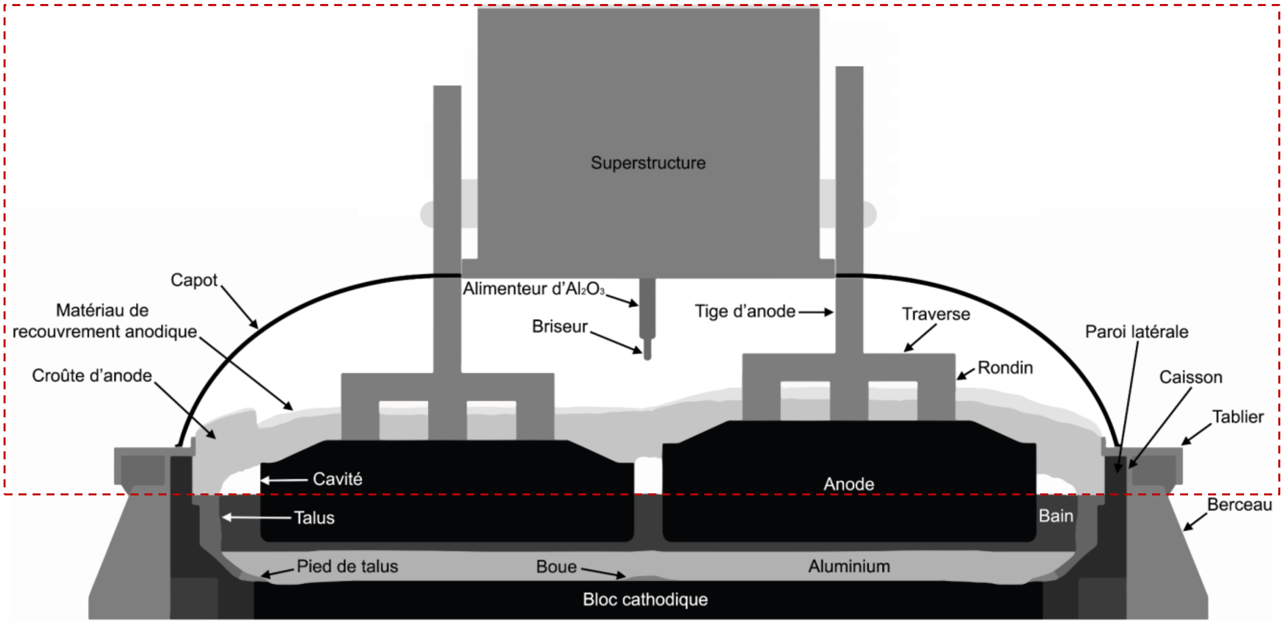

Figure 1-2 Cellule d'électrolyse d'aluminium, avec l'emphase sur les parties du dessus

Le bilan thermique de la cellule d'électrolyse doit être finement ajusté afin de maintenir une couche d'électrolyte solide sur la surface de chaque paroi latérale. Cette couche protectrice, appelée talus, protège les composantes latérales de la haute corrosivité du bain liquide et elle doit être présente durant toutes les années d'opération afin d'atteindre une durée de vie raisonnable.

L'énergie générée par effet Joule est principalement dissipée par le haut et le côté de la cellule d'électrolyse. Dans la section du haut, la chaleur traverse le recouvrement anodique et les ensembles anodiques pour sortir ensuite par les capots, la superstructure et la ventilation. Dans les parties latérales, la chaleur est dissipée par le talus, les parois, le caisson d'acier et les berceaux entourant la cellule d'électrolyse. Le bas de la cellule contient davantage de matériaux réfractaires et isolants afin de maintenir une température suffisante en dessous de l'aluminium liquide, entre autres pour éviter la formation excessive de pied de talus et de boues.

Dans le cadre de cette thèse, une emphase majeure est mise afin d'améliorer la prédiction de la dissipation thermique par les composantes du dessus de la cellule d'électrolyse. Les composantes supérieures sont encadrées en rouge dans la Figure 1-2. La dissipation thermique par le dessus dépend grandement des propriétés thermiques du matériau de recouvrement anodique. Ce matériau recouvre les anodes de carbone pour les isoler, les protéger de l'oxydation engendrée par l'air et absorber une partie des gaz fluorés. Le matériau de recouvrement anodique poudreux se transforme en un matériau solide, appelé croûte d'anode, lorsqu'il entre en contact du bain liquide ou vapeur. Il y a très peu d'études scientifiques qui se sont intéressées à l'évaluation des propriétés thermiques de ces matériaux, ainsi qu'à l'amélioration de la modélisation numérique des phénomènes thermiques évoluant au-dessus des cellules d'électrolyse d'aluminium. De plus, l'amélioration de la prédiction de la dissipation thermique par le dessus permet de mieux contrôler le bilan énergétique des cellules d'électrolyse. Ainsi, la conception et l'opération des cellules d'électrolyse peuvent être étudiées par des modèles numériques afin d'améliorer la durabilité du procédé et de diminuer sa consommation d'énergie.

1.1.3 Efficacité énergétique du procédé

Au cours du siècle dernier, la quantité d'énergie nécessaire pour produire l'aluminium dans les cellules d'électrolyse a diminué grandement. La consommation énergétique de la cellule d'électrolyse a été améliorée, entre autres, en utilisant des anodes précuites, en améliorant la conductivité électrique des matériaux, en augmentant l'efficacité de courant d'électrolyse et en contrôlant rigoureusement l'équilibre thermique. La Figure 1-3 détaille l'historique de la consommation énergétique des cellules d'électrolyse de 1900 à aujourd'hui, en considérant le courant continu alimentant les cellules d'électrolyse. En 2017, la moyenne mondiale de la consommation d'énergie par le procédé était de 13.3 kWh par kg d'Al produit [International Aluminium Institute, 2017].

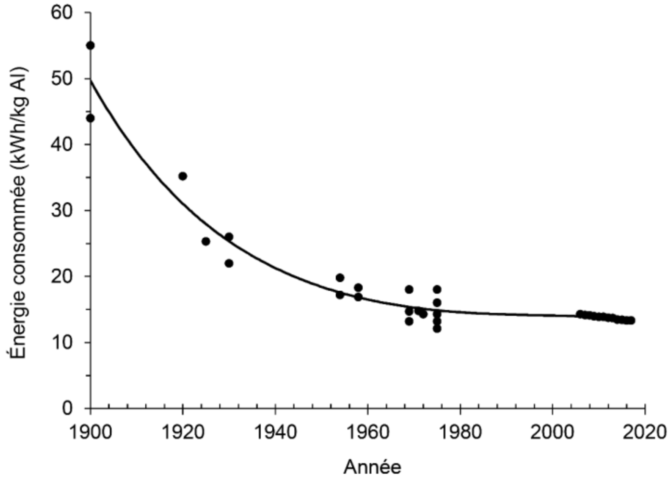

Figure 1-3 Historique de l'énergie consommée par les cellules d'électrolyse, adaptée des références : [Beck, 1982; International Aluminium Institute, 2017]

Afin d'augmenter la production d'aluminium, l'industrie augmente le courant électrique fourni aux cellules d'électrolyse. Toutefois, la génération supplémentaire de chaleur liée à l'augmentation du courant vient perturber le bilan énergétique des cellules d'électrolyse. Cette perturbation vient modifier l'état des matériaux à changement de phase situés sur le dessus (recouvrement anodique) et sur le côté (talus) de la cellule d'électrolyse. Par conséquent, en améliorant les connaissances des phénomènes liées aux pertes énergétiques, il serait possible de poursuivre l'augmentation de la production tout en maintenant une efficacité énergétique supérieure.

1.1.4 Problématique et question de recherche

Dans un contexte d'augmentation de la capacité de production des alumineries et d'optimisation de la performance énergétique du procédé, l'équilibre thermique de la cellule d'électrolyse doit être finement ajusté afin d'atteindre ces deux objectifs. De plus, la durabilité des matériaux composant la cellule d'électrolyse doit être maximisée afin de maintenir la viabilité du procédé. Une génération de chaleur supplémentaire occasionne une contrainte thermique plus importante sur les ensembles anodiques et le recouvrement anodique. Au-delà d'un certain seuil de température, le matériau de recouvrement anodique se transforme et la croûte d'anode peut fondre ou encore s’effondrer dans la cellule d’électrolyse. L’effondrement du recouvrement anodique engendre :

- la déstabilisation de l’équilibre thermique dans la cellule d’électrolyse et l’augmentation des pertes thermiques localisées à certains endroits,
- l’augmentation des émissions de fluorures provenant de la cellule d’électrolyse,
- la formation de dépôt à la surface de la cathode.

Au niveau de la littérature scientifique, il y a très peu d’articles dédiés à la caractérisation des matériaux de recouvrement anodique modernes, à base de bain électrolytique et d’Al_2O_3. De plus, les études récentes de la modélisation des pertes de chaleur par le dessus des cellules d’électrolyse simplifient grandement le comportement de l’*ACM* et de la croûte d’anode dans leurs hypothèses de modélisation. La variation de la chimie des matériaux peut occasionner une variation importante dans les propriétés thermochimiques et augmenter le risque d’effondrement de ces matériaux.

Récemment, les chercheurs dans le domaine de l’aluminium ont commencé à s’intéresser davantage aux pertes de chaleur au-dessus des cellules d’électrolyse. Il y a de 40 % à 50 % de la dissipation thermique totale qui se situe au-dessus de la cellule d’électrolyse d’aluminium. Toutefois, il y a encore très peu d’études sur ce domaine particulier, en dépit de son importance.

Afin d’augmenter la performance de l’industrie de l’aluminium et d’améliorer les connaissances du procédé d’électrolyse, voici la question de recherche qui est proposée :

Comment améliorer l’efficacité énergétique de la production d’aluminium en étudiant le comportement des matériaux et la dissipation thermique au-dessus des cellules d’électrolyse?

Caractérisation chimique et thermique du recouvrement anodique

Pour répondre à cette question, une meilleure compréhension des phénomènes thermochimiques se déroulant dans le recouvrement anodique est primordiale. De plus, les modèles prédisant la dissipation thermique doivent être alimentés par des propriétés thermiques adéquates, et aucune propriété thermique n’est disponible pour la croûte d’anode industrielle à des températures d’opération (se situant entre 700 °C à 950 °C). Par conséquent, le premier aspect de cette thèse sera d’approfondir les méthodes de caractérisation chimique et thermique de matériaux utilisés dans les cellules d’électrolyse d’aluminium.

Modélisation thermique-électrique de la cellule d'électrolyse d'aluminium

Le deuxième aspect de cette thèse est d'élaborer des modèles couplant les phénomènes thermiques et électriques pour prédire le comportement des cellules d'électrolyse, en régime permanent et transitoire. Avec l'aide des propriétés thermiques améliorées, il sera possible de prédire précisément la distribution des flux thermiques et températures à l'intérieur des cellules d'électrolyse. Pour y arriver, de nouvelles méthodes de modélisation, qui prennent en considération la géométrie réelle du recouvrement anodique, devront être développées en incluant les principaux phénomènes physiques se déroulant dans la cellule d'électrolyse. Ces modèles seront validés par des campagnes de mesures industrielles afin qu'ils soient conformes à la réalité. Avec des modèles thermiques-électriques validés par des mesures expérimentales, il sera possible d'effectuer l'analyse de différents paramètres susceptibles d'améliorer la performance du procédé Hall-Héroult.

1.2 Objectifs du projet de recherche

Globalement, le projet de recherche consiste à déterminer les propriétés chimiques et thermiques du recouvrement anodique et à développer des modèles thermiques-électriques afin d'obtenir des outils de prédiction permettant d'améliorer la conception et l'opération des cellules d'électrolyse. Ainsi, l'efficacité énergétique de la cellule d'électrolyse pourra être améliorée en répondant aux objectifs suivants :

Déterminer la composition chimique, le comportement thermochimique et les propriétés thermiques du recouvrement anodique

a) Caractériser des échantillons industriels de matériau de recouvrement anodique et de croûte d'anode pour obtenir leurs compositions chimiques.

b) Caractériser le comportement thermochimique du recouvrement anodique, déterminer ses températures de transformation et prédire son comportement à des températures d'opération (~100 °C à ~950 °C).

c) Déterminer les propriétés thermiques (diffusivité thermique, capacité thermique massique et conductivité thermique) de la croûte d'anode industrielle.

Élaborer des modèles numériques de prédiction du transfert thermique et du potentiel électrique, avec l'emphase sur le dessus de la cellule d'électrolyse

a) Développer des modèles 3D couplant les phénomènes thermiques et électriques, en incluant les propriétés thermochimiques des matériaux à changement de phase.

b) Résoudre les équations mathématiques reliées au transfert thermique et à la conduction électrique par la méthode des éléments finis.

c) Améliorer la méthode de modélisation pour représenter correctement les transformations se déroulant dans le recouvrement anodique.

Valider et alimenter les modèles numériques par des mesures en milieu industriel

a) Effectuer des campagnes de mesures thermiques, à l'aide d'instruments tels que : capteur de flux thermique, thermocouple et caméra infrarouge.

b) Déterminer les conditions limites au-dessus du recouvrement anodique à l'aide des instruments.

c) Mesurer la dimension et le profil du recouvrement anodique, en fonction de la consommation de l'anode, afin de bâtir une géométrie représentative.

d) Valider les résultats de simulations par les mesures thermiques.

Utiliser les modèles numériques pour simuler le comportement thermique de la cellule d'électrolyse d'aluminium, selon différents paramètres et conditions d'opération

a) Prédire le comportement thermique typique d'une cellule d'électrolyse en résolvant le régime permanent.

b) Évaluer l'impact des paramètres ci-dessous sur le comportement thermique d'une cellule d'électrolyse.

    i. Épaisseurs de matériaux de recouvrement anodique.

    ii. Taille de la cavité située sous la croûte d'anode.

c) Prédire l'effet de la consommation de l'anode sur le transfert thermique transitoire se déroulant au-dessus de la cellule d'électrolyse.

d) Évaluer l'impact d'une augmentation d'énergie ponctuelle sur le comportement transitoire de la cellule d'électrolyse.

Les travaux menés dans cette thèse permettent de fournir des outils de prédiction thermique servant à l'amélioration de la conception et de l'opération des cellules d'électrolyse d'aluminium. De plus, de nouvelles méthodes de caractérisation expérimentale et de diagnostic thermique industriel ont été développées et elles sont désormais disponibles pour étudier d'autres composantes du procédé d'électrolyse.

1.3 Contributions originales

D'un point de vue global, le développement de nouvelles méthodes expérimentales contribue à la discipline de la caractérisation chimique et thermique des matériaux inorganiques. L'amélioration des méthodes de mesures thermiques permet de contribuer au domaine du diagnostic thermique, permettant ainsi de fournir des outils efficaces pour diagnostiquer un procédé industriel. La conception de nouvelles approches de prédiction numérique permet de contribuer à discipline de la modélisation par éléments finis du transfert thermique et de la conduction électrique.

Plus spécifiquement, les contributions scientifiques originales provenant des chapitres 3 à 7 sont résumées dans les cinq sous-sections suivantes et elles sont détaillées dans les avant-propos de chacun des chapitres.

1.3.1 Caractérisation de la composition chimique des matériaux

La composition chimique de la croûte d'anode formée dans les cellules d'électrolyse d'aluminium a été caractérisée par la diffractométrie de rayons X (DRX), l'analyse quantitative Rietveld et l'analyse élémentaire de l'oxygène. Les résultats ont démontré les gradients verticaux de [$Na_5Al_3F_{14}$], [Na_3AlF_6], [$Na_2Ca_3Al_2F_{14}$] et [Al_2O_3] qui sont engendrés par la pénétration de bain liquide et de vapeur ($NaAlF_4$). La partie du dessus de la croûte d'anode n'atteint pas une température suffisante pour transformer les alumines de phases γ, δ, θ, β et amorphe en la phase cristalline α-Al_2O_3. La croûte d'anode est composée par un réseau de particules α-Al_2O_3 et de bain solidifié, selon les analyses de microscopie électronique à balayage (MEB) et les analyses dispersives en énergie (*EDS*). Le comportement de ce matériau industriel a été prédit par des analyses d'équilibre chimique, démontrant ainsi les températures de fusion des phases de bain électrolytique. Selon le diagramme de phases calculé à l'équilibre thermodynamique, la croûte d'anode qui présente un ratio de cryolite plus faible est davantage susceptible de fondre partiellement et de s'effondrer à une plus basse température.

1.3.2 Caractérisation des propriétés thermochimiques des matériaux

La microstructure, les propriétés thermiques et les compositions chimiques ont été caractérisées sur des échantillons de croûte d’anode provenant de cellule d’électrolyse d’aluminium. Les propriétés thermiques et thermochimiques (diffusivité thermique, capacité thermique massique, les enthalpies de transition de phase et de fusion, la densité et conductivité thermique) ont été déterminées sur des échantillons de composition chimique préalablement évaluée. Comme la croûte d’anode est formée à une température d’environ 700 °C et qu’elle peut atteindre jusqu’à 950 °C, une nouvelle méthode de détermination de la diffusivité thermique par l’analyse à flash laser (*LFA*) a été établie. Avant cette étude, la conductivité thermique de la croûte d’anode n’avait pas été déterminée en couvrant toute sa plage de température d’opération (principalement 700 °C à 950 °C). La haute corrosivité du bain liquide et de ses vapeurs rend cette analyse très risquée pour les appareils de mesure. Avec ces résultats d’analyses, des propriétés thermiques primordiales pour la modélisation thermique ont pu être établies. De plus, les méthodes de caractérisation ont été détaillées afin qu’elles puissent être appliquées à d’autres types d’échantillons, tels que les sels électrolytiques à l’état solide, solide-liquide ou encore liquide. Finalement, cet article démontre avec un diagramme de phases que la dégradation de la croûte d’anode est accentuée à partir d’une température d’environ 935 °C.

1.3.3 Effet de la cavité sur la dissipation thermique

Une cavité remplie de gaz se forme lorsque la croûte d’anode se dégrade et tombe dans le bain liquide de la cellule d’électrolyse. Dans le cadre du projet, les premières campagnes de mesures en usine ont permis de mesurer la taille de cette cavité et d’obtenir une taille moyenne. La géométrie qui était utilisée auparavant dans les modèles thermique-électrique a été modifiée pour y inclure cette cavité. Un module de radiosité servant à la prédiction des flux thermiques par rayonnement a été intégré dans un modèle thermique-électrique de cellule d’électrolyse. Considérant la cavité, les flux thermiques, les températures et les potentiels électriques ont été simulés par le modèle numérique. En comparant les résultats de simulation avec des mesures expérimentales de flux thermiques et températures, l’ajout de la cavité améliore la justesse des prédictions. Il a aussi été démontré que plus que la taille de cette cavité augmente, plus la dissipation thermique par le haut sera élevée.

1.3.4 Modélisation thermique-électrique en régime permanent

La géométrie servant à représenter le recouvrement anodique a été améliorée par des mesures industrielles des profils de l'*ACM* et de la croûte d'anode et par des mesures supplémentaires de tailles de cavité. Dans cet article, un modèle numérique intègre cette géométrie améliorée. De plus, ce modèle thermique-électrique est résolu de manière itérative par un algorithme permettant de prédire l'emplacement de la frontière entre la croûte d'anode et la cavité. Afin d'améliorer la prédiction du transfert thermique par rayonnement dans la cavité, l'émissivité de l'*ACM* et de la croûte a été déterminée expérimentalement par thermographie infrarouge et rapportée dans la littérature pour la première fois. De plus, les valeurs de conductivité thermique de l'*ACM* et de la croûte d'anode déterminée par *LFA* (Chapitre 4) ont été validées par des mesures thermiques dans une cellule d'électrolyse en opération. Ce nouveau modèle thermique-électrique contient une géométrie, des propriétés thermiques et une méthode de modélisation améliorées. Ce modèle a été résolu en régime permanent afin d'étudier l'effet de l'épaisseur de l'*ACM* sur les pertes thermiques et l'impact d'un film de boue à la surface de la cathode sur la distribution de la dissipation thermique. Finalement, une corrélation numérique a été établie afin d'estimer le ratio entre la dissipation thermique totale par le dessus et par le côté de la cellule d'électrolyse, en utilisant des mesures industrielles du flux thermique. En prenant ces mesures systématiquement aux mêmes endroits sur la cellule d'électrolyse, il est possible de rapidement diagnostiquer une cellule d'électrolyse présentant une dissipation thermique anormale ou problématique.

1.3.5 Modélisation thermique-électrique en régime transitoire

Une approche de modélisation considérant les variations géométriques temporelles a été développée et appliquée au transfert thermique transitoire de cellules d'électrolyse d'aluminium. Cette stratégie de modélisation a été programmée et intégrée dans un logiciel de simulation par éléments finis, dans l'objectif de prédire les deux cas de simulation suivant :

L'effet d'un traitement de potentiel électrique dans la cellule d'électrolyse sur le comportement des matériaux à changement de phase, soit le recouvrement anodique et le talus

Étant donné que le recouvrement anodique se caractérise par des transformations irréversibles et que le talus est un matériau à changement de phase réversible, il a été démontré qu'une génération de chaleur plus importante engendre un nouvel équilibre thermique. Suite à cette excursion thermique, le dessus de la cellule d'électrolyse dissipe davantage de chaleur tandis que le talus s'adapte à ce nouvel équilibre en épaississant. Dans ces conditions, la croûte fond et coule au fond de la cellule d'électrolyse, causant la formation de dépôt résistif sur la surface des blocs cathodiques. Pour ce cas, la nouvelle approche de modélisation a permis de déplacer la frontière entre la croûte d'anode et la cavité en suivant l'isotherme de fusion de la phase Na_3AlF_6.

L'évolution de la dissipation thermique par le dessus des cellules d'électrolyse durant toute la vie de l'anode

La stratégie de modélisation a permis de résoudre ce problème de modélisation à l'aide d'un algorithme qui déplace la géométrie, met à jour le maillage et interpole les températures. Pour ce cas, le mouvement de l'ensemble anodique suivant la consommation de l'anode de carbone a été intégré dans la résolution. Pour la première fois, il a été possible de prédire les températures et potentiels électriques tout au long de la vie de l'anode industrielle. De plus, ces résultats de modélisation transitoire ont été validés rigoureusement à l'aide d'anodes instrumentées placées dans des cellules d'électrolyse en opération.

Les deux cas de modélisation ci-dessus ont permis d'appliquer la méthode prédiction développée dans le cadre du projet de recherche. Cette nouvelle approche a été nommée : « *a strategy for moving geometry, mesh update and nodal interpolation* » en anglais ou « une stratégie de déplacement de géométrie, de mise à jour du maillage et d'interpolation nodale » en français. Il s'agit d'une approche utile pour résoudre des problèmes comprenant des variations géométriques temporelles par la méthode des éléments finis. En plus de contribuer à la discipline de la modélisation thermique-électrique, cette méthode peut être appliquée à d'autres problèmes traitement de déplacement géométrie important.

1.4 Plan du document

Ce premier chapitre porte sur la mise en contexte général, la problématique et les contributions scientifiques liées au projet de recherche sur la modélisation numérique et la caractérisation expérimentale de la dissipation thermique au-dessus de cellules d'électrolyse d'aluminium. Le Chapitre 2 présente la mise en contexte scientifique et la revue de la littérature qui sont liées à ce projet de caractérisation des matériaux et de modélisation numérique des phénomènes thermiques se déroulant dans la cellule d'électrolyse. Les résultats de cette thèse sont présentés sous forme d'articles, qui sont intégrés dans les chapitres 3 à 7.

Le Chapitre 3 présente les résultats de la caractérisation chimique de l'*ACM* et de la croûte d'anode, ainsi qu'une analyse du comportement thermodynamique des matériaux en fonction de la température d'opération. Le Chapitre 4 expose en détail les résultats de la caractérisation thermique, chimique et microstructurale de la croûte d'anode formée dans les cellules d'électrolyse. Le Chapitre 5 présente les résultats de la modélisation thermique-électrique d'une cellule d'électrolyse, en incluant la cavité. L'effet de la taille de la cavité et l'impact sur la précision de la modélisation ont été détaillés dans ce chapitre. Le Chapitre 6 montre un modèle numérique intégrant un algorithme de prédiction de la taille de cavité. Ce modèle a été validé expérimentalement par des mesures de flux thermiques et de températures. Le Chapitre 7 démontre deux cas de simulation transitoire en utilisant une nouvelle approche de modélisation par éléments finis. Les résultats des simulations et les détails de la méthode de modélisation se retrouvent dans ce chapitre. Finalement, le Chapitre 8 présente les conclusions de ces travaux de recherche, les principales contributions à la science et de nouvelles perspectives de recherche.

CHAPITRE 2 ÉTAT DE L'ART

2.1 Introduction à la cellule d'électrolyse d'aluminium

2.1.1 Réduction de l'alumine pour produire l'aluminium

L'aluminium est produit par la réduction de l'alumine (Al_2O_3) en aluminium dans une cellule d'électrolyse. Le procédé inventé par Hall et Héroult en 1886 demeure le seul procédé commercial utilisé pour produire de l'aluminium à l'échelle industrielle. Le procédé est alimenté par de l'alumine qui est produite au préalable dans le procédé Bayer. Ce procédé extrait l'alumine par la digestion caustique de la bauxite broyée à une haute température et pression. La bauxite contient de 40 % à 60 % d'alumine hydratée, sous plusieurs formes telles que la gibbsite [$Al(OH)_3$], la boehmite [γ-AlO(OH)] et le diaspore [α-AlO(OH)] [Thonstad *et al.*, 2001]. L'alumine hydratée est ensuite clarifiée, précipitée, lavée et finalement calcinée pour produire l'alumine anhydre qui est alimentée aux cellules d'électrolyse d'aluminium.

L'alumine de grade métallurgique contient principalement les phases α-Al_2O_3 et γ-Al_2O_3, tout dépendant du niveau de calcination. La composition en phases cristallines de l'alumine métallurgique suit typiquement le chemin de transformation suivant : $\gamma \rightarrow \delta \rightarrow \theta \rightarrow \alpha$. La Figure 2-1 présente en détail les transformations dans l'alumine en fonction de la température de calcination.

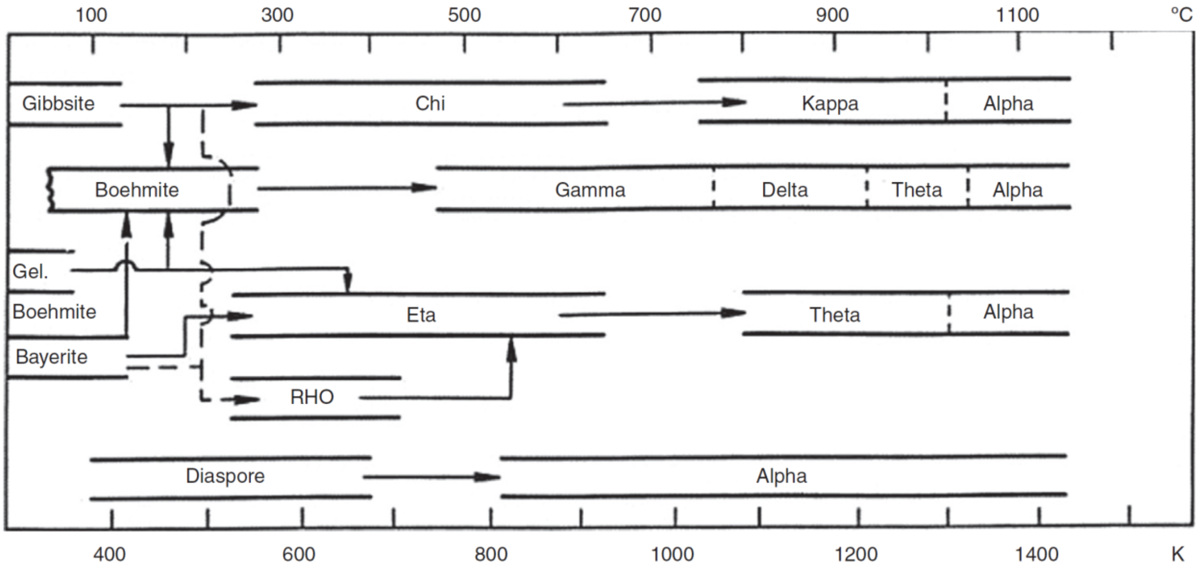

Figure 2-1 Séquence de transformation des alumines hydratées jusqu'à la phase stable α-Al_2O_3 [Wefers et Misra, 1987]

Dans la cellule d'électrolyse, l'alumine de grade métallurgique est acheminée de façon semi-continue par des « briseurs-alimenteurs ». Ces dispositifs exercent la fonction de percer la croûte d'anode et le bain solidifié afin d'y laisser passer l'alumine. L'Al_2O_3 est ensuite réduite en aluminium (Al) en utilisant le bain électrolytique liquide. Le courant électrique est fourni à la cellule d'électrolyse et il est distribué entre les différentes anodes consommables qui sont immergées dans le bain liquide. Les ions oxyde formés à partir de la dissolution de l'alumine réagissent à la surface des anodes de carbone, libérant ainsi du dioxyde de carbone (CO_2). L'aluminium est produit à la cathode électrochimique, qui est la surface supérieure de l'aluminium liquide. L'équation 2-1 est la réaction électrochimique globale se produisant dans la cellule d'électrolyse [Thonstad *et al.*, 2001]:

$$2\ \mathrm{Al_2O_{3(dissous)}} + 3\ \mathrm{C_{(s)}} \xrightarrow{\text{courant}} 4\ \mathrm{Al_{(l)}} + 3\ \mathrm{CO_{2(g)}} \qquad (2\text{-}1)$$

2.1.2 Description générale des composantes de la cellule d'électrolyse

Les principales composantes d'une cellule d'électrolyse moderne comprennent les anodes de carbone précuites, le bain électrolytique fondu avec de l'alumine dissoute (appelée bain liquide), l'aluminium liquide et les blocs cathodiques en carbone graphitisé. Le courant électrique circule à travers les anodes consommables qui sont immergées dans le bain liquide pour produire l'aluminium. Les blocs cathodiques sont recouverts par de l'aluminium liquide qui s'étend au fond de la cellule d'électrolyse. Finalement, le courant électrique rejoint les barres collectrices et le réseau de barres externes qui se connecte à la prochaine cellule d'électrolyse d'aluminium de la série (voir Figure 2-2).

La section du dessus de la cellule d'électrolyse englobe tout ce qui est plus élevé que le bain électrolytique liquide. Par conséquent, cette zone inclut l'ensemble anodique (anode, rondins, traverse, renfort et tige d'anode) et le recouvrement anodique. Les parties externes de la cuve qui sont exposées à l'environnement de la salle d'électrolyse, telles que les capots et la superstructure, sont aussi incluses dans les composantes supérieures. La Figure 2-2 présente un schéma général du procédé Hall-Héroult, avec les composantes d'intérêts en rouge.

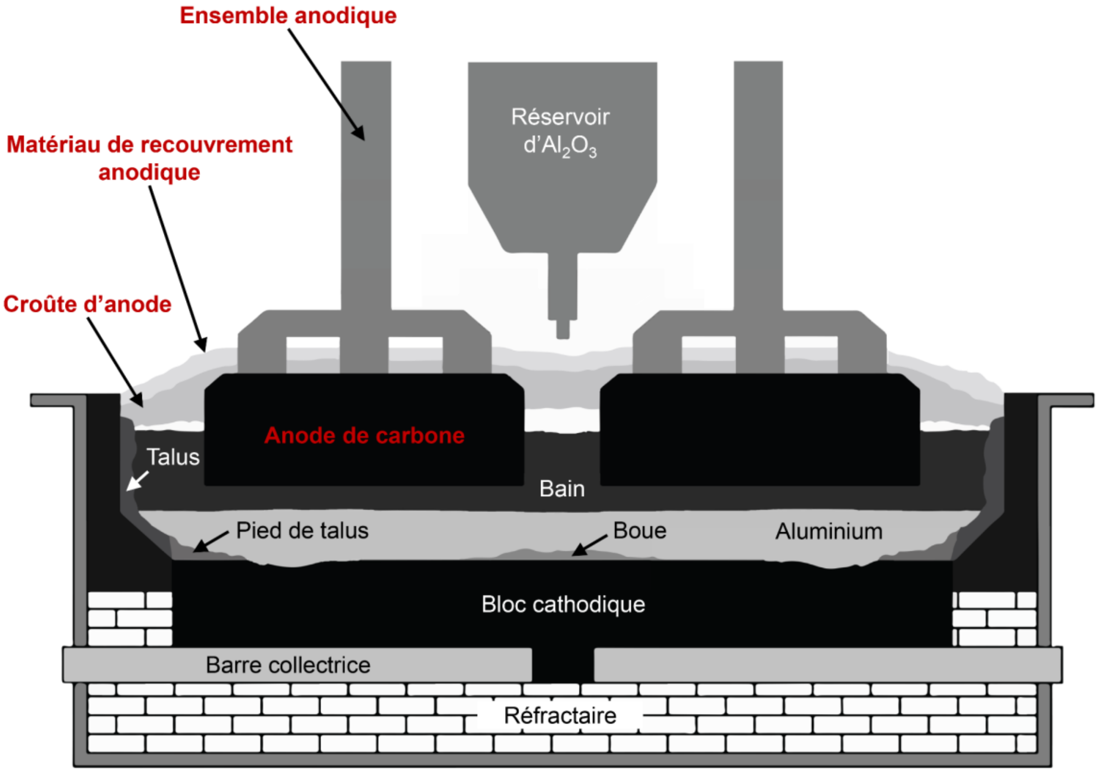

Figure 2-2 Schéma général du procédé Hall-Héroult

L'anode de carbone est reliée aux parties de l'ensemble anodique par un scellement à la fonte. Lors de la préparation de l'ensemble anodique, la tige d'anode métallique, la traverse et les rondins sont placés dans les trous de l'anode de carbone. Par la suite, la fonte liquide est coulée pour supporter l'anode en la reliant aux rondins d'acier [Thonstad *et al.*, 2001]. Selon les technologies, la forme des ensembles anodique peut varier et ils peuvent contenir d'un à six rondins. Les anodes consommables sont remplacées tous les 20 à 30 jours environ, selon la masse des anodes, la teneur en carbone et le courant utilisé dans le procédé [Sørlie et Øye, 2010].

La croûte qui recouvre les anodes doit être brisée à l'aide d'un piqueur industriel afin d'effectuer un changement d'anode. Cette routine manuelle s'effectue tous les jours ou presque, dépendamment de la durée de vie des anodes et de leurs nombres dans la cellule d'électrolyse. Pour effectuer le remplacement, le piqueur brise la croûte entourant l'anode et elle est ensuite substituée par une nouvelle anode. Le bain liquide entourant la nouvelle anode est alors en contact direct avec l'anode froide et les gaz sous les capots. Dans ces conditions, le dessus du bain se solidifie. Par la suite, le matériau de recouvrement anodique poudreux est ajouté sur la nouvelle anode et sur le bain solidifié afin de protéger l'anode de l'oxydation, d'absorber une partie des gaz fluorés et d'isoler le dessus de la cellule d'électrolyse.

2.1.3 Opération de la cellule d'électrolyse

La cellule d'électrolyse fonctionne typiquement à une température d'environ 965 °C, soit 15 °C au-dessus de la température de solidification de la cryolite pour former le talus. Cette température de solidification est directement reliée à la composition chimique du bain électrolytique, qui est maintenue constante par des procédures opérationnelles.

Le bain liquide et l'aluminium sont entourés par le talus, une couche épaisse composée principalement de cryolite gelée. La cellule d'électrolyse est conçue pour dissiper la chaleur par ses côtés afin de bâtir une couche d'épaisseur appropriée pour protéger les parois latérales contre le bain liquide, qui est hautement corrosif et érosif. Par conséquent, la génération d'énergie et la dissipation thermique de la cellule d'électrolyse sont contrôlées finement afin de maintenir un bilan thermique favorable à l'efficacité du procédé et à la durée de vie de ses composantes, qui atteint normalement quelques années.

La dissipation thermique dépend des matériaux composant la cellule d'électrolyse d'aluminium et entourant celle-ci. Typiquement, le côté de la cellule d'électrolyse est composé d'un revêtement de réfractaire en carbure de silicium (SiC) et de pâte de carbone. La partie du bas contient des blocs de carbone graphitisés, de la pâte de carbone, des matériaux isolants et des briques réfractaires. Ces composantes de la cellule d'électrolyse sont assemblées dans un caisson d'acier qui est renforcé par des berceaux.

La section du dessus de la cellule d'électrolyse comprend principalement les ensembles anodiques et le recouvrement anodique. Les propriétés thermiques et électriques des anodes de carbone varient selon leurs compositions et leur température de cuisson dans les fours. Ensuite, les propriétés des composantes métalliques des ensembles anodiques (tige d'anode, traverse, rondins) dépendent des alliages choisis lors du design des cellules d'électrolyse. Une des parties les plus complexes de la section du dessus est le recouvrement anodique. Les propriétés thermiques de ce matériau à changement de phase varient dans le temps et selon son degré de transformation. Composant le recouvrement anodique, le matériau de recouvrement anodique poudreux, ou *anode cover material* (*ACM*) en anglais, se transforme en le matériau solide appelé croûte d'anode.

2.1.4 Dissipation thermique au-dessus de cellules d'électrolyse d’aluminium

Afin de présenter l’état des travaux antérieurs au sujet des propriétés et de la dissipation thermique des composantes situées au-dessus des cellules d’électrolyse d’aluminium, la revue de littérature qui suit couvre les principaux thèmes suivants :

- Matériau de recouvrement anodique et croûte d’anode
- Matériaux composant les ensembles anodiques
- Modélisation numérique de la cellule d’électrolyse
- Modélisation avec l’emphase sur le dessus de la cellule d’électrolyse

Le recouvrement anodique est le principal élément responsable d’isoler le dessus des cellules d’électrolyse. Il s’agit d’un matériau complexe comprenant une multitude de phases cristallines, ainsi qu’une fraction de bain électrolytique à l’état liquide. Par ailleurs, ce matériau recouvre partiellement les ensembles anodiques qui sont ensuite décrits dans l’état de l’art. Une fois les propriétés de ces matériaux abordés, les modèles numériques qui sont utilisés pour prédire certains phénomènes physiques présents dans la cellule d’électrolyse sont décrits de façon générale. Finalement, les modèles qui mettent l’emphase sur la prédiction thermique des composantes supérieures de la cellule d’électrolyse sont exposés en détail. Ainsi, cette revue de la littérature présente les informations qui permettent de comprendre à la fois les propriétés des matériaux et les phénomènes de transfert de chaleur se déroulant au-dessus de la cellule d’électrolyse.

2.2 Matériau de recouvrement anodique et croûte d’anode

2.2.1 Matériaux de recouvrement anodique

Au cours du siècle dernier, la composition du matériau de recouvrement anodique (*ACM*) est passée de l’alumine uniquement [Less, 1977; Johnston et Richards, 1983], à un mélange d’alumine et de bain électrolytique. Depuis les dernières décennies, ce mélange compose l’*ACM* qui est utilisé dans les technologies de cellules d’électrolyse utilisant des anodes précuites [Taylor, 2007]. En 1998, la composition chimique de l’*ACM* la plus fréquemment utilisée dans les usines contenait de 33 à 50 % d’alumine et 50 à 67 % de croûte d’anode récupérée [Richards, 1998].

Les méthodes de fabrication de l'*ACM* varient selon les usines. Entre autres, la croûte d'anode qui est récupérée provient du dessus des anodes qui ont été consommées par le procédé d'électrolyse (Figure 2-3).

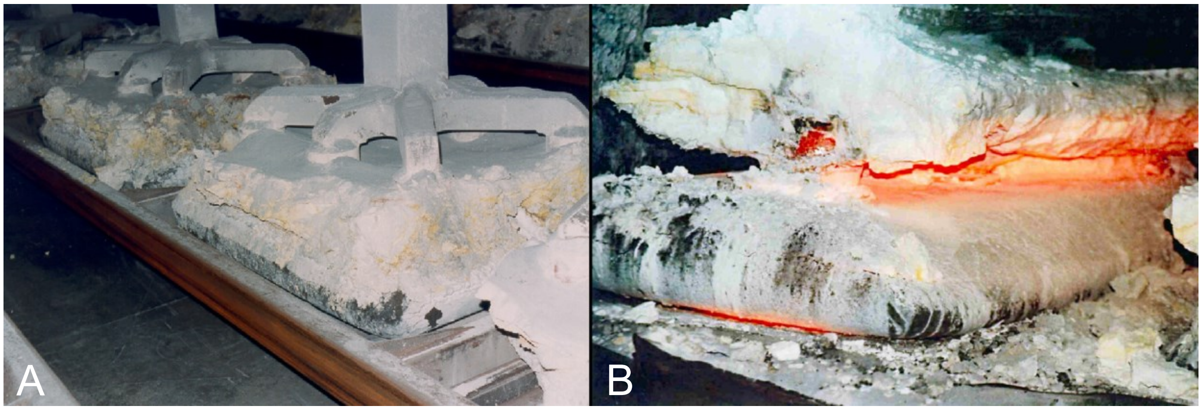

Figure 2-3 Anodes consommées et retirées de la cellule d'électrolyse [Wilkening *et al.*, 2005]

La partie A de la Figure 2-3 présente une anode consommée et la croûte d'anode qui est restée relativement intacte. La partie B présente un exemple d'inondation de l'anode par le bain électrolytique liquide, occasionnant une fonte du dessous de la croûte d'anode. L'inondation de l'anode est une situation irrégulière et elle mène à la dégradation des rondins d'acier et de la croûte d'anode. En plus de la croûte d'anode, le bain peut aussi être récupéré et broyé pour fabriquer l'*ACM*. Lors de sa préparation, la plupart des usines utilisent un séparateur magnétique pour retirer les particules de fer des matériaux broyés [Richards, 1998]. La Figure 2-4 présente un procédé simplifié pour préparer l'*ACM*.

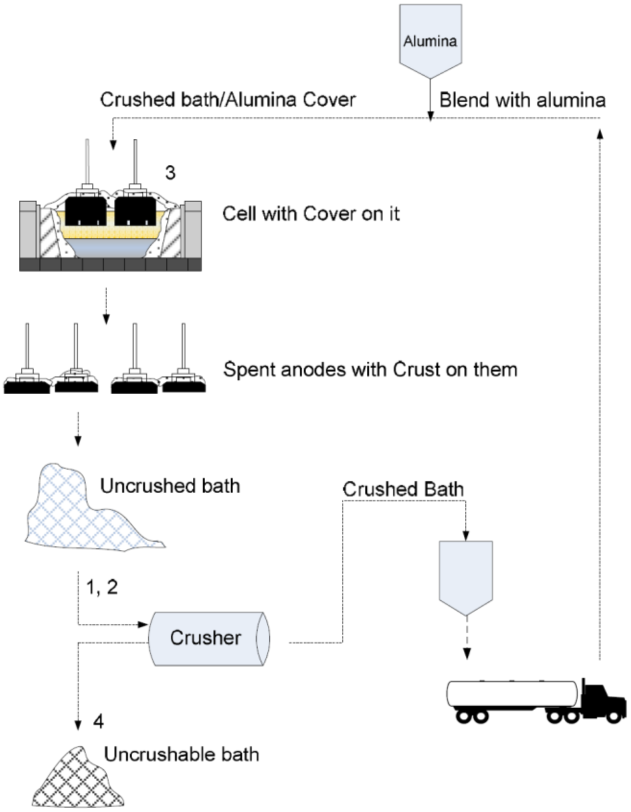

Figure 2-4 Procédé de préparation de l'*ACM* [Groutso *et al.*, 2009]

Afin de donner un aperçu de la proportion des matériaux utilisés pour fabriquer l'*ACM*, le bilan de masse du procédé de fabrication d'*ACM* de l'usine Rheinwerk en Allemagne (235 000 t Al / an) a été détaillé dans le Tableau 2-1.

Tableau 2-1 Bilan de masse du procédé de préparation de l'*ACM* [Eick *et al.*, 2010]

Masse (t)	Produit
58 000	SACM (secondary or used ACM)
31 000	CCM (cavity-cleaning material)
7000	lumps from the autogenous grinding mill
6000	PB (pure tapped bath)
2900	floor and basement cleaning
3000	skimming and crucible cleaning
1100	crust from stopped pots
109 000	recycled material
12 000	reacted alumina
121 000	PACM (primary anode cover material)

La matière première pour fabriquer l'*ACM* provient de différentes sources, occasionnant une insertion importante de différents contaminants. Les contaminants magnétiques peuvent être retirés par des séparateurs magnétiques placés dans le procédé de fabrication. Toutefois, l'aluminium et le carbone sont non magnétiques et ils demeurent plus difficiles à séparer.

Néanmoins, la composition chimique de l'*ACM* moderne peut être décrite globalement par un mélange de bain électrolytique avec de l'Al_2O_3.

2.2.2 Formation de la croûte d'anode

Les mécanismes de formation de la croûte ont été étudiés par plusieurs chercheurs dans les dernières décennies. Premièrement, la formation de croûte a été évaluée en laboratoire avec de l'*ACM* composé uniquement d'Al_2O_3 [Less, 1977; Johnston et Richards, 1983; Townsend et Boxall, 1984; Oedegard *et al.*, 1985; Llavona *et al.*, 1990; Eggen *et al.*, 1992]. Selon Less, les vapeurs fluorées émises par le bain favorisent la conversion de la phase γ-Al_2O_3 à la phase stable α-Al_2O_3. Il a démontré expérimentalement que la transformation de γ-Al_2O_3 (phase de transition) en α-Al_2O_3 favorise la formation d'un réseau de cristaux imbriqués les uns dans les autres (plaquettes hexagonales de la Figure 2-5).

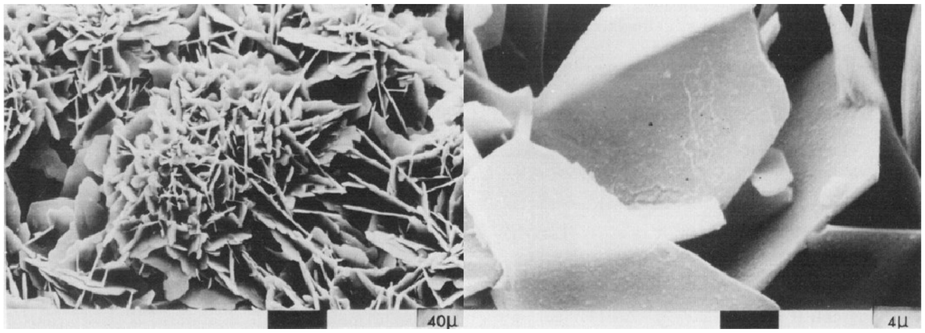

Figure 2-5 Réseau de particules α-Al_2O_3 dans un bain de cryolite [Less, 1977]

Ce réseau de particules alpha imbriquées augmente la résistance de la croûte à l'effondrement [Liu *et al.*, 1992]. La formation de ce réseau de particules est favorisée par la présence d'alumine de transition (γ-Al_2O_3) et ce phénomène est atténué lorsque le taux de α-Al_2O_3 dans l'*ACM* augmente. L'utilisation d'Al_2O_3 qui a déjà réagi avec les vapeurs de bain électrolytique ou qui est composé majoritairement de particules fines diminue le taux de formation de la croûte [Townsend et Boxall, 1984]. La formation de la croûte d'anode est initiée lorsque le bain pénètre dans l'*ACM* [Gerlach et Winkhaus, 1985], un phénomène illustré dans la Figure 2-6.

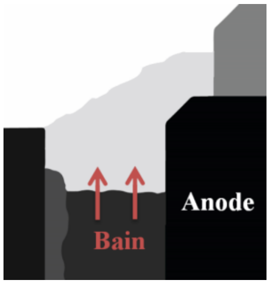

Figure 2-6 Pénétration du bain dans l'*ACM*

Le bain pénètre à l'intérieur de la poudre d'Al_2O_3 dans la direction inverse de la gravité par les forces capillaires [Eggen *et al.*, 1992]. La pénétration du bain favorise la formation d'une croûte composée de particules de α-Al_2O_3 imbriquées et entourées de bain solidifié. La formation de croûte dans les cellules d'électrolyse industrielles, utilisant un mélange de bain et d'Al_2O_3 pour fabriquer l'*ACM*, a été étudiée par très peu de chercheurs. En 1992, Liu *et al.* ont évalué la formation de la croûte située entre l'anode et la paroi latérale de la cellule d'électrolyse. Cette formation a été mesurée à l'aide de thermocouples placés initialement dans l'*ACM* (Figure 2-7).

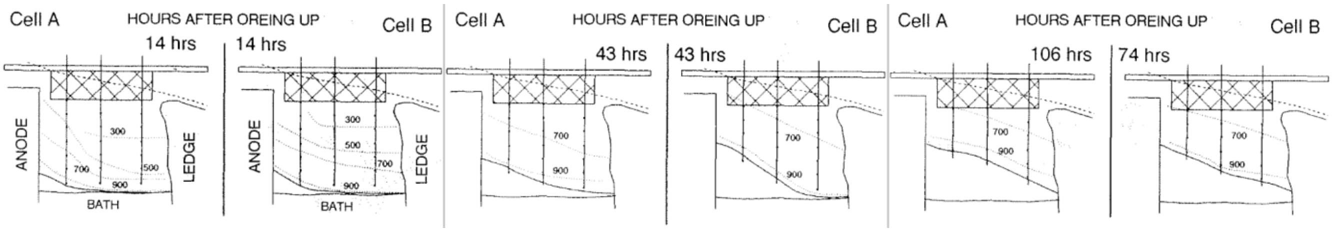

Figure 2-7 Évaluation de la température dans la croûte [Liu *et al.*, 1992].

Selon les mesures prises par les thermocouples, l'*ACM* poudreux se transforme en une croûte solide à partir d'environ 700 °C et la croûte d'anode devrait fondre à une température d'environ 900 °C [Liu *et al.*, 1992].

2.2.3 Composition chimique de la croûte d'anode

Les échantillons de croûte ont été analysés qualitativement par diffractométrie de rayons X (DRX) et quantitativement par des méthodes de chimie humide par Liu *et al.* [Liu *et al.*, 1992]. Ces analyses ont démontré l'existence de phase liquide dans la croûte à une température de 740 °C et la présence d'un gradient d'AlF_3 dans la croûte. La phase liquide est engendrée par la fonte de la chiolite ($Na_5Al_3F_{14}$). En 2009, Groutso *et al.* ont aussi étudié la composition chimique de la croûte d'anode. Ils ont présenté la morphologie de la croûte par microscopie électronique à balayage (MEB) et démontré la présence d'une faible quantité de cryolite de calcium ($Na_2Ca_3Al_2F_{14}$) dans la croûte (<10 %). La croûte d'anode forme une matrice de particules d'alumine (α-Al_2O_3) imbriquées dans des cristaux de $Na_5Al_3F_{14}$, $Na_2Ca_3Al_2F_{14}$ et de Na_3AlF_6. La résistance au broyage de cette matrice est très élevée [Groutso *et al.*, 2009]. En 2013, Zhang *et al.* ont évalué la composition chimique de plusieurs échantillons industriels. Ils ont démontré le gradient de chiolite dans la croûte et ont illustré la formation de stalactite sous la croûte (Figure 2-8).

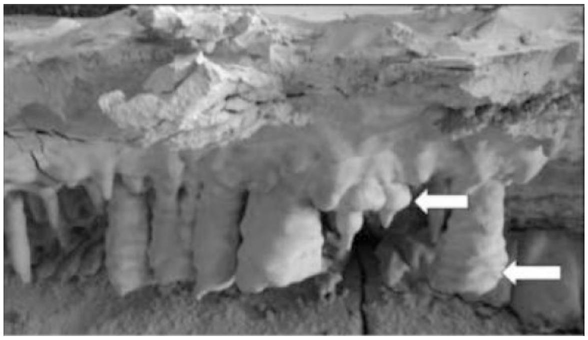

Figure 2-8 Cristaux de la forme de stalactite [Zhang *et al.*, 2013]

Les cristaux de la forme de stalactites sont causés par des vagues de bain électrolytique qui frappent le dessous de la croûte. Le bain électrolytique gèle rapidement et refond par la suite en coulant, occasionnant la formation stalactites de texture microcristalline [Zhang *et al.*, 2013]. Les macroporosités dans la croûte créent un passage pour la diffusion des vapeurs et des phases liquides provenant du bain électrolytique.

La fonte et l'effondrement de la croûte occasionnent divers problèmes qui déstabilisent l'opération de la cellule d'électrolyse. Lorsque la croûte s'effondre, les anodes de carbone et le bain électrolytique deviennent en contact avec l'air et les émissions provenant de la cellule d'électrolyse ne sont plus captées par la croûte. De plus, la croûte n'a pas le temps d'être dissoute par le bain liquide et elle va atteindre le fond de la cellule d'électrolyse pour former des dépôts qui restreignent le passage du courant (boue et pied de talus) [Geay *et al.*, 2001; Allard *et al.*, 2014].

2.2.4 Émissions provenant de la cellule d'électrolyse

Les émissions de la cellule d'électrolyse incluent les vapeurs de bain électrolytique et les gaz formés par l'électrolyse. Tout d'abord, la réaction de réduction de l'Al_2O_3 en aluminium produit du CO_2 et du CO, gaz engendrés par la consommation de l'anode. De plus, il y a production de $C_2F_{6(g)}$ et de $CF_{4(g)}$ dans des conditions d'effet anodique [Thonstad *et al.*, 2001]. L'effet anodique se produit lorsque la concentration locale d'Al_2O_3 dissout dans le bain électrolytique n'est plus suffisante pour alimenter l'électrolyse. Alors, le bain d'électrolyse se décompose, d'où la formation de fluorocarbures.

Du côté du bain cryolitique, la principale espèce composant sa vapeur est le $NaAlF_{4(g)}$ [Kvande, 1983]. Cette espèce chimique, métastable à l'état solide, a été identifiée pour la première fois en 1954 par Howard *et al.*, en effectuant la trempe des vapeurs condensées [Howard *et al.*, 1954]. Les vapeurs de $NaAlF_4$ diffusent à l'intérieur de la croûte d'anode [Zhang *et al.*, 2013], telle qu'illustrée par la Figure 2-9.

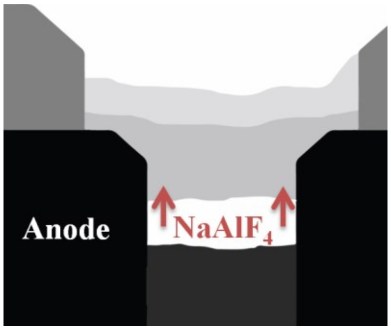

Figure 2-9 Diffusion des vapeurs dans la croûte et l'*ACM*

La phase $NaAlF_4$, synthétisée à partir de vapeur, est thermodynamiquement stable uniquement entre 690 °C et 730 °C [Kirik et Zaitseva, 2010]. En pénétrant dans la croûte, les vapeurs de $NaAlF_4$ se décomposent en chiolite ($Na_5Al_3F_{14}$) et en AlF_3. Ce phénomène occasionne l'acidification de la croûte et la dilution de la concentration d'Al_2O_3. Gaertner *et al.* ont décrit les principales réactions engendrées par la production de $NaAlF_{4(g)}$ [Gaertner *et al.*, 2011].

$$Na_3AlF_{6(l)} \leftrightarrows NaAlF_{4(g)} + 2\ NaF_{(l)} \qquad (2\text{-}2)$$

$$5\ NaAlF_{4(g)} \leftrightarrows Na_5Al_3F_{14(s)} + 2\ AlF_{3(s)} \qquad (2\text{-}3)$$

$$3\ NaAlF_{4(g;s)} + 3\ H_2O_{(g)} \leftrightarrows 6\ HF_{(g)} + Na_3AlF_{6(s)} + Al_2O_{3(s)} \qquad (2\text{-}4)$$

$$2\ AlF_{3(diss)} + 3\ H_2O_{(g;diss)} \leftrightarrows 6\ HF_{(g)} + Al_2O_{3(s;diss)} \qquad (2\text{-}5)$$

$$3\ Na_5Al_3F_{14(s)} + 6\ H_2O_{(g)} \leftrightarrows 12\ HF_{(g)} + 5\ Na_3AlF_{6(s)} + 2\ Al_2O_{3(s;diss)} \qquad (2\text{-}6)$$

La cryolite produit des vapeurs de $NaAlF_4$ et du $NaF_{(l)}$ qui demeure dans le bain électrolytique. En contact avec des hydrates d'Al_2O_3 ou de la vapeur d'eau provenant de l'air, les vapeurs de $NaAlF_4$, la chiolite ou l'AlF_3 vont produire du $HF_{(g)}$ ainsi que de la $Na_3AlF_{6(s)}$ et de l'$Al_2O_{3(s)}$.

La production d'$HF_{(g)}$ a été étudiée et modélisée par Yang *et al.* en 2014. Ils ont mesuré des concentrations entre 3000 et 5000 ppm de HF dans le trou de siphonnage et entre 9000 et 10 000 ppm dans un trou sous l'alimenteur d'Al_2O_3, un endroit où il y avait une flamme [Yang *et al.*, 2014]. La Figure 2-10 présente les endroits où ces mesures ont été prises.

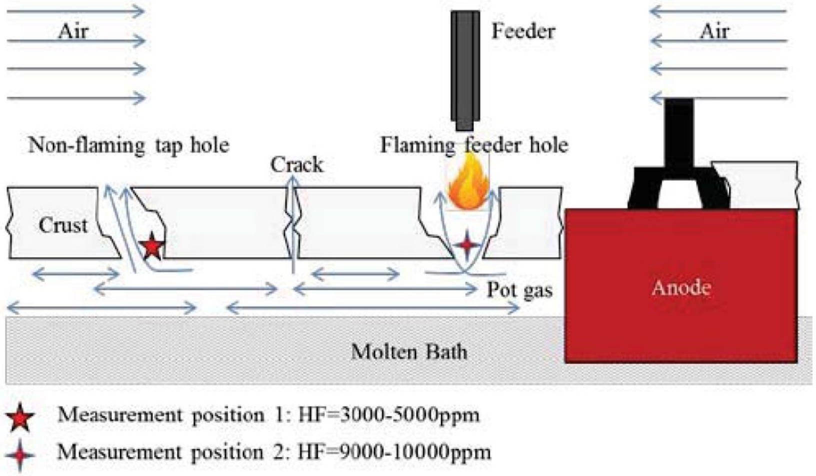

Figure 2-10 Mesures de HF émis par la cellule d'électrolyse [Yang *et al.*, 2014]

L'émission de HF peut atteindre entre 9 et 16 kg/t Al lorsque la croûte est en mauvaise condition [Yang *et al.*, 2014]. La croûte doit demeurer en bonne condition afin d'éviter l'augmentation de la production de $HF_{(g)}$.

2.2.5 Propriétés thermodynamiques du bain électrolytique et de l'alumine

Le système $NaF\text{-}AlF_3\text{-}CaF_2\text{-}Al_2O_3$ a été étudié par plusieurs chercheurs dans les dernières décennies. L'*ACM* et la croûte d'anode sont des matériaux sursaturés en Al_2O_3. Ils possèdent des ratios molaires de cryolite pouvant varier entre 1.2 et 2.8 [Zhang *et al.*, 2013]. Le logiciel FactSage permet de prédire le comportement de ces matériaux en se basant sur les précédentes études thermodynamiques et thermochimiques [Chartrand et Pelton, 2002]. Le taux de saturation d'Al_2O_3 dans le bain électrolytique a été déterminé par Skybakmoen *et al.* en 1997. Le système $NaF\text{-}AlF_3\text{-}CaF_2\text{-}Al_2O_3$ avec des additifs ou contaminants a été étudié par plusieurs auteurs [Craig et Brown, 1980; Peterson et Tabereaux,1994; Tissot, 1994; Solheim *et al.*, 1996; Zaitseva *et al.*, 2009; Apisarov *et al.*, 2010], pour n'en nommer que quelques-uns. Les changements de phases dans le système $NaF\text{-}AlF_3\text{-}CaF_2\text{-}Al_2O_3$ ont été principalement étudiés avec un ratio de cryolite variant de 1.5 à 3.0. Il y a très peu d'études avec des ratios de cryolite basique ($CR > 3.0$) ou plus bas que 1.5 [Chartrand et Pelton, 2002]. Typiquement, les bains électrolytiques industriels standards ont un ratio de cryolite d'environ 2.2 [Utigard, 1999].

2.2.6 Granulométrie, densité et propriétés thermiques de l'*ACM* et de la croûte

L'*ACM* et la croûte recouvrent presque totalement le dessus de la cellule d'électrolyse. Ces matériaux exercent donc un impact majeur sur les pertes de chaleur par le dessus. La densité, la température et la granulométrie des matériaux de recouvrement anodique influencent la conductivité thermique. La densité et les propriétés de la croûte fabriquée en laboratoire ont été étudiées par différents chercheurs [Johnston et Richards, 1983; Hatem *et al.*, 1989; Llavona *et al.*, 1990; Rye, 1992]. La conductivité de l'Al_2O_3 polycristalline (99.5 %) et dense diminue avec la température [Powell *et al.*, 1966]. Toutefois, lorsque l'Al_2O_3 ou l'*ACM* est sous forme de poudre, la conductivité thermique augmente avec la température [Shen, 2006]. Le Tableau 2-2 établit les équations pour calculer la conductivité thermique de l'*ACM*, valable pour une plage de température allant de 160 °C à 600 °C. En général, la conductivité thermique augmente lorsque la densité des matériaux augmente, ou lorsque la fraction de vide diminue.

Tableau 2-2 Conductivité thermique de l'*ACM* et de mélanges de bain broyés [Shen, 2006]

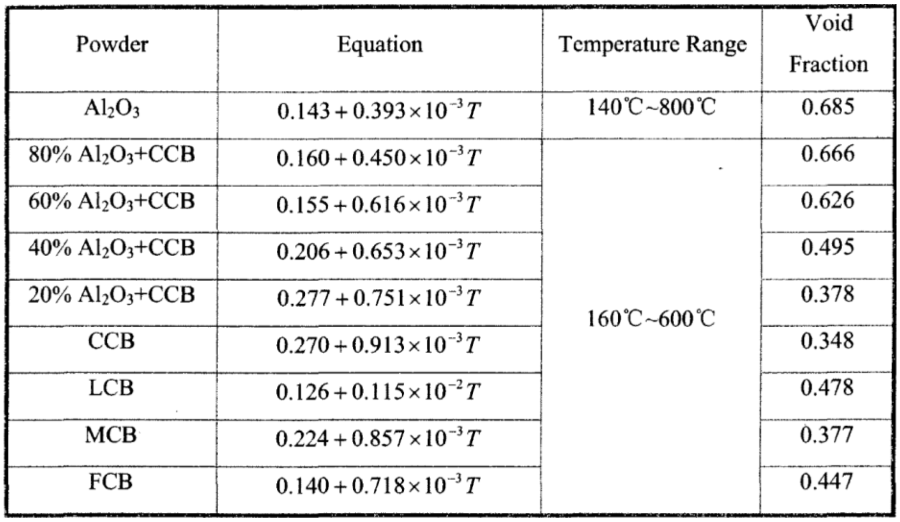

Powder	Equation	Temperature Range	Void Fraction
Al_2O_3	$0.143+0.393\times10^{-3}T$	140℃~800℃	0.685
80% Al_2O_3+CCB	$0.160+0.450\times10^{-3}T$	160℃~600℃	0.666
60% Al_2O_3+CCB	$0.155+0.616\times10^{-3}T$		0.626
40% Al_2O_3+CCB	$0.206+0.653\times10^{-3}T$		0.495
20% Al_2O_3+CCB	$0.277+0.751\times10^{-3}T$		0.378
CCB	$0.270+0.913\times10^{-3}T$		0.348
LCB	$0.126+0.115\times10^{-2}T$		0.478
MCB	$0.224+0.857\times10^{-3}T$		0.377
FCB	$0.140+0.718\times10^{-3}T$		0.447

Coarse crushed bath (CCB), large crushed bath (LCB), medium crushed bath (MCB), fine crushed bath (FCB)

La conductivité thermique de la croûte d'anode se situe typiquement entre 1.0 et 2.0 W/m·K considérant une densité allant de 2.0 à 2.5 g/cm^3 [Shen, 2006]. En 2011, Wijayaratne *et al.* ont évalué la conductivité thermique selon la composition et la granulométrie, toutefois en donnant les valeurs de façon relative. La conductivité thermique des croûtes fabriquées en laboratoire diminue avec la température [Hatem *et al.*, 1989; Shen, 2006]. Les croûtes d'anodes prélevées dans des cuves industrielles présentent une conductivité thermique comparable à celles faites en laboratoire [Llavona *et al.*, 1990; Shen, 2008]. À la connaissance de l’auteur, la conductivité thermique de la croûte d’anode n’a jamais été déterminée à des températures dépassant significativement 600 °C, malgré que la température vécue par la croûte industrielle s’élève jusqu’à environ 900 °C.

Le comportement très corrosif des composés fluorés présents dans la croûte anodique rend difficile l’analyse à haute température. À partir d’une température de 700 °C, les liquides et vapeurs fluorés peuvent endommager les composantes de l’appareil à fil chaud, servant à la détermination de la conductivité thermique [Llavona *et al.*, 1990]. La conductivité thermique des croûtes fabriquées en laboratoire a été étudiée à l'aide de thermocouples et d'un capteur de flux thermique [Rye, 1992; Rye *et al.*, 1995]. Selon ces résultats, la conductivité thermique du bas de la croûte est plus élevée et cette valeur diminue vers le haut. Les croûtes fabriquées en laboratoire à partir d’un mélange incluant uniquement de l’alumine possèdent une conductivité thermique inférieure à celles faites à partir d’un mélange de bain broyé et d'alumine.

En 2014, Zhang *et al.* ont décrit le comportement de la croûte d’anode à l’aide d’un montage expérimental reproduisant un appareil d’analyse thermodifférentielle (*DTA*). Ils ont décrit sommairement le comportement et les réactions en fonction de la température évoluant dans ce matériau, en se basant sur les mesures industrielles faites par Liu *et al.* en 1992.

2.3 Matériaux composant les ensembles anodiques

Les ensembles anodiques sont composés principalement par le bloc de carbone (la partie consommable), les rondins d’acier, la traverse et la tige d’anode. La tige d’anode et la traverse sont reliées par un renfort ou encore par un connecteur intermétallique, selon la technologie de cellule d’électrolyse. La tige d’anode peut être fabriquée en cuivre ou en aluminium, tandis que les rondins et la traverse sont en acier. Pour assembler les composantes, les rondins d’acier sont placés dans des trous préformés dans l’anode de carbone et ils sont scellés avec de la fonte liquide. La Figure 2-11 présente un exemple d’ensemble anodique, provenant pour ce cas d’une technologie opérant avec des anodes précuites.

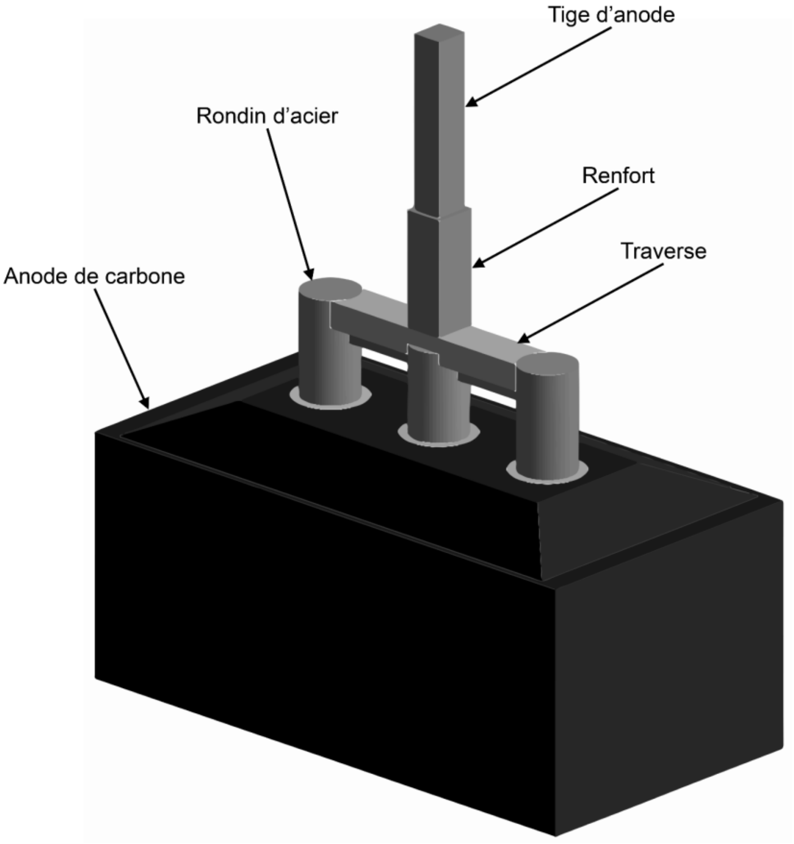

Figure 2-11 Schéma d'un ensemble anodique à trois rondins

Les anodes précuites sont fabriquées à partir de coke de pétrole (coproduit des raffineries de pétrole) et de grains de mégots d'anode [Fischer and Perruchoud, 1986]. Elles sont maintenues ensemble par le brai (une substance pâteuse et collante qui sert de liant). L'anode précuite est fabriquée à partir d'environ 65 % d'agrégat de coke de pétrole, 15 % de brai liquide et 20 % de mégots d'anode concassée [Fisher *et al.*, 1995; Fortin, 2009]. Ce mélange est moulé et ensuite placé dans des fours à cuisson. Les anodes sont cuites à une température atteignant environ 1100 °C. Une fois prêtes, après scellement des tiges avec la fonte, les anodes sont installées dans la cellule d'électrolyse et suspendues par le cadre anodique.

Les effets de la température de cuisson sur les propriétés de l'anode de carbone ont été résumés par les travaux de Dreyer *et al*. en 1996.

En augmentant la température de cuisson :

- le niveau de cristallinité augmente,
- la résistivité électrique diminue,

- la porosité augmente, selon l'évolution des espèces souffrées,
- la réactivité à l'air diminue considérant une plage typique de calcination,
- le coefficient d'expansion thermique diminue.

La Figure 2-12 présente la résistivité électrique de l'anode en fonction de la température de cuisson.

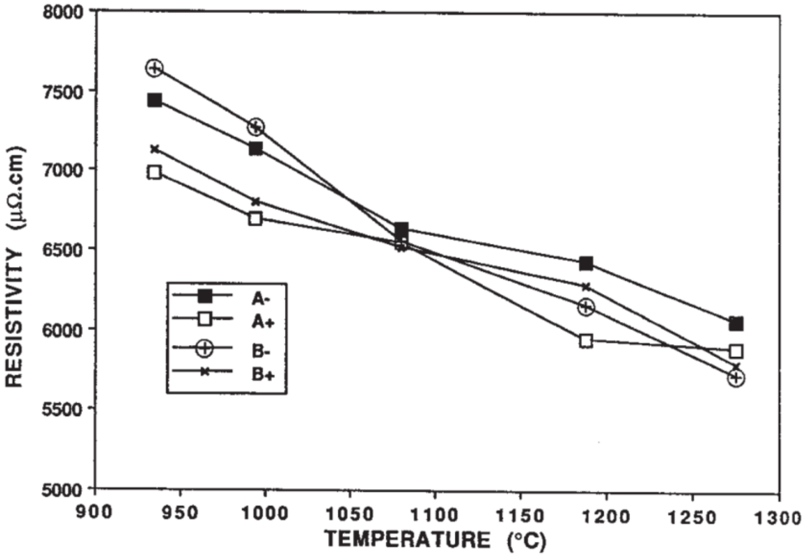

Figure 2-12 Résistivité électrique de l'anode précuite selon la température de cuisson [Dreyer *et al.*, 1996]

Plus récemment, une méthode alternative pour déterminer les propriétés électriques des anodes a été développée [Rouget *et al.*, 2017]. Cette méthode développée par Van der Pauw en 1958 permet de déterminer la conductivité électrique d'échantillon caractérisé par une forme arbitraire ou possédant des fissures. La méthode standard ISO 11713 s'effectue en appliquant un courant de 1 ampère (A) et en mesurant la perte de potentiel électrique [ISO, 2000]. La méthode de Van der Pauw offre l'avantage d'être plus fiable et répétable que la méthode standard. La précision de la méthode de Van der Pauw en présence de fissures a aussi été validée par la méthode des éléments finis.

Les propriétés thermiques des anodes varient selon la composition et les méthodes de fabrication. Plus précisément, la conductivité thermique de l'anode de carbone augmente avec la température finale de cuisson, selon les résultats présentés dans la Figure 2-13A [Fischer et Perruchoud, 1987]. Ces résultats ont aussi été confirmés par Perruchoud *et al.* en 2001, voir Figure 2-13B. Les courbes ci-dessous représentent l'influence de la température finale de cuisson sur la conductivité thermique des anodes précuites, ce qui a été déterminée par la méthode ASTM C767 (*standard method of test for thermal conductivity of carbon refractories*).

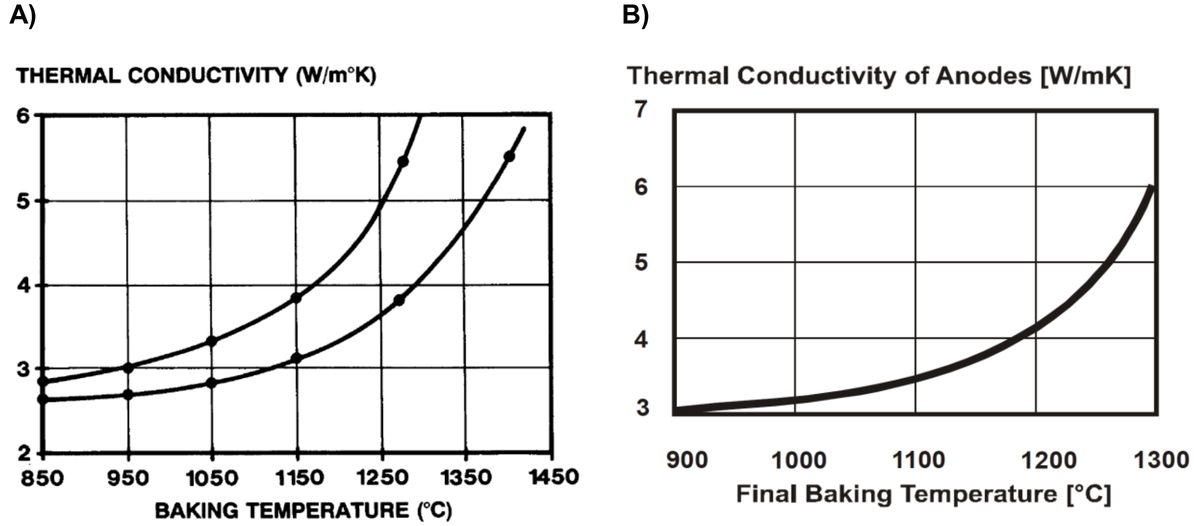

Figure 2-13 A) Conductivité thermique de l'anode précuite selon la température de cuisson [Fischer et Perruchoud, 1987] et B) Conductivité selon la température finale de cuisson [Perruchoud *et al.*, 2001]

La conductivité thermique des anodes est directement reliée à la densité. Une augmentation de la densité de l'anode de 0.01 g/cm^3 engendre une augmentation de la conductivité thermique de 0.1 W/m·K [Perruchoud *et al.*, 2001]. La majorité des anodes utilisées mondialement, selon l'étude de Perruchoud *et al.*, avait une conductivité thermique se situant entre 3 et 5 W/m·K. Certaines usines utilisent des anodes avec des rainures pour laisser circuler les bulles de CO_2 formées par la réaction d'électrolyse. Ces anodes rainurées ont un faible impact sur le transfert thermique lorsqu'elles sont comparées avec des anodes pleines. [Yang *et al.*, 2014].

Ces propriétés thermiques et électriques permettent d'alimenter des modèles, tel que le modèle transitoire présenté par Gunasegaram et Molenaar en 2013. L'objectif de ce modèle thermique-électrique-mécanique était d'étudier les contraintes mécaniques et thermiques lors de l'assemblage des composantes de l'anode et aussi de valider son comportement à des températures d'opération dans la cellule d'électrolyse. La section suivante détaille les travaux qui portent sur la simulation des cellules d'électrolyse et de ses composantes.

2.4 Modélisation numérique de la cellule d'électrolyse

2.4.1 Introduction aux équations représentant les phénomènes thermiques

La modélisation complète de la cellule d'électrolyse est très complexe puisqu'il y a une multitude de phénomènes chimique, électrochimique, électrique, électromagnétique, mécanique et thermique. Dans le cadre de ce projet, les phénomènes de transfert de chaleur, de conduction électrique et les réactions thermochimiques se déroulant à l'équilibre thermodynamique sont intégrés dans les modèles thermiques-électriques. Cette section présente, en résumé, les fondations des équations du transfert thermique jusqu'à l'application de la théorie aux modèles thermiques-électriques.

Les modes de transport de l'énergie

Dans un système, la chaleur est transportée par la conduction, la convection et le rayonnement thermique. La conduction dans un milieu est directement liée au phénomène de diffusion thermique, qui est provoqué par une différence de température présente dans un domaine continu ou encore entre deux régions en contact direct. Physiquement, cette conduction représente la diffusion de l'énergie associée à l'activité moléculaire (mouvement moléculaire aléatoire) dans un milieu [Bergman *et al.*, 2011]. La conduction de chaleur, considérant une seule dimension (1D), est exprimée mathématiquement par l'équation 2-7. Cette équation est basée sur la loi de Fourier [Bird *et al.*, 2007].

$$\frac{q}{A} = k\frac{\Delta T}{\Delta y} \text{ ou } q''_y = -k\frac{\partial T}{\partial y} \tag{2-7}$$

Où q est le taux de transfert d'énergie (J/s ou W), A est l'aire (m^2), q''_y est le flux thermique (W/m^2) dans la direction y, k est la conductivité thermique (W/m·K), T est la température (K ou °C) et y la distance (m).

L'énergie peut aussi être transportée par le phénomène de convection, qui est définie par l'ensemble des mouvements dans l'espace physique qui animent un fluide. Dans le domaine de la modélisation thermique, la convection se définit plus spécifiquement par l'écoulement d'un fluide au-dessus d'une surface et considère le transfert de chaleur qui y est associé. Le transfert d'énergie se déroule lorsque le fluide en mouvement et la surface possèdent des températures différentes. Le taux de transfert d'énergie par convection (W) vers une surface est défini par l'équation 2-8 [Bergman *et al.*, 2011].

$$q''_s = h(T_s - T_\infty) \tag{2-8}$$

Où q''_s est le flux thermique (W/m^2), h est le coefficient de transfert de chaleur par convection (W/m^2·K), T_s est la température de la surface (K ou °C), T_∞ est la température du fluide (K ou °C).

Le rayonnement thermique qui est émis va interagir avec la matière par les phénomènes de réflexion, d'absorption et de transmission. La Figure 2-14 présente l'incidence du rayonnement sur un milieu semi-transparent (A) et sur un milieu opaque (B).

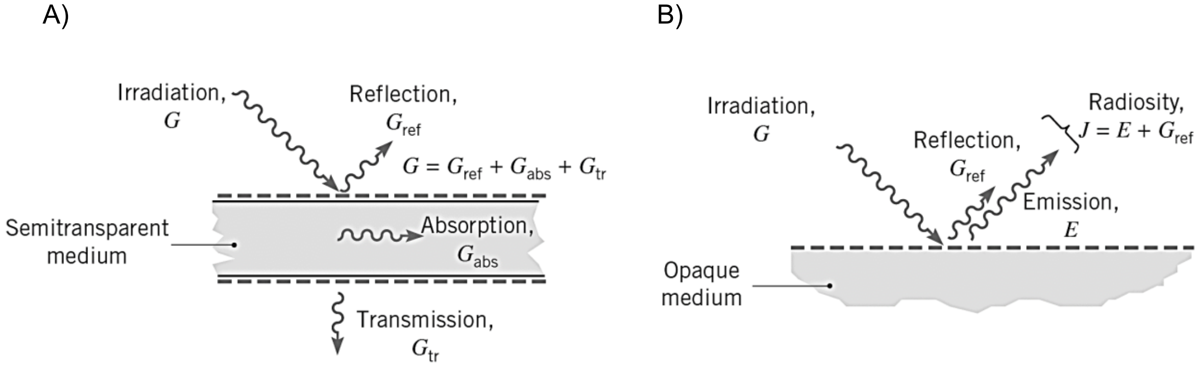

Figure 2-14 Rayonnement sur une surface : A) Réflexion, absorption et transmission du rayonnement pour un milieu semi-transparent et B) La radiosité pour un milieu opaque [Bergman *et al.*, 2011]

Le rayonnement thermique est donc en partie ou complètement réfléchi, absorbé ou transmis selon les propriétés du milieu et suivant la relation suivante :

$$\rho + \alpha + \tau = 1 \qquad (2\text{-}9)$$

Où ρ est la réflectivité, α est l'absorptivité et τ est la transmissivité. La puissance d'émission par une surface est définie par la relation suivante :

$$E = \varepsilon \sigma T_s^4 \qquad (2\text{-}10)$$

Où E est la puissance d'émission (W/m^2), ε est l'émissivité, σ est la constante de Stefan-Boltzmann ($5.67 \cdot 10^{-8}$ W/m$^2\cdot$K^4) et T_s est la température absolue de la surface (K).

Le flux thermique par rayonnement augmente donc rapidement avec la température selon l'équation 2-10. En prenant comme exemple un cas où le rayonnement se produit entre une surface et un environnement suffisamment large (les murs d'une pièce par exemple), le bilan thermique par rayonnement peut être calculé avec l'équation 2-11, en assumant que l'absorption est identique à l'émission ($\alpha = \varepsilon$) [Bergman *et al.*, 2011].

$$q''_{rad} = \varepsilon \sigma (T_s^4 - T_\infty^4) \qquad (2\text{-}11)$$

Où ε est l'émissivité, T_s est la température absolue d'une surface (K) et T_∞ est la température absolue de l'environnement (K).

Il est possible d'assumer que $\alpha = \varepsilon$ lorsqu'il s'agit d'une surface dite « grise ». Le corps gris n'absorbe qu'une partie du rayonnement qu'il reçoit, à la différence d'un corps noir qui l'absorbe totalement. De plus, l'absorptivité du corps gris est indépendante de la longueur d'onde du rayonnement électromagnétique incident. Une hypothèse généralement formulée pour simplifier les problèmes de rayonnement thermique est que la surface est diffuse, ce qui signifie qu'elle possède des propriétés indépendantes de la direction du rayonnement.

Il est possible de résoudre des problèmes complexes en utilisant le concept de radiosité (*J*), ce qui exprime le taux d'énergie par rayonnement thermique quittant une surface par unité de surface. Pour une surface opaque ($\tau = 0$), la radiosité se calcule à l'aide de l'équation 2-12.

$$J = E + \rho G \tag{2-12}$$

Où G est l'irradiation, c'est-à-dire le rayonnement qui est incident à la surface de référence. Considérant les phénomènes de conduction, de convection et de rayonnement thermique, les problèmes complexes de transfert thermique dans la cellule d'électrolyse peuvent être résolus par la méthode des éléments finis.

2.4.2 Résolution des équations par la méthode des éléments finis

Dans le cadre de ce projet, le transfert thermique et la génération de chaleur sont prédits mathématiquement en couplant les physiques thermique et électrique dans un modèle résolu par la méthode des éléments finis. Un système global d'équations algébriques est obtenu avec un assemblage d'éléments finis. La méthode des éléments finis résout les équations différentielles et intégrales en utilisant des éléments finis 3D pour les solides et des éléments 2D pour les surfaces aux conditions limites. L'ensemble des équations algébriques est développé par la méthode des résidus pondérés et la méthode de Newton-Raphson est appliquée pour résoudre ce système non linéaire. Le solveur utilise l'algorithme du gradient conjugué préconditionné (PCG), assemble la matrice de rigidité complète et calcule la solution en itérant jusqu'à la convergence. Le solveur ANSYS Mechanical et le langage APDL (ANSYS Parametric Design Language) sont utilisés pour résoudre chaque cas de simulation utile pour cette thèse.

Dans le cas de la cellule d'électrolyse d'aluminium, l'énergie est générée par l'effet Joule et elle est dissipée suivant les lois de la conduction et par convection sur les surfaces externes. Pour le cas de la dissipation thermique transitoire, l'équation 2-13 présente l'équation de conduction, avec le terme de génération de chaleur (ici par effet Joule) et le terme d'accumulation de l'énergie [Reddy et Gartling, 2010; ANSYS, 2017].

$$\rho c_p\left(\frac{\partial T}{\partial t}\right)+\frac{\partial}{\partial x}\left(k_x\frac{\partial T}{\partial x}\right)+\frac{\partial}{\partial y}\left(k_y\frac{\partial T}{\partial y}\right)+\frac{\partial}{\partial z}\left(k_z\frac{\partial T}{\partial z}\right)=\dot{q} \tag{2-13}$$

Où ρ est la densité apparente (kg/m^3), c_p la capacité thermique massique (J/kg·K), T la température (K ou °C), t le temps (s), $\dot{q}$ le taux de génération d'énergie par unité de volume (W/m^3), k la conductivité thermique (W/m·K) et x, y, z les positions dans l'espace.

Pour une analyse électrique transitoire ou en régime permanent, la chaleur générée par effet Joule dans un conducteur est décrite par l'équation 2-14, en utilisant les valeurs centroïdes du champ électrique et de la densité de courant.

$$\dot{q}=\boldsymbol{J}\cdot\boldsymbol{E} \tag{2-14}$$

Où $\boldsymbol{J}$ est le vecteur représentant la densité de courant électrique (A/m^2) et $\boldsymbol{E}$ est le vecteur représentant le champ électrique (V/m).

Le champ électrique peut quant être lui être dérivé par :

$$\boldsymbol{E}=\ -\nabla V \tag{2-15}$$

Où ∇ est l'opérateur gradient du potentiel électrique, V.

La distribution du potentiel électrique est calculée à partir de l'équation 2-16, dans laquelle la conductivité électrique (σ) dépends de la température du solide :

$$-\nabla\cdot([\sigma]\nabla V)=0 \tag{2-16}$$

Dans le domaine décrivant la géométrie de la cellule d'électrolyse, la chaleur est aussi conduite dans une région appelée « cavité », située entre le dessous de la croûte d'anode et le dessus du bain liquide. Dans cette région, le transfert de chaleur par rayonnement est effectué dans une cavité dite « parfaite ». L'échange de chaleur par rayonnement dans la cavité est détaillé par les équations qui suivent.

La méthode de radiosité thermique est appliquée afin de calculer le transfert de chaleur dans la cavité formée entre le dessous de la croûte d'anode et le haut du bain liquide. Un ensemble d'équations algébriques linéaires est utilisé pour obtenir les flux de rayonnement sortants (radiosité) pour chaque surface. En prolongeant la loi de Stefan-Boltzmann pour un système de N enceintes (cavité), le bilan énergétique de chaque surface dans la cavité considérant un corps gris diffus est donné par l'équation 2-17 [Siegel et Howell, 1981; ANSYS, 2017].

$$\sum_{i=1}^{N}\left(\frac{\delta_{ji}}{\varepsilon_i}-F_{ji}\frac{1-\varepsilon_i}{\varepsilon_i}\right)\frac{1}{A_i}Q_i=\sum_{i=1}^{N}\left(\delta_{ji}-F_{ji}\right)\sigma T_i^4 \tag{2-17}$$

Où N est le nombre de surfaces (en rayonnement), δ_{ji} est le delta de Kronecker, ε_i est l'émissivité effective de la surface i, F_{ji} est le facteur de vue, A_i est l'aire de la surface i, Q_i est la perte d'énergie de la surface i, σ est la constante de Stefan-Boltzmann et T_i est la température (en Kelvin) de la surface i.

La méthode de solution par radiosité appliquée à des surfaces grises et diffuses est résolue en conjonction avec le problème de conduction thermique. Pour la résolution, l'équation 2-17 est réarrangée par une série d'équations [ANSYS, 2017]:

$$\sum_{j=1}^{N}\left[\delta_{ij}-(1-\varepsilon_i)F_{ij}\right]q_j''^{,0}=\varepsilon_i\,\sigma T_i^4 \tag{2-18}$$

Et

$$q_i''=q_i''^{,0}-\sum_{j=1}^{N}F_{ij}\,q_j''^{,0} \tag{2-19}$$

Où $q_j''^{,0}$ est le flux de rayonnement (radiosité) sortant de chaque surface et le flux net pour chaque surface est q_i''. Pour chaque surface de température connue, T_i, dans la cavité, l'équation 2-19 forme une série d'équations algébriques pour les flux de radiosité inconnus à chaque surface.

L'équation 2-19 peut être réécrite en l'équation 2-20, qui permet de déterminer le flux de radiosité quittant des surfaces, considérant la matrice $[A]$ qui contient les facteurs de forme et les valeurs d'émissivité des surfaces.

$$[A]\left\{q_j''^{,0}\right\}=\{D\} \tag{2-20}$$

Où

$A_{ij}=\delta_{ij}-(1-\varepsilon_i)F_{ij}$

$q_j''^{,0}$ = flux de radiosité pour une surface j

$D_i=\varepsilon_i\sigma T_i^4$

L'équation 2-20 est résolue avec la procédure de Newton-Raphson pour le flux de radiosité $\{q_j^{\prime\prime,0}\}$. Pour les surfaces faisant face à la cavité, les conditions aux limites pour la conduction thermique sont fournies par les flux nets de radiosité de chaque surface. L'équation 2-20 est résolue par le couplage avec l'équation de conduction de la chaleur, en utilisant une procédure séparée et jusqu'à la convergence du flux de radiosité et de la température pour chaque étape de temps (*time-step*).

Les facteurs de vue de rayonnement, F_{ij}, sont nécessaires pour résoudre le module de radiosité. Les facteurs de vue globale pour chaque surface sont calculés en utilisant la méthode des hémicubes [ANSYS, 2017]. Chaque surface sur l'hémicube a un facteur de vue donné par l'équation 2-21 [Cohen et Greenberg, 1985].

$$F_{ij} = \frac{1}{A_i}\int_{A_i}\int_{A_j}\frac{\cos\varphi_i\,\cos\varphi_j}{\pi r^2}\mathrm{d}A_j\mathrm{d}A_i \qquad (2\text{-}21)$$

Le résultat est un ensemble complet de facteurs de forme pour les environnements complexes :

$$F_{ij} = \sum_{n=1}^{N}\Delta F_n \qquad (2\text{-}22)$$

Où N est le nombre de pixels (surfaces) et ΔF_n est le delta du facteur de vue pour chaque pixel.

2.4.3 Introduction à la modélisation de la cellule d'électrolyse d'aluminium

Les modèles numériques sont développés pour prédire les phénomènes physiques suivants : les chutes de potentiel électrique dans les conducteurs, les contraintes mécaniques dans les composantes de la cuve, la génération de chaleur et la dissipation thermique, le champ magnétohydrodynamique et le transfert de masse dans le bain liquide [Hou *et al*., 1995; Safa *et al*., 2009; Marceau *et al*., 2011; Blais *et al*., 2013; Ariana *et al*., 2014; Langlois *et al*., 2015; Bardet *et al*., 2016]. Pour ce projet, les phénomènes d'intérêts sont la dissipation thermique, la génération de chaleur par effet Joule et la distribution du potentiel électrique.

Bilan thermique déterminé par des campagnes de mesures

En 1975, le bilan thermique de la cellule d'électrolyse était validé par des équations thermiques en régime permanent et par des mesures de flux thermiques [Arai et Yamazaki, 1975]. Dans le cadre de cette étude, le bilan thermique d'une cellule d'électrolyse a été validé avec des capteurs tous les trois mois, en suivant une très longue procédure. Une étude similaire a été complétée pour établir des conditions optimales d’opération de cellule d’électrolyse « moderne », utilisant des anodes précuites, par des campagnes de flux thermiques [Tsukahara *et al.*, 1983]. Cette étude a démontré l’augmentation du flux thermique sortant du recouvrement anodique en fonction de l’âge de l’anode, selon des mesures de capteur de flux.

Introduction de la modélisation par éléments finis en 2D

Au cours des dernières décennies, le transfert thermique a été modélisé à l’aide de la méthode des éléments finis afin d'améliorer la conception de la cellule d’électrolyse. En 1989, les chercheurs Pfundt *et al.* ont développé un modèle de conduction thermique résolu par la méthode des éléments finis, en 2D, pour prédire les températures et la taille de la gelée protectrice se formant sur les parois de la cellule d’électrolyse (talus). Les coefficients de transfert de chaleur entre les liquides (bain liquide et aluminium) et le talus étaient calculés pour résoudre le problème. La Figure 2-15 présente le profil de température dans ce modèle 2D représentant une demi-tranche de cellule d’électrolyse.

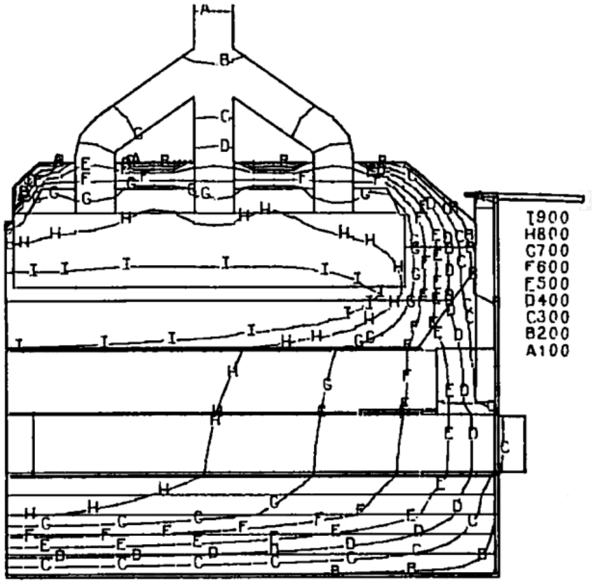

Figure 2-15 Modèle 2D d’une cellule d’électrolyse (tranche) [Pfundt *et al.*, 1989]

La distribution du courant électrique a été prédite par des modèles 2D résolus par la méthode des éléments finis [Zoric *et al.*, 1997]. À l’aide de cette méthode, il a été possible de démontrer l’influence de la taille du talus sur la distribution du courant électrique.

Perte de chaleur par le côté des cellules d'électrolyse

Les phénomènes de transfert de chaleur par conduction, convection et rayonnement au niveau du caisson influencent fondamentalement le comportement de la cellule d'électrolyse. Les études portant sur la dissipation thermique au niveau du côté ou du caisson sont nombreuses, si l'on compare avec celle portant sur le dessus de la cellule d'électrolyse. Plusieurs chercheurs se sont intéressés à la modélisation de l'évolution du talus dans la cellule d'électrolyse [Taylor et Welch, 1987; Fraser *et al.*, 1990; Taylor *et al.*, 1996; Wei *et al*, 1997; Haugland *et al.*, 2003; Kiss et Raymond, 2008]. En 2003, Haugland *et al.* ont étudié l'effet de la température ambiante de l'usine et de la ventilation sur les températures du caisson, sur la distribution de la dissipation thermique et sur l'épaisseur du talus. Ils ont utilisé le logiciel commercial ANSYS Fluent pour simuler les transferts de chaleur. Dans cette étude, les équations 2-23 et 2-24 ont été utilisées pour déterminer le transfert de chaleur par convection et rayonnement sur le caisson.

$$q_{conv} = Ah(T_{shell} - T_{room}) \tag{2-23}$$

$$q_{rad} = A\varepsilon\sigma(T_{shell}^4 - T_{room}^4) \tag{2-24}$$

Le taux de transfert de chaleur par convection se divise en deux types : la convection naturelle et la convection forcée. Lorsque le mouvement de l'air est initié par son contact avec la paroi chaude du caisson qui modifie la densité, il s'agit de convection naturelle. Lorsque le mouvement de l'air est causé par des sources externes, comme le vent ou encore l'utilisation d'un jet d'air sur le caisson, il s'agit de convection forcée [Haugland *et al.*, 2003]. Le coefficient de transfert de chaleur, h, peut être approximé à partir des nombres sans dimension suivant : Nusselt (*Nu*), Reynolds (*Re*), Prandtl (*Pr*) et Grashof (*Gr*), selon l'équation générale 2-25 [Haugland *et al.*, 2003]. Chaque nombre adimensionnel a été développé pour approximer certains paramètres reliés aux transferts de chaleur et de masse, par exemple Nusselt permet de déterminer le ratio de convection sur la conduction thermique pure [Bergman *et al.*, 2011].

$$Nu = \frac{hL}{k} = \mathrm{f}(Re, Pr, Gr) \tag{2-25}$$

Aujourd'hui, les logiciels de modélisation de la dynamique des fluides, soit *computational fluid dynamics* (*CFD*) en anglais, permettent l'approximation des coefficients de convection locale pour faciliter les calculs de transfert thermique aux frontières.

Les pertes de chaleur par le côté doivent demeurer suffisamment élevées pour maintenir une épaisseur de talus appropriée, afin de protéger la paroi latérale contre la corrosion et l'érosion du bain électrolytique liquide. Kiss et Raymond ont prédit l'épaisseur du talus dans la cellule d'électrolyse à l'aide d'un circuit de résistance et ils ont validé le modèle à l'aide de simulations basées sur la méthode des éléments finis [Kiss et Raymond, 2008]. En 2009, Namboothiri *et al.* ont proposé de contrôler les pertes de chaleur par le côté à l'aide d'un échangeur de chaleur utilisant de l'air comme fluide caloporteur. Marois *et al.* ont comparé deux méthodes numériques afin de prédire la formation de gelée dans un réacteur métallurgique [Marois *et al.*, 2009]. La formation de la gelée a été évaluée par Bertrand *et al.* à partir d'un montage expérimental et prédite à l'aide de la méthode inverse [Bertrand *et al.*, 2013]. En 2010, Nan et Changhong ont évalué, à l'aide de la méthode des éléments finis, les pertes de chaleur par le côté d'une cellule d'électrolyse utilisant des blocs cathodiques graphitisés. L'utilisation de blocs graphitisés vient modifier la dissipation thermique puisque ce type de bloc est plus conducteur que les blocs cathodiques conventionnels [Nan et Changhong, 2010].

Mouvements magnétohydrodynamiques

La modélisation du comportement magnétohydrodynamiques (*MHD*) d'une cuve d'électrolyse permet de prédire le déplacement du métal selon le champ magnétique le traversant. Les champs magnétiques créés par l'important courant électrique (~200 kA à ~600 kA) alimentant les cellules d'électrolyse d'aluminium sont très complexes à prédire, puisqu'ils requièrent la considération des réseaux de conducteurs externes, et l'intégration de cellules d'électrolyse adjacentes dans la géométrie pour être fidèle à la réalité. La Figure 2-18 présente un exemple de géométrie utilisé pour prédire les mouvements *MHD* dans le métal liquide, et ainsi prédire son instabilité durant des conditions d'électrolyse [Renaudier *et al.*, 2013]. L'instabilité du métal liquide est le principal facteur limitant la réduction de la distance interpolaire dans la cellule d'électrolyse. Ce mouvement de métal liquide occasionne des « vagues » à l'interface entre le bain liquide et le métal, ce qui influence l'efficacité de la production de l'aluminium.

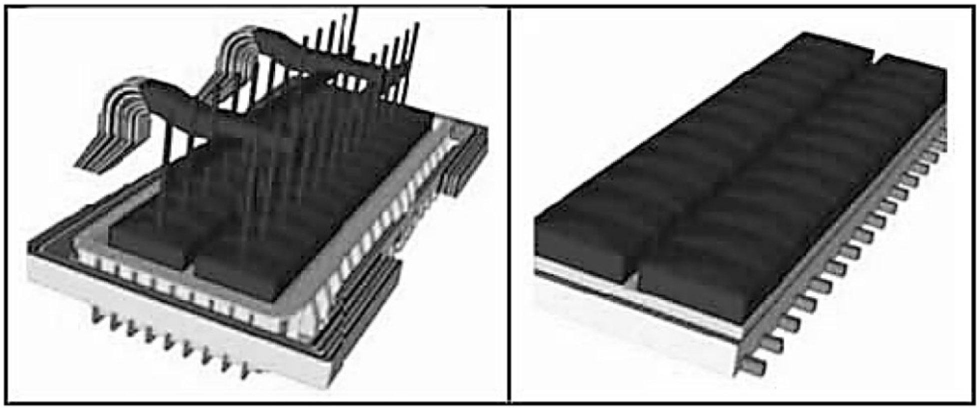

Figure 2-16 À gauche : cellule d'électrolyse P155 modélisée et à droite : cellule d'électrolyse P155 sans le caisson, sans les *busbar* et sans les tiges d'anode [Renaudier *et al.*, 2013]

De plus, le mouvement dans le métal liquide influence le taux de transfert de chaleur entre le métal et le talus. La distance entre l'anode de carbone et le métal liquide est ajustée afin de réduire les réactions secondaires et ainsi pour maintenir une efficacité de courant élevée. Toutefois, la distance anode-cathode doit suffisamment être petite pour maximiser l'efficacité énergétique, pour ainsi éviter la génération excessive de chaleur dans le bain liquide résistif ($\sigma_{\text{bain liquide}}$ ~ 190 S/m) [Hives *et al.*, 1996]. Les mouvements *MHD* ont été simulés par plusieurs chercheurs dans la dernière décennie [Dupuis et Bojarevics, 2005; Safa *et al.*, 2009; Einarsrud *et al.*, 2014; Langlois *et al.*, 2015]. Un modèle thermique-électrique faiblement couplé avec un modèle MHD a été présenté en 2005 [Dupuis et Bojarevics, 2005]. Les coefficients de transfert de chaleur dans le bain et l'aluminium liquide ont été calculés en utilisant la vitesse locale dans ces liquides, un paramètre qui a été déterminé à partir de la simulation du champ magnétique. Ainsi, les coefficients de transfert de chaleur ont pu être intégrés dans le modèle thermique-électrique pour effectuer un couplage « faible ».

Modèles 3D de la cellule d'électrolyse, résolus par la méthode des éléments finis

Au début des années 90, les chercheurs dans le domaine de l'aluminium ont migré graduellement vers des solutions commerciales pour simuler la cellule d'électrolyse [Dupuis et Tabsh, 1991; Dupuis et Tabsh, 1994; Vallés et Lenis, 1995]. Présentement, les solutions commerciales de modélisation thermique-électrique sont principalement utilisées dans le domaine de l'aluminium et elles sont basées sur la méthode de résolution par éléments finis [Hou *et al.*, 1995; Valles *et al.*, 1995; Dupuis, 1998, 2000; Blais *et al.*, 2013; Fortin *et al.*, 2012]. Par exemple, Dupuis a présenté un modèle thermique d'une cellule d'électrolyse fonctionnant à

400 kA [Dupuis, 2000]. La Figure 2-17 présente la géométrie 3D d'un quart de la cellule d'électrolyse.

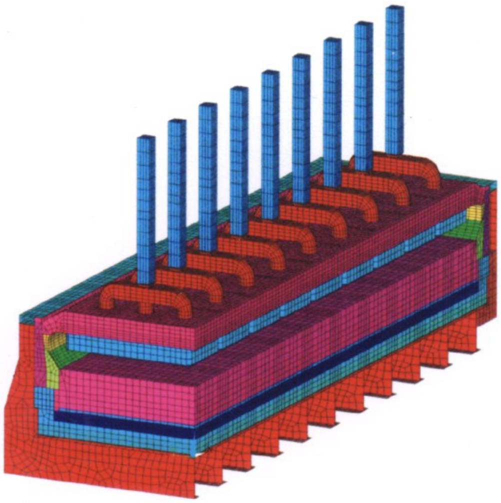

Figure 2-17 Géométrie du quart d'une cellule d'électrolyse en 3D [Dupuis, 2000]

Il faut noter que le recouvrement anodique présenté dans la Figure 2-17 utilise une géométrie simple par rapport à son état réel. En observant des cellules d'électrolyse, on remarque qu'il y a formation d'une « marche » au niveau du couloir latéral. Un détachement entre la croûte d'anode située près du tablier et la croûte sur l'anode de carbone est typiquement observé durant les premiers jours de la vie de l'anode.

En 2014, un modèle plus complexe a été développé pour prédire le démarrage d'une cellule d'électrolyse, aussi avec une géométrie de quart de cuve [Hacini *et al.*, 2014]. La Figure 2-18 présente la géométrie AP-60 utilisée pour prédire le comportement thermique-électrique-mécanique.

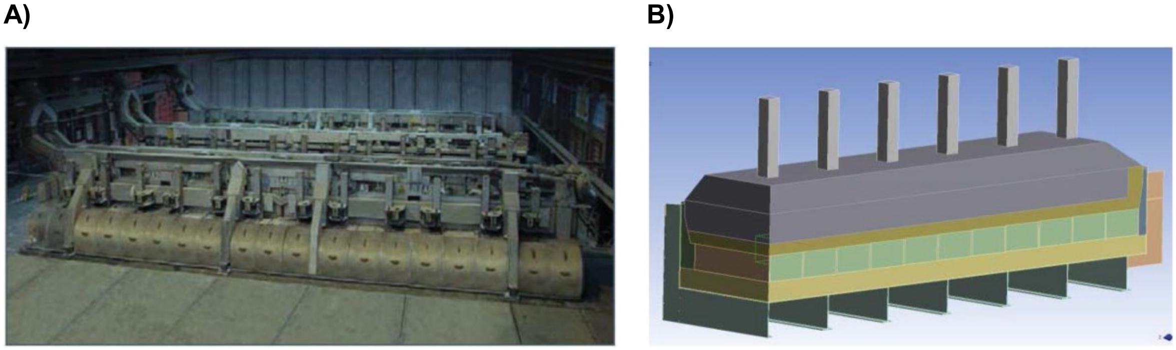

Figure 2-18 A) Vue sur une cellule d'électrolyse AP-60 et B) Géométrie du quart de la cellule d'électrolyse en 3D [Hacini *et al.*, 2014]

Ainsi, de plus en plus de chercheurs se tournent vers la simulation en 3D des cellules d'électrolyse [Dupuis, 1998; Hacini *et al.*, 2014; Xifeng *et al.*, 2014], puisqu'il s'agit d'une représentation plus réaliste de la cellule d'électrolyse et que la puissance des systèmes informatiques actuels permet de résoudre ces problèmes dans un temps acceptable. Récemment, Xifeng *et al.*, 2014 ont présenté un modèle améliorant la prédiction thermique et électrique du comportement de la cellule d'électrolyse en considérant des événements et phénomènes tels que le siphonnage du métal, l'extraction d'anode, la sortie de gaz et le chauffage de matériaux primaires dans le bilan thermique prédit. La Figure 2-19 présente le profil de température prédit par ce modèle thermique-électrique.

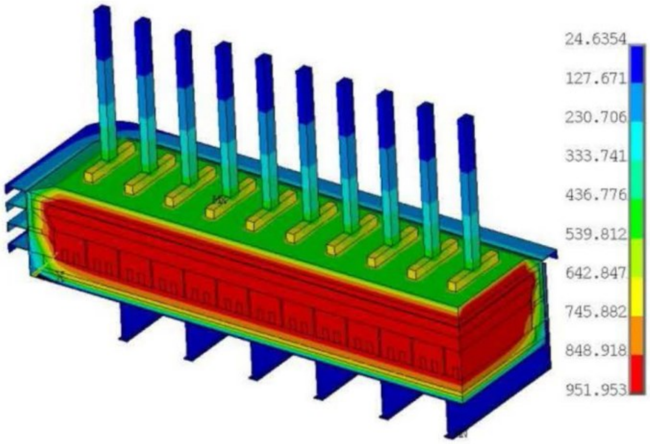

Figure 2-19 Profil de température dans la cellule d'électrolyse [Xifeng *et al.*, 2014]

Un courant électrique de 305 kA alimentait cette cellule d'électrolyse et un potentiel électrique de 4.0 V a été calculé par l'équation 2-26, en considérant la géométrie présentée dans la Figure 2-19.

$$V_{total} = V_{anode} + V_{bath} + V_{cath.} + V_{gas} + V_{contact\ cath.} + V_{dec.} + V_{pol.} \qquad (2\text{-}26)$$

Où V_{anode}, V_{bath} et $V_{cath.}$ sont les pertes de potentiel électrique ohmique (de l'anode, du bain liquide et de la cathode), V_{gas} est la surtension engendrée par les bulles de gaz sous l'anode, $V_{contact\ cath.}$ est la perte de potentiel causée par le contact entre la barre collectrice et le bloc de carbone cathodique, $V_{dec.}$ est le potentiel de décomposition et $V_{pol.}$ est le potentiel de polarisation [Xifeng *et al.*, 2014]. Le tableau suivant présente les potentiels électriques typiques dans les cellules d'électrolyse :

Tableau 2-3 Distribution du potentiel électrique [Grjotheim et Kvande, 1993]

Composante	Détail de la perte de potentiel électrique	Valeur approximative
V_{anode}	Résistance de l’anode (ensemble)	~0.2 V - 0.3 V
V_{bath}	Résistance dans l’électrolyte liquide	~1.3 V - 2.0 V
$V_{cath.} + V_{contact\ cath.}$	Résistance de la cathode (ensemble), incluant le contact entre la barre collectrice et le bloc	~0.5 V
V_{gas}	Bulles dans l’électrolyte liquide	~0.2 V
$V_{dec.}$	Décomposition de l’Al_2O_3	1.2 V
$V_{pol.}$	Surpotentiel aux électrodes	0.5 V – 0.7 V
$V_{ext.}$	Résistance des parties externes	0.25 V

Ainsi, le potentiel électrique d’opération (incluant les externes) se situe approximativement entre 4.15 V et 4.45 V, en considérant les valeurs du Tableau 2-3 et une perte de potentiel dans le bain liquide constante se situant à 1.3 V. Typiquement, $V_{ext.}$ n’est pas inclut dans le bilan de génération et de dissipation d’énergie, puisque cette chaleur produite est dissipée en dehors de la zone définissant la cellule d’électrolyse.

Distribution de la dissipation thermique

La distribution typique de la dissipation thermique d’une cellule d’électrolyse industriel est répartie comme suit: 43 % par le haut (ensemble anodique et recouvrement anodique), 50 % par le côté (tablier, caisson et barre cathodique) et 7 % par le bas [Grjotheim et Kvande, 1993]. Environ 35 % des pertes de chaleur totales sont dissipées par le recouvrement anodique, tandis qu’également 35 % est dissipées par les parois latérales. En conséquence, l'équilibre thermique de la cellule d’électrolyse dépend grandement des matériaux à changement de phase situés sur les parois latérales (talus) et sur le dessus de la cellule (*ACM* et croûte d’anode). Des efforts considérables ont été faits pour améliorer la prédiction du talus, bien qu'il y ait encore des améliorations possibles pour se rapprocher de son comportement réel dans la cellule d'électrolyse.

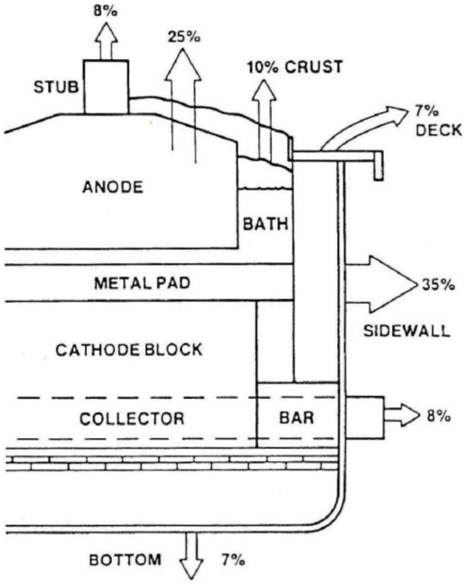

Figure 2-20 Distribution des pertes de chaleur dans une cellule d'électrolyse [Foosnaes *et al.*, 1993]

La modélisation de la partie du dessus de la cellule d'électrolyse n'a été étudiée que par très peu de chercheurs dans les dernières décennies. Les modèles globaux qui incluent la partie du haut des cellules d'électrolyse simplifient grandement le comportement des matériaux dans cette zone. Par exemple, le recouvrement anodique est souvent défini comme un seul matériau de composition chimique et granulométrie uniforme et représenté par une géométrique simple.

2.5 Modélisation avec l'emphase sur le dessus de la cellule d'électrolyse

La modélisation thermique-électrique de la cellule d'électrolyse doit rigoureusement prendre en considération les composantes supérieures afin de prédire précisément la dissipation thermique. En effet, il y a environ 40 % à 50 % de la chaleur totale qui est dissipée par le recouvrement anodique et par l'ensemble anodique [Kjelstrup *et al.*, 1998; Gadd *et al.*, 2000]. Par conséquent, une large gamme de matériaux, isolants et conducteurs, doivent être considérés pour représenter le comportement thermique d'une cellule d'électrolyse. Selon l'objectif de la simulation, il existe deux frontières définissant la zone du dessus. La première frontière suit les capots de cuve et la superstructure et la deuxième frontière suit le recouvrement anodique et les ensembles anodiques.

2.5.1 Frontière du dessus de la cellule d'électrolyse : capots, superstructure et tige d'anode

En 2000, Gadd *et al.* ont présenté un modèle tenant compte des pertes par la superstructure, par les capots et par la ventilation. La Figure 2-21 présente les conditions limites définies par Gadd *et al.* :

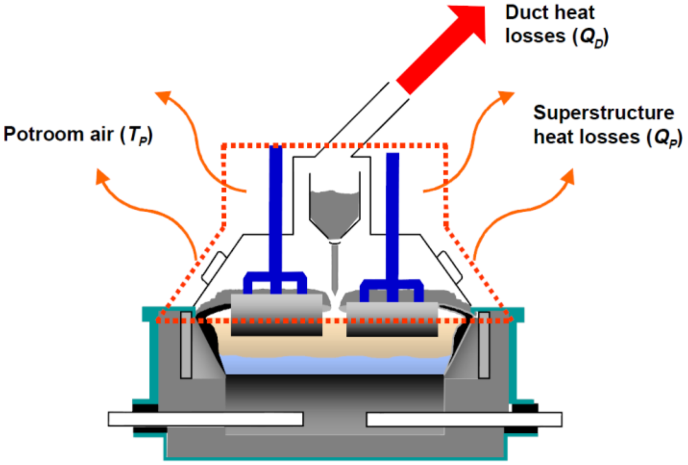

Figure 2-21 Conditions limites supérieures pour étudier les pertes par le dessus [Gadd *et al.*, 2000]

Les pertes de chaleur par la ventilation peuvent être calculées en continu, si le débit et la température du gaz sont mesurés par des instruments. Les taux de transfert d'énergie perdu par le haut de la cellule d'électrolyse sont décrits par l'équation 2-27.

$$\text{Perte par le haut} = q_D + q_P = \dot{m}_D \int_{T_P}^{T_D} c_P \mathrm{d}T + q_{P(conv)} + q_{P(rad)} \qquad (2\text{-}27)$$

Où q_D est le taux de transfert d'énergie (kW) par la ventilation, q_P est le taux de transfert d'énergie (kW) vers la salle de cuve et $\dot{m}_D$ est le débit massique (kg/s) de gaz dans la ventilation.

En 2009, Abbas *et al.* ont mesuré l'impact de la ventilation sur les pertes de chaleur par le dessus des cellules d'électrolyse. Ils ont démontré que 74 % des pertes de chaleur par le dessus de la cellule d'électrolyse étaient évacuées par la ventilation. La somme des pertes par le dessus d'une cellule d'électrolyse de 225 kA était de 234.4 kW. Voici la répartition des pertes par le haut, selon les simulations d'Abbas *et al.* : 173.2 kW par la ventilation, 42.6 kW par les capots, 15.1 kW par la superstructure et 3.5 kW par les autres pièces. Les pertes de chaleur par le haut de la tige d'anode, qui est en contact avec l'air de la salle d'électrolyse, ont été calculées par des calculs simples et des mesures de profil de températures en usine [Shen *et al.*, 2004]. Selon ces résultats, les tiges d'anode d'une cellule d'électrolyse de 300 kA dissipaient environ 300 W chacune.

En 2013, Zhao *et al.* ont présenté un modèle de prédiction des pertes thermiques en représentant les différentes parties par un circuit thermique [Zhao *et al.*, 2013a]. Le modèle possède l'avantage de se résoudre rapidement. Il est donc possible d'effectuer simplement une étude de sensibilité en variant certains paramètres. Zhao *et al.* ont aussi développé un modèle *CFD* du dessus d'une cellule d'électrolyse 350 kA pour déterminer les coefficients de transfert de chaleur [Zhao *et al.*, 2013b]. De plus, l'impact de la ventilation sur les pertes thermiques par le haut a aussi été étudié par Zhao *et al.* [Zhao *et al.*, 2013c]. En augmentant la ventilation, la dissipation thermique augmente, mais la température des gaz diminue.

2.5.2 Frontière du dessus de la cellule d'électrolyse : croûte d'anode, *ACM* et ensemble anodique

La modélisation de la dissipation thermique et du champ électrique suit typiquement les frontières définies dans la Figure 2-22. Ces frontières sont situées au niveau du caisson (dessous et côté) et au niveau du recouvrement anodique et des ensembles anodiques (dessus).

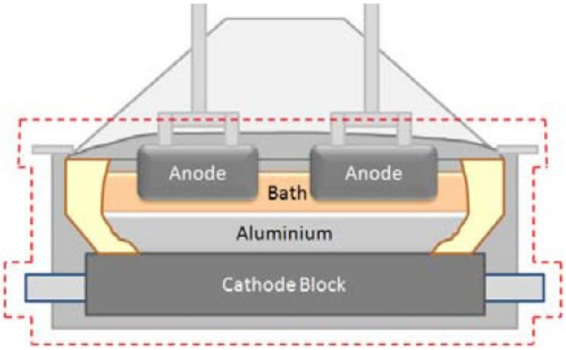

Figure 2-22 Conditions limites traditionnelles utilisées pour la modélisation thermique-électrique [Gusberti *et al.*, 2012]

Cette frontière est encore utilisée dans la modélisation thermique-électrique récente, tel qu'illustrée dans la Figure 2-23. En 2016, Dupuis a démontré l'importance de la validation des prédictions thermiques sur le terrain par des campagnes de mesures, afin que les températures prédites se rapprochent davantage de la réalité. Dans la cellule d'électrolyse réelle, les matériaux s'usent et leurs propriétés s'écartent de leurs valeurs initiales.

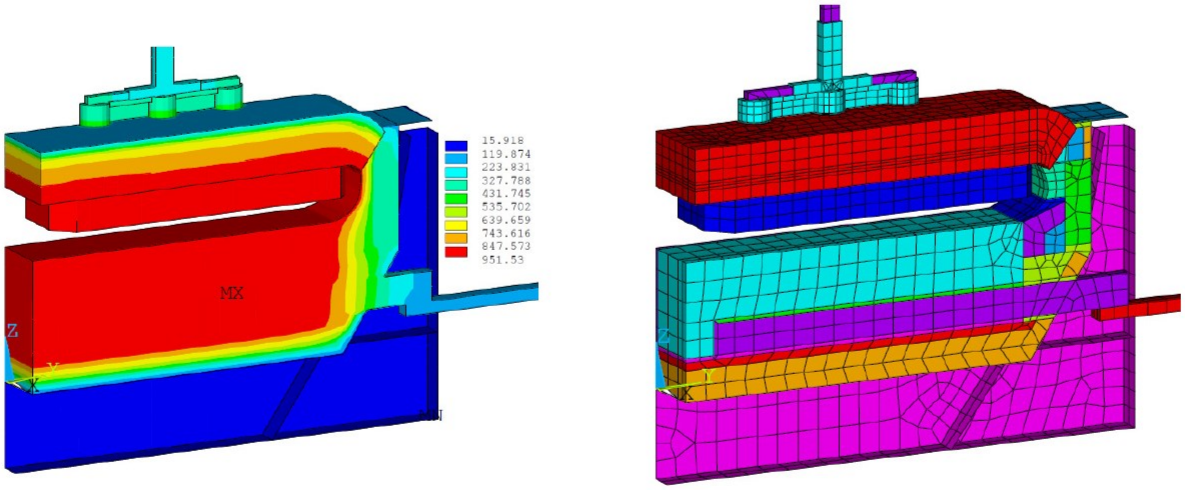

Figure 2-23 Profil de température avec le maillage d'une tranche de cellule d'électrolyse [Dupuis, 2016]

2.5.3 Expérimentation avec l'emphase sur le dessus de la cellule d'électrolyse

En 1995, le profil de température dans la croûte a été étudié en laboratoire à partir d'un mélange de bain et d'Al_2O_3 [Rye *et al.*, 1995]. La Figure 2-24 présente le montage de thermocouples installé dans la croûte.

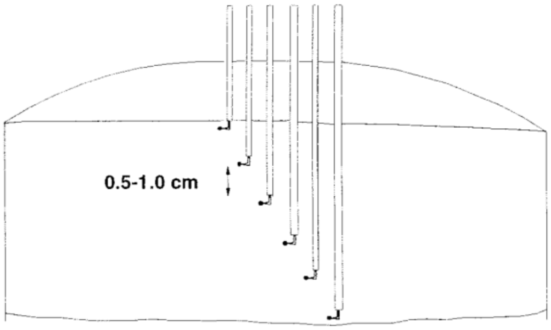

Figure 2-24 Assemblement de thermocouples dans la croûte étudiée par Rye *et al.*

Dans la cavité entre le bain liquide et la croûte, la chaleur est transmise principalement par rayonnement [Rye *et al.*, 1995]. Selon ces auteurs, la valeur d'émissivité de l'*ACM* a été estimée à 0.4, en spécifiant qu'elle n'a jamais été mesurée auparavant. L'émissivité du dessous de la croûte, face au bain liquide, a été estimée à partir du flux de chaleur et sa valeur se situerait entre 0.11 et 0.35 [Rye *et al.*, 1995]. Rye *et al.* assument une émissivité de 1.0 pour le bain liquide. Toutefois, les valeurs d'émissivités ont été calculées à partir d'un bilan thermique grandement simplifié et elles n'ont pas été déterminées par une méthode analytique. Le flux thermique de la croûte d'anode de laboratoire fabriquée à partir d'Al_2O_3 se situait autour de 1700 W/m^2 et

1900 W/m^2. Le flux thermique de croûte fait à partir d'un mélange de bain et d'Al_2O_3 augmentait avec la quantité de bain électrolytique dans le mélange [Rye *et al.*, 1995].

En 2006, une thèse a été publiée sur les matériaux de recouvrement anodique et le bilan thermique du dessus de la cellule d'électrolyse [Shen, 2006]. Cet auteur a mesuré la conductivité thermique de différents mélanges d'Al_2O_3 et de bain électrolytique pour fabriquer l'*ACM* (voir section *2.2.6*). De plus, Shen a modélisé la conductivité thermique de l'*ACM* par les modèles de Kunii-Smith, Deissler-Eian et Maxwell. Le modèle de Kunii-Smith a permis de reproduire en grande partie les résultats expérimentaux. L'équation 2-28 présente le modèle simplifié de Kunii-Smith utilisé par Shen [Kunii et Smith, 1960].

$$\frac{k_{mix}}{k_g} = \emptyset + \frac{\propto_c (1 - \emptyset)}{\beta + \gamma(\frac{k_g}{k_s})} \tag{2-28}$$

Où k_{mix} est la conductivité de la poudre (solide et gaz), k_g est la conductivité du gaz, k_s est la conductivité du solide, α_c est un facteur de compacité variant normalement de 0.9 à 1.0, β est la mesure de l'épaisseur effective et $\emptyset$ est la fraction de vide rempli par du gaz. Toutefois, le modèle simplifié utilisé par Shen ne tient pas compte du rayonnement. L'effet du rayonnement devient majeur à partir de 400 °C pour des particules d'environ 1 mm [Schotte, 1960].

2.5.4 Modélisation numérique transitoire avec l'emphase sur le dessus

L'évolution de la croûte dans les cellules d'électrolyse a été étudiée par LeBreux *et al.* à l'aide d'un modèle mathématique résolu par la méthode des différences finies et simulé avec Matlab [LeBreux *et al.*, 2016; LeBreux *et al.*, 2014]. Les conditions limites du modèle numérique sont illustrées dans la Figure 2-25 [LeBreux *et al.*, 2014].

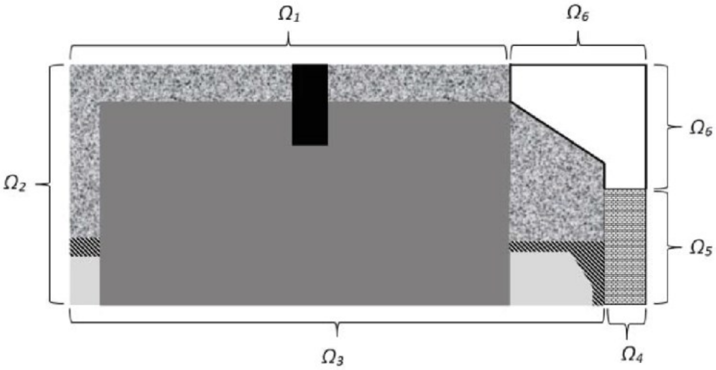

Figure 2-25 Conditions limites du modèle numérique utilisé par LeBreux *et al.*

Ω_1 représente la frontière entre le dessus de la croûte et l'air sous les capots (h = 70 W/m^2·K, T_∞ = 125 °C), Ω_2 est une symétrie du centre de la cellule, Ω_3 représente la frontière entre le dessous de l'anode et le bain (T = 960 °C), Ω_4 est considéré comme une région isolée, Ω_5 est la frontière entre la paroi de la cellule et l'air ambiant (h = 30 W/m^2·K, T_∞ = 30 °C) et Ω_6 est la frontière entre le tablier et l'air ambiant de l'usine (h = 100 W/m^2·K, T_∞ = 125 °C, T_∞ = 30 °C). L'équation 2-29 a été utilisée par LeBreux *et al.* pour représenter mathématiquement la conduction de la chaleur avec l'aspect transitoire, la génération de chaleur et l'enthalpie de changement de phase.

$$\rho C_p \frac{\partial T}{\partial t} = \nabla(k\nabla T) + \dot{q} - \delta H \frac{\partial f}{\partial t} \tag{2-29}$$

Où $\dot{q}$ est la génération de chaleur volumique par effet Joule (W/m^3), f est la fraction liquide qui varie avec la température et δH est la variation d'enthalpie volumique (J/m^3). La prédiction thermique transitoire a été complétée en utilisant la relation d'Arrhenius pour déterminer le taux de transformation d'ACM en croûte d'anode en fonction de la température.

2.5.5 Validation des prédictions par des mesures de flux thermiques

Les mesures de flux thermiques servent à valider les modèles numériques de cellules d'électrolyse. En 1982, Tsukahara *et al.* ont déterminé le flux de chaleur sortant par les matériaux de recouvrement anodique. Il y a environ 40 % (178 kW) des pertes de chaleur de cette cellule opérant à 155 kA qui étaient perdues par l'anode et le recouvrement anodique (ici un mélange fait d'Al_2O_3). Les taux de transfert de chaleur (q'') au-dessus de l'anode et du recouvrement anodique étaient de 2.21 kW/m^2 et de 2.33 kW/m^2 respectivement [Tsukalhara *et al.*, 1982]. En 2006, Shen a évalué le flux thermique provenant des matériaux de recouvrement à l'aide de l'appareil présenté dans la Figure 2-26.

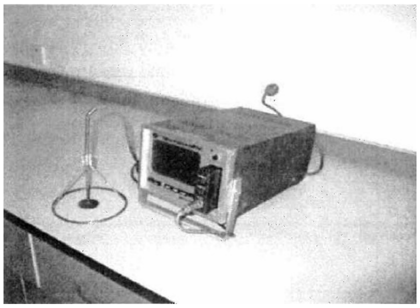

Figure 2-26 Appareil pour mesurer les flux thermiques (modèle SKD-HFM) [Shen, 2006]

La sonde de flux thermique était placée directement sur l'*ACM* et elle nécessita environ 10 min pour se stabiliser. Le flux thermique est également corrélé avec la température mesurée sur l'*ACM* [Dupuis *et al.*, 2004; Shen, 2006, 2008]. De plus, le flux thermique diminue avec l'épaisseur d'*ACM* poudreux déposé sur la croûte d'anode et les anodes. Les graphiques présentés dans la Figure 2-27 démontrent la corrélation entre le flux thermique et la température de surface et l'effet de l'épaisseur d'*ACM* à base d'Al_2O_3 sur le flux thermique.

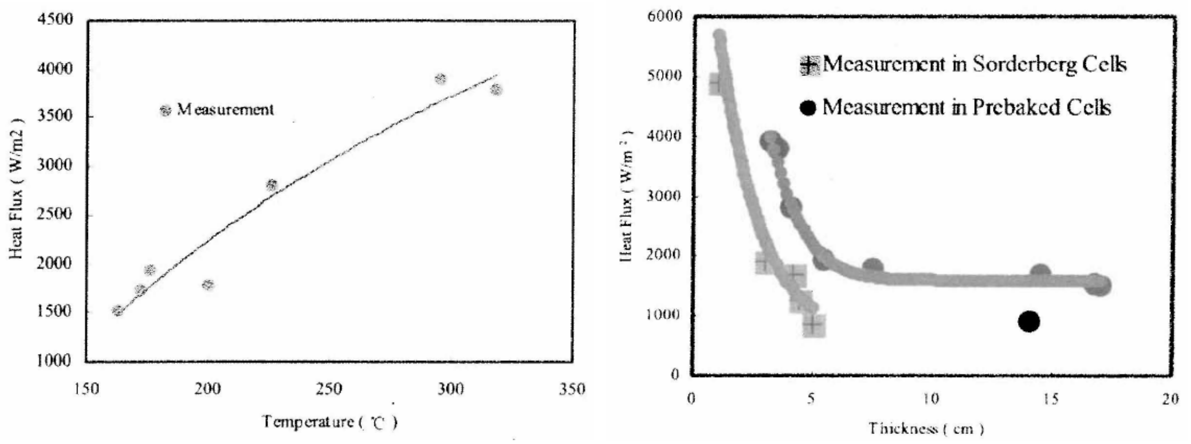

Figure 2-27 Flux thermiques en fonction de la température et de l'épaisseur d'*ACM* [Shen, 2006].

2.6 Conclusion de l'état de l'art

Selon la revue de la littérature antécédente, il y a très peu d'articles scientifiques se consacrant à la caractérisation chimique et thermique du recouvrement anodique moderne, fait à partir de bain électrolytique et d'alumine. Avec les techniques de caractérisation actuelles qui utilisent la DRX, la méthode Rietveld et l'analyse élémentaire d'oxygène, il est possible d'approfondir la composition cristalline de l'*ACM* et de la croûte d'anode. De plus, il n'y a pas d'étude qui caractérise les phases amorphes et peu d'études traitent des phases d'Al_2O_3 en transition (γ, δ, θ, β) composant ces matériaux. La transformation de l'*ACM* en croûte d'anode a été discutée et détaillée de façon sommaire. Toutefois, les phénomènes thermochimiques entourant cette transformation n'ont pas été approfondis suffisamment pour être intégrés dans des modèles thermiques transitoires. La conductivité thermique (k), la capacité thermique massique (c_p), l'enthalpie de transition de phase et la densité (ρ) en fonction de la fraction solide-liquide du recouvrement anodique doivent être déterminées analytiquement par des méthodes récentes, telles que la calorimétrie différentielle à balayage (*DSC*) et l'analyse à flash laser (*LFA*). La conductivité thermique de la croûte d'anode a été déterminée expérimentalement avec l'appareil à fil chaud jusqu'à ~600 °C, toutefois aucune donnée n'a été déterminée par *LFA* et les données précédentes omettent la plage de température principale vécue par ce matériau, soit entre ~700 °C et ~950 °C. De plus, les valeurs d'émissivité de l'*ACM* et de la croûte d'anode ont été estimées en utilisant des matériaux fabriqués en laboratoire. Toutefois, la méthode d'estimation utilisée précédemment comporte une grande faiblesse puisqu'elle ne détermine pas directement la valeur, elle la calcule indirectement à partir d'un bilan thermique simplifié. La croûte d'anode se détériore et elle forme une cavité à une certaine température. Les travaux précédents ne démontrent pas la température exacte de formation de cette cavité. Toutefois, le dessous du recouvrement anodique présente systématiquement une cavité qui devrait être considérée dans les modèles numériques.

Tout d'abord, un cadre de référence a été présenté pour décrire les théories expliquant les phénomènes de transfert thermique et de conduction électrique. La représentation des phénomènes thermiques évoluant dans le recouvrement anodique mérite d'être approfondie afin d'améliorer la justesse de prédiction dans les composantes situées au-dessus des cellules d'électrolyse d'aluminium. La revue de la littérature précédente démontre que peu d'études scientifiques ont approfondi la modélisation thermique de cette zone, malgré qu'elle représente environ 40 % à 50 % de la dissipation thermique totale. De plus, les modèles numériques utilisent une géométrie simplifiée du recouvrement anodique. Une grande partie des modèles thermiques ne distinguent pas l'*ACM* de la croûte d'anode, pourtant il s'agit de deux matériaux présentant des propriétés thermiques très différentes. Dans les cellules d'électrolyse industrielles, le recouvrement anodique se sépare en deux parties distinctes lors de l'abaissement de l'ensemble anodique. Cette particularité n'a pas été intégrée dans les modèles numériques précédents. La dynamique des fluides au-dessus du recouvrement anodique a été simulée par une étude de *CFD* et des coefficients de convection en fonction du débit de ventilation ont été déterminés. Ces données pourront être comparées avec les conditions limites des modèles numériques développés au cours de ce projet de recherche. Dans les modèles thermiques-électriques précédents, la présence de la cavité n'a pas encore été considérée, à la connaissance de l'auteur. De plus, la consommation des anodes et l'abaissement des ensembles anodiques engendrent un déplacement des composantes supérieures. Selon la littérature récente, aucun modèle numérique ne considère ce phénomène dans leur géométrie. De plus, l'évolution thermique durant le cycle de vie complet de l'ensemble anodique n'a pas été mesurée ou prédite dans les études scientifiques précédentes. Par conséquent, un effort considérable doit être fait pour améliorer la géométrie du recouvrement anodique et améliorer ses propriétés thermiques. De plus, un lien doit être fait entre la dissipation thermique par le dessus et celle par le côté. La dissipation thermique par le côté permet de maintenir une couche de talus d'épaisseur suffisante pour protéger les parois latérales contre la haute corrosion du bain électrolytique liquide. Donc, en maîtrisant mieux le comportement thermique du dessus de la cellule d'électrolyse, il serait possible d'envisager de mieux contrôler la dissipation thermique latérale et l'épaisseur du talus. Comme le recouvrement anodique se caractérise par des matériaux à changement de phase qui contiennent des transformations irréversibles, il est possible de supposer que certains événements temporaires pourraient perturber l'équilibre thermique de la cellule d'électrolyse et que celle-ci ne retournerait pas nécessairement à son état initial. Par conséquent, la modélisation thermique-électrique transitoire devrait être un outil essentiel pour étudier le comportement de la cellule d'électrolyse. Par exemple, l'effet de différentes contraintes opérationnelles, telles que des excursions thermiques ou des ajouts d'ACM, pourrait être étudié.

CHAPITRE 3 CARACTÉRISATION DE LA COMPOSITION CHIMIQUE DES MATÉRIAUX

3.1 Avant-propos

Auteurs et affiliation :

François Allard : étudiant au doctorat, Département de génie chimique et génie biotechnologique, Université de Sherbrooke, Québec, Canada.

Martin Désilets : professeur titulaire, Département de génie chimique et génie biotechnologique, Université de Sherbrooke, Québec, Canada.

Marc LeBreux : professionnel de recherche, Département de génie chimique et génie biotechnologique, Université de Sherbrooke, Québec, Canada.

Alexandre Blais : scientifique de recherche, Rio Tinto Aluminium, Centre de recherche et développement Arvida, Québec, Canada.

État de l'acceptation : Version finale publiée.

Revue : *Light Metals, The Minerals, Metals and Materials Society*.

Référence :

Allard, F., Désilets, M., LeBreux, M. et Blais, A. (2015). Chemical characterization and thermodynamic investigation of anode crust used in aluminum electrolysis cells. *TMS Light Metals*, p. 565-570.

Lien d'accès : https://doi.org/10.1007/978-3-319-48248-4_94

Contributions à la thèse :

Dans une première étape, la chimie des matériaux de recouvrement anodique (*ACM*) et de la croûte d'anode a été caractérisée par la diffractométrie de rayons X (DRX) et analyses quantitatives Rietveld, par des analyses élémentaires et par la microscopie électronique à balayage (MEB). L'objectif global était d'obtenir une plus profonde compréhension de la chimie et du comportement des matériaux qui recouvrent les anodes de carbone dans les cellules d'électrolyse. Les points suivants ont été démontrés par les résultats :

- La croûte d'anode présente un ratio de cryolite (CR) plus élevée que l'*ACM* puisqu'elle est produite par la réaction entre l'*ACM* poudreux et le bain liquide qui y pénètre. Cette transformation s'effectue à une température suffisante pour favoriser la transformation des phases Al_2O_3 de transition (γ, δ, θ, β) et amorphe en la phase stable α-Al_2O_3. Le réseau de particules α-Al_2O_3 et de bain solidifié a été exposé par les images de MEB. Cette caractéristique est favorable à la production d'une croûte d'anode solide qui se maintient en place durant l'opération des cellules d'électrolyse.

- Les analyses élémentaires ont démontré que la concentration d'oxygène, provenant principalement de l'Al_2O_3, augmente verticalement dans la croûte d'anode. Le haut de la croûte d'anode à une [Al_2O_3] se rapprochant de l'*ACM* et le bas est dilué par la pénétration du bain. Une fraction d'Al_2O_3 de transition et amorphe demeure présente dans le haut de la croûte d'anode jusqu'à la fin de vie de l'anode. Par conséquent, le dessus de la croûte d'anode n'atteint pas la température minimum pour favoriser la transformation complète des phases d'Al_2O_3 en la phase stable α-Al_2O_3. Il a été observé en laboratoire qu'une couche mince friable se situe à l'interface entre le dessus de la croûte et le dessous de l'*ACM*.
- Le comportement des échantillons à des températures allant jusqu'à 1000 °C a été examiné par des calculs d'équilibre chimique. Un digramme de phase théorique a été produit pour représenter les transformations se déroulant dans le recouvrement anodique. La croûte d'anode typique demeure à l'état solide jusqu'à 696 °C, une température où les phases plus acides ($NaCaAlF_6$ et $Na_5Al_3F_{14}$) de la solution commencent à fondre. La croûte se retrouve à l'état solide-liquide à partir de cette température et sa dégradation est favorisée lorsque toutes les phases de bain électrolytique se retrouvent liquides. Dans cette condition, la croûte est supportée uniquement par le réseau d'Al_2O_3, qui se fait dissoudre par les éclaboussures de bain liquide et par la pénétration de vapeur très acide ($NaAlF_4$).

Titre français :

Caractérisation chimique et étude thermodynamique de la croûte d’anode utilisée dans les cellules d’électrolyse d’aluminium

Résumé :

Les matériaux de recouvrement anodique (*ACM*) sont nécessaires pour contrôler les pertes de chaleur au-dessus des cellules d’électrolyse d’aluminium, pour réduire les émissions gazeuses de fluorures et pour empêcher l’oxydation des anodes de carbone. Afin de comprendre le comportement de l'*ACM* et de la croûte d’anode dans des conditions d’opération, des échantillons de ces matériaux sont prélevés dans une cellule d'électrolyse industrielle dans le canal latéral, le canal central et entre les anodes. Les compositions chimiques sont analysées par diffractométrie de rayons X (DRX) tandis que les températures à l'intérieur de la croûte sont validées par des mesures de température. Les réactions se produisant dans l'*ACM* et la croûte d’anode sont ensuite déterminées par des calculs d'équilibre thermodynamique. Des gradients de concentrations de chiolite ($Na_5Al_3F_{14}$), de cryolite (Na_3AlF_6), de $Na_2Ca_3Al_2F_{14}$ et d’Al_2O_3 sont observés dans la croûte d’anode, ce qui implique une variation du ratio de cryolite (*CR*) et de la température de fusion de la croûte. L'analyse thermodynamique démontre l'état et le comportement de la croûte d’anode dans des cellules d’électrolyse d’aluminium.

3.2 Chemical characterization and thermodynamic investigation of anode crust used in aluminum electrolysis cells

Keywords: Aluminum electrolysis, Crust, Anode cover material, X-ray diffraction, Thermodynamic, Alumina

3.2.1 Abstract

The anode cover material (ACM) is necessary to control the top heat losses of aluminum electrolysis cells, to decrease the fluoride fumes emissions and to prevent air burn of carbon anodes. In order to understand the behavior of the ACM and anode crust at operating conditions, samples of these materials are taken from an industrial electrolysis cell in the side channel, center channel and between anodes. Their chemical compositions are analyzed by X-ray diffraction while the temperatures inside the crust are validated by temperature measurements. The reactions occurring in the ACM and anode crust are then determined by thermodynamic equilibrium calculations. Concentration gradients of chiolite ($Na_5Al_3F_{14}$), cryolite (Na_3AlF_6), $Na_2Ca_3Al_2F_{14}$, and Al_2O_3 are observed in the anode crust, implying a variation of the cryolite ratio and melting temperature of the crust. The thermodynamic analysis describes the state and behavior of the anode crust in aluminum electrolysis cells.

3.2.2 Introduction

The Hall-Héroult process can be improved through a better understanding of the chemical composition and behavior of the anode cover material (ACM) and anode crust. These materials are necessary to control the top heat losses of aluminum electrolysis cells, to decrease the fluoride fumes emissions and to prevent air burn of carbon anodes. The ACM is usually composed of recycled crushed bath and alumina. The granulometry is characterized by a mix of fine to coarse particles. At each anode change, the ACM is deposited over the anode. The anodes are replaced typically after a few weeks. This frequency varies depending on the cell technology and the rate of consumption of the carbon anode. The anode consumption is proportional to the current used in the process. Figure 3-1 depicts the main components of an industrial electrolysis cell.

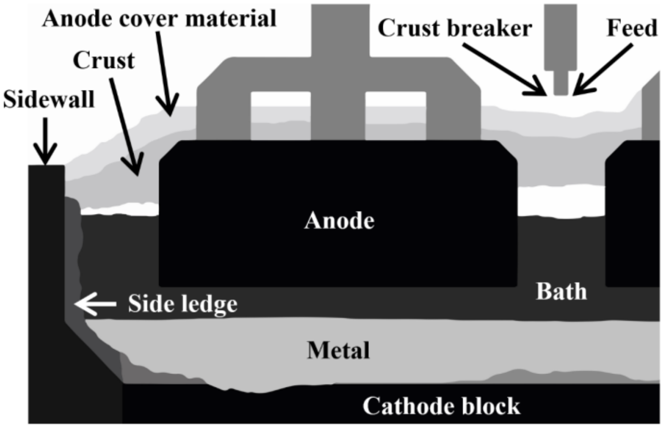

Figure 3-1 Schematic of an aluminum electrolysis cell

The formation of anode crust was studied by several researchers in the last decades. Firstly, laboratory experiments have been conducted with alumina based ACM in order to study the mechanism of formation [Less, 1977; Johnston et Richards., 1983; Townsend et Boxall, 1984; Oedegard *et al*., 1985]. According to Less, the fluorides from the bath act as "mineralizers" and increase the conversion rate of γ-Al_2O_3 to α-Al_2O_3 [Less, 1977]. He demonstrated the crusting behavior of alumina added in a cell with a standard cryolite melt. A low calcination temperature of the ore or a high content in γ-Al_2O_3 helps to form a strong crust due to the formation of a network between the α-Al_2O_3 particles. The crust formation is reduced when the ore has already reacted with bath fumes or when the alumina is mainly composed of fines particles [Townsend and Boxall, 1984]. The interaction of the bath with the alumina added on a cell was investigated by Gerlach and Winkhaus [Gerlach and Winkhaus, 1985]. The bath penetrates into the alumina powder by capillary forces implying the formation of a crust consisting of solidified bath and embedded alumina particles.

The chemical composition of the crust taken from industrial cells has been investigated in a few studies [Liu *et al*., 1992; Groutso *et al.*, 2009; Zhang *et al.*, 2013]. Liu *et al.* observed the temperature profiles inside the side channel crust and determined the chemical composition by elemental analysis and by the wet chemistry method [Liu *et al*., 1992]. They demonstrated the gradient of AlF_3 in excess in the crust and the existence of liquid bath at temperature above 740 °C. More recently, Groutso *et al.* showed the gradient of chiolite in the crust with X-ray diffraction analysis [Groutso *et al.*, 2009]. The chemical composition of anode crust made from crushed bath mixed with alumina was demonstrated by Zhang *et al.* [Zhang *et al.*, 2013]. They revealed the development of porosity in the crust, thus allowing the penetration of bath and fumes. The crust in industrial cells has a vertical gradient of cryolite ratio (CR). The bottom is more concentrated in cryolite and the top zone is more acidic [Zhang *et al.*, 2013].

In the present study, samples of crust were collected in the side channel, between anodes and in the center channel. The chemical composition of each sample was determined by the Rietveld method performed on X-ray diffraction results. The reactions occurring in the ACM and crust were predicted by thermodynamic equilibrium calculations based on the temperatures measured in the crust. The thermodynamic studies help to understand the behavior of the crust and predict the melting temperatures of the phases inside the crust.

3.2.3 Methodology

Some samples were collected in an industrial cell in order to understand the anode crust chemical composition and behavior. Moreover, the temperature inside the crust of the side channel was measured throughout the life of the anode. The samples were taken at three different locations around the anode: 1) side channel, 2) between the anodes, and 3) center channel (Figure 3-2).

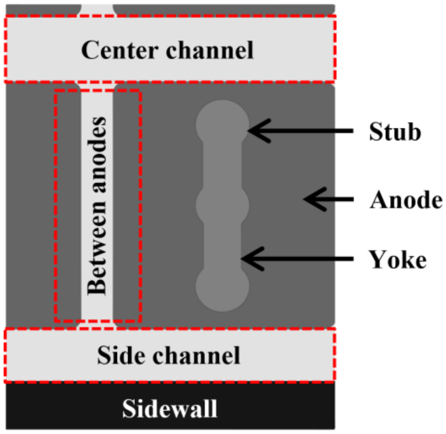

Figure 3-2 Position of the crust samples collected in the industrial cell (top view)

Firstly, three samples were taken before anode replacement, i.e. at the end of life of the anode. Secondly, three other samples were taken after the temperature measurements, also at the end of life of the anode. Thus, two sets of samples were collected for each position. The granular ACM used to cover the anode before the temperature measurements was also sampled. Finally, each sample was characterized in order to obtain their chemical compositions.

Characterization of the ACM and crust samples

Each sample of crust was cut in such a way to study the vertical concentration gradients. Afterward, the sample was ground in fine powder using a ball mill for X-ray diffraction (XRD) and oxygen analysis. A diffraction pattern of the crystalline phases in the sample was obtained with the XRD. The XRD data were also analyzed with a Rietveld method to obtain the chemical composition. The Al_2O_3 concentration was determined by oxygen measurement (LECO).

X-Ray Diffraction (XRD)

A PANalytical X'Pert PRO MPD diffractometer was used to obtain the diffraction pattern of the samples. The rotation speed of the sample holder was set to 1 s^{-1} and the data were obtained with the Cu Kα X-ray radiation. The diffraction pattern was acquired by using a $PIXcel^{1D}$ detector. The XRD data were collected from 10° to 74° at a 2θ angle with a resolution of 0.0263° and a time of 0.12 s per step.

Oxygen measurement

The oxygen content was determined using a TCH-600 (LECO) in order to calculate the Al_2O_3 in each sample. The samples were each placed inside a nickel capsule and were analyzed in triplicate. This method is useful to quantify the crystalline and amorphous phases of Al_2O_3 in the sample assuming that all the oxygen detected comes from Al_2O_3.

Scanning Electron Microscopy (SEM)

Some samples of crust were observed with a Hitachi S-4700 SEM. The elemental composition was evaluated with an Oxford X-Max 50 mm^2 energy dispersive X-ray spectroscopy (EDS) module. The analyses were conducted at an acceleration voltage of 20 kV, an intensity of the beam of 10 μA and a working distance of 12 mm.

Rietveld quantification

The crystalline phases in the various samples were quantified with a Rietveld method performed on XRD data. The Rietveld refinements were obtained with the software PANalytical HighScore Plus. The following phases were selected for the quantification: Na_3AlF_6, $Na_5Al_3F_{14}$, $NaAlF_4$, $Na_2Ca_3Al_2F_{14}$, $NaCaAlF_6$, $Na_4Ca_4Al_7F_{33}$, CaF_2, NaF, AlF_3, α-Al_2O_3, γ-Al_2O_3, δ-Al_2O_3, θ-Al_2O_3, β-Al_2O_3, Al_4C_3, Al and C. The chemical composition of each sample discussed in this article is expressed in weight percentage. The CR of the sample is the molar ratio of NaF/AlF_3 and is calculated with the stoichiometric concentration of compounds as determined by the Rietveld method.

Amorphous quantification

Each XRD analysis was conducted on powdered samples and on samples mixed with an internal standard of quartz (99.5 % SiO_2). The amorphous content was completed by adding 20 % of quartz in the sample. Equation 3-1 was used to determine the amorphous fraction in the quartz doped samples.

$$w_{amorphous} = \frac{1}{1 - w_1} - \frac{w_1}{w_2(1 - w_1)} \tag{3-1}$$

Where $w_{amorphous}$ is the mass fraction of the amorphous content in the sample, w_1 is the mass fraction of the quartz added (20 %) and w_2 is the mass fraction of quartz as determined by the Rietveld method. The amorphous content gives the fraction of the sample which could not be detected with the XRD.

Thermodynamic investigation

The thermodynamic equilibrium analysis was based on the results of Rietveld quantification and the Al_2O_3 concentration obtained by oxygen measurement. This investigation helped to describe the behavior of the ACM and the crust in industrial electrolysis cells. The reactions in the crust and the temperatures of phase transitions were calculated using the FactSage software (version 6.4). FactSage calculates the thermodynamic equilibrium based on the minimization of Gibbs free energy [Chartrand and Pelton, 2002]. The NaF-AlF_3-CaF_2-Al_2O_3 system was modeled with the FTHall database. The thermodynamic equilibrium calculations were carried out at atmospheric pressure.

3.2.4 Results and discussion

To investigate the crust chemical composition, samples of crust were taken at the end of life of two anodes. During the anode replacement, samples were collected in the side channel (SC), in the center channel (CC) and between the anodes (BA). After the anode change and before adding the ACM, the liquid bath was in contact with air. The top part of bath froze quickly. A sample of this freeze was collected before adding the ACM. Some thermocouples were placed in the side channel in order to verify the temperature of the ACM and crust during the life of the anode. A set of samples was taken before the temperature measurements and another set after the temperature measurements, both at the end of life of the anodes. The chemical compositions of the ACM and crust samples are described in the Table 3-1.

Table 3-1 Chemical compositions of the ACM and crust samples

Sample	Height* (mm)	Na_3AlF_6 (%)	$Na_5Al_3F_{14}$ (%)	AlF_3 (%)	$Na_2Ca_3Al_2F_{14}$ (%)	$NaCaAlF_6$ (%)	α-Al_2O_3 (%)	T-Al_2O_3** (%)	Amorph. Al_2O_3 (%)	Other (%)	Amorph. (%)	Total Al_2O_3 (%)	CR
ACM	-	7.4	12.2	0.9	1.6	0.5	26.3	30.0	19.9	1.2	35.8	76.2	1.82
Freeze	-	58.0	29.5	0.4	4.8	3.3	1.7	0.6	0.0	1.7	23.2	2.3	2.29
SC-before	0-45	79.9	10.9	0.0	5.0	2.7	0.5	0.1	0.0	0.9	34.3	0.6	2.64
	45-90	80.0	10.8	0.0	5.3	2.6	0.6	0.0	0.0	0.7	49.7	0.6	2.65
	90-125	85.1	7.6	0.0	4.1	2.2	0.1	0.0	0.0	0.9	40.0	0.1	2.72
	125-160	85.5	7.4	0.0	3.8	1.7	0.1	0.0	0.0	1.5	40.2	0.1	2.76
BA-before	0-22	14.8	38.7	1.0	3.6	0.0	41.4	0.0	0.0	0.5	27.4	41.4	1.84
	22-44	11.2	45.1	1.2	2.1	0.0	39.8	0.0	0.0	0.6	34.1	39.8	1.77
	44-66	4.5	42.4	2.0	1.4	0.0	38.3	2.5	4.5	4.4	42.3	45.3	1.55
CC-before	0-32	37.6	17.2	0.6	10.3	1.4	31.5	0.5	0.0	0.9	34.0	32.0	2.20
	32-64	9.9	44.7	1.0	4.3	1.2	34.9	3.5	0.0	0.5	32.5	38.4	1.73
	64-96	2.3	53.8	1.5	0.9	0.0	26.2	5.5	9.0	0.8	25.3	40.7	1.61
SC-after	0-50	1.4	50.9	3.8	1.0	1.2	37.0	0.5	0.0	4.2	50.8	37.5	1.43
	50-100	2.4	39.4	7.2	0.9	1.0	45.4	0.8	0.0	2.9	44.8	46.2	1.27
	100-150	8.0	27.0	3.5	0.7	0.7	54.7	4.3	0.0	1.1	36.6	59.0	1.57
BA-after	0-5	80.6	10.3	0.0	4.5	2.0	0.4	0.1	0.0	2.1	23.7	0.5	2.67
	5-16	38.7	19.8	0.0	7.6	0.0	31.9	1.0	0.0	1.0	41.9	32.9	2.29
	16-32	27.6	30.6	0.7	6.5	0.0	34.0	0.0	0.0	0.6	37.2	34.0	2.05
	32-48	7.3	49.9	2.7	1.4	0.7	21.4	4.3	10.4	1.9	32.8	36.1	1.60
	48-53	1.4	37.5	6.2	1.3	0.0	9.7	10.7	28.9	4.3	19.0	49.3	1.29
CC-after	0-11	31.2	25.9	0.0	7.8	2.7	31.4	0.6	0.0	0.4	35.0	32.0	2.12
	11-22	21.3	37.6	0.5	3.0	0.0	36.7	0.8	0.0	0.1	51.1	37.5	1.98
	22-33	3.3	56.8	2.4	1.2	0.4	23.6	4.9	6.1	1.3	29.3	34.6	1.57
	33-41	2.3	36.6	4.9	0.6	0.0	7.9	10.2	34.5	3.0	15.0	52.6	1.36

* Position from the bottom to the top of the sample; ** T-Al_2O_3 is the sum of the Al_2O_3 transition phases (γ, δ, θ, β)

The main crystalline phases detected by XRD are described in Table 3-1 (Na_3AlF_6, $Na_5Al_3F_{14}$, AlF_3, $Na_2Ca_3Al_2F_{14}$, $NaCaAlF_6$, α-Al_2O_3). T-Al_2O_3 is the sum of each transition phase of alumina detected by XRD (γ, δ, θ, β). The column "Other" includes the following phases: $NaAlF_4$, $Na_4Ca_4Al_7F_{33}$, CaF_2, Aluminum, and Carbon. The amorphous fraction of Al_2O_3 was labeled "Amorph. Al_2O_3". The column "Amorph." is given as an indication. It describes the part of the sample which could not be quantified by XRD (without considering Al_2O_3). The "Total Al_2O_3" is the Al_2O_3 content determined by oxygen analysis.

Composition of the industrial samples

ACM sample

The ACM is made of recycled anode cover, crushed bath and alumina. It was added around the anode in order to form the crust which was studied by temperature measurements. The ACM sample showed a high content of Al_2O_3 composed of 30.0 % of Al_2O_3 transition phases (γ, δ, θ, β), 19.9 % of amorphous Al_2O_3 and 26.3 % of stable α-Al_2O_3. The ACM contained a low concentration of calcium species and Na_3AlF_6 compared to the freeze above the bath. The CR of the ACM added around the anode (1.82) was lower than the CR of the freeze formed above the bath (2.29).

Side channel samples

The chemical composition of each sample varied depending on the nature of the sample and on the position in the cell. Regular operations were maintained during the life of the studied anodes. Firstly, the sample collected in the side channel before the temperature measurements (SC-before) had a similar chemical composition to the ledge on the sidewall. The anode cover was thin in this region and thus the sample was taken on the top of the side ledge. The sample was white and the texture was more like crystals. It was also irregular compared to the other samples of anode crust. Moreover, the CR was very high (2.64 to 2.76) and the Al_2O_3 concentration was low (0.6 to 0.1 %). The appearance of the sample SC-after was similar to the other samples of crust taken in the CC and BA. This sample did not demonstrate a clear vertical gradient of CR or acid species. The middle and the bottom of the sample SC-after were very acidic. The XRD analysis demonstrated a concentration of $Na_4Ca_4Al_7F_{33}$, a very acid species. Concentrations of 3.5 % and 1.2 % were detected in the bottom and the middle of the sample. $Na_4Ca_4Al_7F_{33}$ was only detected in this sample, and was included in the column "Other". Results showed also the presence of a vertical gradient of Al_2O_3. The top of the sample was more concentrated in Al_2O_3

than the bottom (59.0 % to 37.5 %). The CR of the sample was lower than the ACM. The same trend was observed with the Al_2O_3 concentration.

Samples between anodes

The samples taken between anodes showed clearly the vertical gradients of Na_3AlF_6, $Na_5Al_3F_{14}$, AlF_3, $Na_2Ca_3Al_2F_{14}$, and Al_2O_3. The bottom part of theses samples contained more Na_3AlF_6 and $Na_2Ca_3Al_2F_{14}$. The top part contained more $Na_5Al_3F_{14}$, AlF_3, and Al_2O_3. At the beginning of the crust formation, the liquid bath penetrates by capillary forces in the ACM to form crust [Gerlach and Winkhaus, 1985]. The penetration of the bath in the ACM increased the content in $Na_2Ca_3Al_2F_{14}$ and Na_3AlF_6 in the bottom part of the sample. The top part of the sample BA-after (48-53 mm) also showed a concentration of $NaAlF_4$ (2.3 %) according to XRD. The top of the sample BA-after had a very low CR (1.29). Both samples BA showed a vertical gradient of CR.

Center channel samples

The samples collected at the CC had similar chemical compositions than the samples located BA. They demonstrated a significant concentration gradient of acid species ($Na_5Al_3F_{14}$, AlF_3), calcium cryolite ($Na_2Ca_3Al_2F_{14}$), Na_3AlF_6 and Al_2O_3. The concentration gradient of $Na_2Ca_3Al_2F_{14}$ was more important in the CC crust compared to the crust BA. A concentration of $NaAlF_4$ (1.7 %) was also detected in the sample CC-after (33-41 mm) and its CR was also very low (1.36).

Al_2O_3 in the crust

The samples of anode crust investigated in this study showed a vertical gradient of Al_2O_3. Moreover, the Al_2O_3 at the bottom part of the crust had a higher fraction of α-Al_2O_3 than the top. The top of the crust contained more T-Al_2O_3 (γ, δ, θ, β) and amorphous Al_2O_3. The bottom of the crust had a higher temperature as it is closer to the bath. According to Less, a higher temperature and a contact with fluoride vapor increase the conversion of the transition phases of Al_2O_3 to the stable alpha phase [Less, 1977]. The samples SC-after (50-100 mm) and CC-after (11-22 mm) were observed by SEM-EDS (Figure 3-3 and Figure 3-4).

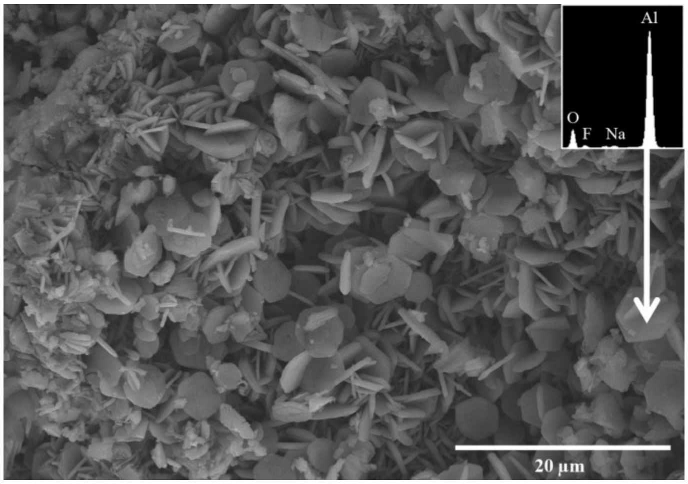

Figure 3-3 Alumina platelets in the sample SC-after (50-100 mm)

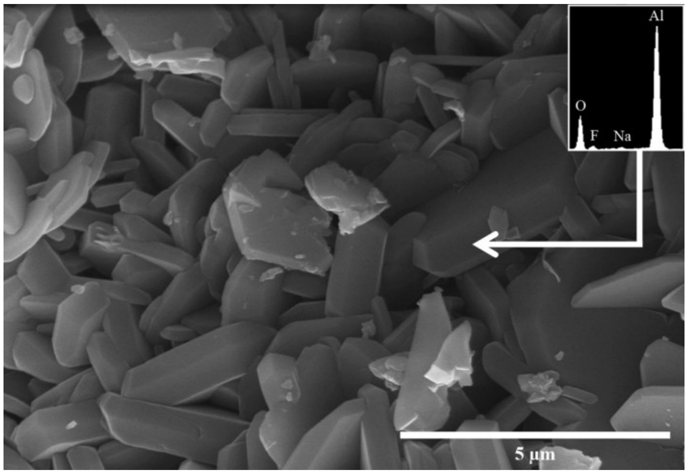

Figure 3-4 Alumina platelets in the sample CC-after (11-22 mm)

Figure 3-3 was taken at a magnification of 2000 x and Figure 3-4 at 10 000 x. The Al-O content in the platelets was demonstrated by elemental analysis (EDS). Thus, both figures show the network of α-Al_2O_3 inside the crust. The α-Al_2O_3 particles consolidate together in order to form a network, thus increasing the strength of the crust [Townsend and Boxall, 1984]. The solid bath around the particles also increases the strength of the crust [Liu *et al.*, 1992]. SEM-EDS analysis of the crust also showed areas where the hexagonal Al_2O_3 particles are embedded by solid bath.

Temperature measurements in the crust

The temperature evolving in the SC was evaluated in order to investigate the reactions occurring in the ACM and crust. The thermocouples (type K with Inconel sheath) were positioned following the installation of the new anode. Afterward, the SC was covered with the ACM. The bottom thermocouple (T_1) was placed on the surface of the top freeze, T_2 was located in the middle of the ACM in the SC and T_3 was close to the top. Figure 3-5 depicts the location of the thermocouples and Figure 3-6 shows the temperature measurements in the SC.

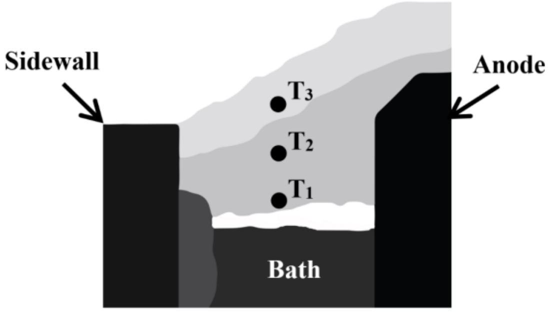

Figure 3-5 Location of the thermocouples in the SC

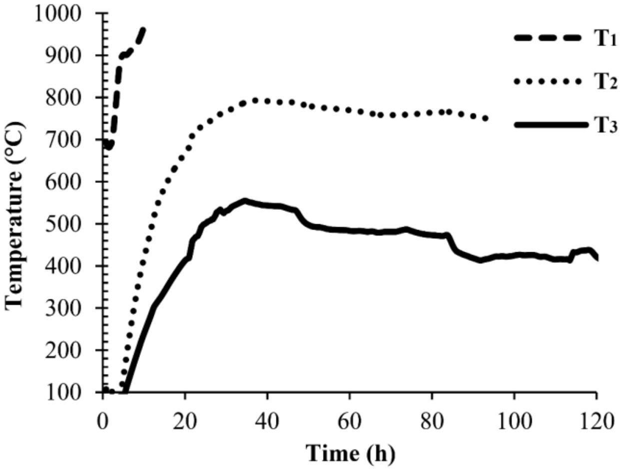

Figure 3-6 Temperature measurements in the SC crust

The temperature in the bottom of the crust increased quickly. After 10 hours, it reached 970 °C and the thermocouple became unstable. At this temperature, the top freeze under T1 melted and the liquid bath likely corroded the thermocouple. Liquid bath is very aggressive for any metallic instruments, even with an Inconel sheath. The temperature of T2 reached 792 °C after 40 hours and it began to decrease over the time. T3 also got to a maximum after 40 hours (555 °C). The reactions in the ACM and crust as a function of the temperature are described by the thermodynamic investigation.

Thermodynamic investigation of industrial anode crust

The behavior of the ACM and crust in an industrial cell is described by thermodynamic equilibrium calculations. The NaF-AlF_3-CaF_2-Al_2O_3 system, supersaturated in Al_2O_3, describes the reactions occurring in the ACM and crust. The temperature of phase transitions varied significantly depending on the cryolite ratio. Figure 3-7 shows the phase diagram of anode crust in industrial cells. The concentration of Al_2O_3 and CaF_2 was kept at 40 % and 2 % respectively in order to reproduce the typical chemical composition of the crust.

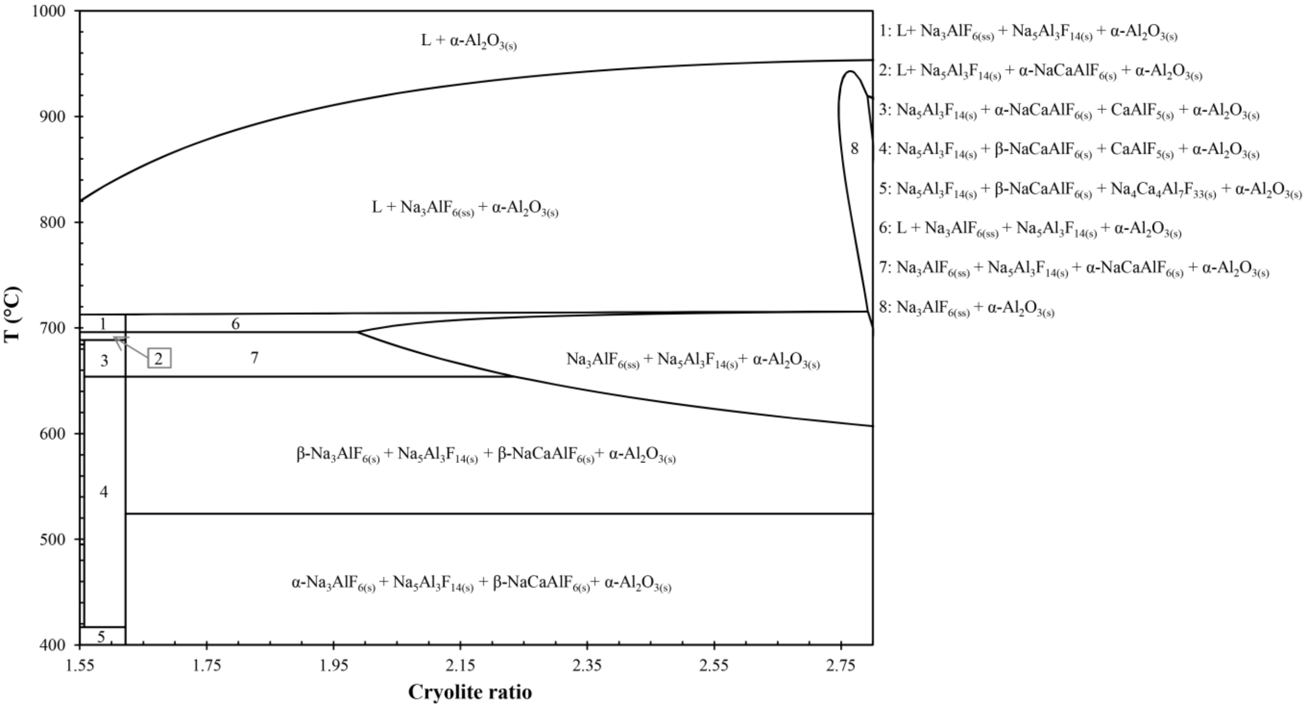

Figure 3-7 Phase diagram of the crust depending on the cryolite ratio (Al_2O_3 = 40 % and CaF_2 = 2 %)

Reactions in the ACM and crust

A wide range of temperatures was measured in the crust. The phase diagram (Figure 3-7) demonstrates the behavior of the crust at temperature between 400 °C to 1000 °C. At low temperature, the crust contains Na_3AlF_6, $Na_5Al_3F_{14}$, $NaCaAlF_6$, and Al_2O_3, at CR between 1.62 and 2.80 and at thermodynamic equilibrium conditions. The conversion of the Na_3AlF_6, from alpha to beta, occurs at a temperature of 524 °C.

$$\alpha - Na_3AlF_{6_{(s)}} \rightarrow \beta - Na_3AlF_{6_{(s)}} \quad (1.62 < CR < 2.80)$$

The crust of CR < 1.62 is composed by $Na_5Al_3F_{14}$, $NaCaAlF_6$, $Na_4Ca_4Al_7F_{33}$, and Al_2O_3 at a temperature below 417 °C. The acidic calcium cryolite, $Na_4Ca_4Al_7F_{33}$, was detected in the sample SC-after. The crust begins to melt at temperature of 696 °C due to the presence of $NaCaAlF_6$ (1.62 < CR < 2.0). At the same temperature, $NaCaAlF_6$ is dissolved in the Na_3AlF_6 solid solution at CR > 2.0. Na_3AlF_6 is produced at CR < 1.62 due to the melting of $NaCaAlF_6$

and $Na_5Al_3F_{14}$. The thermodynamic analysis shows a small concentration of stable $NaCaF_5$ between 417 °C and 688 °C ($1.56 < CR < 1.62$). $NaCaF_5$ melts at a temperature of 688 °C.

Excluding Al_2O_3, the major part of the crust is composed of $Na_5Al_3F_{14}$. The incongruent melting of the $Na_5Al_3F_{14}$ varies slightly depending on the CR. This compound melts at 713 °C and 715 °C with a CR of 1.55 and 2.79 respectively. At $CR < 1.37$, the $Na_5Al_3F_{14}$ melts completely at 712 °C, without producing Na_3AlF_6.

$$\mathrm{Na_5Al_3F_{14}}_{(s)} \rightarrow \mathrm{L} + \mathrm{Na_3AlF_6}_{(s)} \qquad (1.37 < CR < 2.79)$$

$$\mathrm{Na_5Al_3F_{14}}_{(s)} \rightarrow \mathrm{L} \qquad (CR < 1.37)$$

The $Na_5Al_3F_{14}$ content also decreases with increasing CR. The liquid fraction in the sample is very low at high CR. At CR around 2.8, the melting begins at a temperature of 920 °C. A lower CR also decreases the melting temperature of the Na_3AlF_6. Na_3AlF_6 completely melts at 953 °C with CR of 2.8 and 818 °C with CR of 1.55. Industrial crust of $CR < 1.37$ does not contain Na_3AlF_6 at any temperature and the bath phases completely melt at 712 °C. The main phase transitions occurring in the industrial samples of ACM and crust are described in Table 3-2. $T_{Na5Al3F14}$ and $T_{Na3AlF6}$ are the melting temperatures of the corresponding compounds.

Table 3-2 Summary of the main phase transitions in the ACM, freeze and crust

Sample	Height (mm)	CR	$T_{Na_5Al_3F_{14}}$ (°C)	$T_{Na_3AlF_6}$ (°C)
ACM	-	1.82	709	892
Freeze	-	2.29	714	970
SC-before	0-45	2.64	715	993
	45-90	2.65	715	994
	90-125	2.72	716	1000
	125-160	2.76	717	1002
BA-before	0-22	1.84	714	895
	22-44	1.77	717	878
	44-66	1.55	717	807
CC-before	0-32	2.20	700	928
	32-64	1.73	711	875
	64-96	1.61	719	824
SC-after	0-50	1.43	711	762
	50-100	1.27	702	-
	100-150	1.57	714	826
BA-after	0-5	2.67	716	997
	5-16	2.29	709	937
	16-32	2.05	711	921
	32-48	1.60	717	830
	48-53	1.29	704	-
CC-after	0-11	2.12	704	925
	11-22	1.98	716	915
	22-33	1.57	718	-
	33-41	1.36	713	-

In the samples, $Na_5Al_3F_{14}$ melts at temperatures between 700 °C and 719 °C depending on the CR and CaF_2 content. The CaF_2 decreases the melting temperature of $Na_5Al_3F_{14}$ according to thermodynamic equilibrium calculations. Na_3AlF_6 begins to melt from $T_{Na_5Al_3F_{14}}$ and finishes to melt at $T_{Na_3AlF_6}$. Thus, this compound melts gradually between ~700 °C and ~1000 °C in the anode crust, depending on the chemical composition. The gradient of CR in the crust implies a variation in the melting temperature of the bath phases present in the crust. The higher part of the crust has more risk to collapse compared to the bottom due to its lower CR. If the temperature reaches 700 °C, most of the bath phases, in the middle and top of the crust, would be in liquid state. In this condition, the crust is only supported by the Al_2O_3 platelets.

Behavior of the crust in industrial cells. At the beginning of anode life, the SC was filled with ACM deposited on a thin layer of freeze. Due to the insulating effect of ACM, this freeze begins to melt at 714 °C and finishes to melt at 970 °C according to thermodynamic calculations (Table 3-2). Thus the bottom of the crust, initially composed by frozen bath, melts after 10 hours, when it reaches a temperature of 970 °C (Figure 3-6). The thermodynamic analysis demonstrated the presence of liquid phases in the ACM and crust due to the acidic phases detected by XRD ($Na_5Al_3F_{14}$, $Na_2Ca_3Al_2F_{14}$, $NaCaAlF_6$, $Na_4Ca_4Al_7F_{33}$, and $NaAlF_4$). The liquid phase appears in the ACM at a temperature of 696 °C due to the $NaCaAlF_6$ content. The melting of $Na_5Al_3F_{14}$ occurs at 709 °C and melting of Na_3AlF_6 finishes at 892 °C. Consequently, the consolidation of the ACM into crust is initiated at a temperature of 696 °C due to the liquid species inside the ACM. Moreover, the weakness of the crust increases with a higher content of liquid. Thus, a highly acidic crust has more risk to collapse. For instance, a crust of $CR < 1.37$ will be only supported by the α-Al_2O_3 network if its temperature reaches 712 °C (2 % of CaF_2), as all acidic compounds melt at this temperature.

Formation of the crust. The formation of crust begins with the penetration of liquid bath in the ACM at the beginning of anode life [Gerlach and Winkhaus, 1985]. This process is also achieved when the $NaAlF_4$ vapor coming from the bath fumes diffuses into the ACM [Liu *et al.*, 1992]. $NaAlF_{4(g)}$ freezes in the ACM and decomposes to form $Na_5Al_3F_{14(s)}$ and $AlF_{3(s)}$. According to thermodynamic analysis, $NaAlF_4$ freezes at a temperature of 685 °C. Consequently, the temperature must be higher than 685 °C to form crust. Otherwise, the $NaAlF_4$ will be solid and no liquid phase will favor the consolidation of the crust. The top of the crust in industrial samples did not completely transform into stable α-Al_2O_3, as the temperature was not sufficient. The liquid in the ACM increases the conversion of the transition phases of Al_2O_3 (γ, δ, θ, β) to stable α-Al_2O_3. In this process, the α-Al_2O_3 platelets cement together and grow to form a strong network.

Industrial implications of the results. The melting temperatures of the phases in the industrial crust are strongly influenced by the gradients of acid species. The bottom of the crust is less acidic (CR close to the bath) and the top is highly acidic. While the electrolysis cell is in operation, the liquid bath splashes on the bottom of the crust, thus causing partial melting of the crust and forming stalactite crystal as observed by Zhang *et al.* [Zhang *et al.*, 2013]. Bath vapor, mainly composed of $NaAlF_4$, also diffuses in the crust. As detected by XRD, this increases the content in acid species over time, making the crust more vulnerable to collapse. Moreover, the vapor pressure of $NaAlF_4$ increases with temperature [Kvande, 1983]. Consequently, a higher quantity of $NaAlF_4$ will diffuse in the crust when the bath is at a higher local temperature. Thus, high bath temperature and frequent anode effects are detrimental to the stability of the crust. At plant scale, the acidity of the ACM could also increase over time, as the ACM is made from recycled crust. Additionally, $NaAlF_4$ vapor and bath splashes which penetrate in the crust contain a low Al_2O_3 concentration, thereby reducing its concentration in the crust. The crust made from ACM with a lower CR and lower Al_2O_3 presents a higher risk to collapse, thus amplifying operational problems. The crust is supersaturated in Al_2O_3 and it may sink into the bath leading to sludge formation.

3.2.5 Conclusions

The Rietveld method applied to X-ray diffraction results demonstrated the existence of vertical gradients of $Na_5Al_3F_{14}$, Na_3AlF_6, $Na_2Ca_3Al_2F_{14}$, and Al_2O_3 in the crust taken in the center channel and between anodes. Only a gradient of Al_2O_3 was found in the side channel. The top of the crust also showed a concentration of amorphous Al_2O_3 and transition phases of Al_2O_3, while the bottom was crystalline. An acidic crust is more likely to melt or collapse due to a lower melting temperature. Thermodynamic analysis demonstrated that the melting temperature of the crust is 712 °C when the CR is less than 1.37. The presence of liquid phase in the crust is due to the concentration of $Na_5Al_3F_{14}$, $Na_2Ca_3Al_2F_{14}$, $NaCaAlF_6$, $Na_4Ca_4Al_7F_{33}$, and $NaAlF_4$. The consolidated crust is weakened by the bath vapor, by splashing of the bath and by a high content of acid species.

3.2.6 Acknowledgements

This work is financed and supported by Rio Tinto Alcan, “Conseil de Recherches en Sciences Naturelles et en Génie du Canada” (CRSNG) and “Fonds de Recherche du Québec - Nature et Technologies” (FRQNT).

CHAPITRE 4 CARACTÉRISATION DES PROPRIÉTÉS THERMOCHIMIQUES DES MATÉRIAUX

4.1 Avant-propos

Auteurs et affiliation :

François Allard : étudiant au doctorat, Département de génie chimique et génie biotechnologique, Université de Sherbrooke, Québec, Canada.

Martin Désilets : professeur titulaire, Département de génie chimique et génie biotechnologique, Université de Sherbrooke, Québec, Canada.

Alexandre Blais : scientifique de recherche, Rio Tinto Aluminium, Centre de recherche et développement Arvida, Québec, Canada.

État de l'acceptation : Version finale publiée.

Revue : *Thermochimica Acta*.

Référence :

Allard, F., Désilets, M. et Blais, A. (2019). Thermal, chemical and microstructural characterization of anode crust formed in aluminum electrolysis cells. *Thermochimica Acta*, volume 671, p. 89-102.

Lien d'accès : https://doi.org/10.1016/j.tca.2018.11.008

Contributions à la thèse :

Une fois la composition chimique de la croûte d'anode industrielle démontrée, l'emphase a été mise pour déterminer ses propriétés thermiques et son comportement thermochimique. Ce chapitre présente les résultats de la caractérisation d'échantillons de croûte d'anode prélevés dans des cellules d'électrolyse industrielles. Une emphase est mise pour détailler une nouvelle méthode de détermination de la diffusivité thermique de bain électrolytique à l'état solide-liquide. Les points suivants résument les avancements exposés dans ce chapitre :

- Une nouvelle méthode a été développée pour mesurer la diffusivité thermique d'échantillon de bain électrolytique à haute température. Cette méthode a été appliquée aux échantillons de croûte d'anode industrielle, pour ainsi obtenir leur conductivité thermique sur une plage allant de 100 °C à 950 °C. Il s'agit des premiers résultats de conductivité thermique présents dans la littérature qui surpassent le point de fusion des phases de bain électrolytique, soit plus élevé qu'environ 700 °C.

- Les propriétés physiques et thermiques suivantes : diffusivité thermique, capacité thermique massique, enthalpies de transition de phase et de fusion, densité et conductivité thermique ont été déterminées expérimentalement, tout en ayant préalablement quantifié leurs compositions chimiques et observé leurs microstructures. Avec ces résultats, les propriétés thermiques sont disponibles pour couvrir l'entière plage de température, en condition d'opération, pour la croûte d'anode. Ces données thermiques sont cruciales pour modéliser de façon précise le transfert thermique dans les cellules d'électrolyse d'aluminium.
- Durant l'opération, la croûte d'anode fond, se dégrade et tombe dans la cellule d'électrolyse entrainant la formation d'un espace rempli de gaz que l'on appelle la cavité. Ce phénomène de dégradation est accentué à partir d'une température d'environ 935 °C, selon les analyses chimiques et les calculs d'équilibre chimique.

Un résultat supplémentaire concernant cette étude a été présenté dans l'Annexe A.1. Une image de microtomographie a été produite afin qu'il soit possible d'observer la morphologie 3D d'un échantillon solide qui a été analysé par *LFA* dans ce chapitre.

Titre français :

Caractérisation thermique, chimique et microstructurale de la croûte d’anode formée dans les cellules d’électrolyse d’aluminium

Résumé :

Le matériau de recouvrement anodique (*ACM*) réagit avec le bain liquide et la vapeur qui pénètrent à l'intérieur de celui-ci pour former un matériau plus dense, qui est appelé la croûte d’anode. Les propriétés thermiques de la croûte d'anode influencent les pertes thermiques supérieures des cellules d'électrolyse d'aluminium. Le fonctionnement et la conception de la cellule d'électrolyse peuvent être contrôlés grâce à une meilleure compréhension de l'évolution thermochimique de la croûte d’anode. La croûte d'anode typique se trouve à l'état solide jusqu'à 696 °C ou à l'état solide-liquide à des températures plus élevées. Sa conductivité thermique est déterminée de 100 °C à 950 °C sur les échantillons extraits d'une cellule industrielle. Par exemple, la conductivité thermique de la partie inférieure de la croûte d’anode diminue de 1.38 W m^{-1} $°C^{-1}$ à 100 °C jusqu’à 0.89 W m^{-1} $°C^{-1}$ à 950 °C. La capacité thermique massique, l'enthalpie, la densité apparente et la diffusivité thermique sont également déterminées à partir de mesures expérimentales. Les phases cristallines composant la croûte d’anode sont quantifiées par une méthode de Rietveld appliquée aux patrons de diffraction des rayons X. Le comportement thermochimique de la croûte d’anode industrielle est étudié à l'aide de la calorimétrie différentielle à balayage et grâce à des calculs d'équilibre thermodynamique. Les phases cristallines, $Na_5Al_3F_{14}$, α-Al_2O_3 et Na_3AlF_6, sont les principales phases qui composent la croûte d’anode. L'analyse chimique met également en évidence la quantité importante d'alumine amorphe et la présence d’une faible quantité de composés de cryolite de calcium. À partir de 717 °C, une solution d’α-$Al_2O_{3(s)}$, de $Na_3AlF_{6(s)}$ et de bain liquide compose la croûte d’anode selon les résultats d'équilibre thermodynamique. De plus, les propriétés thermiques de chaque échantillon sont données avec la composition chimique correspondante.

4.2 Thermal, chemical and microstructural characterization of anode crust formed in aluminum electrolysis cells

Keywords: Anode crust, anode cover material, thermal property, chemical composition, aluminum electrolysis

4.2.1 Abstract

The anode cover material (ACM) of aluminum electrolysis cells reacts with the liquid bath and vapor penetrating inside this powdered material to form a denser material, which is called the anode crust. The thermal property of the anode crust affects the top heat losses of aluminum electrolysis cells. The operation and design of electrolysis cells can be controlled through a better understanding of the thermochemical evolution of the anode crust. The typical anode crust is found either in the solid state up to 696 °C or in the solid-liquid state at higher temperatures. Its thermal conductivity is determined from 100 °C up to 950 °C on the samples extracted from an industrial electrolysis cell. For example, the thermal conductivity of the lower part of the anode crust decreases from 1.38 W m^{-1} $°C^{-1}$ at 100 °C to 0.89 W m^{-1} $°C^{-1}$ at 950 °C. The specific heat capacity, enthalpy, bulk density and thermal diffusivity are also determined from experimental measurements. The crystalline phases composing the anode crust are quantified with a Rietveld method performed on X-ray diffraction patterns. The thermochemical behavior of the industrial anode crust is investigated with differential scanning calorimetry and thermodynamic equilibrium calculations. The $Na_5Al_3F_{14}$, α-Al_2O_3 and Na_3AlF_6 are the main phases composing the anode crust. The chemical analysis also demonstrates a significant amount of amorphous alumina and a low amount of calcium cryolite compounds. From a temperature of 717 °C, the α-$Al_2O_{3(s)}$, $Na_3AlF_{6(s)}$ solution and liquid bath solution compose the anode crust according to the thermodynamic equilibrium results. Furthermore, the thermal property of each sample is given with the corresponding chemical composition.

4.2.2 Introduction

The aluminum is produced by the reduction of alumina (Al_2O_3) to aluminum in an electrolysis cell. The main components of a modern electrolysis cell consist of prebaked carbon anodes, molten salt with dissolved alumina (usually referred to liquid bath), liquid aluminum and graphitized carbon cathode blocks. The electrical current flows through the consumable anodes immersed into the liquid bath to produce aluminum at the cathode, which is the top of the aluminum pad. A schematic of the industrial aluminum electrolysis cell and its main components is described in Figure 4-1.

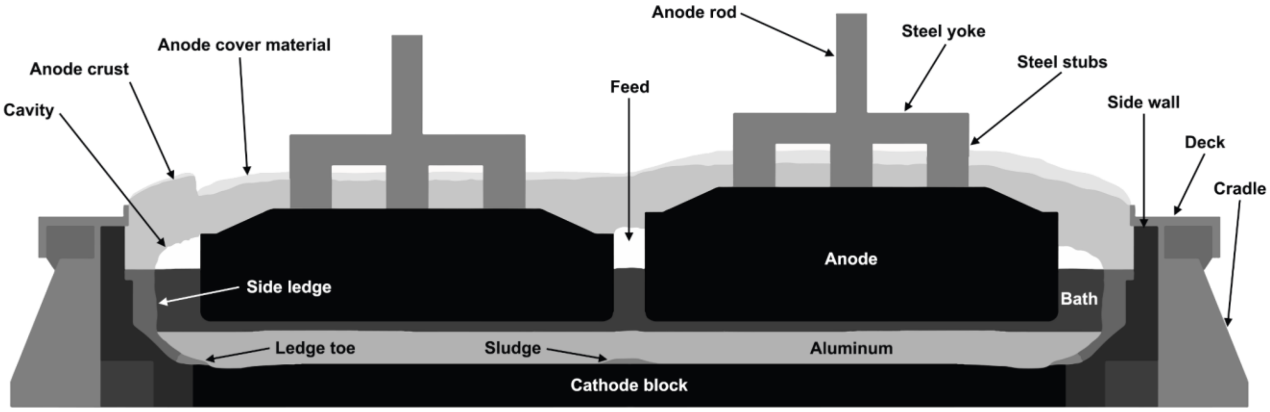

Figure 4-1 Schematic of an aluminum electrolysis cell with its main components

Over the last decades, the electrical current in electrolysis cells was risen to increase the productivity of the industrial cells. The heat generation and the dissipation in the electrolysis cell rise when the electrical current input increases due to Joule heating taking place in the resistive components. Typically, the electrolysis cell efficiency depends on the electrolyte chemistry, the cell materials and design, the operating temperature, the voltage disturbance and the phase change materials located on the side walls and the top of the cell. Since the electrolysis cell is self-heating, its energy efficiency relies on the magnitude of the energy generation and the corresponding heat losses, which is linked to the thermal properties and thermochemical behavior of these phase change materials. Accordingly, the thermal properties of the anode cover can influence the heat loss distribution and consequently affect the energy efficiency.

Industrial electrolysis cells operate with an electrolytic bath primarily composed of a mixture of Na_3AlF_6 (cryolite), AlF_3 (aluminum fluoride), CaF_2 (calcium fluoride) and Al_2O_3. The electrolyte usually contains additives and impurities in the form of lithium, potassium and magnesium fluoride salts. The electrolysis cell operates at a temperature of approximately 965 °C and is designed to dissipate heat from its sides in order to build a thick layer of freeze, essentially composed of frozen cryolite, on the side walls. This layer of freeze, usually called side ledge, is mandatory to protect the side walls from the highly corrosive and erosive behavior of liquid bath and liquid aluminum. The ledge grows on the side materials by the solidification of Na_3AlF_6 at a temperature of approximately 950 °C and its thickness depends on the heat flow that regulates the thermal balance of the electrolysis cell.

The heat balance of the electrolysis cell can be improved through a better understanding of the thermal properties of the anode cover, which is mandatory to insulate the top of the cell, to absorb an important fraction of the fluoride fumes emissions and to prevent air burn of the carbon anodes. During the process of aluminum production, dissolved oxide ions react with the prebaked carbon anodes to form carbon dioxide (CO_2) that exits through the cracks and holes of the anode cover. The carbon anodes are typically replaced after a few weeks, a frequency which depends on the anode size and the rate of carbon consumption. When a carbon anode is almost totally consumed, it is removed and a new anode is set. Since the liquid bath enters in contact with the cold anode, a layer of frozen bath grows around the anode and at the top of the channels in contact with colder gases. A top layer of frozen bath of a few centimeters is built in the channels, which helps to support the ACM. Then, after a few hours of operation, the anode cover material (ACM) is spread over the new anode. Afterwards, a new thermal equilibrium is established where the previously frozen layer melts due to the insulating properties of the ACM and the heat dissipated from the liquid bath. However, a large amount of frozen bath remains around the anode and melts gradually. More precisely, the frozen bath on the sides of the anode is the first part to melt and dissolve in the bulk liquid bath due to the flow pattern generated by the gas being formed on the adjacent anodes. On the other hand, the undersurface freeze will melt at a lower rate until about two days after the new anode was set. Meanwhile, the liquid fluoride salts coming from the bulk liquid bath, the vapor condensate ($NaAlF_4$) and the phases of low melting point in the ACM ($Na_5Al_3F_{14}$, $NaCaAlF_6$, $Na_2Ca_3Al_2F_{14}$) penetrate in the ACM powder, a phenomenon at the origin of the formation of a dense crust consisting of solidified bath and alumina. During all the anode life cycle, the fluoride vapor ($NaAlF_4$) from the liquid bath enters and acidifies the anode cover.

The anode cover of electrolysis cells is separated in two distinct parts: the ACM and the anode crust. The ACM processing methods and its composition vary depending on the industrial plant. The main specifications considered to process the ACM mixture is its thermal conductivity, mechanical stability, airtightness, angle of repose, storage properties and ease of transportation [Eick *et al.*, 2010]. The ACM is usually made from recycled anode crust, crushed bath and smelter grade alumina (SGA) and contains impurities such as carbon, iron, silicon and aluminum [Wilkening *et al.*, 2005]. A mix of fine to coarse particles characterizes the granulometry of this material. The thermal conductivity of the ACM increases with its bulk density according to measurements performed with the hot wire method [Llavona *et al.*, 1988], and it also increases with temperature according to other analysis performed on various mixtures of ACM with a laboratory-made apparatus [Shen, 2006; Wijayaratne *et al.*, 2011]. The chemical composition has a less significant effect on the thermal conductivity of ACM when compared to the particle size distribution [Wijayaratne *et al.*, 2011].

The interaction of ACM with liquid bath implies the formation of a hard crust located around the anodes. The anode crust consolidates when fluoride vapor and liquid bath enter in contact with alumina particles in the ACM. The fluorides from the bath favor the conversion rate of γ-Al_2O_3 to the stable α-Al_2O_3 and lower the transformation temperature [Less, 1977; Oedegard *et al.*, 1985]. A network of interlinked α-Al_2O_3 platelets is built inside the crust when the ACM enters in contact with the liquid bath. ACM composed by highly calcined metallurgical grade alumina or with alumina which already reacted with bath fumes forms a weaker crust [Townsend and Boxall, 1984; Gerlach and Winkhaus, 1985].

Two decades ago, the elemental chemical composition of anode crust was quantified using the wet chemistry method and X-ray fluorescence (XRF) [Liu *et al.*, 1992]. According to these methods, the crust contains a higher AlF_3 concentration than the bulk liquid bath inside the electrolysis cell. X-ray diffraction (XRD) patterns of crust suggested that it is mainly composed of α-Al_2O_3, $Na_5Al_3F_{14}$ (chiolite) and Na_3AlF_6 [Liu *et al.*, 1992; Groutso *et al.*, 2009]. In the last decade, the Rietveld quantification method performed on XRD patterns replaced gradually elemental analysis methods and it allowed a proper characterization of the crystalline phases in the electrolytic bath of electrolysis cells [Feret, 2008]. The anode crust contains more Na_3AlF_6 closer to the bulk liquid bath, while the top of the anode crust shows more Al_2O_3 according to the Rietveld characterization [Zhang *et al.*, 2013, Allard *et al.*, 2015b]. The top of the crust also contains a higher concentration of amorphous Al_2O_3 and transition phases of Al_2O_3, while the bottom contains more crystalline phases of Al_2O_3 [Allard *et al.*, 2015b].

The thermochemical processes evolving in the industrial anode crust were only investigated with an experimental setup replicating the basis of differential thermal analysis (DTA) [Zhang *et al.*, 2014]. Capillary forces drive the rate of penetration of the liquid bath in the ACM, while the progression stops when the local temperature reaches the solidus of the bath [Eggen *et al.*, 1992]. The melting temperature of the bath phases in anode crust usually range from around

700 °C to 950 °C, depending on the complex chemical composition of this material [Allard *et al.*, 2015b; Zhang *et al.*, 2014]. The γ-Al_2O_3 to α-Al_2O_3 transformation occurs near 800 °C with 2 % of AlF_3 additive in the alumina [Oedegard *et al.*, 1985; Živkovic *et al.*, 1995; Riello *et al.*, 2016]. However, the ACM consolidation to anode crust occurs at around 700 °C in industrial electrolysis cells [Liu *et al.*, 1992; Eggen *et al.*, 1992]. This temperature corresponds approximately to the peritectic temperature of $Na_5Al_3F_{14}$ and is very close to the moving boundary between ACM and crust, as confirmed by temperature measurements in industrial cells [Liu *et al.*, 1992]. The overall peritectic and solidification temperatures of typical anode crust are 725 °C and 685 °C [Zhang *et al.*, 2015]. These temperatures match with the peritectic solidification of $Na_5Al_3F_{14}$ and the solidus in a highly acidic NaF-AlF_3-CaF_2-Al_2O_3 system [Allard *et al.*, 2015b].

The top of the anode cover is usually made of unreacted ACM and it also contains a layer of low-density crust in which there is more alumina and less absorbed bath. The low-density crust demonstrates a lower hardness than the high-density crust, which absorbs more bath [Johnston and Richards, 1983]. The thermal conductivity of laboratory made alumina crust increases by a close-to-linear relationship with its density, according to experimental results performed with the hot wire method at 400 °C [Hatem *et al.*, 1989]. The thermal conductivity of laboratory crust shows a slight decrease with temperature (from 25 °C to 800 °C) [Hatem *et al.*, 1989; Shen, 2006]. Anode crusts sampled in industrial cells demonstrate comparable thermal conductivity than the laboratory ones [Shen *et al.*, 2008; Llavona *et al.*, 1990]. However, the thermal conductivity of industrial anode crusts has not been measured at temperature higher than 600 °C, although the temperature inside this material in operating cells reaches up to 950 °C. The highly corrosive behavior of the fluoride compounds in the anode crust at temperature close to 700 °C can damage the components in the hot wire apparatus [Llavona *et al.*, 1990]. The thermal conductivity of the crust decreases from the bottom up to the top, according to measurements in laboratory using thermocouples and a heat flux sensor [Rye, 1992]. With a similar methodology, laboratory crusts only made from primary alumina demonstrated a lower thermal conductivity than crusts made with a mixture of crushed bath and alumina [Rye *et al.*, 1995].

In the last years, the laser flash method has been performed on side ledge samples collected in industrial electrolysis cells to determine the thermal diffusivity and conductivity at temperature up to 550 °C [Poncsák *et al.*, 2014; Poncsák *et al.*, 2015; Gheribi *et al.*, 2017]. Results from the laser flash method are in line with theoretical and literature values of refractory ceramics, and are similar to hot wire methods results [Hemrick *et al.*, 2003]. Theoretical models of thermal conductivity were built to predict the thermal behavior of essential materials in the aluminum electrolysis cells [Gheribi *et al.*, 2016, 2017]. Recently, the thermal conductivity of a high temperature liquid fluoride salt used in the nuclear industry was measured using a graphite crucible and a laser flash apparatus [An *et al.*, 2015]. The anode crust contains a more acidic chemical composition and a higher concentration of alumina phases compared to the side ledge or the liquid bath. The thermal conductivity of the anode crust must be determined to obtain critical data for modeling and heat transfer predictions, which are used by the aluminum industry for electrolysis cell design.

In this work, thermal analyses combined with chemical and microstructural characterization are performed to determine the properties of anode crusts from electrolysis cells. An exhaustive characterization with the newest methods is mandatory to get a rigorous understanding of the thermochemical behavior of such critical material for the stable operation of the electrolysis cell. A new method to determine the thermal diffusivity and conductivity of solid-liquid electrolytic salts up to 950 °C is detailed in this work. The chemical reactions involved in the process of anode crust consolidation and its typical composition are established using XRD analysis and Rietveld quantification. The phase transitions and reactions are determined with differential scanning calorimetry (DSC) analysis combined with thermodynamic equilibrium calculations in order to understand the processes involved in the anode crust formation. The experimental methods involved in this study aim to bring new data for modeling studies, new characterization methods for researchers in the field of aluminum electrolysis or molten salts characterization and new scientific knowledge on the thermal and chemical processes occurring during the transformation of ACM into anode crust.

4.2.3 Materials and methods

Materials

The thermal, chemical and microstructural properties of ACM and anode crust were characterized on samples collected in industrial electrolysis cells. The cells were operated as usual and without special events noticed. Some samples of crusts were collected on the center channel (middle of the electrolysis cell), on the anode and on the side channel (next to the deck), see Figure 4-2. The sample collected in the side channel (SC) was extracted at the mid-life of the anode. The samples collected on the anode (OA) and on the center channel (CC) were taken at the end of life of the anode. In order to compare the chemical compositions, samples of ACM and side ledge were collected in cells from the same plant. The ACM was made from recycled anode crust, crushed bath and SGA. The samples produced from the anode crusts taken in the SC, OA and in the CC were selected in order to globally represent the anode crust covering the anodes of electrolysis cells. The surface of the anode crust covering the top of an electrolysis cell is distributed as follows: 15 % in SC, 80 % OA and 5 % in CC.

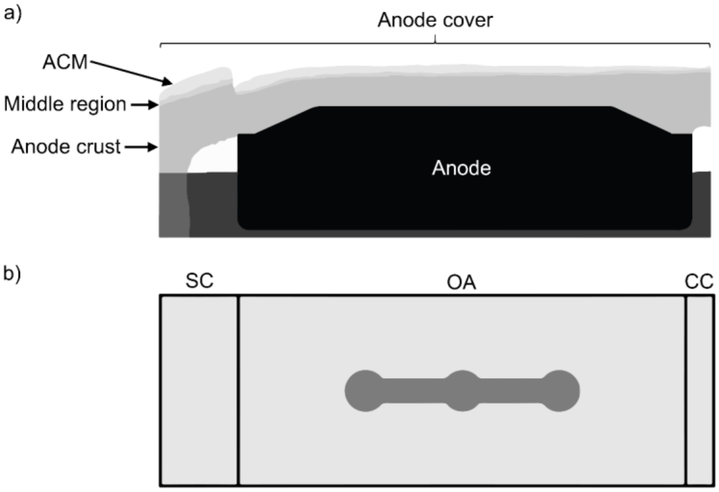

Figure 4-2 Diagrams of the top of the electrolysis cell: a) side view illustrating the three components included in the anode cover and b) top view defining the side channel (SC), on the anode (OA) and center channel (CC) parts of the anode crust

As mentioned in the introduction, before the ACM is poured on the anodes, the top part of the bulk bath freezes in contact with colder gases. A sample of this “top freeze” was also extracted. The samples of crusts were drilled with a diamond hole saw in order to build cylinder shaped samples. A cylinder was extracted at each required height to quantify the vertical gradient of properties. The orientation of the samples of crust remains the same as in the electrolysis cell. The following sections describe the detailed methods of each characterization technique employed.

Thermal analysis

Laser flash analysis

The thermal diffusivity was measured with a laser flash apparatus (NETZSCH LFA 457 *MicroFlash*). The cylindrical samples extracted from the anode crusts were sliced using a small circular saw equipped with a diamond blade. Disk-shaped samples of approximately 3 mm of thickness and 12 mm of diameter were made from the cylindrical samples. The thickness and diameter of each disk were measured at 5 positions and the average was used to compute the thermal diffusivity. The thermal diffusivity of disk-shaped sample was determined by following the standard test method ASTM E1461-13 [ASTM, 2013]. Each sample was coated twice with a thin layer of colloidal graphite spray (GRAPHIT 33 from KONTAKT CHEMIE). A short laser pulse operating at 2882 V was shot on the front side of the disk and the temperature rise on the rear side was measured with an InSb infrared detector. The thermal diffusivity of each sample was determined during a cooling ramp. The temperature was stabilized at 600, 550, 500, 450, 400, 300, 200 and 100 °C. At each temperature, five laser pulses were shot. All thermal diffusivity tests were performed in a controlled chamber purged with N_2 at a rate of 200 mL min^{-1}. The thermal diffusivity values were calculated with the improved Cape-Lehman model, which considers the finite pulse effect and takes into account facial and radial heat losses [Cape and Lehman, 1963; Blumm and Opfermann, 2002]. The Cape-Lehman model was found to determine the thermal diffusivity within 1.5 % of the original value [Blumm and Opfermann, 2002]. A standard deviation of 0.8 % was evaluated by performing 15 laser pulses at 400 °C on the OA-2 sample to evaluate the repeatability. The thermal diffusivities of the crust disks were not determined at temperatures higher than 600 °C in order to avoid the melting of phases inside the crust and prevent damages to the apparatus.

After the disk-shaped samples were taken from the cylinders of crust, the parts directly above and below the cut sections were crushed and mixed together to form a fine powder (Figure 4-3). This powder was used to determine the high temperature thermal diffusivity, to conduct the DSC analysis and to perform the chemical analysis. The thermal diffusivity of the crust was measured at a temperature up to 950 °C by placing the powdered sample in a platinum-rhodium container with a lid (NETZSCH part no. 6.256.4-91.5 made from Pt 90 % / Rh 10 %). A space for liquid expansion is located between the lid and the edge of the container. The lid has four holes to let vapor escape. The temperature was limited by the evaporation of the corrosive species exiting the container, thus to reduce the risk of corroding the quartz chamber. The thermal diffusivity of the crust in solid-liquid state was determined with a three-layer model resolved with the NETZSCH LFA Software. The three-layer model considers the heat losses and pulse correction. Therefore, the energy produced by the laser pulse is transmitted through these three-layers of known dimensions: Pt/Rh container, sample and Pt/Rh lid. The Pt/Rh container and lid were coated with a colloidal graphite spray before each experiment. During experiments, the temperature of the three-layers system was first risen at a maximum and decreased to reach each of the desired temperature for thermal diffusivity measurements (from 950 to 700 °C at intervals of 50 °C). At each stabilized temperature, five laser pulses were shot. The temperature of the top of the lid was recorded with an IR sensor. The maximum temperature was chosen to be immediately over the melting temperature of the Na_3AlF_6 in order to prevent evaporation of corrosive species, but still be sufficient to melt all the bath phases inside each sample according to the chemical composition and DSC analysis. During the experiments, the alumina phases were not completely dissolved, accordingly to the real industrial conditions experienced by the anode crust.

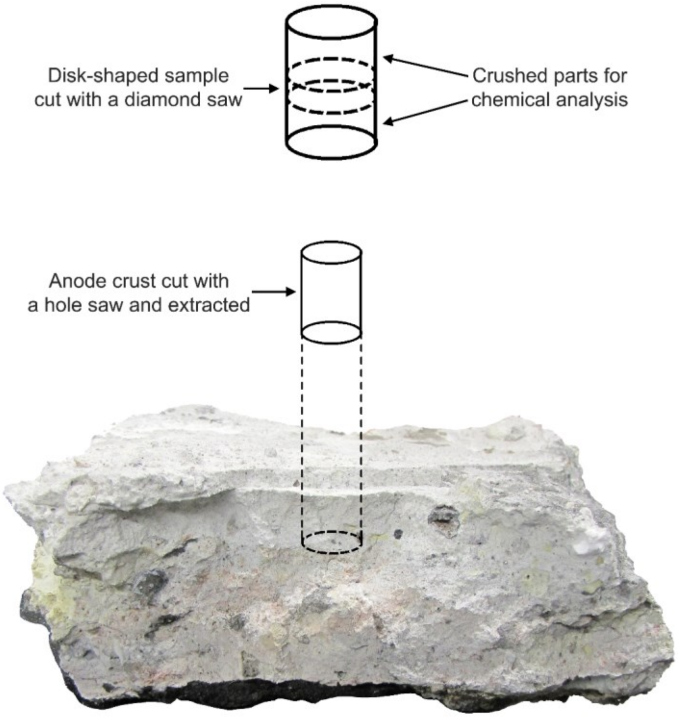

Figure 4-3 Sample preparation performed on anode crust (CC) for the LFA and the chemical analysis

Differential scanning calorimetry

The heat capacity, enthalpy and temperatures of phase transitions were investigated with a NETZSCH DSC 404 F3 Pegasus. The heat flow calibration was achieved using a synthetic sapphire disk in order to measure the specific heat capacity (c_p). The temperature calibration was realized with the following reference material: In, Sn, Bi, Zn, Al and Au. The method used to conduct the experiments follows ASTM E1269-11 recommendations [ASTM, 2011]. The

DSC equipped with a platinum furnace can reach a temperature of 1500 °C. The samples analyzed in this study were measured from 50 °C to 1050 °C at a heating rate of 10 °C min^{-1}. The controlled atmosphere of each test was assured by a continuous flow of nitrogen at 20 mL min^{-1}. The samples were put in a graphite crucible of 85 µL and a graphite lid was installed on the crucible before measurements. The graphite lid has a small vent hole in the center, such that pressure build-up cannot occur inside the crucible. The lid helps to obtain a better baseline, to lower the evaporation and to achieve a better repeatability. For each analysis, 40 mg of powdered sample coming from the cylinder of crust were used. The results were treated with the NETZSCH Proteus software for thermal analysis. The enthalpy of phase transitions was determined by calculating the peak area with the software.

Thermal conductivity calculations

The thermal conductivity was determined on disk-shaped samples and on samples placed in the Pt/Rh container for high temperature measurements. The thermal conductivity was calculated using the general relationship Equation 4-1.

$$k = \alpha \, c_p \, \rho_{bulk} \tag{4-1}$$

The thermal conductivity (k) can be derived from the thermal diffusivity (α), the specific heat capacity (c_p) and the bulk density (ρ_{bulk}). All α values were obtained with the LFA. The theoretical c_p values were computed with the chemical thermodynamic software FactSage using the measured chemical composition. These values were confirmed with the DSC analysis performed on industrial samples. The ρ_{bulk} values were measured on the disk-shaped samples at room temperature, neglecting thermal expansions. The uncertainty of the ρ_{bulk} calculations was 2.1 %. The error of the thermal conductivity determination is approximately 10 % considering the measurements of α, c_p and ρ_{bulk}.

For high temperature measurements, anode crust samples were firstly heated above the melting temperature of Na_3AlF_6 and then cooled down. The ρ values were calculated from the true density of the bath saturated in Al_2O_3 (liquid) and with the true density of α-Al_2O_3 (solid). As solidification processes occurred during the cooling ramp, the solid-liquid composition of the mixture in function of the temperature was computed with thermodynamic equilibrium calculations. Consequently, FactSage was used to calculate the true density (theoretical density without porosity) of the crust mixture in function of the temperature. Using the true density implies the hypothesis that no gas or void was present between the Pt/Rh container and its lid. The amount of powder added in the container before an experiment was sufficient to fill this volume completely.

Chemical analysis

X-ray diffraction and Rietveld quantification

A fine powder was produced in a ball mill from the cylinder sampled from anode crust. The same powder was used to perform the diffraction pattern, the DSC analysis, the high temperature LFA and the oxygen analysis. The crystalline phases which composed the industrial anode crusts were observed with a PANalytical X'Pert PRO diffractometer. The rotation speed of the sample holder was set to 1 s^{-1} and the data were obtained with the Cu Kα X-ray radiation. The diffraction pattern was acquired with a $PIXcel^{1D}$ detector. The XRD data were collected from 10° to 74° at a 2θ angle with a resolution of 0.0263° and a 0.12 s time step.

The phases in the various samples were quantified with a Rietveld method performed on XRD data. The Rietveld refinements were obtained with the software PANalytical HighScore Plus. The following phases were selected for the quantification: Na_3AlF_6, $Na_5Al_3F_{14}$, $NaAlF_4$, $Na_2Ca_3Al_2F_{14}$, $NaCaAlF_6$, $Na_4Ca_4Al_7F_{33}$, CaF_2, NaF, AlF_3, α-Al_2O_3, γ-Al_2O_3, δ-Al_2O_3, θ-Al_2O_3, β-Al_2O_3, Al_4C_3, Al and C. The chemical composition of each sample discussed in this article is expressed in mass percent. The cryolite ratio (CR) of a sample is the molar ratio of NaF/AlF_3 and is calculated with the molar stoichiometric proportions of elements in the compounds quantified by the Rietveld method.

Oxygen analysis

The total oxygen content was determined with a LECO TCH-600 in order to calculate the total Al_2O_3 in each sample. Each sample was placed inside a nickel capsule and was analyzed in triplicate. The method is useful to quantify the crystalline and amorphous phases of Al_2O_3 assuming that all the oxygen detected comes from Al_2O_3. The amorphous alumina content is calculated by subtracting the crystalline amount from the total amount.

Microstructural characterization

Scanning electron microscopy

The scanning electron microscopy (SEM) was performed with a Hitachi S-4700 on some samples of anode crust. The elemental composition was evaluated with an Oxford X-Max

50 mm^2 energy dispersive X-ray spectroscopy (EDS) module. The SEM was conducted with an acceleration voltage of 20 kV, an intensity of the beam of 10 µA and a working distance of 12 mm.

Thermodynamic equilibrium calculations

The temperatures of phase transitions and reactions were computed from thermodynamic equilibrium calculations. Firstly, the chemical compositions of anode crusts were analyzed to allow the chemical equilibrium calculations with the FactSage 7.1 software. Then, the FTHall database was used to calculate the thermodynamic equilibrium of the NaF-AlF_3-CaF_2-Al_2O_3 system. The model used in FactSage to represent the Gibbs energy of the electrolytic bath was previously detailed [Bale *et al.*, 2016]. The minimization of the total Gibbs energy of a system at a given temperature, pressure and composition is performed using Equation 4-2.

$$G = \sum_{\phi} N^{\phi}\, G_m^{\phi} \tag{4-2}$$

In Equation 4-2, ϕ is a phase index, N^{ϕ} is the amount and G_m^{ϕ} is the integral molar Gibbs energy of phase ϕ [Eriksson and Hack, 1990]. The thermochemical properties for each chemical composition of anode crust were calculated with the Equilib module of FactSage. The theoretical specific heat capacity of each sample was calculated with FactSage, and was also measured experimentally with the DSC apparatus. FactSage was also used to determine the true density at chemical equilibrium. Thermodynamic calculations allowed to study the behavior of the ACM and the anode crust at the prevailing high temperatures of the industrial process.

4.2.4 Results

Chemical composition of materials

<u>XRD patterns, Rietveld quantification and amount of Al_2O_3</u>

The materials collected in industrial electrolysis cells were characterized in order to observe their crystalline structure, to quantify their phases composition and to determine the total Al_2O_3 content. The thermochemical behavior, the specific heat capacity, the reactions and the phase transitions can be determined by knowing the chemical composition and performing the thermodynamic calculations. The process of anode crust formation begins when liquid bath penetrates into the ACM and when the temperature inside the ACM is superior to the melting temperature of the liquid phases rising in this material. This process continues with the fluoride vapor ($NaAlF_4$) penetrating in the anode crust and ACM. The mass transfer of liquid bath and vapor into the ACM also modifies its chemical composition. Figure 4-4 provides examples of XRD data from samples of ACM and anode crust. The anode crust called OA-2 was extracted from the middle part of a sample taken on the top of an anode.

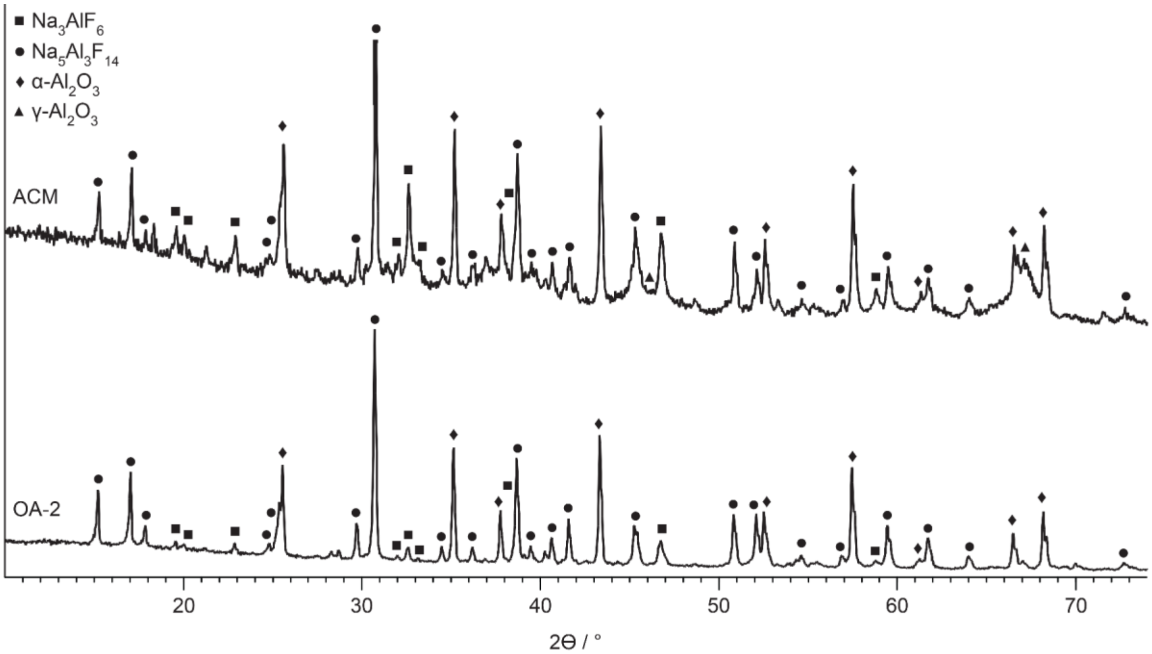

Figure 4-4 XRD patterns of ACM and anode crust (OA-2) with the main peaks identified

The main crystalline phases detected with the XRD analysis are Na_3AlF_6, $Na_5Al_3F_{14}$ and α-Al_2O_3 for the anode crust and ACM. The ACM contains an important quantity of transition aluminas, mainly in the structure of γ-Al_2O_3. However, the peak at approximately 67° in the ACM data extends on a few degrees and overlaps angles which can also be identified to other transition phases in the structure of δ-Al_2O_3 and θ-Al_2O_3. The alumina follows the phase transformation path of $\gamma \rightarrow \delta \rightarrow \theta \rightarrow \alpha$ when exposed to favorable conditions (detailed in section *Transformation of ACM into anode crust*). The baseline of the ACM is typical for this kind of material when compared to other samples analyzed in our laboratory. Furthermore, the baseline of OA-2 is less noisy and similar to all other samples investigated in this study. The anode crust OA-2 exhibits no significant amount of transition aluminas and mostly all the alumina detected comes from the α phase. This part of the crust was close enough to the bulk liquid bath and the transition to α-Al_2O_3 is favored when in contact with liquid or vapor fluorides at high temperature. The chemical composition of crystalline phases was determined with a Rietveld method optimized for bath with a high concentration of Al_2O_3. The total Al_2O_3 content, including all alumina phases, was determined with oxygen analysis. Table 4-1 details the sample locations, the total Al_2O_3 content and the CR.

Table 4-1 Description of the sample locations, alumina content and molar cryolite ratio (CR)

Sample	Height* / cm	Total Al_2O_3 / %	CR
SC-1	11.0-14.0	43.5	1.72
SC-2	6.0-8.0	34.8	1.58
SC-3	0.0-3.0	27.3	1.75
OA-Top	11.5-12.5	58.6	1.48
OA-1	8.5-12.5	47.9	1.59
OA-2	5.5-8.5	34.6	1.64
OA-3	0.0-5.5	38.5	2.16
CC-1	6.0-9.0	49.7	1.56
CC-2	3.0-6.0	37.9	1.67
CC-3	0.0-3.0	30.1	2.29
ACM	-	60.0	1.96
Side ledge	-	0.0	2.81
Top freeze	-	2.3	2.35

**Position from the bottom to the top of the sample, in cm.*

The samples were named according to their location in the electrolysis cells. The anode crust samples (SC, OA and CC) were divided into three parts and they were identified from 1 to 3, starting from the top (1) and ending with the bottom (3), close to the bath liquid level. Each sample of anode crust was extracted with a hole saw and prepared to obtain both the chemical composition and thermal properties. The first centimeter of crust from the top demonstrated a different appearance and was easy to crumble. Hence, a sample (OA-Top) was collected to observe the difference in the composition. The top of the anode crust is often friable, while the bulk anode crust is normally very hard to break. In general, the anode cover can be divided in three parts: 1) ACM formed by a mixture of powders and chunks, 2) middle region which can be easily perforated or broken and 3) the hard anode crust attached to the anode or to the side wall. The ACM was sampled during its spreading on an anode. The side ledge was extracted close to the top of the bulk liquid bath in the electrolysis cell. The top freeze was taken out from the top of the bulk bath before adding the ACM.

The ACM contained 60.0 % of Al_2O_3 while the anode crust samples had an average of 38.3 % of Al_2O_3. The Al_2O_3 concentration in the friable top part of OA crust was very close to the ACM composition. The Al_2O_3 concentration decreases when liquid bath and vapor penetrate inside the ACM or the anode crust. The bulk liquid bath usually has a CR of around 2.2, but this value depends on the electrolysis cell operating target, the cell technology and the quantity of $NaAlF_4$ evaporated during electrolysis. The bottom part of anode crusts has a higher CR and contains a lower concentration of Al_2O_3 since it is diluted by liquid bath splashes and penetration. The lower parts of the anode crusts (OA and CC) had a CR very close to the bath value. The anode crust at these locations typically follows the movement of the carbon anode during its consumption. At the end of the anode life, the bottom part of the crust attached to the anode is closer to the liquid bath and can easily get in contact with it. As a result, the CR of OA-3 and CC-3 are 2.16 and 2.29 respectively. On the other hand, the SC crust remains attached to the side wall. A cavity filled with gases and fluoride vapor separates the bottom of the crust from the top of the liquid bath. SC-3 showed a CR of 1.75, a low value compared to the OA and CC samples. The CR of top part of all anode crust samples were lower than the CR of the ACM, as $NaAlF_4$ vapor absorbed by the anode crust increased its acidity and also diluted the concentration of other species. The OA-Top demonstrated the lowest CR value at 1.48.

Quantitative analysis of crystalline phases

The main crystalline phases were quantified with the Rietveld analysis performed on XRD data. The results of the Rietveld quantification providing the mass fractions of the phases composing the anode crusts and the other samples investigated in this study are presented in Table 4-2. The crystalline phases of $Na_5Al_3F_{14}$, α-Al_2O_3 and Na_3AlF_6 mostly composed the samples of anode crusts according to their contribution to the Rietveld fit of XRD data. An average mass fraction of 43.5 % $Na_5Al_3F_{14}$, 31.5 % α-Al_2O_3 and 11.7 % Na_3AlF_6 represents the main phases of anode crust samples. A significant mass fraction of 3.0 % of $Na_2Ca_3Al_2F_{14}$ also contributed to the average anode crust composition. The ACM contained an important quantity of transition phase γ-Al_2O_3 (9.2 %) and amorphous Al_2O_3 (20.8 %). For comparison, anode crust presented amounts of 0.9 % for γ-Al_2O_3 and 5.8 % for the amorphous part (average value). The lower parts of anode crusts contained a higher amount of Na_3AlF_6, while the top parts were more acidic and even contained small quantities of $NaAlF_4$ and AlF_3 (OA and CC). SC crust showed a slightly different chemical composition when compared to OA and CC crusts, as it showed no significant gradient of $NaAlF_4$, AlF_3 or Na_3AlF_6 compared to the OA and CC crusts. In electrolysis cells, the side ledge is located below the SC crust, thus reducing the frequency of bath splashes or vapor penetration affecting the composition. The OA and CC crusts, both located close to the channels between anodes, are more susceptible to be penetrated by liquid bath and vapor.

Moreover, the anode crust of electrolysis cells is subject to a higher thermal constraint in the center than at the sides. The crust attached to the anode moves closer to the bulk liquid bath during the anode life, while the crust on the side remains fixed.

Table 4-2 Mass fraction in % of the various materials composing the top part of an electrolysis cell (anode crusts, ACM, top of side ledge and top freeze)

Sample	**Na_3AlF_6** / %	**$Na_5Al_3F_{14}$** / %	**$NaAlF_4$** / %	**AlF_3** / %	**$NaCaAlF_6$** / %	**$Na_2Ca_3Al_2F_{14}$** / %	**$Na_4Ca_4Al_7F_{33}$** / %	**CaF_2** / %	**NaF** / %	**α-Al_2O_3** / %	**β-Al_2O_3** / %	**γ-Al_2O_3** / %	**Al_4C_3** / %	**Al** / %	**Carbon** / %	**Amorphous Al_2O_3** / %
SC-1	6.5	45.5	0.3	0.9	0.5	1.0	0.0	0.9	0.0	42.3	0.3	0.2	0.3	0.2	0.4	0.7
SC-2	2.7	52.8	0.1	1.0	2.8	2.9	2.1	0.0	0.0	34.4	0.2	0.2	0.4	0.0	0.4	0.0
SC-3	9.3	57.8	0.0	0.5	1.0	3.4	0.0	0.0	0.0	27.0	0.0	0.3	0.3	0.0	0.4	0.0
OA-Top	4.4	28.0	1.3	3.4	1.3	0.9	0.0	0.4	0.2	20.1	0.0	4.3	0.5	0.7	0.3	34.2
OA-1	4.2	41.5	1.2	2.2	0.0	1.1	0.0	0.2	0.1	24.1	0.0	2.9	0.8	0.4	0.4	20.9
OA-2	6.3	54.0	0.2	2.2	0.4	1.1	0.0	0.4	0.0	34.5	0.0	0.1	0.3	0.1	0.4	0.0
OA-3	29.0	25.9	0.0	0.3	0.0	5.3	0.0	0.2	0.0	38.5	0.0	0.0	0.0	0.3	0.5	0.0
CC-1	3.6	40.2	1.3	2.4	0.0	1.1	0.0	0.1	0.0	19.5	0.0	4.2	0.7	0.5	0.4	26.0
CC-2	4.5	53.9	0.0	1.2	0.2	1.3	0.0	0.0	0.0	33.0	0.1	0.5	0.4	0.2	0.4	4.3
CC-3	38.8	19.2	0.3	0.2	0.0	10.0	0.0	0.0	0.3	30.1	0.0	0.0	0.2	0.4	0.5	0.0
ACM	14.1	20.0	0.3	0.9	0.0	3.0	0.0	0.2	0.1	27.6	2.4	9.2	0.4	0.5	0.5	20.8
Side ledge	86.4	6.2	0.1	0.0	2.1	3.3	0.1	0.0	0.5	0.0	0.0	0.0	0.1	0.5	0.7	0.0
Top freeze	58.9	28.5	0.3	0.3	3.2	5.4	0.0	0.0	0.3	1.5	0.0	0.8	0.0	0.1	0.7	0.0
Average crust*	11.7	43.5	0.4	1.2	0.5	3.0	0.2	0.2	0.0	31.5	0.1	0.9	0.4	0.2	0.4	5.8

*Average mass fraction of SC, OA and CC samples of anode crust.

Thermochemical processes inside industrial anode cover

From the center to the bottom of the crust, the thermal and the chemical conditions are sufficient to almost entirely transform the Al_2O_3 phases into the stable α phase. However, the temperature in the top part of anode crust does not reach the value needed to transform completely γ-Al_2O_3 and amorphous phases into the more crystalline and stable α phase. From our previous work, a temperature of approximately 300 °C was measured on the top of ACM covering the upper part of the anode crust OA [Allard *et al.*, 2016]. The top of the ACM on the SC crust had a lower temperature of approximately 200 °C at mid-life. The approximate temperature range inside the anode cover goes from 200 °C to approximately 950 °C. Nevertheless, the temperature gradient depends on the thermal boundary conditions, the heat generated from the cell and the thermochemical behavior of the multiphases system describing the anode crust. The transition phases of alumina in the ACM are transformed to the α phase up to the location where the local temperature is sufficient and where liquid or gaseous fluorides are available.

At a sufficient temperature, the liquid phases rise in the ACM and anode crust due to capillary forces. The solidification process inhibits the rise of these phases and is controlled by the local temperature within these materials. The heat flow generates the crystallization of the phases and creates chemical composition gradients inside the anode crust. Accordingly, the anode crust presented concentration gradients of Na_3AlF_6 and $Na_2Ca_3Al_2F_{14}$. The bulk liquid bath contains more Na_3AlF_6 and calcium species which are mainly absorbed at the bottom of the crust. The chemical processes and the mass transport inside the anode crust are thus dependent on the thermal properties and boundary conditions.

Thermal analysis of anode crusts

Bulk density, true density and porosity

The thermal conductivity of anode crust was determined from 100 °C to 600 °C for the disk-shaped samples and up to 950 °C for the powdered samples melted in the Pt/Rh container. This temperature range was selected to cover the typical industrial conditions seen by the anode crust. The thermal conductivity was determined from thermal diffusivity, specific heat capacity and bulk density. The true density of anode crust was modeled with FactSage using the NaF-AlF_3-CaF_2-Al_2O_3 system and the chemical composition quantified by Rietveld and oxygen analysis. The bulk density was quantified measuring the dimensions of each disk-shaped samples and their mass. Table 4-3 shows the bulk density of the anode crust samples measured at room temperature, the true density computed with FactSage and the calculated porosity (where porosity = 1 - $\rho_{bulk} / \rho_{true}$). A sample of side ledge taken near the top of the bath is also presented for comparison with the anode crust. Also, the ACM demonstrated a ρ_{bulk} of 1.60 g cm^{-3} considering the mass and the bulk volume, which were measured using a scale and a graduated cylinder for this particular case.

Table 4-3 Bulk and true density of anode crusts and side ledge at room temperature with the corresponding porosity

Sample	ρ_{bulk} / g cm^{-3}	ρ_{true} / g cm^{-3}	Porosity
SC-1	2.56	3.35	0.24
SC-2	2.85	3.27	0.13
SC-3	2.65	3.20	0.17
OA-1	2.27	3.40	0.33
OA-2	2.55	3.28	0.22
OA-3	2.26	3.27	0.31
CC-1	2.22	3.41	0.35
CC-2	2.57	3.31	0.22
CC-3	2.77	3.18	0.13
Side ledge	2.49	2.90	0.14

The bulk densities at the top were lower than the middle or bottom parts of the samples, even though the top parts demonstrated higher true densities. The top parts of the anode crusts were more porous when compared with their middle or bottom counterparts and also contained more Al_2O_3, as demonstrated in Table 4-1, thus increasing its true density. For comparison, the true densities of α-Al_2O_3, $Na_5Al_3F_{14}$ and Na_3AlF_6 are respectively 3.987, 2.995 and 2.900 g cm^{-3} at room temperature.

A part of the porosity may be attributed to the shrinking effect caused by the solidification of the liquid phases inside the anode crust, which occur during the cool down of the samples, when extracted from the electrolysis cell. To give examples, the following anode crusts density values were calculated with FactSage at the operating temperature. The middle part of the crust on anode (OA-2) has a true density of 2.52 g cm^{-3} at 750 °C according to thermodynamic calculations, while the bulk density at room temperature is 2.55 g cm^{-3}. The lower part (OA-3) has a true density of 2.30 g cm^{-3} at 900 °C and the measured bulk density is 2.26 g cm^{-3} at 25 °C. These examples show that samples at room temperature have higher porosity, which can be partly attributed to shrinkage during solidification. For the top part (OA-1), the true density at a temperature close to the ACM to crust transformation (700 °C) is 3.05 g cm^{-3}, while the bulk density was 2.27 g cm^{-3}. The top part of the anode crust contains less bath and more Al_2O_3, as shown in Table 4-1. Consequently, a lower amount of liquid bath reached this part of the cell, producing an anode crust with a lower density.

Specific heat capacity and enthalpy of the industrial material

The sample OA-2 was selected to describe its thermochemical behavior at operating temperatures. OA-2 contains 54.0 % of $Na_5Al_3F_{14}$, 6.3 % of Na_3AlF_6, 1.1 % of $Na_2Ca_3Al_2F_{14}$ and 0.4 % of $NaCaAlF_6$ as quantified with Rietveld. The crystal structure of the cryolite transforms at 524 °C into its high temperature form (from α-Na_3AlF_6 to β-Na_3AlF_6). The high temperature Na_3AlF_6 is a solid solution containing a significant number of compounds related to calcium fluoride and aluminum fluoride dissolved into its structure. The solid mixture OA-2 begins to melt at 696 °C with the calcium cryolite ($NaCaAlF_6$) and also with the chiolite ($Na_5Al_3F_{14}$) according to thermodynamics calculations. The $Na_5Al_3F_{14}$ melts incongruently up to 717 °C, producing liquid bath and solid Na_3AlF_6. Na_3AlF_6 melts gradually up to 845 °C.

The experimental measurements obtained with the DSC method include the heat associated to dissolution, transformation or fusion of species involved in each sample. Figure 4-5 shows a comparison between the specific heat capacity of a typical sample (OA-2) calculated with FactSage and determined from experimental measurements.

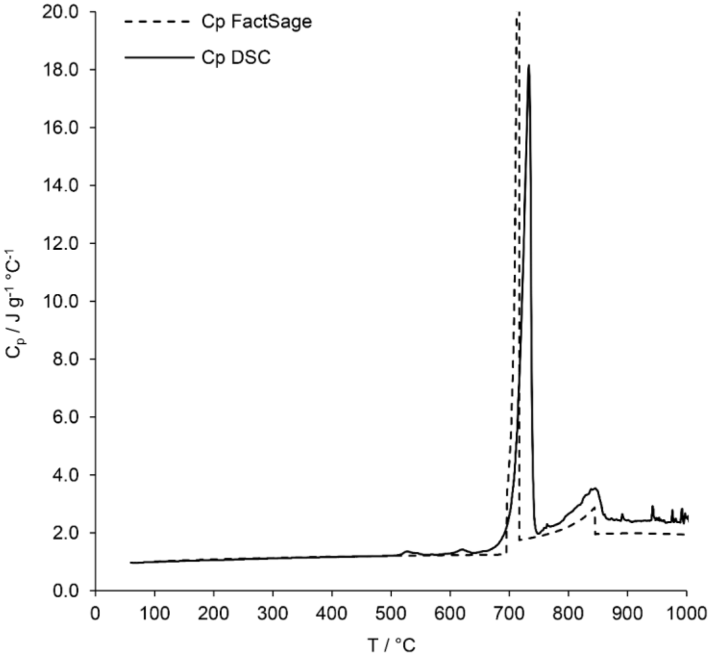

Figure 4-5 Specific heat capacity of the anode crust (OA-2) measured with DSC during a heating ramp of 10 °C min^{-1} and equilibrium results as computed with FactSage 7.1

A major endothermic peak appears around 700 °C mainly due to the enthalpy of peritectic fusion of the $Na_5Al_3F_{14}$ composing 54.0 % of the sample. The gradual melting of the Na_3AlF_6 follows and ends at approximately 845 °C according to the endothermal peak measured with DSC (Figure 4-5). After 845 °C, thermodynamic equilibrium calculations showed that the sample OA-2 was composed of liquid bath solution and solid α-Al_2O_3. The peak temperature taken from the DSC curve is slightly delayed compared to its corresponding equilibrium value. However, it should be noted that a constant heating rate introduce a thermal lag due to the heat transfer phenomena occurring inside the sample and within the parts of the apparatus [Haines, 1995]. Moreover, the DSC measurements were disturbed at high temperature due to the evaporation of bath species (from around 850 °C). The evaporation caused small endothermic peaks on the experimental c_p curve. The specific heat values related to phase transitions are detailed in Table 4-4 for the various samples of anode crust and the sample of side ledge.

Table 4-4 Enthalpy of phase transitions occurring in each sample measured with the DSC apparatus

Sample	$T_{peak\ 1}$	ΔH_1 / J g^{-1}	$T_{peak\ 2}$	ΔH_2 / J g^{-1}	$T_{peak\ 3}$	ΔH_3 / J g^{-1}
SC-1	525.4	2.8	727.4	208.5	870.1	44.0
SC-2	517.6	1.0	724.6	259.9	833.0	37.3
SC-3	518.3	6.1	730.3	236.9	872.4	20.9
OA-1	527.0	-	695.4	198.7	-	-
OA-2	512.0	2.3	732.6	264.8	-	-
OA-3	525.1	24.2	726.2	93.2	938.4	147.3
CC-1	512.1	0.7	688.6	238.0	-	-
CC-2	518.6	1.6	731.8	281.5	834.0	15.6
CC-3	520.9	50.9	725.9	68.7	943.8	241.6
Side ledge	525.9	65.1	-	-	1007.7	501.4

**Numbers in subscript indicate the order of the peaks identified on the DSC curves.*

In Table 4-4, T_{peak} indicates the temperature at the peak and ΔH designates the enthalpy related to a phase transitions from the DSC curves. According to the thermodynamic results, ΔH_1 corresponds to the enthalpy of transformation of α-Na_3AlF_6 to β-Na_3AlF_6, while ΔH_2 is the enthalpy of fusion of the $Na_5Al_3F_{14}$ and calcium cryolites ($Na_2Ca_3Al_2F_{14}$ and $NaCaAlF_6$), which usually overlap depending on the sample analyzed. ΔH_3 is the enthalpy of fusion of Na_3AlF_6. For samples OA and CC, the bottom part contained more Na_3AlF_6 and it showed a more important enthalpy of fusion (OA-3: 147.3 J g^{-1} and CC-3: 241.6 J g^{-1}). The top of OA and CC crusts did not exhibit a significant endothermic peak at temperatures close to the melting point of Na_3AlF_6, because of their low CR. Since most of the samples of anode crusts have already reached a temperature approaching 950 °C in the industrial process, the irreversible reactions occurring inside these materials were already completed. Accordingly, the DSC experiments have only demonstrated the enthalpy of phase transitions associated to the reversible processes. Nevertheless, the top of the anode crust (OA-1 and CC-1) exhibited a small fraction of unreacted γ-Al_2O_3 and a large portion of amorphous Al_2O_3 which came from the SGA added in the mixture of ACM. In Appendix A, the Figure 4-10 shows a comparison between the c_p of a typical anode crust (OA-2) and the ACM. The ACM demonstrated a transition starting at 730 °C and ending at around 900 °C, corresponding to the transformation of transition phases of Al_2O_3 to the stable α phase which is favored in the presence of fluorides.

Thermal diffusivity and thermal conductivity measurements performed on disk-shaped samples

The LFA experiments were performed at conditions close to thermal equilibrium. The experimental c_p measured with DSC was used to calculate the thermal conductivity of the industrial samples. The c_p determined from thermodynamic calculations is also presented, in order to compare with the industrial sample, which may contain impurities not quantified with Rietveld. The mean absolute error between the $c_{p,exp}$ and $c_{p,theo}$ was 5.7 % according to the results in Table 4-5. The specific heat capacity of the samples increases following a linear relationship from 100 °C to 500 °C. At temperatures between 500 °C and 600 °C, an endothermal peak produced from the α-Na_3AlF_6 to β-Na_3AlF_6 transformation was typically observed. Thus, to determine the experimental c_p under this peak, a line with the same linear slope was traced. The thermal properties of the anode crusts and the side ledge near the top are described in Table 4-5.

Table 4-5 Thermal diffusivity (α), experimental and theoretical specific heat capacity ($c_{p,exp}$ and $c_{p,theo}$) and calculated thermal conductivity (k). The thermal conductivity is calculated with the bulk density from Table 4-3

Sample	Property	100 °C	200 °C	300 °C	400 °C	450 °C	500 °C	550 °C	600 °C
SC-1	α / mm^{2} s^{-1}	0.546	0.517	0.515	0.497	0.478	0.456	0.438	0.419
	$c_{p,exp}$ / J g^{-1} °C^{-1}	0.932	0.966	0.999	1.032	1.049	1.065	1.082	1.099
	$c_{p,theo}$ / J g^{-1} °C^{-1}	0.995	1.077	1.133	1.175	1.193	1.210	1.227	1.230
	k / W m^{-1} °C^{-1}	1.30	1.28	1.32	1.31	1.28	1.24	1.21	1.18
SC-2	α / mm^{2} s^{-1}	0.505	0.477	0.468	0.445	0.420	0.385	0.374	0.358
	$c_{p,exp}$ / J g^{-1} °C^{-1}	0.899	0.924	0.949	0.973	0.986	0.998	1.010	1.023
	$c_{p,theo}$ / J g^{-1} °C^{-1}	1.005	1.082	1.133	1.171	1.187	1.201	1.214	1.227
	k / W m^{-1} °C^{-1}	1.29	1.26	1.27	1.23	1.18	1.10	1.08	1.04
SC-3	α / mm^{2} s^{-1}	0.565	0.526	0.521	0.500	0.474	0.443	0.428	0.409
	$c_{p,exp}$ / J g^{-1} °C^{-1}	0.985	1.022	1.058	1.095	1.113	1.132	1.150	1.168
	$c_{p,theo}$ / J g^{-1} °C^{-1}	1.022	1.097	1.148	1.188	1.207	1.225	1.244	1.241
	k / W m^{-1} °C^{-1}	1.47	1.42	1.46	1.45	1.40	1.33	1.30	1.27
OA-1	α / mm^{2} s^{-1}	0.409	0.390	0.380	0.370	0.357	0.335	0.307	0.282
	$c_{p,exp}$ / J g^{-1} °C^{-1}	1.070	1.127	1.183	1.240	1.268	1.296	1.324	1.353
	$c_{p,theo}$ / J g^{-1} °C^{-1}	0.984	1.070	1.126	1.167	1.184	1.198	1.211	1.224
	k / W m^{-1} °C^{-1}	0.99	1.00	1.02	1.04	1.03	0.99	0.92	0.87
OA-2	α / mm^{2} s^{-1}	0.513	0.496	0.500	0.484	0.465	0.444	0.423	0.415
	$c_{p,exp}$ / J g^{-1} °C^{-1}	1.006	1.059	1.113	1.166	1.192	1.219	1.245	1.272
	$c_{p,theo}$ / J g^{-1} °C^{-1}	1.006	1.085	1.137	1.175	1.190	1.205	1.218	1.231
	k / W m^{-1} °C^{-1}	1.32	1.34	1.42	1.44	1.41	1.38	1.34	1.35
OA-3	α / mm^{2} s^{-1}	0.618	0.552	0.526	0.492	0.457	0.413	0.404	0.386
	$c_{p,exp}$ / J g^{-1} °C^{-1}	0.989	1.049	1.110	1.170	1.200	1.230	1.260	1.290
	$c_{p,theo}$ / J g^{-1} °C^{-1}	1.033	1.091	1.150	1.208	1.237	1.267	1.296	1.256
	k / W m^{-1} °C^{-1}	1.38	1.31	1.32	1.30	1.24	1.15	1.15	1.13
CC-1	α / mm^{2} s^{-1}	0.405	0.383	0.374	0.363	0.348	0.324	0.307	0.277
	$c_{p,exp}$ / J g^{-1} °C^{-1}	0.987	1.031	1.075	1.119	1.141	1.164	1.186	1.208
	$c_{p,theo}$ / J g^{-1} °C^{-1}	0.981	1.068	1.125	1.166	1.184	1.197	1.210	1.223
	k / W m^{-1} °C^{-1}	0.89	0.88	0.89	0.90	0.88	0.84	0.81	0.74
CC-2	α / mm^{2} s^{-1}	0.528	0.503	0.502	0.490	0.470	0.442	0.426	0.402
	$c_{p,exp}$ / J g^{-1} °C^{-1}	0.997	1.042	1.086	1.130	1.153	1.175	1.197	1.219
	$c_{p,theo}$ / J g^{-1} °C^{-1}	1.002	1.082	1.135	1.174	1.191	1.206	1.222	1.237
	k / W m^{-1} °C^{-1}	1.35	1.35	1.40	1.42	1.39	1.33	1.31	1.26
CC-3	α / mm^{2} s^{-1}	0.534	0.481	0.456	0.408	0.386	0.349	0.331	0.317
	$c_{p,exp}$ / J g^{-1} °C^{-1}	1.020	1.077	1.134	1.191	1.220	1.249	1.277	1.306
	$c_{p,theo}$ / J g^{-1} °C^{-1}	1.044	1.105	1.166	1.227	1.257	1.288	1.318	1.349
	k / W m^{-1} °C^{-1}	1.51	1.43	1.43	1.35	1.30	1.21	1.17	1.15
Side ledge	α / mm^{2} s^{-1}	0.344	0.299	0.274	0.253	0.245	0.237	0.274	0.309
	$c_{p,exp}$ / J g^{-1} °C^{-1}	1.089	1.168	1.246	1.325	1.364	1.404	1.443	1.482
	$c_{p,theo}$ / J g^{-1} °C^{-1}	1.111	1.170	1.233	1.308	1.355	1.414	1.489	1.335
	k / W m^{-1} °C^{-1}	0.93	0.87	0.85	0.83	0.83	0.83	0.98	1.14

The thermal conductivity is calculated with Equation 4-1 using the bulk density measured at room temperature. The anode crust contains a high mass fraction of α-Al_2O_3 which exhibit a low linear thermal expansion of approximately 0.4 % between room temperature and 600 °C [Touloukian *et al.*, 1977]. The thermal expansion contributes to the measurements errors of the thermal diffusivity. The average standard deviation from 5 repetitions performed on each sample is 0.65 % for all the thermal diffusivity. According to the measurements, the thermal diffusivity typically decreased with temperature, while the specific heat capacity increased. Globally, the thermal conductivity of the anode crusts has decreased with temperature from 100 °C to 600 °C, in accordance with the behavior of alumina-based crust made in laboratory [Hatem *et al.*, 1989]. OA-1 and CC-1 demonstrated the lowest thermal conductivity at temperature close to operational conditions considering their location in the electrolysis cell (0.87 W m^{-1} °C^{-1} and 0.74 W m^{-1} °C^{-1} at 600 °C). These samples also exhibited the highest porosities of 0.33 (OA-1) and 0.35 (CC-1). The 9 samples of anode crusts investigated in this study do not show a linear relationship between thermal conductivity and the bulk density or porosity, as observed in other study [Hatem *et al.*, 1989]. While the thermal conductivity is affected by the porosity, several other parameters also affect its value. The thermal conductivity is influenced by the crystalline structure of the phases composing the samples, the grain boundaries in these polycrystalline materials, the orientation of the crystal structure, the impurities, the heat exchange inside the pores and the defects in the microstructure. The thermal conductivity of the sample of side ledge decreased from 100 °C to 500 °C and increased from 500 °C to 600 °C. The transformation of α-Na_3AlF_6 to β-Na_3AlF_6 might have influenced the thermal conductivity.

High temperature thermal diffusivity and thermal conductivity performed on solid-liquid samples

The anode crust OA was selected to characterize the thermal properties at a higher temperature, as this part cover most of the top of an electrolysis cell. The anode crust can reach a temperature up to 950 °C under industrial conditions. However, vapors are produced at a significant rate at this temperature, which is above the melting point of Na_3AlF_6. Therefore, a series of LFA analysis were conducted using a Pt/Rh container, starting from a temperature slightly higher than the last DSC peak, which corresponds to the liquidus of the bath phases composing the crust. Table 4-6 details the thermal properties of the anode crust in solid-liquid state at high temperature. The theoretical specific heat capacity was determined using the Equilib module of FactSage with the quantified chemical composition as input.

Table 4-6 Thermal diffusivity with Pt/Rh container, true density, theoretical specific heat capacity and calculated thermal conductivity

Sample	Property	700 °C	750 °C	800 °C	850 °C	900 °C	950 °C
OA-1	α / mm^2 s^{-1}	0.152	0.157	0.167	0.181	-	-
	ρ_{true} / g cm^{-3}	3.166	2.693	2.631	2.560	-	-
	$c_{p,theo}$ / J g^{-1} °C^{-1}	1.763	1.771	1.778	1.788	-	-
	k / W m^{-1} °C^{-1}	0.85	0.75	0.78	0.83	-	-
OA-2	α / mm^2 s^{-1}	0.188	0.197	0.208	0.225	0.217	-
	ρ_{true} / g cm^{-3}	3.052	2.522	2.458	2.366	2.303	-
	$c_{p,theo}$ / J g^{-1} °C^{-1}	1.955	1.961	1.966	1.972	1.977	-
	k / W m^{-1} °C^{-1}	1.12	0.97	1.01	1.05	0.99	-
OA-3	α / mm^2 s^{-1}	0.189	0.185	0.183	0.177	0.150	0.173
	ρ_{true} / g cm^{-3}	3.198	2.925	2.892	2.838	2.714	2.429
	$c_{p,theo}$ / J g^{-1} °C^{-1}	1.512	1.562	1.685	1.847	1.974	2.121
	k / W m^{-1} °C^{-1}	0.91	0.85	0.89	0.93	0.80	0.89

The thermal conductivity was determined using the true density in function of the temperature calculated with FactSage. The thermal diffusivity was determined with a cooling ramp, starting after the melting of the bath phases. The ρ_{bulk} is assumed to be similar to the ρ_{true} with this procedure, whereas the liquid phases fill the spaces between the lid and the container. The true density decreased with temperature, accordingly with the liquid fraction. Figure 4-6 shows the thermal conductivity ranging from 100 °C to 950 °C for the anode crust OA, combining the results at low temperatures from the previous section with the results obtained at higher temperatures.

According to previous work on heat transfer modeling with finite element analysis, the temperature inside the industrial anode crust usually ranges from 600 °C to 950 °C [Allard *et al.*, 2016]. The determination of the thermal diffusivity with the solid-liquid samples in the Pt/Rh container fills an important lack of data in this high temperature range. According to these results, the thermal conductivity of the anode crust decreased with temperature up to the process local temperature. OA-2 and OA-3 contained a large fraction of $Na_5Al_3F_{14}$ and Na_3AlF_6 and their thermal conductivity decreased quickly at 700 °C, corresponding to the beginning of the melting of the bath phases. A higher fraction of Al_2O_3 is composing OA-1 resulting in a lower drop in thermal conductivity.

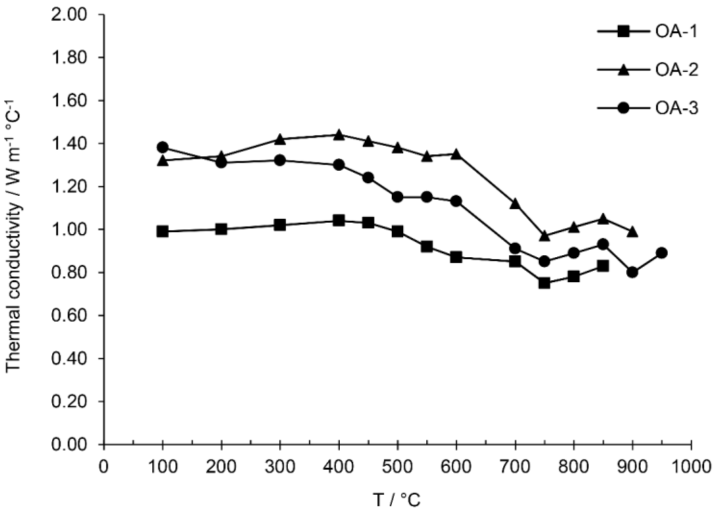

Figure 4-6 Thermal conductivity of anode crust (OA) between 100 °C and 950 °C

Microstructural properties of anode crust

A sample of anode crust was investigated with SEM analysis in order to observe its morphology. The anode crust is composed of alumina, mainly α-Al_2O_3, surrounded by bath phases. In operating electrolysis cells, either liquid or solid bath phases are found depending on the local temperature. The strength of the anode crust depends on the network of α-Al_2O_3 particles mainly surrounded by chiolite, cryolite or calcium cryolite.

The OA-2 sample was also broken into two pieces in order to be analyzed with SEM analysis (Figure 4-7). The SEM analysis revealed the α-Al_2O_3 crystals network surrounded by bath phases. The strength of the crust is maximized when the α-Al_2O_3 particles are cemented together. The embedded network of α-Al_2O_3 also exhibited a void part, which can contribute to the porosity measured at room temperature. The pores between the α-Al_2O_3 particles are visible on the SEM pictures in Figure 4-7. At temperature approaching 950 °C, only the α-Al_2O_3 hexagonal platelets remain solid. While the solid bath also contributes to build a solid crust, melting of the bath phases causes its deterioration. Once melted, the bath phases can percolate through the crust and reach the bulk liquid bath while dissolving alumina during their displacement.

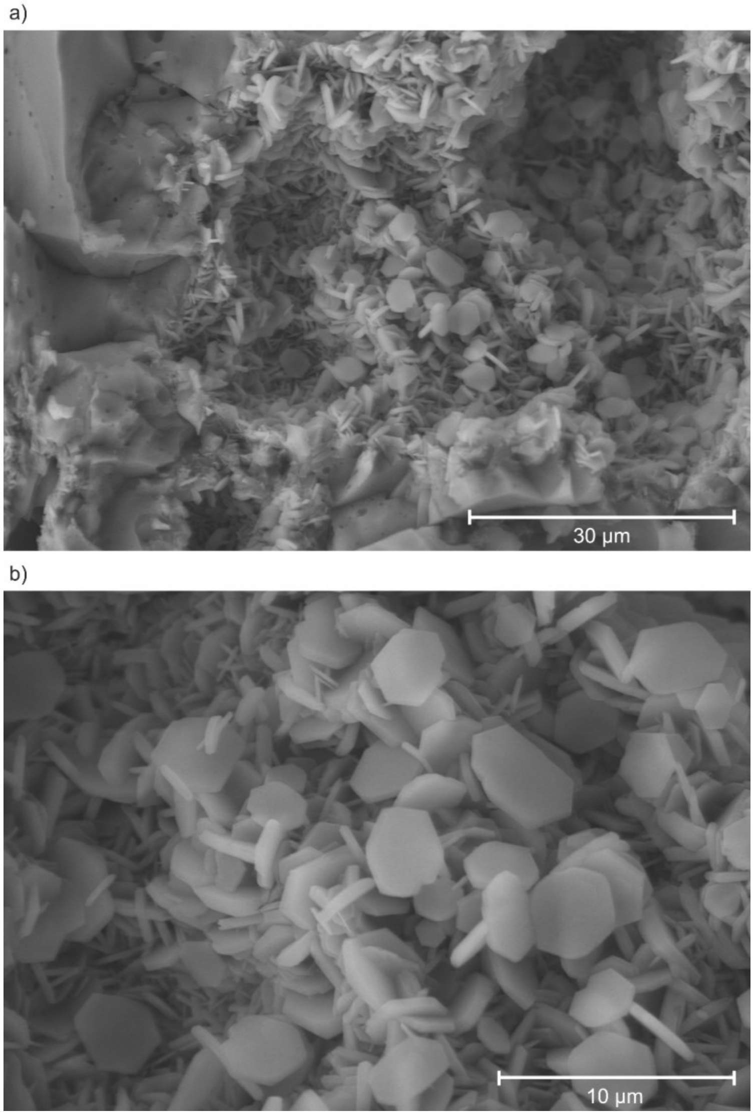

Figure 4-7 Alumina platelets (hexagonal particles) surrounded by bath phases in the sample OA-2: a) magnification of 1500 x and b) magnification of 4000 x

4.2.5 Discussion

Transformation of ACM into anode crust

The anode cover of electrolysis cells must remain in place during the few weeks of the anode life span. In order to produce a strong anode cover, a network of α-Al_2O_3 crystals must be produced. The growth of this network is favored when transition phases of alumina crystallize into the stable α-Al_2O_3. The main transition phase of Al_2O_3 in the ACM is typically the γ phase, however XRD results also show the presence of the metastable structures consisting of δ-Al_2O_3 and θ-Al_2O_3. The ACM also contains amorphous alumina phases which are not detected by XRD, but quantified with oxygen analysis. The amorphous alumina may come from the aluminum hydroxides composing the SGA added in the ACM mixture. The transformation of the alumina phases ($\gamma \rightarrow \delta \rightarrow \theta \rightarrow \alpha$) affects the sintering process and controls the microstructure of the anode crust. This α-Al_2O_3 transformation implies nucleation and grains growth mechanisms, processes favored in the presence of fluorides. The formation of crystalline α-Al_2O_3 in the anode crust results in a wide porous network with hexagonal platelets sintered together, as confirmed with SEM. The microstructure of the anode crust can be globally characterized by a matrix of solid bath enveloping the network of alumina crystals.

The transformation of ACM into anode crust begins when liquid bath and vapor penetrate into the powdered ACM. The liquid bath is generated by the melting of $Na_5Al_3F_{14}$, $NaCaAlF_6$, $Na_2Ca_3Al_2F_{14}$ in the anode cover and by the condensation of vapor ($NaAlF_4$). Moreover, the bulk liquid bath can also enter in contact with the bottom of the anode cover (direct contact or splashes) and will supply liquid bath of higher CR. The vertical penetration of liquid bath is driven by capillary forces, while the diffusion is also expected to occur since the anode cover demonstrates gradients of crystalline phases (see Table 4-2). The extent of each of these phenomena (capillary motion and diffusion) has not been demonstrated, but they are both expected to occur in porous media like the ACM and the anode crust. The liquid bath will flow between ACM particles and favor the transformation of the transition phases of alumina to the α-Al_2O_3. The unsaturated liquid bath coming from the bulk electrolyte also dissolves a fraction of the Al_2O_3 from the ACM. This upward mass transfer is inhibited when the local temperature reaches the solidus of the solution (saturated in Al_2O_3), which depends on the local chemical composition (from 696 °C with $CR = 1.8$ to 716 °C with $CR = 2.2$ according to the phase diagram of the anode crust shown in Figure 4-9). The location of the liquid bath front in the ACM is consequently controlled by heat transfer mechanisms. The mass transfer of liquid bath and vapor through the ACM also brings some of the heat needed to move the liquid front even further. It is enhanced by heat transport phenomena from the electrolysis cell: thermal conduction inside the anode crust and ACM, convective heat transfer induced by the rise of liquid and vapor and thermal radiation when a cavity is created between the liquid bath surface and the bottom of the anode crust. Accordingly, the ACM-crust moving boundary depends on both heat and mass transport. Furthermore, the penetration rates of the liquid bath and vapor were not quantified in this thermochemical study. The contribution of each of these phenomena could be studied in order to deepen the knowledge of mass transport in these materials.

The required temperature to achieve the transformation of ACM to anode crust depends on the thermochemical properties of the bath phases or the vapors diffusing in the ACM. The NaF-AlF_3-CaF_2-Al_2O_3 phase diagram describes the thermodynamic behavior of the materials involved in the anode cover. The measured ACM had an equivalent chemical composition of 60.0 % Al_2O_3, 1.7 % CaF_2 and a CR of 1.96. At room temperature, the crystalline phases α-Al_2O_3, $Na_5Al_3F_{14}$ and β-$NaCaAlF_6$ compose the ACM according to thermodynamic equilibrium calculations. The β-$NaCaAlF_{6(s)}$ transforms into α-$NaCaAlF_{6(s)}$ at a temperature of 654 °C. The first liquid bath phases in the ACM appear at 696 °C and comes from the melting of both α-$NaCaAlF_6$ and $Na_5Al_3F_{14}$. The α-$NaCaAlF_6$ melts completely at this temperature, while the $Na_5Al_3F_{14}$ gradually melts up to 711 °C and also produces $Na_3AlF_{6(s)}$ (Equation 4-3).

$$Na_5Al_3F_{14(s)} \rightarrow Na_3AlF_{6(s)} + Bath_{(l)} \qquad (4\text{-}3)$$

$Bath_{(l)}$ is the liquid bath solution with dissolved Al_2O_3. The $Na_3AlF_{6(s)}$ is a solid solution with dissolved AlF_3 and CaF_2 related species. The $Na_3AlF_{6(s)}$ solution melts gradually up to 912 °C. Consequently, the liquid fraction of the ACM increases quickly from 696 °C to 912 °C, when heated. All the bath phases are liquid at 912 °C and the liquid fraction increases slowly with the dissolution of Al_2O_3 inside the liquid bath.

The ACM begins to transform itself into crust at a temperature of 696 °C, in presence of liquid bath. The liquid fraction of the ACM goes from 2.6 % at 696 °C to 18.7 % at 711 °C according to the thermodynamic calculations carried out. The ACM to anode crust transformation may be enhanced with a higher liquid fraction at 711 °C, or when all the $Na_5Al_3F_{14}$ melts.

The ACM located above the channel between anodes is penetrated quickly by the liquid bath during the first hours of the anode life, as demonstrated in previous work [Allard *et al.*, 2015b]. Based on industrial measurements, the temperature of the bottom of the SC anode crust quickly rose to 700 °C and stabilized during 2 hours. The temperature reached 800 °C after 3 hours of anode life and 970 °C after 10 hours. The temperature at the bottom of the SC crust also stabilized to 900 °C during 1.5 hours, corresponding to the melting temperature of the Na_3AlF_6. The enthalpy of fusion of $Na_5Al_3F_{14}$ and Na_3AlF_6 might have affected the temperature rises measured with thermocouple in the ACM of an industrial electrolysis cell.

The liquid bath fraction rises quickly at around 700 °C and 900 °C for the ACM (Figure 4-8). The liquid bath fraction of the OA-2 sample increases more quickly due to a lower content of Al_2O_3 and a higher content of acidic bath phases.

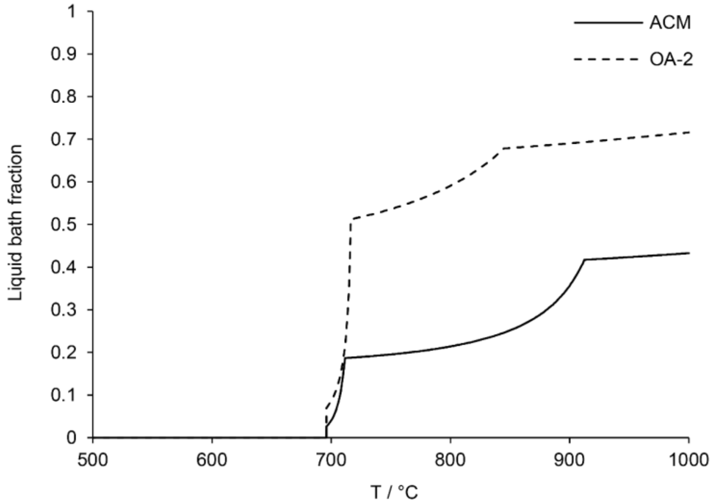

Figure 4-8 Liquid bath fraction in function of the temperature of the ACM and the OA-2 sample, obtained from thermodynamic equilibrium calculations

The ACM located above the channels is also penetrated by fluoride vapors, mainly $NaAlF_4$ released by the bulk liquid bath operating around 970 °C, which decreases the CR. The $NaAlF_4$ vapor solidifies at 685 °C according to thermodynamic calculations (Equation 4-4). The thermodynamic stability of the $NaAlF_4$ compound lies between 690 °C and 730 °C [Kirik and Zaitseva, 2010]. At room temperature, the metastable phase $NaAlF_4$ contributes to increase the $Na_5Al_3F_{14}$ and AlF_3 content detected by XRD.

$$5\ NaAlF_{4(g)} \rightarrow Na_5Al_3F_{14(s)} + 2\ AlF_{3(s)} \tag{4-4}$$

The ACM located in the SC, in the CC and between anodes transforms into anode crust when it reaches a temperature from 685 °C, due to the $NaAlF_4$ vapor which penetrates and condenses upon contact with this material. However, the ACM located OA may receive a lower amount of vapors coming from the bulk liquid bath. The ACM located OA can transform into crust from 696 °C, according to thermodynamic calculations. The experimental measurements also demonstrated a similar trend. A DSC analysis of the ACM also showed an important endothermic peak at a temperature of 724 °C corresponding to the fusion of both the chiolite and calcium cryolite species.

The ACM particles may begin to sinter in contact with the hot bath fumes and gas exiting the electrolysis cell. The sintering will result in the compaction of the powder. A weak crust may be formed with this mechanism. The gas leaving the electrolysis cells are typically composed of hydrogen fluoride (HF), carbon monoxide (CO) and carbon dioxide (CO_2) [Girault *et al.*, 2011; Yang *et al.*, 2014]. A fraction of $NaAlF_4$ vapor also composes this mixture. Nevertheless, a strong anode crust, which remains in place during the operation, is only formed with the contact of liquid bath or vapor (mainly $NaAlF_4$) and must contain a crystalline network with phases interlocked such as α-Al_2O_3 and solid bath.

Thermodynamic investigation of anode crust in industrial conditions

The anode crust is almost totally formed during the first 2 days of the anode life [Allard *et al.*, 2015b]. Once formed, the operating events modify and deteriorate its structure. The displacement of the anodes during metal siphoning generates pressure inside the anode cover, which can create cracks and holes. Moreover, the liquid bath coming from the electrolysis cell increases the content of Na_3AlF_6 and calcium species (mainly $NaCaAlF_6$ and $Na_2Ca_3Al_2F_{14}$) in the newly formed anode crust. Additionally, $NaAlF_4$ vapor increases its acidity resulting in a lower content of Na_3AlF_6 and a higher content of $Na_5Al_3F_{14}$. The highly acidic calcium cryolite phases, $Na_4Ca_4Al_7F_{33}$ and $NaCaAl_2F_9$, are then thermodynamically favored. According to thermodynamic calculations, $Na_4Ca_4Al_7F_{33}$ melts incongruently at 687 °C forming $CaAlF_{5(s)}$ and $NaCaAl_2F_{9(s)}$. The phase diagram in Figure 4-9 details the acidity effect on the behavior of the anode crust, as represented by the sample OA-2.

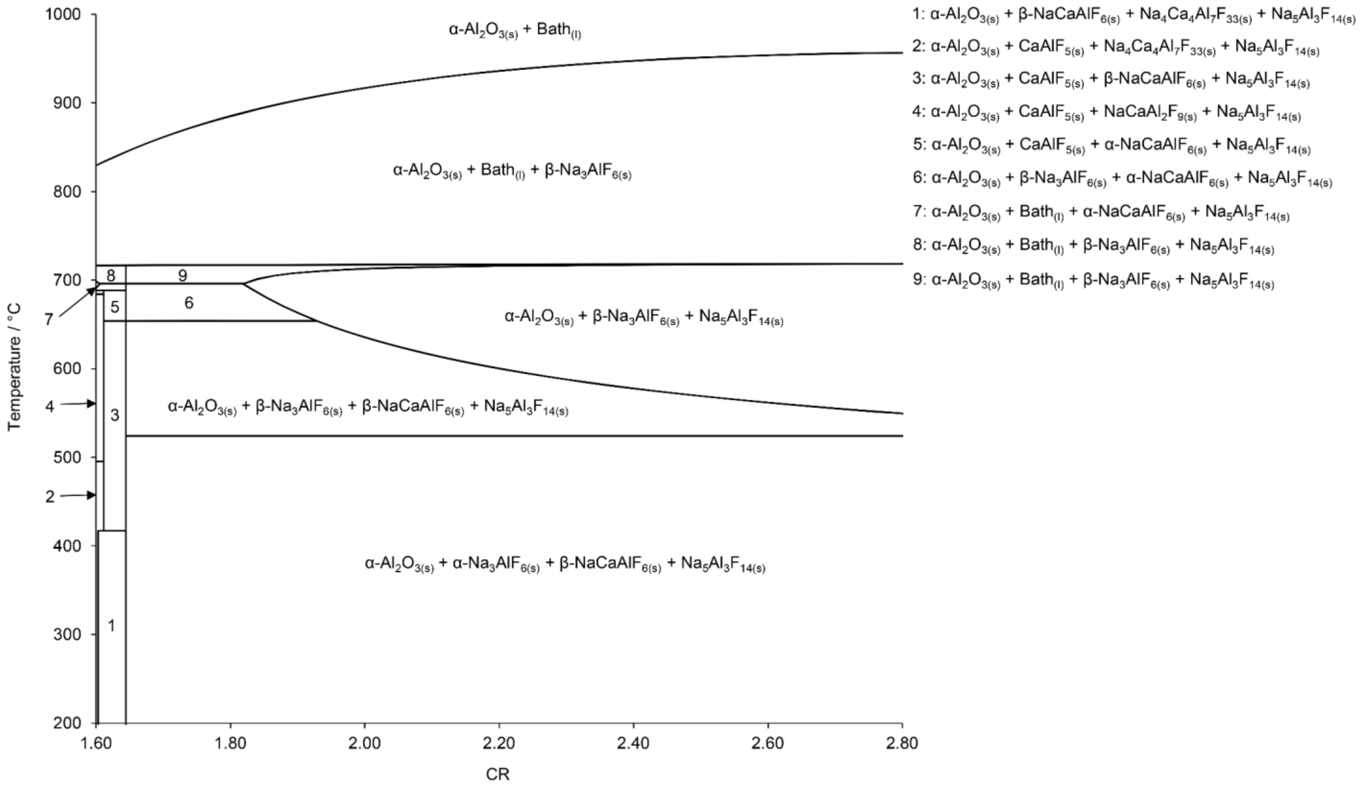

Figure 4-9 Phase diagram of the anode crust in function of the CR. The chemical composition was based on the OA-2 sample, which contained 1.1 % of CaF_2 and 34.6 % of Al_2O_3. The OA-2 sample had a CR = 1.64. The CaF_2 content was determined by means of a molar balance calculated with all the calcium cryolite mass fraction

The Na_3AlF_6 is stable at room temperature with a CR ranging from of 1.64 to 2.80. The $Na_4Ca_4Al_7F_{33}$ appears from a CR lower than 1.64. The $NaCaAlF_{6(s)}$ is completely dissolved into the $Na_3AlF_{6(s)}$ solution from 550 °C at CR = 2.80 and from 696 °C at CR = 1.82. From a lower CR than 1.82, $NaCaAlF_{6(s)}$ melts at 696 °C with a part of the $Na_5Al_3F_{14(s)}$. The $Na_5Al_3F_{14(s)}$ completely melts at 717 °C for CR = 1.60 and at 718 °C for CR = 2.80. The $Na_3AlF_{6(s)}$ solution is completely melted at 829 °C with a CR = 1.60 and at 957 °C with a CR = 2.80. The bottom of the anode crust is often in contact with liquid bath splashes caused by the movements inside the electrolysis cell. Consequently, the bottom of the anode crust has a higher CR (OA-3 = 2.16, CC-3 = 2.29 and SC-3 = 1.75).

The CR of the bulk liquid bath is typically around 2.2, but it varies depending on operating conditions. Anode crusts of similar CR, facing the bulk liquid bath, demonstrated endothermal peaks at 938.4 °C (OA-3) and 943.8 °C (CC-3) according to DSC results (Table 4-4). Comparatively, the $Na_3AlF_{6(s)}$ solution completely melts at 936 °C with a CR of 2.2 according to the phase diagram in Figure 4-9. All the bath phases composing the anode crust are in the liquid state at this temperature. With this condition, the degradation of the anode crust is favored due to the liquid bath dissolving the Al_2O_3 and percolating towards the electrolysis cell. The liquid bath may be trapped between the crystal dendrites of α-Al_2O_3 or may percolate through the crust depending on the local microporosity. Also, the bath splashes on the bottom of the anode crust do not freeze and can contribute to the dissolution of Al_2O_3 in the anode crust. Thus, the melting and deterioration of the anode crust is favored from 936 °C and the cavity can consequently grow. At lower temperatures, the Na_3AlF_6 portion of the liquid bath splashes would have frozen and formed stalactite-like structures.

Thermal properties of anode crust

The thermal properties are strongly related to the chemical composition, the thermochemical behavior and the microstructure of the anode crust. The thermal conductivity differs depending on the crystalline or amorphous phases composing the material. The thermal diffusivity was determined with all phases in solid state at a temperature ranging from 100 °C to 600 °C. The only phase transition within this range is the α-Na_3AlF_6 to β-Na_3AlF_6 transformation. The average thermal conductivity decreased from 1.28 W m^{-1} $°C^{-1}$ at 100 °C to 1.11 W m^{-1} $°C^{-1}$ at 600 °C, a lower data range compared to alumina-based crust of similar ρ_{bulk} [Hatem *et al.*, 1989]. Most of the industrial samples of anode crust had already been exposed to a minimum temperature of approximately 700 °C before their extraction from an operating electrolysis cell. Consequently, the irreversible phase transitions up to this temperature already occurred. The Al_2O_3 networks in the anode crust are surrounded by bath phases such as the cryolite, the chiolite and the calcium cryolite, each having their own thermal conductivity. It should be reminded that the thermal diffusivity measured by LFA in this study was performed on materials containing many crystalline and amorphous phases, and these samples were selected to globally represent the anode crust of industrial electrolysis cells.

The top parts of the anode crust typically showed a lower thermal conductivity when compared to the middle or bottom parts. The top of the anode crusts contained more amorphous and transition Al_2O_3 and these parts were more porous. The thermal conductivity, as measured in this study, considers the phenomena of heat transport by radiation, convection and conduction occurring in this porous medium. The anode crust OA covers the most part of the electrolysis cell. The middle of OA crust (OA-2) was selected for additional thermodynamic analyses and structural investigations with SEM. The SEM analysis demonstrated a wide porous network with hexagonal platelets of Al_2O_3 surrounded by a rather dense bath material.

All thermal conductivities determined from the disk-shaped samples were calculated with the experimental c_p in order to get closer to the real value, as in operating cells. Generally, the experimental and theoretical c_p were similar. The anode crust shows a significant porosity at room temperature which may be explained by the shrinkage of the liquid bath phases composing the anode crust. A part of the porosity also comes from the void located into the α-Al_2O_3 crystal network. Moreover, a lower amount of liquid bath reaches the top of the anode crust due to its lower operating temperature.

According to predictions from a finite element model, the vertical component of the heat flux in the anode crust dominates over the horizontal component [Allard *et al.*, 2016]. The anode cover of an electrolysis cell presents a vertical temperature gradient ranging from around 950 °C to 300 °C. The measurements of thermal diffusivity for the disk-shaped crusts were performed in the vertical direction. The anode crust may be characterized by an isotropic thermal conductivity according to the microstructural investigation by SEM, as the anode crust did not show any preferential orientation of its crystalline structure.

Above 700 °C, the chiolite and the calcium cryolites melts, and the anode crust becomes in solid-liquid state. The thermal conductivity drops quickly when liquid bath appears. The thermal conductivity of the OA crust was determined over the whole temperature range at operating conditions, from the bottom to the top. The temperature of the anode crust formed inside industrial cells varies from 600 °C to 950 °C. Once formed, the temperature may decrease below 700 °C if the heat flux decreases due to variations in the electrolysis conditions. These variations may be due to lower heat generation, ACM addition, adjacent anode change or additional heat exiting the cell by holes and cracks in the anode cover. The Pt/Rh liquid container was useful to determine the thermal diffusivity of the anode crust in solid-liquid state. This new method may be applied by the aluminum industry to other phase-changing materials present in the electrolysis cell.

Implication of the results for the aluminum industry

The thermal, chemical and microstructural characterizations of the anode crust provide the data needed for an exhaustive description of the behavior of anode crusts inside industrial electrolysis cells. The thermal conductivity of the crust differs depending on its location in the anode cover. This variation also depends on the chemical composition, the microstructure and the local temperature in the anode cover. The ACM to anode crust transformation must be achieved by forming a strong α-Al_2O_3 network with particles glued together by bath phases. Once the ACM to anode crust transformation is completed, the bath in solid state surrounding the Al_2O_3 contributes to the strength of the anode crust. On the other hand, the same bath components can have a detrimental effect on the structure when the local temperature gets over their solidus temperature. The $NaAlF_4$ vapor coming from the bulk liquid bath acidifies the anode crust and reduces the melting temperature of Na_3AlF_6. Over the anode life, the CR of the anode crust will continuously decrease resulting in a weaker anode crust. The liquefaction of the bath components in the crust, with time and favorable conditions, leads to the formation of a cavity and to potential crust collapses.

The thermal behavior of the anode crust in industrial cells may be modeled by using the thermal properties of the SC, OA and CC crust measured in this study. The heat transfer model must assume that the SC crust exhibits a different behavior than the OA and CC crusts. During the anode beam lowering movements that follow the anode consumption, the SC crust remains attached to the deck and side wall of the electrolysis cell. While the OA and CC crusts follow the vertical downward movement of the anodes, they are constantly approaching the surface of the bulk liquid bath. An increased heat dissipation provoked by process conditions pushes upward the moving boundary between ACM and anode crust, resulting in more crust formation and higher top heat losses.

4.2.6 Conclusions

The thermal diffusivity, specific heat capacity, bulk density and the calculated thermal conductivity of industrial anode crusts were determined for the first time up to the operating temperature inside the electrolysis cell. The thermal properties of each characterized parts of an industrial anode crust can be associated with their specific chemical compositions. The SEM analysis of an anode crust revealed a wide porous network of α-Al_2O_3 hexagonal platelets cemented together and consolidated by bath species. The thermal conductivity of the middle section of the anode crust decreased from 1.32 $W\ m^{-1}\ °C^{-1}$ at 100 °C to 0.99 $W\ m^{-1}\ °C^{-1}$ at 900 °C. The anode crust remains in solid state up to 696 °C. At higher temperature, the calcium cryolite and chiolite begin to melt and the anode crust becomes in a solid-liquid state. At temperatures close to 900 °C, the anode crust is only composed by α-Al_2O_3 surrounded by liquid bath phases saturated in Al_2O_3. The results of this investigation are relevant for modern electrolysis cells using a similar ACM composition and having anode crust of similar bulk density. Nevertheless, different electrolysis cell technologies and work practices may introduce variations in the top profile design and setting patterns which must be considered when interpreting the results. Although this study determined the thermal properties of anode crusts covering the whole operating temperature range, additional investigations on other cell materials may be required to improve the prediction of heat transfer models that are used to optimize electrolysis cell design. For example, the thermal properties up to the process temperature of the frozen bath surrounding a cold anode, the side ledge protecting the side wall and the sludge located on the cathode block, may all be determined using the techniques described in this work.

4.2.7 Acknowledgements

This study is financed and supported by Rio Tinto Aluminium, “Conseil de Recherches en Sciences Naturelles et en Génie du Canada” (CRSNG) and “Fonds de Recherche du Québec - Nature et Technologies” (FRQNT). The authors wish to thank the Rio Tinto smelter and researcher staff for the support provided during the realization of this work. The authors are also grateful to the employees of the “Centre de Caractérisation des Matériaux de l’Université de Sherbrooke” for their help with the various characterization devices.

4.2.8 Appendix A. Supplementary data

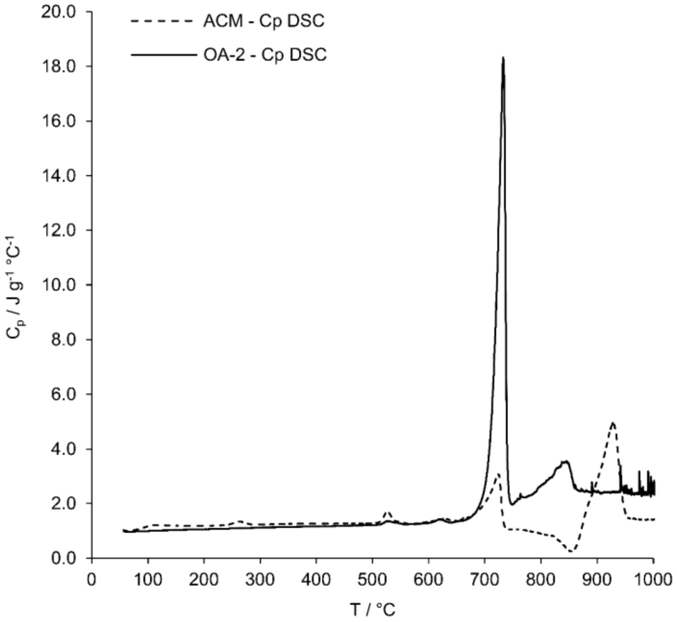

Figure 4-10 Comparison of the specific heat capacity of the anode crust (OA-2) with the ACM, both measured with DSC during a heating ramp of 10 °C min^{-1}

CHAPITRE 5 EFFET DE LA CAVITÉ SUR LA DISSIPATION THERMIQUE

5.1 Avant-propos

Auteurs et affiliation :

François Allard : étudiant au doctorat, Département de génie chimique et génie biotechnologique, Université de Sherbrooke, Québec, Canada.

Martin Désilets : professeur titulaire, Département de génie chimique et génie biotechnologique, Université de Sherbrooke, Québec, Canada.

Marc LeBreux: professionnel de recherche, Département de génie chimique et génie biotechnologique, Université de Sherbrooke, Québec, Canada.

Alexandre Blais : scientifique de recherche, Rio Tinto Aluminium, Centre de recherche et développement Arvida, Québec, Canada.

État de l'acceptation : Version finale publiée.

Revue : *Light Metals, The Minerals, Metals and Materials Society*.

Référence :

Allard, F., Désilets, M., LeBreux, M. et Blais, A. (2016). The impact of the cavity on the top heat losses in aluminum electrolysis cells. *TMS Light Metals*, p. 289-294.

Lien d'accès : https://doi.org/10.1007/978-3-319-48251-4_48

Contributions à la thèse :

Cet article présente l'intégration de la cavité, espace engendrée par la fonte de la croûte, dans un modèle thermique-électrique qui est résolu par la méthode des éléments finis. Les avancées préliminaires concernant l'amélioration de la cartographie du recouvrement anodique (*ACM* et croûte d'anode) ainsi que l'intégration d'une cavité dimensionnée en s'appuyant sur des mesures industrielles sont présentées dans ces travaux. Les points suivants présentent les principales contributions :

- La prédiction des flux thermiques, des températures et potentiels électriques par un modèle thermique-électrique résolu en régime permanent, en incluant un module de calculs du transfert thermique par rayonnement. Le transfert thermique évoluant dans la cellule d'électrolyse a été prédit et aussi validé par des mesures industrielles.

- Les flux thermiques et températures simulés ont été validés par des sondes de flux thermique et des thermocouples placés principalement sur le dessus du recouvrement anodique d'anodes à leurs mi-vies.
- L'augmentation de la taille de la cavité génère une augmentation de dissipation thermique par le dessus de la cellule d'électrolyse, tel que démontré par le modèle thermique-électrique.
- La considération de la cavité et l'intégration du module de transfert thermique par rayonnement diminuent l'écart entre les prédictions et les mesures. L'erreur de prédiction est passée de 21.8 % à 7.3 % selon les prédictions et les mesures prises sur l'*ACM* situé au-dessus du canal latéral.

Conclusion supplémentaire à ce chapitre :

Dans la cavité, le module de transfert thermique par rayonnement ne tient pas compte de l'effet des gaz polaires (CO_2 et gaz fluorés) qui absorbent une partie du rayonnement thermique. Néanmoins, ce milieu participatif présente un impact négligeable sur le transfert thermique entre la surface du bain électrolytique (965 °C et $\varepsilon = 0.97$) et le dessous de la croûte d'anode (935 °C et $\varepsilon = 1.0$) étant donnée la faible distance entre ces deux surfaces qui limite l'absorption volumique.

Titre français :

Impact de la cavité sur les pertes thermiques par le dessus des cellules d'électrolyse d'aluminium

Résumé :

Les producteurs d'aluminium primaire augmentent continuellement le courant électrique pour augmenter la production. Par conséquent, les pertes de chaleur par le dessus des cellules d'électrolyse d'aluminium sont amplifiées, ce qui conduit à des contraintes thermiques plus élevées sur le recouvrement anodique. Un modèle d'éléments finis est développé afin de prédire les flux thermiques et les températures dans les parties supérieures de la cellule d'électrolyse. Le modèle est validé par des mesures prises sur des cellules industrielles. Il considère la cavité, située au-dessus du bain liquide, qui est formée pendant la fusion et la chute de la croûte anodique durant la vie de l'anode. Le flux thermique qui s'échappe du recouvrement anodique augmente avec la hauteur de la cavité selon les prédictions. La considération de la cavité à l'intérieur du modèle favorise une bonne correspondance entre les prédictions du modèle et les mesures industrielles.

5.2 The impact of the cavity on the top heat losses in aluminum electrolysis cells

Keywords: Aluminum, Electrolysis, Top heat losses, Anode cover material, Crust, Cavity, Heat transfer, Thermal radiation

5.2.1 Abstract

The primary aluminum producers are continuously raising the line amperage to increase the productivity. Hence, the top heat losses of aluminum electrolysis cells are amplified which leads to higher thermal constraints on the anode cover. A finite element model is developed in order to predict the heat fluxes and temperatures in the top parts of the cell. The model is validated against measurements from the top surfaces of real industrial cells. It considers the cavity above the liquid bath, which is formed during the melting and falling of anode crust during the life of the anode. The heat flux escaping the anode cover increases with the height of the cavity according to the results. Considering the cavity inside the model is mandatory in order to obtain a good correspondence between the measurements and the model predictions.

5.2.2 Introduction

The efficiency of the Hall-Héroult process is continuously improving in order to achieve better economic and environmental performances. During the last decades, the primary aluminum producers increased the productivity by raising the current delivered to the electrolysis cells. Accordingly, the thermal constraints on the anode cover and anode assembly has increased, which creates additional risk of operating problems. The deterioration of the anode cover induces higher heat losses, fluoride fumes emissions, and air burn of carbon anode. Furthermore, the melting and falling of anode crust due to higher thermal constraints cause the formation of sludge or deposit on the surface of the cathode block. The process of melting and falling of anode crust into the bath also creates a cavity under the remaining anode crust. Figure 5-1 depicts the location of the cavity within the top parts of an industrial electrolysis cell.

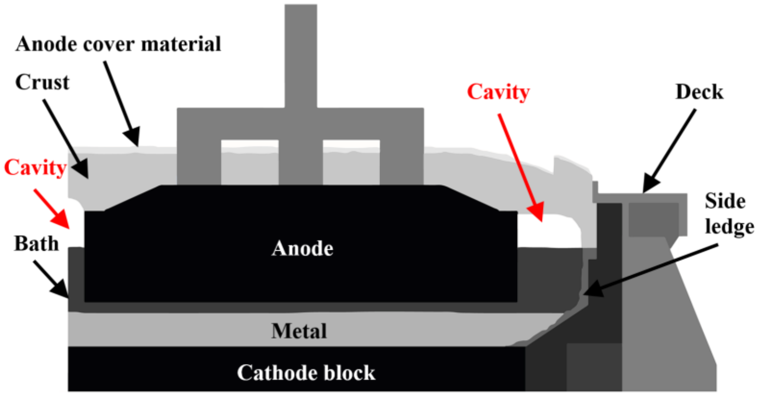

Figure 5-1 Schematic of an aluminum electrolysis cell

During the operation of the electrolysis cell, the carbon anode is consumed and it must be replaced after a few weeks. At each anode change, the anode cover material (ACM) is deposited over the newly set anode and on the layer of frozen bath surrounding the anode. The typical ACM is mainly composed of recycled crushed bath and alumina. A mix of fine to coarse particles characterizes the granulometry of this material. The thermal conductivity of various mixtures of ACM has been measured experimentally [Shen, 2006; Wijayaratne *et al*., 2011]. The thermal conductivity of ACM increases linearly with temperature between 160 °C and 600 °C [Shen, 2006]. The granulometry or particle size distribution of the ACM has a major impact on its thermal conductivity [Wijayaratne *et al*., 2011]. The effect of chemical composition on thermal conductivity is less important than granulometry, according to Wijayaratne et al [Wijayaratne *et al*., 2011]. A larger amount of coarse bath in the mixture of ACM increases the thermal conductivity while higher proportions of fine particles decrease the thermal conductivity.

Once a new anode is set and the ACM is deposited, the layer of frozen bath begins to melt due to the thermal insulation made by the ACM. Afterward, liquid bath begins to penetrate into the particles of ACM by capillary force. The rise of the liquid bath in the ACM generates the formation of a crust consisting of embedded alumina particles into solidified bath [Gerlach and Winkhaus, 1985]. The consolidation of ACM into solid crust is largely controlled by heat transfer [Rye, 1992; Eggen *et al*., 1992]. The heat losses from the bulk liquid bath increase the temperature of the ACM, causing the melting of the bath surrounding the alumina particles. The boundary of the liquid front in the ACM progresses with the temperature profile and depends on melting temperature of the mixture, set at 685 °C by Zhang *et al.* to model the evolution of the anode crust [Zhang *et al*., 2015]. The acidic and calcium phases in the ACM (mainly

$Na_5Al_3F_{14}$, $Na_2Ca_3Al_2F_{14}$, and $NaCaAlF_6$) melt at a lower temperature than the cryolite [Zaitseva *et al.*, 2009; Zhang *et al.*, 2013; Allard *et al.*, 2015b]. In the Na_3AlF_6-AlF_3-Al_2O_3 system, the eutectic crystallization of a highly acidic liquid bath is approximately 685 °C [Foster, 1975; Allard *et al.*, 2015b].

The hardness and thermal conductivity of crust have been investigated by a few researchers [Hatem *et al.*, 1989; Llavona *et al.*, 1990]. The hot wire and hot strip methods were used to determine the thermal conductivity, which increases with the apparent density of the crust by an almost linear relationship [Hatem *et al.*, 1989]. The thermal conductivity and emissivity of the crust were determined by Rye *et al.* with an experimental setup [Rye *et al.*, 1995]. The thermal conductivity of the crust increases strongly with the content of crushed bath in this material. The melting and falling of anode crust create a gas-filled gap between the bulk bath and the crust. The emissivity of the crust in this cavity was estimated to 0.3 [Rye *et al.*, 1995]. The risk of crust failure may be enhanced by the dissolution and melting of the crust in contact with the liquid bath, by mechanical disturbances due to anode movements and by partial collapse of a weak crust [Liu *et al.*, 1992].

The heat transfer in the top parts of the electrolysis cell was recently investigated by CFD modeling [Zhao *et al.*, 2013]. A correlation for the convection coefficients was developed in function of the volumetric flow rate of gas collected from the pot. The heat dissipation and temperature distribution have been measured on the ACM and along the anode rod in industrial cells [Shen *et al.*, 2004, 2008]. The thickness of the ACM layer has a strong impact on the heat flux released by the anode cover [Shen *et al.*, 2008].

The effect of the cavity on the heat dissipation of industrial electrolysis cell was not covered in any of the previous studies. Moreover, most previous modeling studies are limited to 1D or 2D analysis and are rarely based on measurements from industrial cells. In this study, a 3D thermoelectric model of an industrial electrolysis cell is presented. The thickness of the ACM, crust and cavity were measured and used to predict the heat losses. Furthermore, the results are compared with measurements of the heat fluxes and temperatures at specific locations on the top surfaces of the cells.

5.2.3 Numerical model

The impact of the cavity on the heat losses is quantified by modeling four geometries, with and without cavity, of P155 prebake cells. The cavity is located in the side channel (SC), between the anodes (BA) and in the center channel (CC). The general geometry is a slice of an industrial cell containing two cathode blocks and an anode and a half. Various slices of mid-life anodes were measured and predicted in order to ensure the validity of the prediction of the numerical model. Each of the geometries was based on measurements taken at Rio Tinto's Grande-Baie plant located in Québec. The selected mid-life anodes were far enough from the feeder holes or the corners of the cell to neglect their effect. Figure 5-2 shows an example of the geometry used to predict the heat losses.

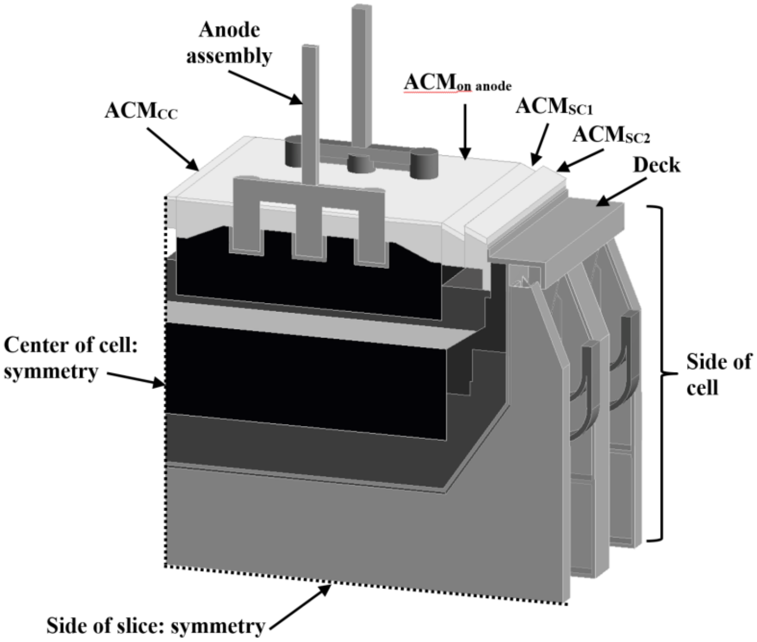

Figure 5-2 Example of geometry used for the simulation

The ACM is divided into four zones ("CC", "on anode", "SC1" and "SC2"). The ACM and crust thicknesses and the boundary conditions above the anode cover vary based on measurements. In general, the ACM is roughly dispersed on the top of the anode in operating cells. Moreover, the consolidation of the ACM is non-uniform and depends on the local mass transfer and thermal constraint.

Assumptions

In order to simulate the top heat losses of electrolysis cells, the following assumptions were taken into account: (1) the heat transfer from a mid-life anode is close to steady-state; (2) the mass transfer effects on heat losses are neglected; (3) the ACM granulometry and thermal conductivity are similar to the data presented in [Shen, 2006]; (4) the properties of all materials are known; (5) the effect of the flow circulation of the liquid bath is accounted by an “augmented effective thermal conductivity”; (6) the heat transfer in the cavity is radiation dominated and (7) the surfaces in the cavity are gray and diffuse.

Governing equations

The top heat losses and heat generation were predicted based on a coupled thermal-electrical finite element analysis (FEA). The equations were solved using ANSYS Mechanical software (release 16.0). The domain for the FEA simulation is a slice of an electrolysis cell (Figure 5-2). Equation 5-1 describes the governing equation for the steady state heat conduction with the volumetric heat generation rate [ANSYS, 2013]:

$$\frac{\partial}{\partial x}\left(k_x \frac{\partial T}{\partial x}\right) + \frac{\partial}{\partial y}\left(k_y \frac{\partial T}{\partial y}\right) + \frac{\partial}{\partial z}\left(k_z \frac{\partial T}{\partial z}\right) = \dot{q} \tag{5-1}$$

The volumetric heat source term $\dot{q}$ is calculated by the Joule effect:

$$\dot{q} = \sigma E^2 \tag{5-2}$$

The electrical field can be derived from:

$$\boldsymbol{E} = -\nabla V \tag{5-3}$$

The potential distribution is computed from the governing equation for steady-state electric conduction [ANSYS, 2013]:

$$-\nabla \cdot ([\sigma]\nabla V) = 0 \tag{5-4}$$

The general equations of heat and electric conduction were described. Further information on the thermoelectric coupling is available in the ANSYS Mechanical documentation [ANSYS, 2013]. The radiosity method was used in order to calculate the heat transfer in the cavity. The radiosity solution was obtained using the Gauss-Seidel iterative solver. A set of linear algebraic equations is used to obtain the outgoing radiative fluxes (radiosity) for each surface [ANSYS, 2013].

$$[A]\{q^{\prime\prime,0}\} = \{D\} \tag{5-5}$$

Where:

$$A_{ij} = \delta_{ij} - (1 - \varepsilon_i)F_{ij}$$

$$q_j^{\prime\prime,0} = \text{radiosity flux for surface } j$$

$$D_i = \varepsilon_i \sigma T_i^4$$

At the surface facing the cavity, the boundary conditions for the heat conduction are provided by the net surface radiosity fluxes. The radiation view factors, $\mathrm{F_{ij}}$, are required to solve the radiosity module. The overall view factors for each surface are calculated using the hemicube method [ANSYS, 2013].

Boundary conditions and properties

The description of the boundary conditions and properties will be detailed for the top parts of the cell and given globally for the side and bottom. Insulating conditions have been applied to the symmetric faces of the numerical model, the center of the cell and the two sides of the slice (Figure 5-2). A potential of 0 V has been applied to the top of each cathode flex. The current delivered to the electrolysis cell was divided by the number of anodes and the corresponding value was applied to the top of each anode rod. An "effective convection coefficient" considering both the convection and radiation has been applied to the side and bottom of the electrolysis cell. Table 5-1 depicts the boundary conditions of the top parts of the numerical model.

Table 5-1 Boundary conditions of the top parts

Boundary	Condition
Anode assembly	Convection (h=70 W/m^2·K, T_∞= measured)
$\mathrm{ACM_{on\ anode}}$	Convection (h= calculated, T_∞= measured)
$\mathrm{ACM_{SC}}$	Convection (h= calculated, T_∞= measured)
Deck	Convection (h= calculated, T_∞= measured)
Top of anode rod	Temperature (T = measured)

The measured and calculated values will be provided in the *results and discussion* section. In the numerical model, an "effective convection coefficient" was applied to the top of the ACM on anode and on the side channel. The convection coefficients were determined from the heat flux sensors placed on the mid-life anodes and the measurements of the gas temperature (T_∞). The convection coefficient applied on the anode assembly (70 W/m^2·K) came from the measurements made by Shen *et al.* [Shen *et al.*, 2004]. The thermophysical properties of the materials are described in Table 5-2.

Table 5-2 Thermophysical properties [Seger, 1975; Hatem *et al.*, 1989; Log and Oye, 1990; Llavona *et al.*, 1990; Windisch *et al.*, 1992; Rye *et al.*, 1995; Shen, 2006]

Boundary	**Value**
ε_{ACM}	0.3
$\varepsilon_{liquid\ bath}$	0.97
$\varepsilon_{carbon\ anode}$	0.9
k_{ACM} (W/m·K)	$0.155 + 0.616 \times 10^{-3}\ T$ (160 – 600 °C)
k_{crust} (W/m·K)	1.6
$k_{anode\ rod}$ (W/m·K)	Confidential
$k_{stubs\text{-}yoke}$ (W/m·K)	Confidential
k_{anode} (W/m·K)	$-0.000003 \times T^2 + 0.0056 \times T + 3.4$
$k_{bath\ solid}$ (W/m·K)	1.2
$k_{bath\ liquid}$ (W/m·K)	3000

The ACM of the mid-life anodes investigated in this study had a similar chemical composition than the 60 % Al_2O_3 and coarse crushed bath (CCB) mixture described in [Shen, 2006]. The granulometry of the ACM in this study was also similar to the CCB. The thermal conductivity of the ACM in the model was adjusted to consider the transformation of ACM into crust. At temperatures of 700 °C and above, k_{ACM} was increased to 1.6 W/m·K. The thermal conductivity of the liquid bath was augmented to reflect the movements generated from the magnetohydrodynamics effect and induced by CO_2 bubbles.

5.2.4 Measurement method

The thicknesses of ACM and crust were measured on the anode and on the side channel, at a location close to the measurement of the heat flux (using a Hukseflux HF01 sensor). The estimated accuracy of these sensors is ± 10 % according to the product manual. Figure 5-3 depicts the locations of the measurements.

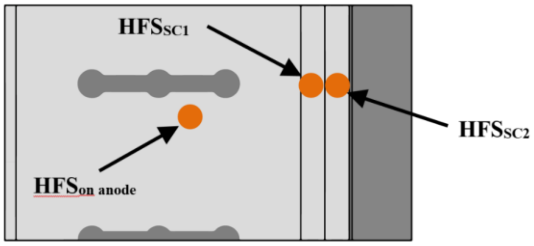

Figure 5-3 Locations of the heat flux sensors (HFS) on the ACM

In each electrolysis cell, the heat flux escaping the anode cover was measured on the anode, close to the stubs. On mid-life anode, the top surface of the anode cover located at the SC is non-uniform. One part of the crust remains fixed to the anode assembly (SC1) while the other part sticks to the sidewall (SC2). The lowering of the anode assembly during the life of the anode causes the formation of a "step", the higher part of the crust which remains attached to the sidewall. The side ledge might create an obstruction to the movement of the crust during the lowering of the anode panel. In two industrial cells, the heat fluxes were measured on the "step" (SC2). In the two others, the heat fluxes were measured close to the anode (SC1). The ACM and crust located on the center channel were hardly accessible. Thus, they were not measured in this study. All measurements were done during the summer and the ventilation of each pot was kept at a "normal" rate. The draft rate exiting the pots was 1.3 Nm^3/s (normal cubic meters per second). The temperatures of the potroom and the gas exiting the pot were approximately 45 °C and 140 °C respectively.

5.2.5 Results and Discussion

The numerical model was run 8 times to simulate 4 different slices with mid-life anodes (4 with and 4 without cavity). These slices are representing 4 sets of measurements conducted on mid-life anodes. Measurements of the height of the cavity were performed on various cells to find a typical size to consider in the model. The anode cover was broken in order to roughly measure the height of the cavity with a ruler. The height was determined from the top of the liquid bath to the bottom of the anode crust. The measurements of the cavity in the side channel were done on 8 different mid-life anodes. The heights of the cavity located between anodes were measured on 6 different mid-life anodes. Figure 5-4 shows the average heights of the cavity in the side channel and between anodes along with the standard deviation.

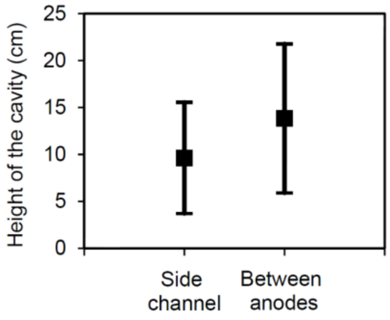

Figure 5-4 Height of the cavity of mid-life anodes

The average heights of the side channel and between anodes cavities were 10 cm and 14 cm respectively. In the numerical model, the heights of the cavities (in the SC and BA) were set to 10 cm and 15 cm respectively. The cavities are approximated by rectangular prisms in the numerical model. The measurement of the cavity in the center channel is difficult during the operation of the industrial cell. Thus, the height of the cavity in the center channel was also set to 15 cm (equal to the cavity BA).

Predictions and measurements of top heat losses

The top heat losses of 4 slices of mid-life anodes are predicted using the numerical model. The results are compared with the measured values of temperatures and heat fluxes. The following measured values were imposed in each simulated slice: heights of ACM and crust on anode, height of ACM on the side channel, temperatures of air and convection coefficients above the anode and above the side channel, and temperature on the anode rod. The “effective convection coefficients” were calculated from the heat flux measurements (q'') with Equation 5-6, knowing the surface (T_s) and gas (T_∞) temperatures.

$$q'' = h\,(T_s - T_\infty) \tag{5-6}$$

The calculated convection coefficients based on measurements were imposed in each slice to consider the real operating conditions and to reflect the local effects. The $T_{air,on\ anode}$ came from the average of two measurements taken on each side of the anode rod, one side close to the center and the other side close to the hood. A negative pressure is imposed inside the pot due to the ventilation system. Thus, the air of the potroom enters by the gaps between the hoods and is heated due to the heat dissipation from the top parts of the cell. The $T_{air,sc}$ was measured close to the gap between the hoods to consider the cooling effect of the air above the ACM on the side channel. The detailed boundary conditions are presented in Table 5-3.

Table 5-3 Boundary conditions for the 4 slices of electrolysis cells based on measurements

Slice	Heights					Boundary conditions			
	$ACM_{on\ anode}$ (cm)	$Crust_{on\ anode}$ (cm)	$*Cavity_{BA}$ (cm)	ACM_{SC} (cm)	$*Cavity_{SC}$ (cm)	$T_{air,on\ anode}$ (°C)	$h_{on\ anode}$ (W/m^2·K)	$T_{air,SC}$ (°C)	h_{SC} (W/m^2·K)
A	2.0	10.0	15	0.5	10	120	19	74	27
B	1.5	10.0		3.0		103	25	70	32
C	2.5	8.0		2.0		134	29	92	42
D	3.5	5.0		3.0		162	25	83	25

**The height of the cavity was imposed based on the average height, as measured in various cells*

The results of the heat flux measurements and the predictions from the model (without and with cavities) are presented in Table 5-4. The locations where the sensors were positioned are described in Figure 5-3.

Table 5-4 Results of the measurements and the predictions

Slice	Measurements			Without cavity			With cavities		
	$q''_{on\ anode}$ (W/m^2)	q''_{SC1} (W/m^2)	q''_{SC2} (W/m^2)	$q''_{on\ anode}$ (W/m^2)	q''_{SC1} (W/m^2)	q''_{SC2} (W/m^2)	$q''_{on\ anode}$ (W/m^2)	q''_{SC1} (W/m^2)	q''_{SC2} (W/m^2)
A	3478	5649	-	3490	4240	-	3685	5006	-
B	3874	3887	-	4023	3221	-	4262	3835	-
C	3566	-	1920	3790	-	1200	4008	-	1557
D	3450	-	1742	3612	-	1017	3842	-	1345

According to previous study, the heat dissipation from the anode cover increases quickly during the first hours and stabilizes after 24 to 48 h [LeBreux *et al.*, 2014]. Thus, the slices with mid-life anodes investigated in this study were simulated at steady-state. However, even if the crust thermal behavior can be considered as stabilized, the heat dissipation will continue to vary slowly, because of the carbon anode consumption and anode panel movements (anode changes, metal tapping, etc.). For all simulated slices, the transformation of ACM into crust and the cavity formation were considered to be completed and stabilized. In the simulations without cavity, the anode crust was in contact with the liquid bath. In the case of slices with cavities, “empty” spaces were added instead of the anode crust. Accordingly, the heat fluxes were computed by the radiosity module. The slices with cavities offer a better representation of the electrolysis cell as they provide more realistic anode crust geometries.

The heat fluxes from the ACM on anode were well predicted in both cases of simulation (with and without cavity). However, the prediction of the heat fluxes from the ACM_{SC} presents a large deviation in the simulations without cavity compared to the measurements. Table 5-5 describes the prediction errors of models without and with cavities.

Table 5-5 Average prediction errors of the simulations compared with the measurements

Average prediction errors	$q''_{on\ anode}$ (%)	q''_{SC1} (%)	q''_{SC2} (%)
Without cavity	3.8	-21.8	-39.5
With cavities	9.9	-7.3	-20.8

The average prediction errors of the models with and without cavity were calculated with the average results of heat fluxes in each slice. As expected, the heat fluxes simulated in the models with cavities were higher than without cavity. The predictions of the heat fluxes escaping the ACM on the side channel close to the anode assembly (SC1) were closer to the measurement in the simulations with cavities (-21.8 % vs -7.3 %). The average prediction errors of the q''_{SC2} (closer to the side wall) were larger than the others.

The “step” made of crust located on the side channel is characterized by an irregular shape. Thus, it is difficult to model precisely the “step” in the simulations. Figure 5-5 depicts the “step” observed in the industrial electrolysis cells.

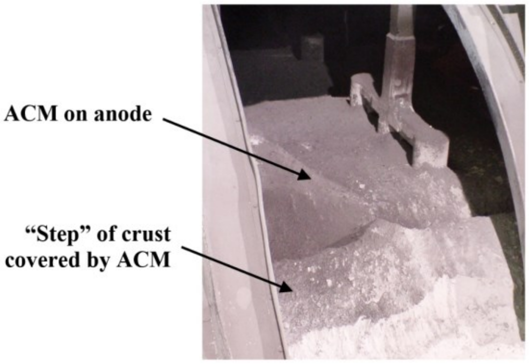

Figure 5-5 Photo of the “step” of crust in the slice D

Only a general shape of crust covered by ACM was used in the simulations to represent the “step”. Except for q''_{SC2}, the predictions of the simulations with cavities were very close to the experimental error of the heat flux sensors (± 10 %). Accordingly, the combination of the chosen thermophysical properties with the measurements of the dimensions of each material enabled a prediction close to the measured values. A part of the error can also be attributed to the general rectangular shape of constant height used to represent the cavity.

General model and boundary conditions

A general model is built to provide the typical heat losses distribution for the studied mid-life anodes, with the average height for each material and boundary conditions previously described. Table 5-6 and Table 5-7 describe the conditions of the mid-life anodes in this general model.

Table 5-6 Average height of each material and cavity

$\text{ACM}_{\text{on anode}}$ (cm)	$\text{Crust}_{\text{on anode}}$ (cm)	$\text{Cavity}_{\text{BA}}$ (cm)	ACM_{SC} (cm)	$\text{Cavity}_{\text{SC}}$ (cm)
2	8	15	2	10

Table 5-7 Average boundary conditions above the ACM

$T_{air,on\ anode}$ (°C)	$h_{on\ anode}$ (W/m^2·K)	$T_{air,SC}$ (°C)	h_{SC} (W/m^2·K)
130	25	80	32

Figure 5-6 gives the temperature distribution in the top parts of the electrolysis cell, based on the simulation of the averaged model with cavities.

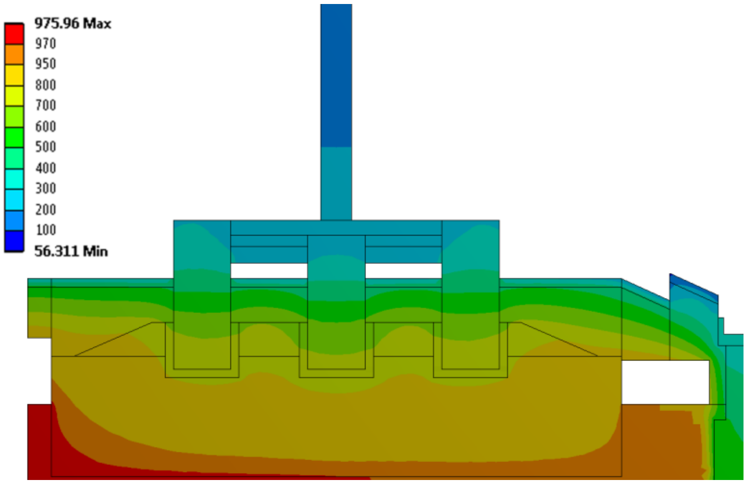

Figure 5-6 Temperature distribution in a mid-life anode

The temperatures predicted with this model on the surface of the ACM are very close to the measured temperatures. The average measured temperature on the surface of the ACM on anode was 282 °C while the predicted was 298 °C. The average measured temperatures on the surface of ACM_{SC1} and ACM_{SC2} were 240 °C and 145 °C respectively, and the predicted was 219 °C and 128 °C respectively. The error on the prediction of temperature follows the same trend as the heat flux (Table 5-5). A part of the error can be attributed to the non-uniform leveling of the ACM and crust in reality. The heat losses distribution without cavity and with cavities is presented in Table 5-8.

Table 5-8 Heat loss distribution

Parts	Without cavity (%)	With cavities (%)
Anode rod	3.9	3.8
Stubs and yoke	16.0	15.9
Anode cover (on anode)	17.4	18.2
Anode cover (SC)	3.2	3.9
Top of deck	6.4	6.9
Side shell and cradles	36.1	34.7
Bar and flex	10.4	10.2
Bottom	6.6	6.4

The general model with cavities predicted higher top heat losses (48.7 % vs 46.9 %). The presence of cavities increased principally the heat losses from the anode cover and from the top of the deck. The heat losses from the side shell and the cradles decreased in the model with cavities. Hence, the top heat losses increased by roughly 2 % when cavities were included in the model, mainly reducing the side heat losses.

The impact of the height of the cavity on the heat flux was evaluated with the general model (conditions in Table 5-6 and Table 5-7). The heights of the cavities in the center channel and between anodes were fixed at 15 cm. The height of the cavity in the SC was varied from 0 cm to 15 cm. Figure 5-7 demonstrates the impact of the cavity in the side channel on the heat flux escaping the ACM.

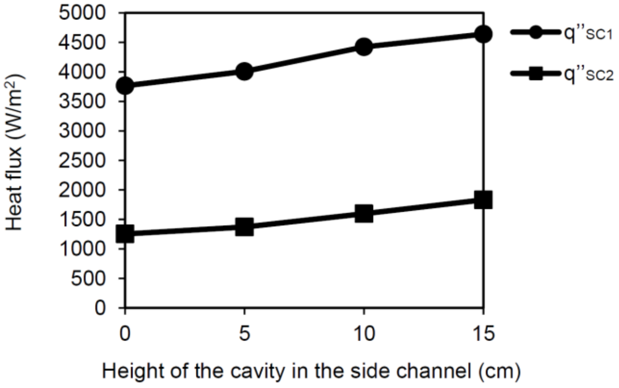

Figure 5-7 Impact of the cavity in the SC on the heat flux

The q''_{SC1} in the model without cavity in the SC was 3765 W/m^2 and was 4639 W/m^2 with 15 cm of cavity (increase of 23 %). With the same condition, the heat fluxes exiting the ACM$_{SC2}$ was 1255 W/m^2 and 1833 W/m^2 respectively (increase of 46 %). The thickness of the crust is reduced by the process of melting and falling. Accordingly, the thermal resistance of the anode crust decreases with increasing height of cavity, thus explaining the growth of the q''_{SC1} and q''_{SC2} values in Figure 5-7. In steady-state, the thermal balance of an electrolysis cell with a larger cavity will be characterized by larger top heat losses and lower heat dissipation on the side.

5.2.6 Conclusions

The heat balance of electrolysis cells have to be rigorously controlled to ensure the optimal performance of aluminum production. The consideration of the cavity for the modeling of heat losses is mandatory in order to obtain a good prediction of the heat fluxes from the anode cover. The average prediction error of the heat flux from the ACM_{SC} close to the anode assembly is reduced from 21.8 % to 7.3 % when the cavities are included in the model. The average heights of cavities surrounding the mid-life anodes investigated in this study are approximately 15 cm between the anodes and 10 cm in the side channel. The heat flux from the anode cover in the side channel increases with the height of the cavity, implying the decrease of the side heat losses.

5.2.7 Acknowledgements

This work is financed and supported by Rio Tinto and “Natural Sciences and Engineering Research Council of Canada” (NSERC). Finally, a part of the research presented in this paper was financed by the “Fonds de Recherche du Québec - Nature et Technologies” (FRQNT) by the intermediary of the Aluminium Research Centre-REGAL.

CHAPITRE 6 MODÉLISATION THERMIQUE-ÉLECTRIQUE EN RÉGIME PERMANENT

6.1 Avant-propos

Auteurs et affiliation :

François Allard : étudiant au doctorat, Département de génie chimique et génie biotechnologique, Université de Sherbrooke, Québec, Canada.

Martin Désilets : professeur titulaire, Département de génie chimique et génie biotechnologique, Université de Sherbrooke, Québec, Canada.

Marc LeBreux: professionnel de recherche, Département de génie chimique et génie biotechnologique, Université de Sherbrooke, Québec, Canada.

Alexandre Blais : scientifique de recherche, Rio Tinto Aluminium, Centre de recherche et développement Arvida, Québec, Canada.

État de l’acceptation : Version finale publiée.

Revue : *International Journal of Heat and Mass Transfer*.

Référence :

Allard, F., Désilets, M., LeBreux, M. et Blais, A. (2019). Improved heat transfer modeling of the top of aluminum electrolysis cells. *International Journal of Heat and Mass Transfer*, en production.

Lien d’accès : https://doi.org/10.1016/j.ijheatmasstransfer.2018.12.062

Contributions à la thèse :

Ce chapitre présente les résultats et le développement d’un nouveau modèle thermique-électrique en régime permanent, qui inclut la prédiction de la taille de la cavité dans une cellule d’électrolyse d’aluminium. Un algorithme a été programmé pour prédire la localisation de l’interface entre la croûte d’anode et la cavité, pour ainsi améliorer la précision de modélisation et comprendre certains phénomènes responsables de problèmes industriels tels que la formation de boue à l’interface cathodique. Les points suivants résument les contributions et nouveautés :

- Les propriétés thermiques de la croûte d’anode, présentées au Chapitre 5, ont été intégrées dans ce modèle thermique-électrique, ce qui a permis d’atteindre une précision de prédiction de 2.4 % en comparaison avec les mesures de thermocouples placés dans ce matériau. De plus, les mesures de températures et de flux thermiques prélevées dans la croûte d'anode d'une cellule d'électrolyse en fonctionnement ont permis de confirmer les valeurs de conductivités thermiques déterminées en laboratoire.

- La géométrie des matériaux de recouvrement a été améliorée à l'aide de mesures manuelles topographiques des matériaux de recouvrement anodique. Les profils typiques des interfaces *ACM*-croûte et croûte-cavité ont donc pu être déterminés.
- Afin d'améliorer la prédiction des flux thermiques par rayonnement se déroulant dans la cavité, les émissivités d'échantillons industriels d'*ACM* et de croûte d'anode ont été déterminées expérimentalement à l'aide d'une caméra infrarouge calibrée.
- Considérant ces propriétés thermiques améliorées et la géométrie représentative des conditions réelles, la précision de prédiction par le modèle thermique-électrique a été validée par des campagnes industrielles exhaustives.
- Les résultats de simulations ont démontré ces deux principaux points :
  - L'augmentation de l'isolation thermique au-dessus de la cellule d'électrolyse conduit à la dégradation de la croûte d'anode et à la croissance de la cavité. De plus, elle engendre l'augmentation de la dissipation thermique par le dessus et la fonte du talus, le dépôt qui est formé sur les parois latérales et responsable de protéger les rebords de la corrosion du bain électrolytique liquide.
  - La dégradation de la croûte d'anode et la chute de ce matériau à haute [Al_2O_3] peuvent occasionner la formation de boue sur la surface des blocs cathodiques. Selon les prédictions, un film de boue augmente la génération de chaleur par effet Joule, ce qui engendre la fonte et chute de croûte. Cette synergie de chute de croûte d'anode et de formation de boue est néfaste pour l'opération des cellules d'électrolyse et augmente la perte de potentiel électrique à l'interface cathodique.
- Finalement, une corrélation numérique a été développée pour permettre un diagnostic thermique de cellule d'électrolyse, à l'aide de mesures de flux thermiques. La corrélation numérique, basée sur les modèles thermiques-électriques, estime le ratio entre la dissipation thermique totale par le dessus et par le côté des cellules d'électrolyse.

Titre français :

Amélioration de la modélisation du transfert thermique au-dessus des cellules d'électrolyse d'aluminium

Résumé :

Un modèle thermique-électrique est développé en utilisant la méthode des éléments finis et il est entièrement validé par des mesures thermiques réalisées dans des cellules d'électrolyse industrielles. La connaissance des géométries du matériau de recouvrement anodique (*ACM*) et de la croûte d’anode est améliorée en mesurant leurs profils dans les cellules industrielles. De plus, la forme de la cavité formée par la fusion de la croûte d’anode est prédite avec le modèle numérique, en utilisant un module de radiosité combiné à une méthode itérative. La conductivité thermique et l'émissivité de l'*ACM* et de la croûte d’anode sont également évaluées par des mesures expérimentales. Le modèle thermique-électrique prédit avec précision les flux thermiques et les températures lorsque l’on compare avec les capteurs installés sur les anodes industrielles. Les résultats de la modélisation démontrent que l'augmentation de l'épaisseur d’*ACM* réduit les pertes de chaleur par le dessus et augmente la dissipation thermique par le côté, tandis que les pertes par le bas demeurent constantes. En isolant davantage le dessus de la cellule d'électrolyse, le talus se rétracte et la croûte d'anode fond. L'impact d'un film de boue sous l'aluminium liquide est quantifié avec le modèle. Par conséquent, la boue augmente la chute de tension à la cathode (*CVD*), agrandit la cavité, réduit l'épaisseur du talus et amplifie la dissipation thermique par le côté. La modélisation thermique-électrique fournit des indications pour améliorer la conception et le fonctionnement de la cellule d'électrolyse afin d'atteindre une meilleure efficacité.

6.2 Improved heat transfer modeling of the top of aluminum electrolysis cells

Keywords: Heat transfer, thermal-electric modeling, anode crust, anode cover material, emissivity, aluminum electrolysis

6.2.1 Abstract

A thermal-electric model is developed using finite elements and thoroughly validated against thermal measurements performed in industrial aluminum electrolysis cells (AEC). Knowledge about the geometries of anode cover material (ACM) and anode crust is improved by measuring their profiles in industrial cells. Moreover, the shape of the cavity formed by the melting of the anode crust is predicted with the numerical model, using a radiosity module combined to an iterative method. The thermal conductivity and the emissivity of both ACM and anode crust are also evaluated based on experimental measurements. The thermal-electric model accurately predicts the measurements obtained from heat flux sensors and thermocouples installed on industrial anodes. Modeling results show that increasing the ACM thickness reduces the top heat losses and increases the heat dissipation from the side, while the bottom losses remain constant. With thicker top insulation, the side ledge shrinks and the anode crust melts. The impact of a film of sludge under the liquid aluminum is quantified with the model. Accordingly, the sludge increases the cathode voltage drop (CVD), enlarges the cavity, reduces the side ledge thickness and amplifies the side heat dissipation. The thermal-electric modeling provides insights to improve the design and operation of AEC in order to reach higher efficiency.

6.2.2 Introduction

The industrial aluminum production is carried out in electrolysis cells since the inventors, Hall and Héroult, patented the process in 1886. Over the last century, this process has been improved in order to reach a better energetic efficiency and environmental balance, while increasing production. The design of the aluminum electrolysis cells (AEC) is continuously optimized in order to achieve these goals.

In operating AEC, the alumina (Al_2O_3) is reduced to aluminum using a liquid electrolytic bath. The liquid bath is primarily composed of a mixture of Na_3AlF_6 (cryolite), AlF_3 (aluminum fluoride), CaF_2 (calcium fluoride) and dissolved Al_2O_3. An electric current with an intensity varying from 200 kA to 600 kA, depending on the technology, is supplied to the AEC and is divided between the several consumable carbon anodes immersed in the liquid bath. The oxide ions formed from the dissolution of alumina react at the surface of the carbon anodes, thus releasing carbon dioxide (CO_2). The aluminum is produced at the electrochemical cathode, which is the top surface of the liquid aluminum pad. Equation 6-1 is the overall electrochemical reaction occurring in AEC [Thonstad *et al*., 2001]:

$$2\ \mathrm{Al_2O_{3(dissolved)}} + 3\ \mathrm{C_{(s)}} \xrightarrow{\text{current}} 4\ \mathrm{Al_{(l)}} + 3\ \mathrm{CO_{2(g)}} \tag{6-1}$$

The main components of modern AEC are the prebaked carbon anodes, the liquid bath containing dissolved alumina, the aluminum pad and the graphitized carbon cathode blocks (shown in Figure 6-1). Typically, the electrolysis cell operates at about 965 °C, which is 15 °C higher than the liquidus of the bath. The liquid bath and aluminum are surrounded by side ledge, a thick layer mainly composed of frozen cryolite. The AEC is designed to dissipate heat from its sides in order to build a layer of suitable thickness to protect the side walls from the highly corrosive and erosive behavior of the bath. The side wall lining of AEC is typically composed of SiC (silicon carbide) refractory and carbon ramming paste. The bottom lining contains carbon blocks, ramming paste, insulating materials and refractory bricks. Both the side and bottom are enclosed by a steel shell with cradles to strengthen the structure.

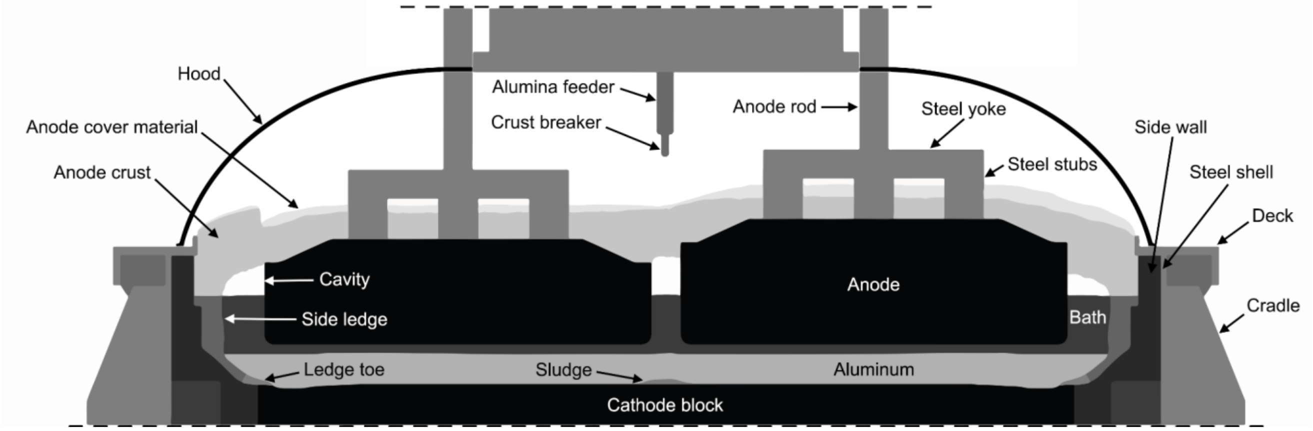

Figure 6-1 An aluminum electrolysis cell with its main components

The carbon anodes are consumed by the electrolysis process and must be replaced after a few weeks. At the end of its life, the anode change procedure is performed, which involves removing the old anode and setting in a new one. During the first hours of the newly set anode, the top of the liquid bath surrounding the new anode is freezing in contact with colder gas. Once a "top freeze" layer of a few centimeters is formed, the anode cover material (ACM) is poured on the anode. The ACM is leveled properly on the carbon anode for the purpose of preventing its oxidation and insulating the top of the AEC. Afterward, the top freeze layer melts due to the insulating property of the ACM, and liquid bath from the cell begins to rise in the powdered ACM by capillary forces. In contact with liquid bath and vapor coming from the cell, the ACM gets transformed into anode crust, a hard material consisting of α-Al_2O_3 particles cemented together with solid or liquid bath [Less, 1977; Liu *et al*., 1992; Allard *et al*., 2015b]. The typical ACM and anode crust remain in solid state up to 696 °C, which is the melting temperature of the calcium cryolite ($NaCaAlF_6$). As reported by previous studies [Allard *et al*., 2015b; Allard *et al*., 2019a], the $Na_5Al_3F_{14}$ melts incongruently decomposing into $Na_3AlF_{6(s)}$ from 696 °C to 710 °C in typical ACM and anode crust. A strong anode crust should remain in place during all the life of the carbon anode. Once the anode crust is formed, its structure begins to deteriorate due to liquid bath splashes and vapor penetration from beneath. The bottom of the anode crust, facing the bulk liquid bath, is deteriorating from around 935 °C, since all the bath phases are liquid at this temperature. Consequently, collapsing of this part leads to the formation of a cavity filled with fumes and gas [Allard *et al*., 2016].

The anode cover of AEC is composed of two distinct parts: the ACM and the anode crust. The ACM is usually made from recycled anode crust, electrolytic bath and alumina, which have been crushed into particles of fine to coarse granulometry. The thermal properties of the ACM have been explored by a few researchers [Llavona *et al*., 1988; Hatem *et al*., 1989; Shen, 2006; Wijayaratne *et al*., 2011]. The thermal conductivity of the ACM increases with its bulk density [Llavona *et al*., 1988]. The effects of composition and granulometry on the thermal conductivity of ACM have been previously evaluated with a laboratory-made apparatus [Shen, 2006; Wijayaratne *et al*., 2011]. These studies demonstrated that thermal conductivity of ACM increases with temperature by an almost linear relationship and showed the significant effect of granulometry on this property.

According to experiments performed on synthetic anode crusts with the hot wire method, the thermal conductivity increased by 30 % with a bulk density varying from 2000 kg/m^3 to 2500 kg/m^3 [Hatem *et al*., 1989]. A higher proportion of crushed bath added in the ACM forms an anode crust having a higher thermal conductivity [Rye *et al*., 1995]. Anode crusts sampled in industrial cells demonstrated a slight decrease of the thermal conductivity in function of temperature [Llavona *et al*., 1990]. The measurements of the thermal conductivity with the hot wire method are limited to approximately 600 °C to prevent damage to the apparatus due to the corrosive behavior of liquid fluorides in the anode crust. More recently, laser flash analysis results demonstrated that the thermal conductivity of certain industrial anode crust decreases from 1.38 W/m·K to 0.89 W/m·K at temperatures ranging from 100 °C to 950 °C [Allard *et al.*, 2019a].

The thermal balance of the AEC is finely adjusted to maintain the protective side ledge layer throughout its lifetime, which typically lasts a few years. The side ledge grows on the side wall by the primary crystallization of Na_3AlF_6. When formed at equilibrium conditions, it shows a composition close to pure Na_3AlF_6. However, the composition also depends on the cooling rate as AlF_3, CaF_2 and Al_2O_3 species can be trapped between the dendrite crystal during a fast-growing step [Allard *et al.*, 2014; Fallah-Mehrjardi *et al.*, 2014; Poncsák *et al.*, 2017]. When the AEC is cooled down, the side ledge evolves by forming an open crystalline layer, in which mass transfer can occur with the bulk liquid bath [Liu *et al.*, 2017]. Ledge toe is also formed on the cathode blocks by solidification of Na_3AlF_6. This deposit contains a higher concentration of Al_2O_3 and higher cryolite ratio (CR) than the bulk liquid bath [Allard *et al.*, 2014; Allard *et al.*, 2015a; Coulombe *et al.*, 2016a]. A thin sludge deposit of thickness ranging from several µm to few mm is often found between the aluminum pad and the cathode blocks. The cathode voltage drop (CVD) is increased when this deposit is found in industrial AEC [Coulombe *et al.*, 2016b]. The side ledge and ledge toe of typical chemical composition grow from approximately 950 °C according to thermochemical evaluations [Allard *et al.*, 2015a]. The thermal conductivity of the side ledge has been measured by the hot wire method and more recently by laser flash analysis [Haupin, 1971; Poncsák *et al.*, 2014; Poncsák *et al.*, 2015; Gheribi *et al.*, 2017]. The thermal conductivity of the principal phases in the side ledge was also determined with equilibrium molecular dynamics simulations [Gheribi *et al.*, 2016, 2017]. However, there remains a lack of experimental data of the thermal conductivity of the side ledge at temperatures higher than 550 °C.

Various numerical models have been developed for the purposes of predicting the voltage drops in conductors, the mechanical stresses in the cell components, their heat generation and thermal dissipation, the magnetohydrodynamic flow and the mass transfer in the liquid electrolyte [Hou *et al.*, 1995; Safa *et al.*, 2009; Marceau *et al.*, 2011; Blais *et al.*, 2013; Ariana *et al.*, 2014; Langlois *et al.*, 2015; Bardet *et al.*, 2016]. The heat transfer has been modeled with the finite element method within the last decades in order to improve the design of the AEC [Hou *et al.*, 1995; Valles *et al.*, 1995; Dupuis, 1998; Fortin *et al.*, 2012; Blais *et al.*, 2013]. The typical heat losses of industrial AEC are distributed as follows: 43 % from the top, 50 % from the side and 7 % from the bottom [Grjotheim *et al.*, 1993]. About 35 % of the total heat losses are dissipated by the anode cover, while 35 % are also escaping by side walls. Accordingly, the thermal balance of AEC strongly depends on the phase change materials located on the side walls (side ledge) and on the top of the cell (anode cover). Considerable efforts have been made to improve the prediction of the ledge profile, although there are still possible improvements to get closer to its actual behavior in the electrolysis cell. The thermal modeling methods of AEC evolved from simpler 1D to more complex 3D geometries to improve the accuracy of heat transfer prediction [Haupin, 1971; Bruggeman and Danka, 1990; Dupuis, 1994, 1998].

Typically, the domain of the AEC can be delimited by two different top boundaries for heat transfer simulation: 1) the traditional boundary located under the hoods (domain ending with the anode assembly and the anode cover) or 2) the domain which includes all the top parts (hoods, superstructure, anode beam and anode rods). The second case is more complex to model since many components are located inside the superstructure. In operating AEC, air from the potroom enters through the gaps between the hoods due to the negative pressure created by the ventilation system. The top heat losses increase when the pot draft is raised, though this will also cause a reduction in the gas temperature exiting by the duct [Abbas *et al.*, 2009]. The top components temperature (stubs, hoods, anode rods) and duct gas temperature increase with the outside temperature, which can be observed with seasonal weather changes [Zhao *et al.*, 2013a]. A correlation between the convection coefficients and the volumetric flow rate of gas collected from the pot has been developed with computational fluid dynamics (CFD) simulations [Zhao *et al.*, 2013b]. The pot must be operated with a sufficient draft rate in order to prevent leakage of gas to the environment. Nevertheless, the leakage may be reduced by improving the pot tightness, thus allowing a reduction of the gas flow rate according to CFD results [Zhao *et al.*, 2017]. On another front, the top heat losses are also strongly related to the ACM thickness, as heat flux decreases with the height of this insulating material [Shen *et al.*, 2008]. The heat losses from the anode cover also increase with the size of the cavity, which occurs when the anode crust melts and falls into the AEC [Allard *et al.*, 2016].

The design and operating conditions of AEC are continuously improving by heat transfer modeling. The electrolysis cell contains critical parts which must be designed to reach a reasonable lifespan of operation and a proper thermal balance. However, the top heat losses are dependent upon the anode cover properties, a complex phase change material. Previous thermal models of AEC used a simple representation of the anode cover, implying a gap between prediction and reality. The purpose of this study is to increase the accuracy of the heat losses prediction by improving the geometry of the anode cover, the boundary conditions and the modeling method. The anode cover has been enhanced by measurements of the ACM and the anode crust typical profiles and by determination of their transformation temperatures. The numerical model predicts the formation of the cavity caused by the melting of the anode crust, using a radiosity module combined to an iterative method. Moreover, new emissivity data for the ACM and anode crust were measured with infrared (IR) thermography. The most recent properties of the anode crust are integrated in the model and validated with temperature measurements. Moreover, the effect of cathode sludge on the heat balance of AEC is demonstrated for the first time, to the authors' knowledge. Finally, the modeling results are thoroughly validated with heat fluxes and temperature measurements at specific locations on the top of industrial AEC.

6.2.3 Thermal-electric model

Geometry

The heat losses of a P155 prebake cell are modeled with emphasis on improving the prediction accuracy of the top parts. The top of the AEC is composed by the anode assembly (anode rod, yoke, stubs and carbon anode) and the anode cover (ACM and anode crust). A cavity is integrated in the geometry to consider the anode crust deterioration process occurring during the operation of AEC. The cavity extends all around the anodes: in the side channel (SC), between the anodes (BA) and in the center channel (CC). At mid-life, the crust on the anode (OA) is directly in contact with the carbon, thus no cavity was included under this part. The geometry also contains all the typical parts of an industrial AEC, starting from the anode rod to the flexible conductors on the collector bar (Figure 6-2). A slice of an industrial cell containing one and a half anodes and two cathode blocks is used to model the heat transfer and the electric field. In operating cells, the average anode age is close to mid-life, but it slightly varies depending on the anode change patterns of each plant. Accordingly, the height of the anodes was adjusted to mid-life in order to replicate the general behavior of the AEC.

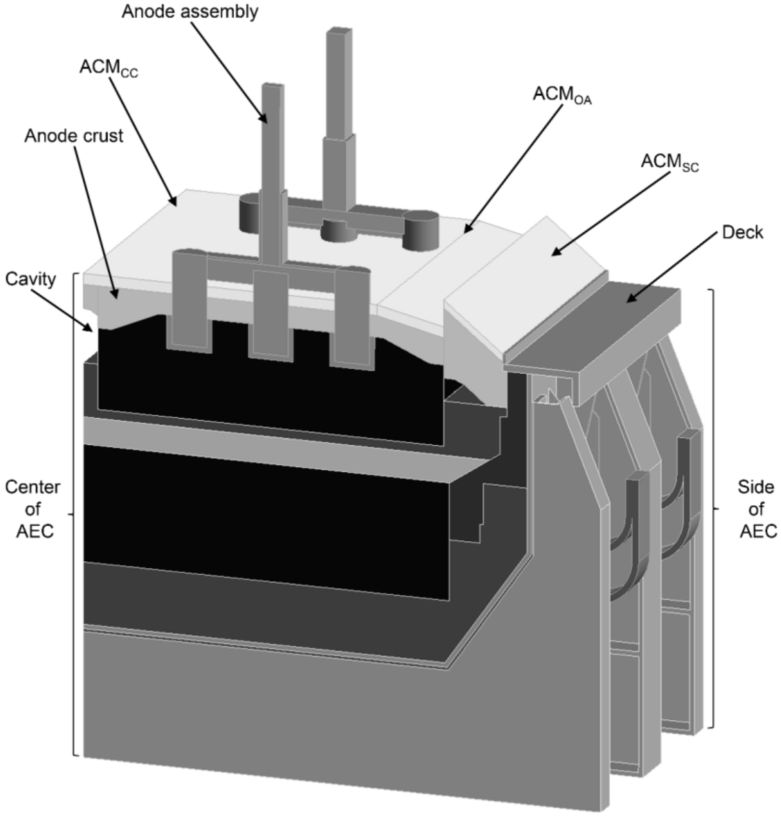

Figure 6-2 The geometry of an aluminum electrolysis cell used for the simulations

The ACM and anode crust geometries are based on measurements made on three mid-life anodes of industrial cells operated by Rio Tinto's Grande-Baie plant. All of the industrial measurements reported in this study were performed at this plant. To set these geometries, the profiles of the ACM and anode crust were measured with an experimental device. This device was explicitly made for the profile measurements, following the method illustrated in Figure 6-3. A steel bar was positioned at each location required to measure the surfaces of ACM and anode crust. The deck was the reference point to locate the measurements.

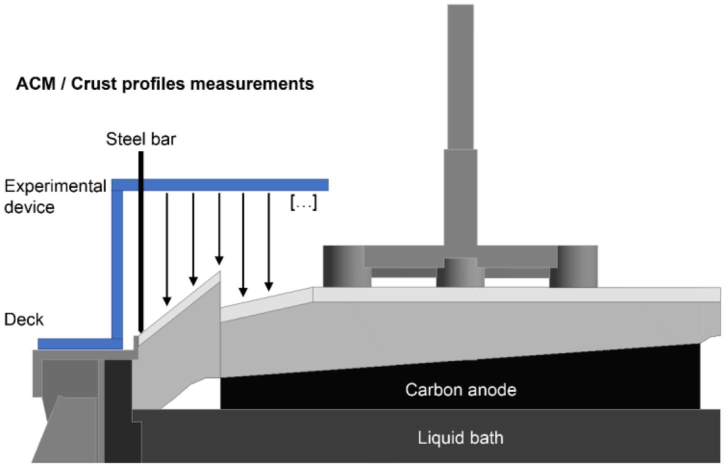

Figure 6-3 ACM and anode crust profiles measurements on a mid-life anode

In industrial operating cells, the anode crust typically breaks into two distinct parts due to mechanical disturbances generated during the anode beam movements. The crust$_{SC}$ is static and remains attached to the side wall, while the crust$_{OA}$ is linked to the anode and follows its movements. After a few days of anode life, the shape of the crust$_{SC}$ resembles a "step" that persists through the anode life. Normally, the separation is very close to the edge of the carbon anode. The average heights of ACM$_{SC}$, ACM$_{OA}$ and crust$_{OA}$ were calculated from the industrial measurements and are given in Table 6-1. The height of the crust$_{SC}$ varied depending on the location and its top surface followed the same slope as the ACM$_{SC}$. The average angle at the top of the ACM$_{SC}$ and ACM$_{OA}$ was also considered. The slope of the ACM$_{OA}$ typically ends next to the first stub. The geometry of the ACM and anode crust in the model was adjusted to these values.

Table 6-1 Geometric parameters of the anode cover of mid-life anodes

Height (cm)			*Angle (°)	
ACM$_{SC}$	**ACM$_{OA}$**	**Crust$_{OA}$**	**ACM$_{SC}$**	**ACM$_{OA}$**
3	4	8	35	15

**Angle from the horizontal*

The geometry of the bottom part of the anode crust is difficult to measure due to the high temperature of the electrolysis process. However, the size of the cavity impacts the top heat losses of AEC [Allard *et al.*, 2016]. In order to improve the prediction, the profile of the crust-cavity interface is computed with an iterative modeling method to find the right isotherm (detailed in section *Modeling method*). A new geometry of the crust is calculated at each step of resolution and the geometric parameters of the crust bottom are adjusted automatically in the computer-aided design (CAD) tool to feed the next iteration. This iterative loop is done until the right profile is reached. This profile is based on the melting temperature of the chemical compounds in the anode crust. The model prediction for the cavity shape is validated by measuring the height of the cavity$_{SC}$ of 4 industrial anodes at mid-life. A hole was drilled in the anode crust next to the carbon anode in order to measure this height. The location of the variable geometric parameters in the CAD geometry and the position where the height of the cavity was measured are described in Figure 6-4.

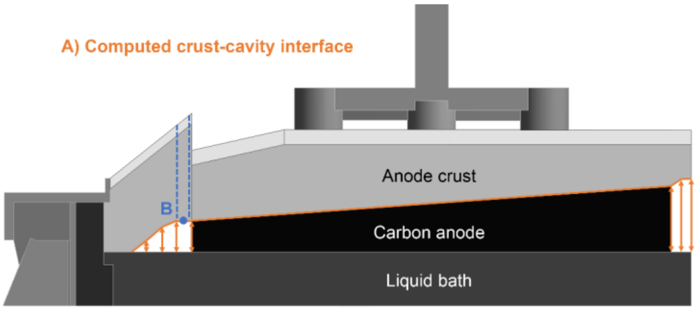

Figure 6-4 A) The computed crust-cavity interface facing the bulk liquid bath. B) ● indicates the location where the height of the cavity was measured

Modeling method

The heat transfer taking place inside the AEC is generated due to Joule heating effect, which depends on the electric current entering from the top conductors and leaving through the collector bars. The heat dissipation is predicted with a steady state thermal-electric model applied to the slice of the AEC (Figure 6-2). This domain is discretized into elements and resolved with the finite element method [Reddy and Gartling, 2010]. Each model is composed of approximately 700 000 elements and has been resolved using an Intel Xeon E5-1650 v4 with 32 GB ECC memory. The commercial software ANSYS Mechanical (release 18.0) was used to perform the thermal-electric calculations.

The prediction of the crust-cavity interface is a new aspect which has been programed with Python 2.7 and APDL scripting languages. The heat transfer in the cavity is computed with a radiosity module that performs the outgoing radiative flux calculations for each surface. The radiosity solution method is solved in conjunction with the thermal-electric resolution. The cavity is added in the model to improve the accuracy even if this module increases the complexity of the resolution. The prediction of this profile also allows to quantify the impact of operating parameters on the heat losses. Furthermore, this profile is laborious to measure in an operating industrial AEC.

The crust-cavity profile is predicted by performing an iterative solution method automated with Python scripting in ANSYS Workbench. The method of resolution is schematized in Appendix A (see Figure 6-12) and summarized by these steps:

1. Generate an initial crust-cavity profile;
2. Apply the generated profile to the geometric parameters in the CAD geometry;
3. Update the thermal-electric model and perform the resolution;
4. Get the nodal temperatures located at crust-cavity interface and compare with the crust melting temperature;
5. Calculate new geometric parameters for the crust-cavity profile according to the local temperatures;
6. Repeat steps 2 to 5 until the crust-cavity interface reaches the crust melting isotherm (± 1 °C).

Assumptions

In order to predict the temperature and electric potential distribution in the slice of an AEC, the following assumptions were considered: (1) the heat transfer from a mid-life anode is close to steady state; (2) the mass transfer effects on heat losses are neglected; (3) the ACM granulometry and thermal conductivity are similar to the data presented in [Shen, 2006]; (4) the properties of all materials are known; (5) the effect of the flow circulation inside the bulk liquid bath and the aluminum pad is accounted by an "augmented effective thermal conductivity" [Vidalain *et al*., 2009]; (6) the heat transfer in the cavity is radiation dominated and (7) the surfaces in the cavity are gray and diffuse.

Governing equations

The heat losses and heat generation are predicted based on a coupled thermal-electric finite element analysis (FEA). The finite element method solves the differential and integral equations using 3D coupled-field elements for solid and surface elements for boundary conditions. The set of algebraic equations is developed with the weighted residual statement and the Newton-Raphson method is applied to solve this nonlinear system. The preconditioned conjugate gradient solver assembles the full stiffness matrix and it calculates the solution by iterating up to convergence.

The general equations of heat and electric conduction are described by the following equations. A vector is denoted by a bold letter and a matrix is represented in brackets. Equation 6-2 describes the governing equation for the steady state heat conduction with the volumetric heat generation rate [ANSYS, 2013]:

$$\frac{\partial}{\partial x}\left(k_x \frac{\partial T}{\partial x}\right) + \frac{\partial}{\partial y}\left(k_y \frac{\partial T}{\partial y}\right) + \frac{\partial}{\partial z}\left(k_z \frac{\partial T}{\partial z}\right) = \dot{q} \tag{6-2}$$

The volumetric heat source term $\dot{q}$ is calculated by the Joule effect:

$$\dot{q} = \sigma E^2 \tag{6-3}$$

The electric field can be derived from:

$$\boldsymbol{E} = -\nabla V \tag{6-4}$$

The potential distribution is computed from the governing equation for steady state electric conduction [ANSYS, 2013]:

$$-\nabla \cdot ([\sigma]\nabla V) = 0 \tag{6-5}$$

The radiosity method is used in order to calculate the heat transfer in the cavity. A set of linear algebraic equations is used to obtain the outgoing radiative fluxes (radiosity) for each surface [ANSYS, 2013].

$$[A]\{q''^{,0}\} = \{D\} \tag{6-6}$$

Where:

$$A_{ij} = \delta_{ij} - (1 - \varepsilon_i)F_{ij}$$

$q_j''^{,0}$= radiosity flux for surface j

$$D_i = \varepsilon_i \sigma T_i^4$$

Equation 6-7 is solved with the Newton-Raphson procedure for the radiosity flux $\{q''^{,0}\}$. At the surface facing the cavity, the boundary conditions for heat conduction are provided by the net surface radiosity fluxes. The radiation view factors, F_{ij}, are required to solve the radiosity module. The overall view factors for each surface are calculated using the hemicube method [ANSYS, 2013]. Each surface on the hemicube has an overall view factor given by:

$$F_{ij} = \sum_{n=1}^{N} \Delta F_n = \frac{\cos\varphi_i \cos\varphi_j}{\pi r^2} \Delta A_j \tag{6-7}$$

Where:

N = number of pixels

ΔF = delta-view factor for each pixel

Material properties

The thermal properties of the top parts of the AEC were improved recently and were also revisited in this study [Shen, 2006; Allard *et al.*, 2019a]. New thermal conductivity data for the ACM and the anode crust are implemented in the model in order to improve the accuracy of the results. Moreover, these properties were validated with thermocouple measurements in industrial AEC. Isotropic thermal conductivity for the ACM and the anode crust are used in the model as these materials do not show preferential alignment in their microstructure [Allard *et al.*, 2019a]. The bulk liquid bath and the aluminum pad are simulated with an augmented effective thermal conductivity to consider the effect of flow circulation. New data for the emissivity of the ACM and the anode crust were determined with an IR camera (see section *Infrared thermography*). The emissivity results were required to predict the heat transfer by radiation inside the cavity. The thermal properties of these materials are detailed in Table 6-2.

Table 6-2 Thermophysical properties of the top materials

Property	Value	Reference
ε_{ACM}	1.0	*Experiment*
ε_{crust}	1.0	*Experiment*
ε_{carbon}	0.95	[Touloukian and DeWitt, 1972]
$\varepsilon_{liquid\ bath}$	0.97	[Windisch *et al.*, 1992]
k_{ACM} (W/m·K)	0.000616 T + 0.155	[Shen, 2006]
k_{crust} (W/m·K)	-0.000541 T + 1.386	[Allard *et al.*, 2019a]
$k_{bath\ solid}$ (W/m·K)	1.2	-
$k_{bath\ liquid}$ (W/m·K)	10 000	-

**T: Temperature in °C.*

The ACM is modeled as a phase change material, which transforms into anode crust from 685 °C (Equation 6-8). The transformation evolves from the contact with liquid or vapor fluoride species, which enhance the growth of the α-Al_2O_3 crystalline network and consolidate the particles. The transformation starts from 685 °C due to $NaAlF_4$ from the vapor leaving the bulk liquid bath. However, the vapor is more likely to penetrate the ACM or the crust in the channels next to the anodes (SC, BA, CC). The ACM_{OA} begins to transform into crust from 696 °C due to the melting of $NaCaAlF_6$ and $Na_5Al_3F_{14}$ [Allard *et al.*, 2019a]. According to thermodynamic equilibrium results, this transformation is favored by the liquid fraction which rises quickly from 696 °C to 710 °C in ACM of typical chemical composition.

$$\text{ACM} \xrightarrow{\text{fluorides}} \text{Anode crust} \qquad (685\ °\text{C to } 710\ °\text{C}) \tag{6-8}$$

For the simulation, the ACM thermal conductivity from room temperature up to 685 °C follows the linear equation determined by Shen [Shen, 2006]. A linear transition is included in order to reach the value of the anode crust (between 685 °C and 710 °C). From 710 °C, the crust transformation is considered completed and the thermal conductivity decreases linearly with temperature [Allard *et al.*, 2019a]. The transformation in Equation 6-8 is an irreversible process, like the deterioration of the crust due to high temperature and liquid bath splashes.

All bath phases composing the crust are melted at around 935 °C according to the phase diagram [Allard *et al.*, 2019a]. At this condition, the crust is only supported by Al_2O_3 and is subject to dissolution by the liquid bath. The crust begins to collapse or flow into the bulk liquid bath, thus generating a larger cavity.

$$\text{Anode crust} \rightarrow \text{Cavity} \qquad (935\ °\text{C}) \tag{6-9}$$

The ledge is formed on the side walls when liquid bath freezes due to the heat dissipated by the shell to the surroundings. The ledge is primarily composed of Na_3AlF_6 with dissolved species inside its microstructure. The melting or freezing temperature of the Na_3AlF_6 depends on chemistry of the bulk liquid bath, which affects the local composition at the liquid bath-ledge interface. The ledge grows or melts typically at 950 °C (Equation 6-10), a temperature that varies depending on the liquid bath composition. This reversible phase change evolves according to operating conditions and heat dissipation to the surroundings.

$$\text{Liquid bath} \leftrightarrow \text{Side ledge} \qquad (950\ °\text{C}) \tag{6-10}$$

Boundary conditions

In order to perform the thermal-electric simulations, the top boundaries were set by considering the top surfaces of the ACM and the anode assembly. These parts are facing the bottom of the superstructure and the hoods which are at lower temperatures. The air flow coming from the potroom and entering through the crack between the hoods also cools down the top parts by convection heat transfer. These are then cooled by both convection and radiation heat transfer. In the simulations, "effective convection heat transfer coefficients" (h_{eff}) considering both the convection and radiation have been applied to the top boundaries of the electrolysis cell. Using Equation 6-11, the h_{eff} values were calculated from both the heat flux measurements (q'') and the temperature measurements of the surface (T_s) and gas (T_∞).

$$q'' = h_{eff}\,(T_s - T_\infty) \qquad (950\ °\mathrm{C}) \tag{6-11}$$

The boundary conditions, h_{eff} and T_∞, were determined based on thermal measurements in industrial cells (detailed in section *Thermal measurements performed on industrial AEC*). T_∞ are the gas temperatures measured above the boundaries. Table 6-3 details the top boundary conditions used in the numerical model.

Table 6-3 Boundary conditions for the top parts of the AEC

Boundary	h_{eff} (W/m^2·K)	T_∞ (°C)
Sides of anode rod	25	120
Steel yoke and stubs	40	120
Top of ACM$_{OA}$ and ACM$_{CC}$	20	120
Top of ACM$_{SC}$	20	100
Top of deck	25	50

The global geometry of the AEC was cut in the center and on two sides to produce the slice shown in Figure 6-2. For each cut section, a symmetric boundary condition has been applied. Heat losses from the side and the bottom were also predicted with h_{eff} and T_∞ data calculated and measured on industrial AEC. For the electrical boundaries, the current delivered to the electrolysis cell was divided by the number of anodes and the corresponding value was applied to the top of each anode rod. A potential of 0 V has been applied to the top of each cathode flexible conductors.

6.2.4 Measurement methods

Thermal measurements performed on industrial AEC

The results of the thermal-electric simulations were validated with measurements performed on industrial AEC. The heat fluxes and temperatures above the ACM and on some metallic surfaces have been validated by heat flux sensors (HFS). Figure 6-5 shows the locations of the HFS placed on the AEC. The heat flux measurements were achieved with Hukseflux HF01 sensors. The estimated accuracy of these sensors is ± 15 % and the repeatability is ± 5 % according to the products manuals [Hukseflux, 2003]. Theses sensors were calibrated in the laboratory before the industrial measurements to ensure the validity of the results. Moreover, the temperature was also measured by the sensors with an accuracy of approximately ± 1 % (type K thermocouple installed inside).

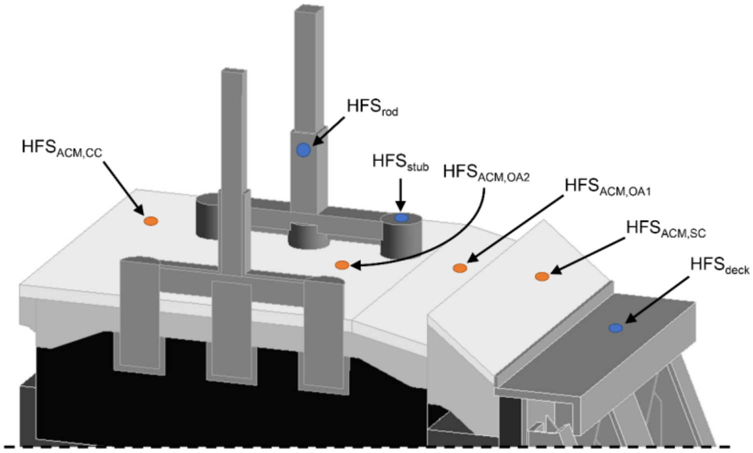

Figure 6-5 Each ● indicates the location on the ACM where a HFS was placed; ● indicates the location of a HFS set on a metallic surface

The temperatures on the anode assembly (rod and stub), the ACM and the anode crust were measured continuously with type K thermocouples installed in the location described in Figure 6-6. The thermocouples in the ACM and crust were installed before the covering of the new anode and were folded in "L" shape, pointing away from the stubs. The ends of these thermocouples were located under the HFS$_{\mathrm{ACM,OA2}}$ shown in Figure 6-5. In the ACM-crust, a thermocouple was installed every 2.5 cm (from 0 cm to 10 cm) from the top of the carbon anode. On the anode rod, a thermocouple was soldered each 10 cm. Two thermocouples were set on the stubs, one on the top and one close to the carbon anode. The gas temperatures above the ACM and anode assembly were measured with type T thermocouples at the locations shown in Figure 6-6. The air temperatures outside the AEC were also measured with the thermocouples at two locations next to the hoods ($T_{\infty,hood\ high}$ and $T_{\infty,hood\ low}$).

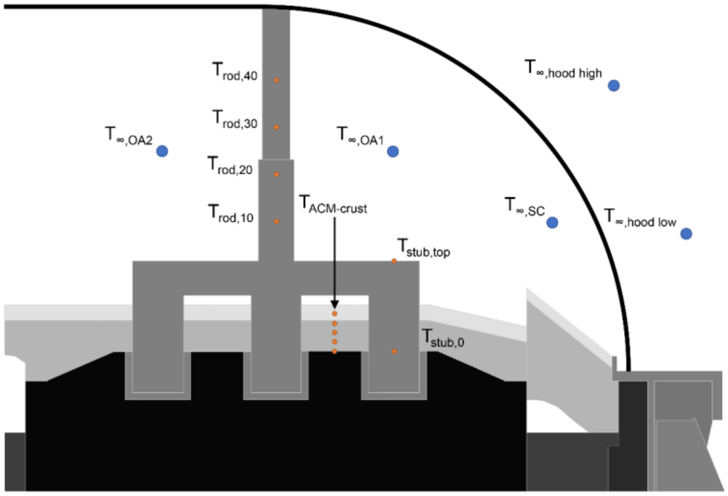

Figure 6-6 ● Thermocouples installed in the ACM, anode crust and anode assembly; ● locations where manual measurements of the gas temperature were made

For this study, all the heat flux and temperature measurements have been reproduced 48 times at the locations shown in Figure 6-5 and Figure 6-6. The thermal measurements were performed on three instrumented industrial anodes during their complete life. All measurements were taken during the fall season. The results are compiled and compared with the prediction of the thermal-electric model in section *Thermal-electric modeling validated by industrial measurements*.

Infrared thermography

The emissivity data of the ACM and anode crust were determined with a calibrated IR camera (FLIR SC620, calibration certificate #10244-01). The IR camera has a resolution of 640 x 480 pixels, a spectral range of 7.5 to 13 µm and an accuracy of ± 2 % at temperatures up to 1500 °C. The IR camera was set up on a tripod and adjusted at a maximum angle of 10° from the normal of each sample. The emissivity determination method is based on the standard practice described in ASTM E1933-14 [ASTM, 2014]. For the ACM and anode crust, the noncontact thermometer method was used by applying a surface-modifying material on these specimens. For this purpose, a paint of high emissivity (KRYLON High Heat black) was applied to partially cover the surface of each sample. The emissivity of this paint was determined with the contact thermometer method, by using a painted aluminum plate and a surface probe type K (OMEGA SPHT-K-6). The software ThermaCAM Researcher 2.10 PRO was used to analyze the IR photos and to compute the emissivity. The average emissivity of the reference paint (KRYLON High Heat black) was 0.98 ± 0.02 at a temperature range from 50 °C to 380 °C.

6.2.5 Results and discussion

Emissivity of the ACM and anode crust

The radiation heat transfer in the cavity has to be simulated with the proper emissivity properties in order to reach good predictions. The emissivity data of ACM and anode crust were determined, since no experimental data of these industrial materials were available in the literature. The emissivity data were measured in the laboratory, in a controlled environment. Six samples were collected on P155 prebake cells: two typical ACM, two crust$_{SC}$ and two crust$_{CC}$. For the anode crust, the bottom and top surfaces were measured to obtain data for all surfaces that exchange heat by radiation in the AEC. In order to determine the experimental emissivity, these samples were partially covered with a thin film of the reference paint and dried. Thereafter, these samples were heated in an oven at 400 °C during 2 h. Subsequently, the samples were placed on a refractory plate and a series of thermograms was taken with the IR camera, until the samples reached room temperature. Figure 6-7 shows an optical photo and two thermograms of the samples taken with the FLIR SC620 equipped with a 24° lens. The following parameters were taken into account for the thermograms: a reflected temperature of 30 °C, an object distance of 0.8 m, an atmospheric temperature of 22 °C and a relative humidity of 10 %.

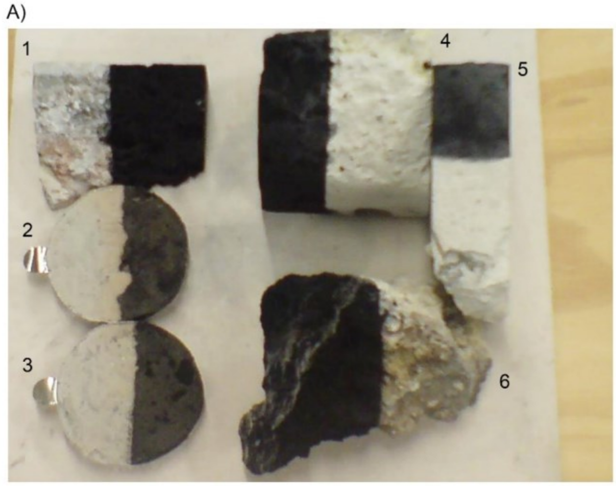

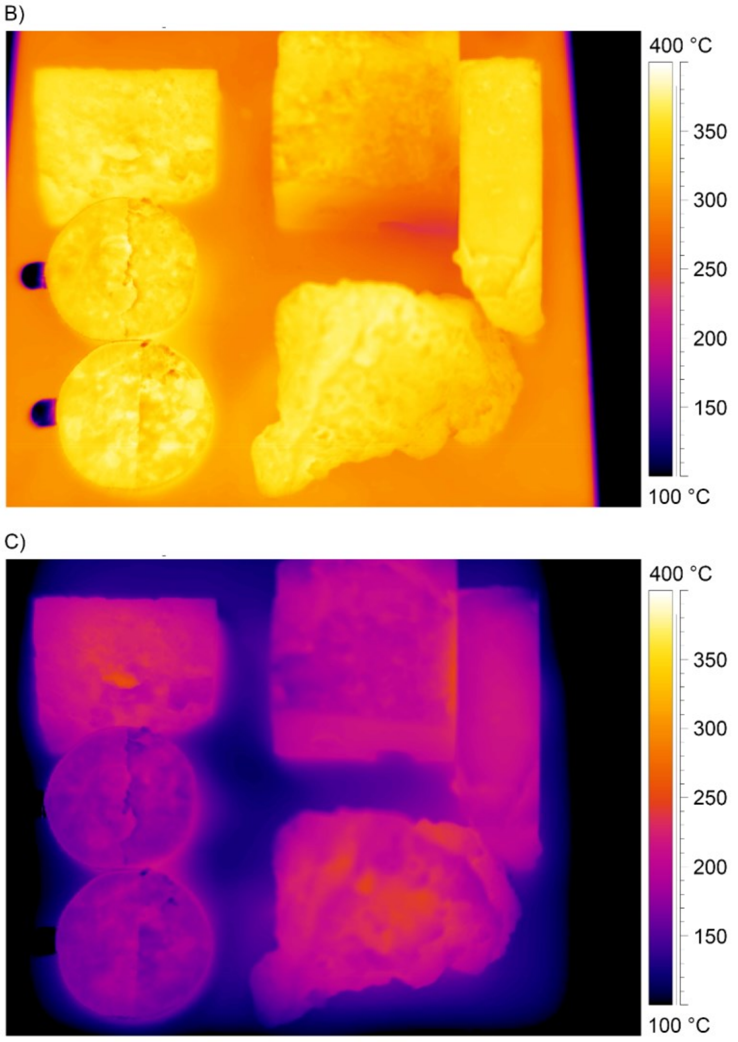

Figure 6-7 A) Optical photo of the samples. B) Thermogram taken at a temperature close to 400 °C. C) Thermogram taken at a temperature close to 200 °C

According to the thermograms, the uncovered surfaces of ACM and anode crust do not show any significant temperature difference with the parts covered by the reference paint. Nevertheless, the temperatures of uncovered parts of the ACM and anode crust were slightly higher than the covered parts, in the order of a few degrees. The emissivity results in Table 6-4 were calculated from the thermograms taken at a temperature close to 400 °C. An emissivity of 0.98 was used for the covered parts. Thereafter, the emissivity of each uncovered part was determined with the known temperature at the immediate border (noncontact thermometer method).

Table 6-4 Identification of the samples and results of the emissivity determination at 400 °C, from Figure 6-7B

#	Sample	Measured surface	Emissivity
1	Crust_{SC}	Bottom	1.00
2	ACM	-	1.00
3	ACM	-	1.00
4	Crust_{SC}	Top	0.99
5	Crust_{CC}	Top	0.99
6	Crust_{CC}	Bottom	0.98

The emissivity data of the ACM and anode crust samples were determined between 50 °C and 400 °C following the same methodology and no significant variation in emissivity was observed for this temperature range. The emissivity data of these materials remained within the error range of the IR camera (accuracy of ± 2 %), with values ranging from 0.98 to 1.00. In order to model the radiation heat transfer inside the cavity, the emissivity of the anode crust was rounded to 1.0 (black body).

The high value observed for these materials may be explained by their microstructural properties and their chemical composition. The ACM and anode crust are both composed mostly from electrolytic bath and alumina. In industrial AEC, the ACM and anode crust are contaminated by carbon dust from the anode and also contains metallic impurities, as demonstrated by XRD analysis of these materials [Allard *et al.*, 2019a]. The microstructure of the anode crust is characterized by pores in the order of µm which may contribute to increase the measured emissivity. These micropores exhibit radiative properties close to a blackbody cavity due to the cumulative effect of emission and reflection inside the enclosures [Bergman *et al.*, 2011]. Inside the electrolysis cell, the bottom of the anode crust reaches a temperature of approximately 900 °C. This material shows a large fraction of liquid bath of high emissivity (0.97) at this temperature. Therefore, the measured high emissivity of the anode crust can be expected to be also valid at high temperature.

Anode crust properties validated by industrial measurements

Temperatures at the anode crust boundaries

The temperatures at the ACM-anode crust interface (ACM-crust) and at the anode crust-cavity boundary (crust-cavity) were measured in industrial AEC in order to confirm the transformation temperatures specified in Equation 6-8 and Equation 6-9. Firstly, the temperature at the top of the anode crust was measured with a type K thermocouple. During each measurement in the ACM powder, some precautions were followed to enter the thermocouple in the horizontal direction in order to minimize heat losses from its metallic sheath, to minimize the displacement of the ACM when entering the probe and to select an anode with a sufficiently high thickness of ACM. Anodes with a few days of operation were selected since the ACM to anode crust transformation was still ongoing. The temperatures of the ACM-crust interface of 4 anodes were measured at the location "OA" (see section *Geometry*) and are given in Table 6-5. The ACM-crust interface showed an average temperature of 657 ± 19 °C, thus 28 °C lower than the transformation temperature according to thermodynamic equilibrium calculations (685 °C). This slight difference can be explained by the errors caused by the thermocouple measurements. Among others, the measuring end of the thermocouple will always be slightly higher than the ACM-crust interface, a few millimeters immediately above. Moreover, the hood was removed during the measurements and the uncovered metallic sheath was in contact with ambient air at 55 °C, thus contributing to lower the measured temperature.

Table 6-5 Measurements performed in the ACM of 4 anodes

#	$\text{Height}_{\text{ACM}}$ (cm)	$T_{ACM\text{-}crust}$ (°C)
1	6.0	679
2	6.5	633
3	6.0	660
4	4.0	655
Average*	5.6 ± 1.1	657 ± 19

**Average with the standard deviation.*

Afterward, the temperature at the crust-cavity boundary and the height of the cavity were validated in industrial AEC by drilling a hole in the location shown in Figure 6-4B. A type K thermocouple, folded in "U" shape, was inserted through the hole and raised to be in contact with the underside of the crust. Both the temperatures of the bottom of the crust and of the gas in the cavity were recorded. Table 6-6 shows the height of the cavity, the temperature under the crust and the gas temperature. An average temperature of 938 ± 12 °C at the crust-cavity boundary was determined, which is close to the temperature of 935 °C calculated at thermodynamic equilibrium [Allard *et al.*, 2019a]. The temperature at crust-cavity boundary used for the radiosity calculation is then close to the industrial data. Accordingly, these industrial measurements support the transformation temperatures given in Equation 6-8 ($T_{ACM\text{-}crust}$) and Equation 6-9 ($T_{crust\text{-}cavity}$).

Table 6-6 Measurements performed in the cavity$_{SC}$ of 4 mid-life anodes

#	**Height$_{cavity}$ (cm)**	**$T_{crust\text{-}cavity}$ (°C)**	**T_{gas} (°C)**
1	12.5	955	972
2	6.5	939	959
3	8.0	930	952
4	4.0	928	933
Average*	7.8 ± 3.6	938 ± 12	954 ± 16

**Average with the standard deviation.*

Thermal conductivity of the anode crust

The thermal conductivity of the anode crust used for the thermal-electric modeling was determined in previous work by the laser flash method performed on similar industrial anode crusts [Allard *et al.*, 2019a]. These experimental results are validated in this study using the thermocouples installed in the anode cover ($T_{ACM\text{-}crust}$ in Figure 6-6) and a calibrated HFS (HFS$_{ACM,OA2}$ in Figure 6-5). The anode crust is a porous material which is penetrated by gas and liquid coming from the bulk liquid bath in the AEC. The temperatures and the heat fluxes were taken on a mid-life anode operating under stable conditions. The effective thermal conductivity (k_{calc}) of this material is computed using the Fourier law (Equation 6-12) and calculated with the results of the temperature acquisition and the manual measurements with HFS. The heat transfer in the ACM and anode crust is close to 1D since the thermocouples were located far enough from the anode stubs. Four measurements of heat flux with the corresponding temperatures were used to calculate the thermal conductivity.

$$q_y'' = -k_{calc} \frac{\mathrm{d}T}{\mathrm{d}x} \tag{6-12}$$

The thermal conductivity data of the ACM (k_{ACM} [Shen, 2006]) and the anode crust (k_{crust} [Allard *et al.*, 2019a]) are compared with k_{calc}. Figure 6-8 demonstrates the k_{calc} determined from Equation 6-12 and the industrial measurements. The k_{calc} (0.90 W/m·K) was 8 % lower than k_{crust} (0.98 W/m·K) at a temperature of 752 °C. In comparison, the k_{calc} (0.55 W/m·K) was 8 % higher than k_{ACM} (0.51 W/m·K) at 577 °C. At a temperature between these two (676 °C), the thermocouples measured temperatures coming from both ACM and anode crust, since they were located in the transition area. As expected, the k_{calc} was located between the k_{ACM} and the k_{crust}.

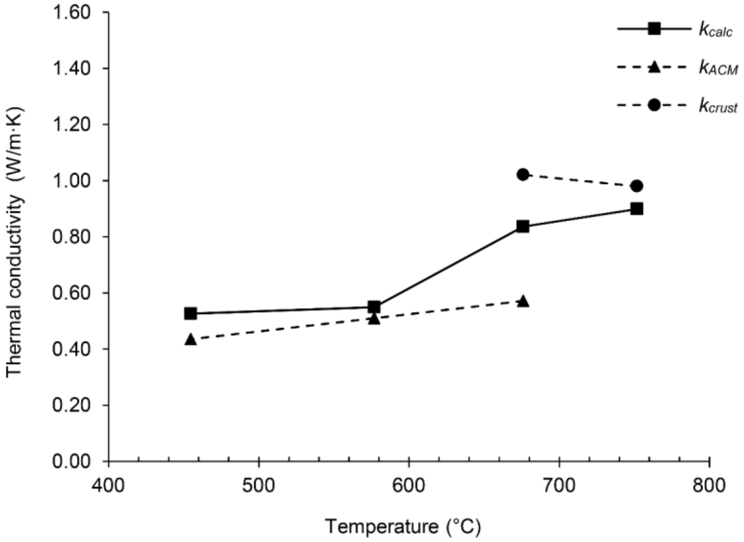

Figure 6-8 Calculated effective thermal conductivity (k_{calc}) in comparison with the corresponding data of the reference materials (k_{ACM} and k_{crust})

Thermal-electric modeling validated by industrial measurements

Considering the material properties and boundary conditions described in the previous sections, a base case of thermal-electric modeling will be compared with the industrial measurements of heat fluxes and temperatures.

Thermal conditions on the top of AEC

The top parts of the AEC are cooled by the air that enters through the free spaces between the hoods. When air enters in the enclosure, it mixes with hot gases generated by the electrolysis (mainly CO_2, CO and HF). The volumetric flow rates of the gas exiting the AEC were evaluated by 6 measurements with the Pitot tube technique. The average draft rate exiting the pot was 1.46 ± 0.05 Nm^3 s^{-1} (normal cubic meters per second) and the temperature was 124 ± 16 °C. The temperatures at the following locations (see Figure 6-6) were measured and given in Table 6-7: $T_{\infty,hood\ high}$, $T_{\infty,hood\ low}$, $T_{\infty,SC}$, $T_{\infty,OA1}$ and $T_{\infty,OA2}$. According to the measurements, the air enters at temperatures between 35 °C and 45 °C. Afterward, the air is mixed with the gas in the enclosure to reach 99 °C above the SC. This gas mixture leaves at a temperature close to 136 °C above the CC.

Table 6-7 Average gas temperatures on the top of the AEC with the standard deviation (based on 48 measurements on three AEC)

$T_{\infty,hood\ high}$ (°C)	$T_{\infty,hood\ low}$ (°C)	$T_{\infty,SC}$ (°C)	$T_{\infty,OA1}$ (°C)	$T_{\infty,OA2}$ (°C)
35 ± 11	45 ± 11	99 ± 23	116 ± 23	136 ± 26

During the anode life, a “step” of crust appears due to the anode beam movements (metal tapping, instability control and anode consumption). This “step” typically remains covered by ACM throughout the anode life. An optical photo and a thermogram were taken simultaneously to show this “step” formed in the crust$_{SC}$ and also the temperatures of the top parts (Figure 6-9). The optical photo and the thermogram of an instrumented anode were taken with the FLIR SC620 equipped with a 24° lens. The emissivity of this thermogram was set to 1.0 and a reflected temperature of 125 °C was used. Since the ACM showed an emissivity close to 1.0, the thermogram demonstrates the range of temperature on the top of this material. The temperature on the top of ACM$_{SC}$ was at 150 ± 31 °C, ACM$_{OA}$ was at 183 ± 26 °C and ACM$_{CC}$ was at 244 ± 31 °C, as determined on the ACM surfaces using the ThermaCAM software.

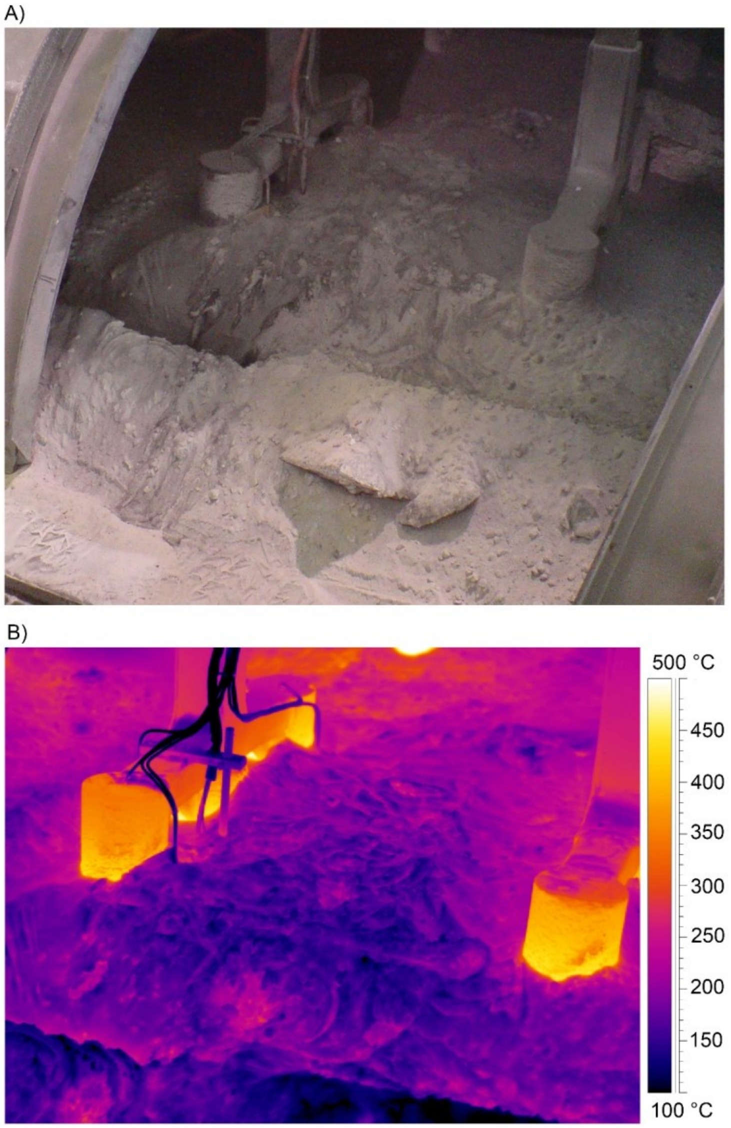

Figure 6-9 A) Optical photo and B) thermogram of an instrumented anode taken when 35 % of the anode lifespan had elapsed. The "step" is seen on the lower portion of the photography

<u>General model for the coupled thermal-electric prediction</u>

A general model is developed considering the measured anode cover geometry (Table 6-1), the latest thermophysical properties (Table 6-2) and the measured boundary conditions (Table 6-3). The results of this thermal-electric simulation are compared with the thermal measurements performed on industrial AEC in order to validate the prediction accuracy. The thermal investigation consists of 48 manual measurements of heat fluxes and temperatures in addition to the temperatures recorded on three instrumented anodes. The temperature distribution calculated with the numerical model of the 3D slice of AEC is shown in Figure 6-10. The average temperatures on the surfaces of the ACM$_{SC}$ and the ACM$_{CC}$ were 174 °C and 278 °C respectively. A large temperature gradient was located between the top of the ACM and the bottom of the anode crust, since the bottom reached 935 °C above the cavity.

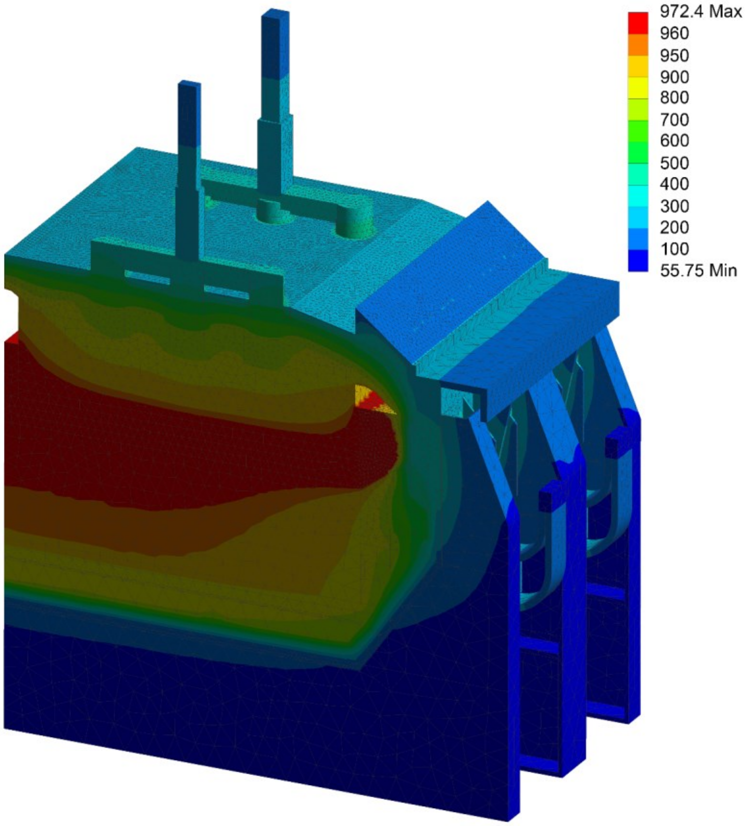

Figure 6-10 Temperature profile (°C) predicted with the general model (3D steady state slice)

The global average of temperature at each location was calculated from the 48 manual measurements (Figure 6-5) and from the temperature recordings of the three instrumented anodes (Figure 6-6). Mid-life temperatures were determined using all the data taken at ± 2 days of the mid-life; these temperatures were considered for the comparison with the general model. Table 6-8 details the global averages, the mid-life data, the predicted results and the relative error between the simulation and the mid-life measurements. The predicted temperatures were determined by selecting the closest node to the location measured with the HFS or thermocouple. According to the simulation, the temperature increased from 239 °C to 315 °C when going from ACM$_{SC}$ to ACM$_{CC}$ location. The vertical temperature gradient into the anode cover (located at ACM$_{OA}$) went from 759 °C to 401 °C, within a vertical distance of 10 cm from the anode, and it reached 300 °C at the top. The predicted height of the cavity (located in the

SC) at the position shown in Figure 6-4 (B) was 8.4 cm, an error of 7.7 % when compared to the measured value of 7.8 cm (Table 6-6).

In order to compare the predicted temperatures to the experimental measurements, both the HFS and the thermocouple were considered. The model's predictions should demonstrate a greater error when compared to HFS measurements than when compared to the thermocouples installed on the anodes, since the thermocouples are fixed, but the positions of the HFS may vary slightly. The absolute relative error was calculated based on the experimental values. Finally, the mean absolute relative error (MARE) was determined by calculating the average of all absolute relative errors. The MARE (expressed in %) helped to quantify the prediction accuracy when compared with the experimental value.

The MARE between the simulation and the temperatures determined with HFS was 4.7 % and it was 3.0 % when compared to the temperatures logged from the thermocouples (error calculated using the Kelvin scale). The MARE of temperature prediction in the anode cover (ACM-crust) was only 2.4 %. Accordingly, the combination between the latest thermal properties of the anode cover and the boundary conditions significantly helped to reach a high prediction accuracy using the thermal-electric model.

Table 6-8 Comparison between the general model and the temperature measurements performed on three instrumented industrial anodes

Instrument	Location	Temperature (°C)			*Error (%)
		Global average	Mid-life	Simulation	
HFS	ACM$_{SC}$	187	207	239	6.7
	ACM$_{OA1}$	313	327	323	-0.7
	ACM$_{OA2}$	288	258	300	7.9
	ACM$_{CC}$	298	296	315	3.3
	Deck	202	220	193	-5.5
	Stub	349	332	374	6.9
	Rod	250	239	248	1.8
Thermocouple	Stub,0	692	701	704	0.3
	Stub,top	377	372	374	0.3
	ACM-crust,0	781	793	759	-3.2
	ACM-crust,2.5	706	712	692	-2.0
	ACM-crust,5	640	646	614	-3.5
	ACM-crust,7.5	545	533	525	-1.0
	ACM-crust,10	448	418	401	-2.5
	Rod,10	303	298	268	-5.3
	Rod,20	279	275	244	-5.7
	Rod,30	253	250	223	-5.2
	Rod,40	228	224	202	-4.4

**Relative error between the simulation and the experimental data at mid-life (temperature error calculated using the Kelvin scale).*

The results of the simulation were compared with the experimental measurements at mid-life since anodes of this age were used in the model. Nevertheless, the MARE between the mid-life results and the global average was 1.9 % and the average error was -0.3 %. Therefore, there is only a small difference between the mid-life data and the average data taken throughout the life of the three anodes. Thus, the measurements on mid-life anodes adequately described the temperature distribution on the top AEC. It also confirms that the mid-life anodes used in the geometry of the numerical model allowed to represent properly the thermal behavior of an AEC.

The MARE between the predicted heat fluxes and the mid-life data was 17.1 % (Table 6-9). The numerical model globally underestimated the heat dissipation on the top parts. A part of the error may come from the measurement locations which vary slightly between each measurement, and also from the HFS accuracy of ± 15 %. The ACM and anode crust geometries in industrial AEC are characterized by a non-uniform surface which cannot be completely considered in the model.

The ACM_{SC} demonstrated a lower heat flux (1758 W/m^2) than the other parts of the ACM, which ranged from 2721 W/m^2 to 2871 W/m^2 according to the simulation. This lower heat flux is both due to the thickness of this part and because it remains attached to the side wall. Accordingly, the top of the $crust_{SC}$ is farther from the bulk liquid bath, while the other parts of crust follow the anode displacement toward the liquid bath.

Table 6-9 Comparison between the general model and the HFS measurements performed on three industrial anodes

Location	Heat flux (W/m^2)			*Error (%)
	Global average	Mid-life	Simulation	
ACM_{SC}	2043	2190	1758	-19.7
ACM_{OA1}	3537	3733	2858	-23.4
ACM_{OA2}	3873	2982	2721	-8.8
ACM_{CC}	3686	3358	2871	-14.5
Deck	4737	4756	3394	-28.6
Stub	10 669	10 213	10 031	-1.8
Rod	3763	4084	3153	-22.8

**Relative error between the simulation and the experimental data at mid-life.*

The heat transfer occurring in the cavity forming beneath the crust is difficult to measure experimentally due to the local high temperature and the chemical corrosiveness of the liquid bath and vapor. Hence, it is complex to install an HFS at this location. In the numerical model, the net incoming radiative flux on the closest node to the location indicated in Figure 6-4B was 4837 W/m^2, while the net outgoing radiative flux from the node in the liquid bath located directly below was 13 923 W/m^2. The radiation heat transfer leaving the liquid bath was also going toward the carbon anodes, which exhibited a temperature range between 910 °C and 966 °C on their surfaces facing the cavity. The convection heat transfer is expected to be negligible compared to radiation at these high temperatures. The integration of the cavity in finite element models allows a proper representation of the real conditions in industrial AEC and improves the heat transfer prediction, as previously demonstrated [Allard *et al.*, 2016]. Nevertheless, it would be possible to further improve the prediction by considering the heat transfer phenomena related to mass transport, such as liquid bath splashes, vapor penetration and gas passing through the empty spaces and cracks in the anode cover.

Effects of the ACM and the sludge on the heat balance of the AEC

The effect of the ACM thickness was evaluated with two other thermal-electric simulations. In the first simulation (less ACM) 2 cm were removed from the top of the ACM and in the second simulation (more ACM) 2 cm were added. The heat loss distribution in the slice of AEC is described in Table 6-10. For this study, the top parts are defined by the anode assembly and the anode cover, thus all the parts dissipating heat under the hoods. Since the deck dissipates heat toward the outside of the AEC, this part was included in the "side" category with the side wall (shell), the cradles, the cathode bars and the flexible conductors. The heat loss distribution in Table 6-10 does not include the heat dissipation by the superstructure, the hoods, the anode rod parts outside the AEC enclosure, nor the anode beam.

Considering the boundaries of the model, the top of the general model dissipated 35.9 % of the total heat losses, while 57.2 % left by the side parts. With less ACM, the top heat dissipation increased to 38.9 % (+3.0 %) and the side decreased to 54.3 % (-2.9 %). The inverse is observed with more ACM (-2.3 % for top and +2.3 % for side). Nevertheless, the bottom dissipation remained fairly constant, like the cathode bars and flexibles in Table 6-10. The increase of the thermal resistance of the top by the addition of ACM generated an increase of the heat dissipation by the anode rods, the deck, the side shell and the cradles. It also decreased the heat dissipation by the stubs and yoke, since in this case, they have less surface exposed to the ambient gas.

Secondly, the effect of the sludge on the heat loss distribution was investigated by adding a film of liquid bath supersaturated in Al_2O_3 all over the surface of the cathode blocks up to the interface between liquid aluminum and side ledge. A thickness of 2 mm for this film of sludge was considered based on the work of Coulombe *et al.* [Coulombe *et al.*, 2016a]. This thickness was measured during an autopsy of a stopped industrial AEC. This simulation case aims at describing an industrial AEC that is completely covered by a thin film of sludge, which could represent the operation of a problematic AEC. The sludge extracted from the industrial AEC was composed of 6.1 % $\alpha\text{-}Al_2O_{3(s)}$ into saturated liquid bath according to thermodynamic calculations. Assuming a mixing rule between the properties of $Al_2O_{3(s)}$ and liquid bath, an electrical conductivity of 207 S/m has been estimated [Coulombe *et al.*, 2016a]. For comparison, the electrical conductivity of the liquid bath is about 190 S/m when saturated in Al_2O_3 [Hives *et al.*, 1996]. The solidification temperature of the sludge was found to be similar to the bulk liquid bath (950 °C) due to the higher cryolite ratio at that specific location in the AEC [Allard *et al.*, 2014]. For this simulation, the thermal conductivity of the bath was applied to the sludge since no experimental data are available.

The sludge decreased the heat dissipation from the bottom by 0.2 % (from 6.9 % to 6.7 %) since it increases its thermal resistance. The sludge also increased the side heat dissipation by 1.4 % (from 57.2 % to 58.6 %) while the top decreased by 1.2 % (from 35.9 % to 34.7 %) when compared to the general model. The impact of the film of sludge was considerable on the side wall and cradle since an absolute increase of 1.7 % of the total heat losses was predicted for these parts only.

Table 6-10 Effects of the ACM thickness (from -2 cm to +2 cm) and the sludge on the heat loss distribution

Part		Heat loss distribution (%)			
		Less ACM	**General**	**More ACM**	**Sludge**
Top	Anode rod	4.7	5.1	5.5	4.9
	Stubs and yoke	14.7	14.2	13.6	13.7
	Anode cover (OA-CC)	17.0	14.4	12.6	13.9
	Anode cover (SC)	2.5	2.2	1.9	2.2
	Subtotal	**38.9**	**35.9**	**33.6**	**34.7**
Side	Top of deck	4.6	4.9	5.1	5.0
	Side wall and cradle	37.4	39.9	41.9	41.6
	Bars and flexibles	12.3	12.4	12.5	12.0
	Subtotal	**54.3**	**57.2**	**59.5**	**58.6**
Bottom	Bottom of shell and cradle	6.8	6.9	6.9	6.7

The heat fluxes on the top parts and the side shell were predicted with the thermal-electric model to quantify the impact of the ACM thickness and the presence of a film of sludge on the cathode surface. The resulting heat fluxes are shown in Table 6-11 using the locations described in Figure 6-5. The heat fluxes on the ACM obviously decreased with the ACM thicknesses (from -2 cm to +2 cm). However, the heat fluxes on the anode parts, the top of stub and the side of anode rod, increased with the ACM thickness. Even if the thermal constraints on the anode assembly increased, the top heat losses still decreased with the higher ACM thickness. Both the heat fluxes on the deck and the side shell, taken at the bath-metal interface (BMI), increased with the ACM thickness.

The sludge mainly increased the heat fluxes of the ACM_{SC} (from 1758 W/m^2 to 1850 W/m^2), the deck (from 3394 W/m^2 to 3582 W/m^2) and the side shell (from 11 712 W/m^2 to

13 050 W/m^2), when comparing the general model to the simulation with sludge. The heat fluxes in the other parts remained relatively constant.

Table 6-11 Effects of the ACM thickness (from -2 cm to +2 cm) and the sludge on the predicted heat fluxes

Location	Heat flux (W/m^2)			
	Less ACM	General	More ACM	Sludge
ACM$_{SC}$	2132	1758	1533	1850
ACM$_{OA1}$	3459	2858	2462	2888
ACM$_{OA2}$	3321	2721	2337	2724
ACM$_{CC}$	3435	2871	2501	2884
Deck	3200	3394	3528	3582
Stub	9213	10 031	10 803	10 070
Rod	2951	3153	3350	3133
Side shell at BMI	10 935	11 712	12 292	13 050

The temperature profile of the top parts is given in Figure 6-11 in order to demonstrate the predicted profiles of the side ledge and also the shape of the cavity. The starting location of the cavity$_{SC}$ (the part closest to the side wall) did not directly connect with the top of the side ledge, since both materials have different melting temperatures (anode crust = 935 °C and side ledge = 950 °C). Also for this reason, it is possible to observe a cavity above the frozen bath layer located in the SC.

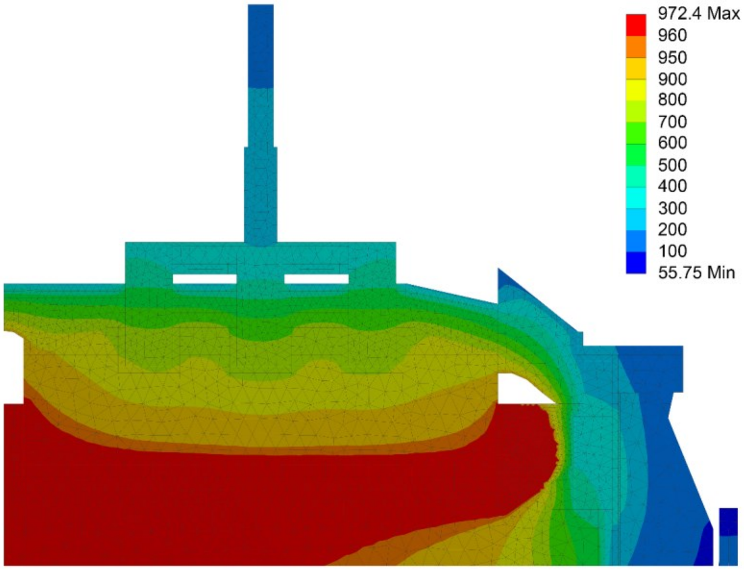

Figure 6-11 Temperature profile (°C) of the top parts predicted with the general model

The effects of the ACM and the sludge on the side ledge thickness, on the height of the cavity and on the electric potential are described in Table 6-12. The results in % expressed a difference from the reference simulation (general model). The electric potential calculated by the thermal-electric model, without considering the electrochemical potential, varied from -0.05 % (-2 cm) to 0.08 % (+2 cm) when increasing the ACM thickness. The electric potential increase can be explained by the amplified thermal constraint on the anode assembly. The electrical resistivity of the metallic conductors increases with the temperature, thus explaining this behavior. The side ledge thickness measured at the bath-metal interface changed with the ACM thickness, from 10.1 % at -2 cm of ACM to -15.0 % at +2 cm. The height of the cavity$_{SC}$ increased from 7.6 cm to 9.7 cm, at the location in Figure 6-4B, when increasing the ACM thickness from -2 cm to +2 cm. Only by adding 2 cm of ACM, the total volume of the cavity in the whole AEC increased from 0.430 m^3 to 0.476 m^3 (+10.7 %), corresponding to 115 kg of anode crust which can have melted into the AEC ($\rho_{bulk,crust}$ = 2500 kg/m^3) [Allard *et al.*, 2019a]. The growth of the cavity may have an effect on the sludge formation, if the anode crust is not dissolved by the bulk liquid bath and then reaches the surface of the cathode blocks.

The electric potential increased by 4.08 % with the 2 mm of sludge, when compared to the general model and considering only the ohmic resistance in the slice of AEC. The film of sludge increased the CVD located at the aluminum to cathode blocks interface. Moreover, the increased heat generation due to joule heating at this location generated a larger cavity (+10.5 %), resulting in the melting of 113 kg of anode crust. Accordingly, the sludge generates a larger cavity due to increased heat generation which may consequently result in more sludge on the cathode blocks surface, when the anode crust is not dissolved. The increased heat generation caused by the sludge also modified the side ledge shape, reducing its length at the bottom. In industrial AEC, the sludge demonstrates a different behavior than the bulk liquid bath when it solidifies. In saturated bath, the deposition of α-$Al_2O_{3(s)}$ firstly occurs and is followed by the solidification of Na_3AlF_6 [Allard *et al.*, 2015a]. In the case of a film of bath saturated in Al_2O_3, a ledge toe is expected to grow by both deposing α-$Al_2O_{3(s)}$ and Na_3AlF_6 next to the side wall, thus forming a persistent deposit. The growth of the ledge toe and side ledge next to the liquid aluminum is dependent on the local concentration of AlF_3, CaF_2 and Al_2O_3, which can be different than inside the bulk liquid bath.

Table 6-12 Effects of the ACM and the sludge on the side ledge, cavity and electric potential, compared to the general model

Simulation	Less ACM	General	More ACM	Sludge
Side ledge at BMI (%)*	10.1	ref.	-15.0	-15.0
Volume of side ledge (%)*	9.1	ref.	-14.9	-21.0
Height of cavity$_{SC}$ (cm)	7.6	8.4	9.7	9.8
Volume of cavity in AEC (m^3)	0.388	0.430	0.476	0.475
Volume of cavity in AEC (%)*	-9.8	ref.	10.7	10.5
Electric potential (%)*	-0.05	ref.	0.08	4.08

Implication of the results for the aluminum industry

In-field validation of thermal properties and boundary conditions

In order to develop the thermal-electric model and to validate its accuracy, three campaigns of industrial measurements were performed using instrumented anodes. The ACM and anode crust profiles were measured to obtain the proper geometry for the mid-life anodes. In previous work, some anode crust samples were extracted to evaluate their thermal properties with laser flash analysis [Allard *et al.*, 2019a]. The thermal conductivity of the anode crust was validated in this study with another methodology implying HFS and thermocouples installed in the anode crust and ACM of industrial AEC. The emissivity of both ACM and anode crust was determined with a calibrated IR camera and was found to be very close to 1.0, a value slightly higher than the reference paint. In the literature, a previous calculation of this property has been made with a thermal balance applied on the anode crust made in the laboratory [Rye *et al.*, 1995], but the emissivity was found to be significantly different compared to the industrial materials investigated in this study (Figure 6-7).

The boundary conditions in the top parts of the AEC were determined by considering the whole life of three anodes. The gas temperature was found to increase quickly when entering in the AEC top enclosure (from ~40 °C to ~100 °C) and slowly above the ACM$_{SC}$ up to the ACM$_{CC}$ (from ~100 °C to ~140 °C). The thermal-electric prediction was validated with the HFS and thermocouples installed on the industrial anodes. The prediction accuracy (considering the MARE) for the temperatures was 4.7 % compared to the HFS (manual measurements) and 3.0 % compared to the thermocouples from the instrumented anodes. The prediction accuracy of the temperatures in the ACM and anode crust was 2.4 % when compared to the thermocouple measurements. The temperatures at the ACM-anode crust interface (657 °C ± 19 °C) was very close to the irreversible transformation temperature of ACM to anode crust (starting from 685 °C to 696 °C depending on local conditions). In summary, the in-field validation performed on industrial AEC quantified the difference between the simulation and the experimental measurements, thus allowing to develop a more accurate thermal-electric model to investigate operating parameters.

Relationship between the top and the side heat losses

The effect of the top heat losses on the side heat dissipation was investigated by changing the ACM thickness. The addition of a small quantity of ACM (2 cm) influences the heat balance by reducing the top heat losses by 2.3 %. Since both the bottom heat dissipation and heat generation only varies slightly in this case, the top heat dissipation is transferred to the side parts. The side ledge adapts itself to the increased insulation of the top by melting (reversible transformation of Equation 6-10). However, the ACM and anode crust are two phase change materials characterized by irreversible phase transformations (Equation 6-8 and Equation 6-9). Accordingly, the ACM and anode crust cannot return to their initial states after such change in the operating conditions, thus generating a new thermal equilibrium. In the case of increased heat generation, both the anode crust-cavity and the ACM-anode crust profiles will be moved upwards, thus resulting in a more conductive anode cover.

The thermal behavior of the AEC must be closely monitored to ensure an optimized operating performance. The protective layer of side ledge has to be maintained during the whole life of the industrial AEC. However, it is complex to perform intrusive measurements of ledge thickness. The thermal-electric simulation demonstrated that side heat dissipation depends on the top thermal insulation. The bottom heat losses are generally constant for a given AEC design and cathode blocks wear, but they still decrease very slightly when sludge is covering the cathode blocks surface. Since a relationship was found between the top and side heat losses, a ratio of heat loss distribution can be calculated in order to help monitoring the thermal behavior of the industrial AEC. The ratio of top heat losses (q_{top}) on the side heat losses (q_{side}) may help to diagnose problematic AEC when an improper anode covering has been performed or when the anode cover is deteriorated. The q_{top} / q_{side} ratio was also found to be proportional to the heat fluxes at ACM$_{OA2}$ ($q''_{ACM_{OA2}}$) and at the side shell BMI ($q''_{Shell_{BMI}}$). The numerical correlation in Equation 6-13 can determine the q_{top} / q_{side} ratio with an absolute relative error of 0.2 %, calculated with all the simulation results in Table 6-10 and Table 6-11. A factor of 1.3 was calculated by minimizing the absolute relative error.

$$\frac{q_{top}}{q_{side}} = 1.3\sqrt{\frac{q''_{ACM_{OA2}}}{q''_{Shell_{BMI}}}} \tag{6-13}$$

This numerical correlation fits the simulation results well, considering the current simulated cases. Nevertheless, this correlation should be validated with other designs and technologies in order to obtain a robust indicator of the thermal dissipation of industrial AEC. A general correlation is given in Equation 6-14, where *f* is a factor which depends on the AEC design, *q* is the heat transfer rate (W or %) and *q''* is the heat flux taken at specific locations (which must remain the same for all technologies).

$$\text{Heat balance indicator: } \frac{q_{top}}{q_{side}} = f\sqrt{\frac{q''_{ACM}}{q''_{Shell}}} \tag{6-14}$$

Effect of the anode crust deterioration on the sludge formation

The anode crust is deteriorated by the anode beam displacement which generates a mechanical stress. This material melts at a temperature close to the melting point of Na_3AlF_6, which depends on the local chemical composition. The melting temperature of the anode crust was determined with the phase diagram, but it was also validated by measuring the temperature at the bottom of the anode crust in industrial AEC. Considering an anode crust of typical composition, its structure is weakened from 935 °C and over, since all the bath phases are melted in these conditions. At this temperature, the liquid bath splashes also deteriorate the anode crust bottom, while at a lower temperature these splashes could have frozen depending on the local chemical, mass and heat transfer phenomena. In industrial AEC, the operating events which generate an increase in heat generation cause the melting of the anode crust, consequently this material will drop toward the bulk liquid bath.

The sludge can be formed by the overfeeding of Al_2O_3, falling of the anode crust during anode replacements or melting of anode crust caused by a higher heat generation. Considering a bulk liquid bath saturated in Al_2O_3, the industrial AEC can enter in a vicious cycle of anode crusts melting and sinking toward the cathode blocks, which lead to sludge production. The sludge itself produces a higher heat generation by Joule heating, thus leading to additional melting of anode crust and so on. The integration of the cavity module in the thermal-electric model helps to predict the behavior of the AEC in order to better understand these operating problems.

6.2.6 Conclusions

An improved thermal-electric model considering an adaptive geometry of the cavity and improved thermal properties of the anode crust was validated by heat flux and temperature measurements performed on industrial AEC. A general geometry of ACM and anode crust was determined by performing profile measurements on mid-life anodes. The effective thermal conductivity of the anode crust was 0.90 W/m·K at a temperature of 752 °C based on thermal measurements performed on an industrial AEC. The emissivity of both ACM and anode crust was found to be close to 1.0 according to IR thermography. The thermal-electric modeling demonstrated the effect of the ACM thickness on both the top and side heat dissipation. A small addition of 2 cm of ACM decreased the top heat losses by 2.3 % (from 35.9 % to 33.6 % of the total dissipation), while the side dissipation increased by 2.3 % (from 57.2 % to 59.5 %). Moreover, the size of the cavity increased by 10.7 %, implying the melting of 115 kg of anode crust in the whole AEC, which would fall into the liquid bath. A simulation was performed with a film of sludge on the cathode blocks, which demonstrated an increase of the electric potential loss due to ohmic resistance of 4.08 %, thus increasing the CVD and the heat generation. Finally, the heat balance of industrial AEC can be quickly approached with a numerical correlation based on the measurement of the heat fluxes at two key locations on the AEC. Nevertheless, further works are needed to adapt the correlation to other AEC technologies.

6.2.7 Acknowledgements

This study was supported by Rio Tinto Aluminium, the “Conseil de Recherches en Sciences Naturelles et en Génie du Canada” (CRSNG) and the “Fonds de Recherche du Québec - Nature et Technologies” (FRQNT). The authors wish to thank the Rio Tinto Grande-Baie smelter and more specifically the Arvida Research & Development Center staff, especially Mr. Jean-François Bilodeau and Mr. Sébastien Guérard, for the support provided during the realization of this work.

6.2.8 Appendix A

The prediction of the crust-cavity interface was programed with Python 2.7 and APDL scripting language in ANSYS Mechanical. The procedure shown in Figure 6-12 is repeated until the local temperatures at the crust-cavity interface reach the melting isotherm.

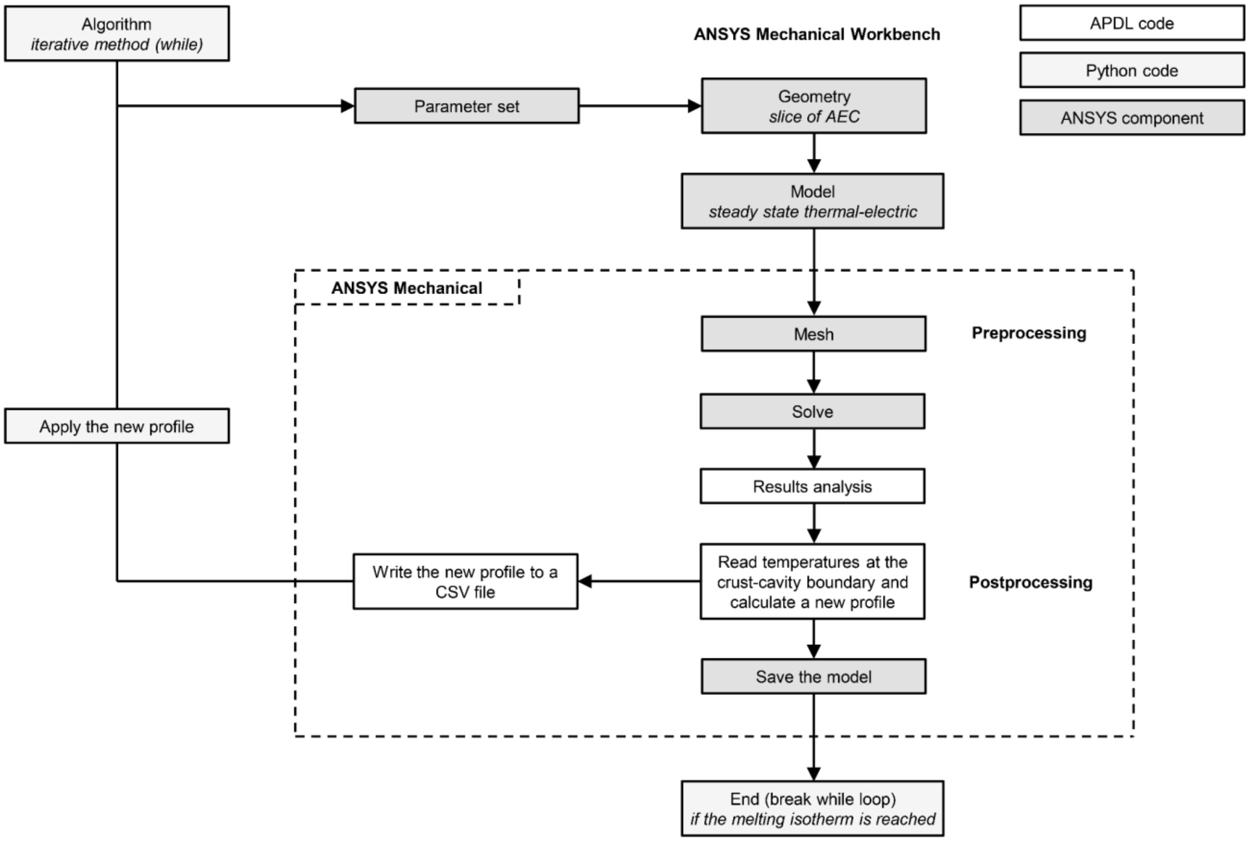

Figure 6-12 Scheme of the modeling algorithm to solve the steady state thermal-electric model with the computation of the crust-cavity interface

CHAPITRE 7 MODÉLISATION THERMIQUE-ÉLECTRIQUE EN RÉGIME TRANSITOIRE

7.1 Avant-propos

Auteurs et affiliation :

François Allard : étudiant au doctorat, Département de génie chimique et génie biotechnologique, Université de Sherbrooke, Québec, Canada.

Martin Désilets : professeur titulaire, Département de génie chimique et génie biotechnologique, Université de Sherbrooke, Québec, Canada.

Alexandre Blais : scientifique de recherche, Rio Tinto Aluminium, Centre de recherche et développement Arvida, Québec, Canada.

État de l'acceptation : En révision (soumis le 26 septembre 2018).

Revue : *Metallurgical and Materials Transactions B*.

Référence :

Allard, F., Désilets, M. et Blais, A. A modeling approach for time-dependent geometry applied to transient heat transfer of aluminum electrolysis cells. *Metallurgical and Materials Transactions B*, en révision.

Lien d'accès : -

Contributions à la thèse :

Afin de démontrer l'évolution de la dissipation thermique par le dessus des cellules d'électrolyse, durant toute la vie de l'anode, une stratégie de modélisation transitoire considérant les variations temporelles du domaine a été établie. Un algorithme permettant de déplacer la géométrie, de mettre à jour le maillage et d'interpoler les températures a été programmé et intégré dans la stratégie de modélisation par éléments finis du problème thermique-électrique transitoire des cellules d'électrolyse. Grâce à ce modèle, il a été possible de prédire les températures et potentiels électriques tout au long de la vie de l'anode industrielle. Les prédictions ont aussi été validées par des anodes instrumentées placées dans des cellules d'électrolyse en opération. Ce chapitre contribue à la thèse en présentant les points suivants :

- Une nouvelle approche de modélisation transitoire par éléments finis est appliquée à deux problèmes de simulation, soit : 1) l'impact d'une augmentation de potentiel électrique d'opération sur une longue période et 2) l'évolution thermique et électrique d'une anode durant tout son cycle de vie. Les diagrammes expliquant le fonctionnement de la stratégie de modélisation sont fournis par cette étude.

- Les toutes dernières propriétés thermiques transitoires de la croûte d'anode (k et c_p déterminés entre 100 °C et 950 °C) ont été intégrées dans ce modèle. Avec ces propriétés thermiques et cette stratégie de modélisation, il a été possible de prédire la température dans la croûte d'anode avec une précision allant jusqu'à 1.2 %, en se comparant avec les thermocouples installés dans ce matériau.
- L'augmentation de la cible du potentiel électrique d'opération, en augmentant physiquement la distance entre l'anode et la cathode électrochimique, a causé : 1) la fonte supplémentaire de croûte d'anode dans la cellule d'électrolyse, 2) la transformation supplémentaire d'*ACM* en croûte d'anode et 3) le rétrécissement du talus sur la paroi latérale. Comme les transformations *ACM* → croûte d'anode → cavité sont irréversibles et que le talus est un matériau réversible, cette excursion thermique a produit un recouvrement anodique plus conducteur. Avec le retour à un potentiel électrique typique, le talus a cru continuellement jusqu'à l'atteinte d'une taille plus importante qu'initialement, engendrant ainsi une nouvelle distribution de la dissipation thermique.
- Finalement, ce modèle transitoire présente par un vidéo : 1) la formation de la cavité, 2) la rupture entre la croûte d'anode du couloir latéral et celle située sur l'anode et 3) la géométrie de la consommation de l'anode. Considérant ces facteurs, la distribution de températures durant toute la vie de l'anode est prédite. La stratégie de modélisation transitoire a permis de prédire avec une erreur relative absolue moyenne de 2.7 %, en comparant avec les mesures de températures acquises de façon continue sur les pièces de l'ensemble anodique (tige d'anode, rondins et traverse) et dans le recouvrement anodique.

Titre français :

Une approche de modélisation considérant les variations géométriques en fonction du temps appliquée au transfert thermique transitoire de cellules d'électrolyse d'aluminium

Résumé :

Le bilan thermique des cellules d'électrolyse d'aluminium doit être rigoureusement contrôlé afin d'améliorer l'efficacité et la durabilité de ce procédé industriel. Une nouvelle stratégie de modélisation est développée pour considérer les déplacements de géométries solides et les frontières mobiles dans les modèles d'éléments finis. La modélisation thermique-électrique transitoire de la cellule d'électrolyse démontre l'effet d'une augmentation de la tension électrique d'opération à la fois sur le recouvrement anodique et sur le talus. Avec une génération d'énergie supplémentaire, la croûte d'anode se détériore et l'épaisseur du talus diminue. Comme les matériaux de recouvrement anodique sont caractérisés par des transformations irréversibles, la dissipation thermique par le dessus demeure plus élevée même lorsque le potentiel électrique d'opération revient à sa valeur typique. Pour la première fois, les températures et les potentiels électriques sont simulés pour toute la vie de l'anode de carbone et aussi validés par des mesures industrielles. Les prédictions de modélisation ont été validées à partir d'anodes instrumentées et de mesures manuelles, toutes ces mesures ont été réalisées sur une cellule d'électrolyse en opération.

7.2 A modeling approach for time-dependent geometry applied to transient heat transfer of aluminum electrolysis cells

Keywords: Heat transfer, thermal-electric modeling, finite element method, adaptive mesh, anode, aluminum electrolysis

7.2.1 Abstract

The thermal balance of aluminum electrolysis cells (AEC) have to be rigorously controlled in order to improve the efficiency and sustainability of this industrial process. A new modeling strategy is developed to consider the displacements of solid bodies and moving boundaries in finite element models. The transient thermal-electric modeling of the AEC demonstrates the effect of an increase in operating voltage on both the anode cover and the side ledge. With higher heat generation, the anode cover deteriorates and the side ledge thickness decreases. Since the anode cover is characterized by irreversible transformations, the top heat dissipation remains higher even when the operating voltage comes back to its typical value. For the first time, the transient temperature and electric fields throughout the anode life are simulated and validated by industrial measurements. The modeling predictions have been validated from instrumented anodes and manual measurements, all performed on operating AEC.

7.2.2 Introduction

The aluminum electrolysis process is continuously improving in order to reach a better energetic efficiency and environmental balance, while increasing the production at the same time. To achieve these goals, the design of the aluminum electrolysis cells (AEC) is optimized by performing modeling and experimental investigations. The industrial aluminum production is carried out by reducing alumina (Al_2O_3) with carbon anodes in a liquid electrolytic bath. The liquid bath is primarily composed of a mixture of Na_3AlF_6 (cryolite), AlF_3 (aluminum fluoride), CaF_2 (calcium fluoride) and dissolved Al_2O_3, but it usually also contains additives in the form of lithium, potassium and magnesium fluoride salts. Equation 7-1 is the overall electrochemical reaction occurring in AEC [Thonstad *et al.*, 2001]:

$$2\ \mathrm{Al_2O_{3(dissolved)}} + 3\ \mathrm{C_{(s)}} \xrightarrow{\text{current}} 4\ \mathrm{Al_{(l)}} + 3\ \mathrm{CO_{2(g)}} \tag{7-1}$$

The liquid aluminum is continuously produced by the electrochemical process and is extracted periodically by siphoning during industrial operations. Carbon dioxide (CO_2) is produced by the reaction of oxide ions at the surface of the carbon anodes immersed in the liquid bath. In order to feed the electrochemical reaction, an electric current is supplied to the AEC and is divided between the several consumable carbon anodes. The total current intensity varies from 200 kA to 600 kA depending on the technology. The main components of the AEC are described in Figure 7-1.

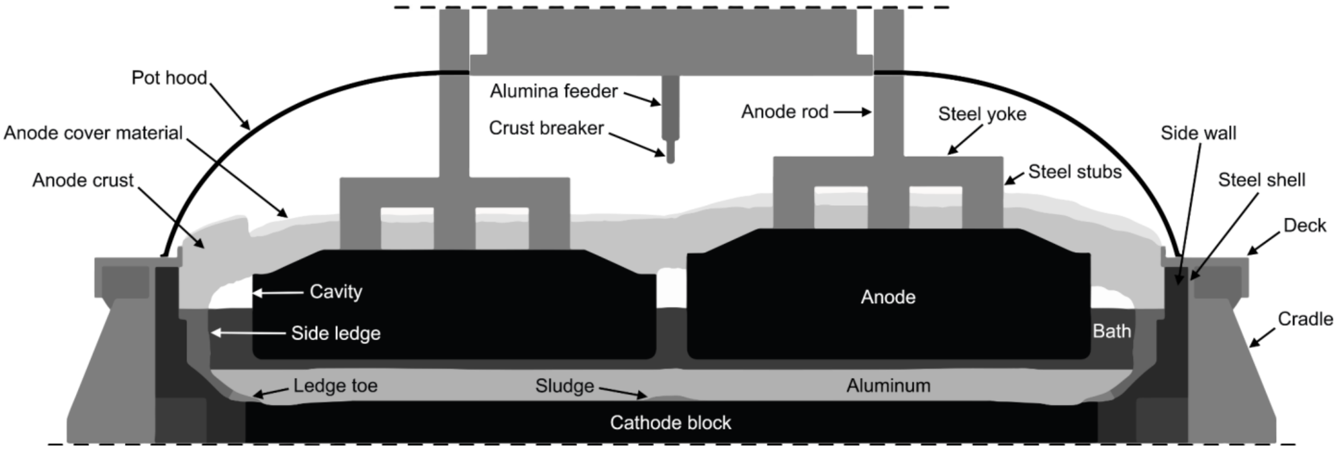

Figure 7-1 An aluminum electrolysis cell with its main components

The heat balance of the AEC is rigorously controlled in order to maintain a protective layer of frozen bath, usually called side ledge, on the side walls. This layer protects the side components from the highly corrosive and erosive behavior of the liquid bath. The thermal conductivity of the side ledge has been recently determined by laser flash analysis at temperature up to 550 °C [Poncsák *et al.*, 2014, 2015; Gheribi *et al.*, 2017]. The side ledge grows by the primary crystallization of the Na_3AlF_6 at a temperature close to 950 °C, while the AEC operates with a bulk liquid bath at around 965 °C. The side ledge formed at equilibrium conditions demonstrates a composition close to pure Na_3AlF_6, while with higher cooling rate the AlF_3, CaF_2 and Al_2O_3 species from the bath can be trapped inside its microstructure [Fallah-Mehrjardi *et al.*, 2014; Allard *et al.*, 2015a; Poncsák *et al.*, 2017]. A ledge toe is also formed on the cathode blocks by both the solidification of Na_3AlF_6 and the precipitation of Al_2O_3 at temperature also close to 950 °C, depending on the local chemical composition [Allard *et al.*, 2015a]. When the AEC is quickly cooled down, the side ledge grows by forming an open crystalline layer, in which mass transfer can occur with the bulk liquid bath [Liu *et al.*, 2017]. The side ledge and ledge toe are modeled with their typical composition, thermal property and behavior, which is expected to be close to chemical equilibrium.

Since the carbon anodes are consumed by the electrolysis process, they must be replaced after a few weeks of operations. The anode change procedure consists of breaking the anode crust, removing the old anode and installing a new one. During the first hours of the newly set anode, the top part of the liquid bath surrounding this anode is freezing in contact with colder gas. Once a "top freeze" layer of a few centimeters is formed, the anode cover material (ACM) is poured on the carbon anode and in the channels around the new anode. The ACM is leveled to prevent the oxidation of the carbon anode and to insulate the top of the AEC. Subsequently, the temperature increases at the bottom of the anode cover due to its insulating property, up to a point where the top freeze layer melts. At this step, the liquid bath from the electrolysis cell begins to rise in the powdered ACM by capillary forces. The ACM is transformed into anode crust when in contact with the liquid bath and vapor coming from the cell, at a temperature range between 685 °C to 710 °C depending on the local conditions [Zhang *et al.*, 2015; Allard *et al.*, 2019a, 2019b]. Once formed, the hard anode crust is composed of α-Al_2O_3 particles cemented together with solid or liquid bath [Allard *et al.*, 2015b; Less, 1977; Liu *et al.*, 1992]. The anode crust should remain in place during all the life of the carbon anode, but its structure deteriorates due to liquid bath splashes and vapor penetration from beneath. At a temperature close to 935 °C, all the bath phases composing the anode crust are liquid and only the network of Al_2O_3 particles supports this material. Consequently, a cavity filled with fumes and gases will be formed when this part melts and collapses [Allard *et al.*, 2016].

The anode cover of AEC is defined by two distinct parts: the ACM located above and the anode crust underneath. The ACM typically consists of alumina, electrolytic bath and recycled anode crust which have been crushed into particles of fine to coarse granulometry. The thermal properties of the ACM and anode crust have been investigated by several researchers [Llavona *et al.*, 1988, 1990; Hatem *et al.*, 1989; Rye *et al.*, 1995; Shen, 2006; Wijayaratne *et al.*, 2011; Allard *et al.*, 2019a]. The thermal conductivity of the ACM increases with both the temperature and the bulk density [Llavona *et al.*, 1988; Shen, 2006; Wijayaratne *et al.*, 2011]. The composition of the ACM affects the thermal conductivity of the anode crust, since a higher proportion of crushed bath in the initial mixture forms an anode crust of higher thermal conductivity [Rye *et al.*, 1995]. Unlike the ACM, anode crusts sampled in industrial cells demonstrate a slight decrease of thermal conductivity with increasing temperature [Llavona *et al.*, 1990]. Recent work reported the thermal conductivity of industrial anode crust measured by the laser flash method, which decreases from 1.38 W/m·°C to 0.89 W/m·°C at temperatures ranging from 100 °C to 950 °C [Allard *et al.*, 2019a]. The emissivity of the ACM and anode crust has been evaluated experimentally and showed a value close to a black body [Allard *et al.*, 2019b]. The recent efforts to improve the thermal properties and geometries of the ACM and anode crust enable better predictions obtained with heat transfer models in steady state [Allard *et al.*, 2019b].

The design and operation of AEC have been investigated by various numerical models taking into account different phenomena. Modeling of the mechanical stresses in the cell components, their heat generation and dissipation, the magnetohydrodynamic flow, the voltage drops in conductors and the mass transfer in the liquid electrolyte have been investigated by many researchers [Hou *et al.*, 1995; Dupuis and Bojarevics, 2005; Safa *et al.*, 2009; Marceau *et al.*, 2011; Blais *et al.*, 2013; Ariana *et al.*, 2014; Bardet *et al.*, 2016; Langlois *et al.*, 2015]. However, most models that relate to thermal-electric modeling are in steady state and use a simplified representation of the anode cover. The thermal-electric modeling in transient state was applied to both preheating and cooling of stopped AEC [Désilets *et al.* 2003; Brimmo *et al.*, 2014; Marceau *et al.*, 2011]. More recently, a 2D finite difference model of the anode cover was built to investigate the transient heat transfer and the effect of the liquid bath temperature on the first days of the crust formation [LeBreux *et al.*, 2016]. The impact of the anode change on the temperature profile and fluid flow, considering the first day of anode life, was investigated with computational fluid dynamics (CFD) simulations [Wang *et al.*, 2016]. A frozen bath layer is formed on the cold anode when it is inserted into the liquid bath. Its crystalline microstructure is rather heterogenous and presents large pores caused by entrapped gas and shrinkage of the sample, according to scanning electron microscopy and tomography analyzes [Picard *et al.*, 2017].

The top parts of the anode assembly and cover are cooled by air from the potroom (a large building housing the AEC) that enters through the gaps between the pot hoods due to the negative pressure created by the pot ventilation system. The top heat losses increase when the pot ventilation rate is raised, while the gas temperature leaving by the duct will reduce [Abbas *et al.*, 2009]. The convection coefficients applied to the top parts depend on the volumetric flow rate of gas collected from the pot according to CFD simulations [Zhao *et al.*, 2013]. The convection heat transfer can be varied by adjusting the gas flow rate, but a sufficient pot tightness must be kept to avoid leakage of harmful gases to the environment [Zhao *et al.*, 2017]. In the computation of flow or fluid-structure interaction, automatic mesh update strategies were previously developed and integrated for these numerical problems [Johnson and Tezduyar, 1994; Stein *et al.*, 2004]. The moving mesh or automatic remeshing allows to resolve problems with moving parts, boundaries and interfaces. However, these techniques are still not available for the thermal and electric models solved with the finite element method, to the authors' knowledge. A modeling approach for moving boundaries and time-dependent geometry is developed to resolve the heat transfer and electric conduction taking place in the industrial electrolysis cell.

The goal of thermal-electric modeling is to optimize the design and operation of AEC in order to reach higher efficiency. While the steady state analysis is useful to predict the overall behavior of an AEC, the transient analysis enables the investigation of time-dependent phenomena. In this study, two transient thermal-electric models are developed to: 1) predict the effect of an electric potential (voltage) increase on the heat balance and 2) evaluate the behavior of an anode throughout its life cycle. The first numerical model quantifies the effect of a voltage increase on both reversible and irreversible phase change materials, which control the thermal behavior of the electrolysis cell. Moreover, industrial measurements of electric potentials, material thicknesses and temperatures were performed in industrial AEC to validate the model's predictions. A second transient thermal-electric model is developed in order to predict the thermal dissipation and the dynamic of the anode cover during the anode life cycle. This new model uses a mathematical algorithm to account for the anode consumption and movement in time, while solving the heat and electric conduction. Since this domain is time-dependent, a strategy is developed for the moving geometry, mesh update and nodal interpolation and is applied to the numerical model. Finally, the prediction results are thoroughly validated with continuous measurements from instrumented anodes installed in an industrial AEC.

7.2.3 Transient thermal-electric models

The transient thermal-electric models predicted the heat transfer and electric potentials of a P155 prebake cell. The simulations were validated by measurements in industrial cells operated by Rio Tinto's Grande-Baie plant. The measurements have been obtained during the fall season and no special events were noticed during the operation of the AEC. Two instrumented anodes were continuously monitored during their operation for the purpose of this study. One evolved with normal conditions, while the other experienced a voltage increase (defined as “voltage treatment” for this study).

The steady state modeling method and the thermal properties of the top parts have been recently enhanced in a recent work; these articles may be consulted for further details [Allard *et al.*, 2019a, 2019b]. These improvements were also applied to the transient models presented here. The modeling methodology will be described with a peculiar emphasis on new modeling methods and thermal properties. The following two transient models, with a geometry and mesh updating algorithm, are developed and detailed in this study:

1) Slice of AEC
2) Anode life cycle

Geometry of the slice of AEC

The domain for the first model is a slice of an industrial AEC containing one and a half anodes and two cathode blocks. The heat transfer and the electric field are predicted inside the following boundaries: from the top of the anode cover, including anode assemblies, to the bottom of the AEC with its steel shell and cradles (shown in Figure 7-2). The top parts include the anode assembly (anode rod, yoke, stubs and carbon anode) and the anode cover (ACM and anode crust). A cavity located between the anode crust and the bulk liquid bath is integrated in the geometry. The cavity extends all around the anodes: in the side channel (SC), between the anodes and in the center channel (CC). The superstructure, anode beam and hoods are excluded from the slice geometry which comprises most parts of an industrial AEC, starting from the anode rod to the flexible conductors on the collector bar. For this model, mid-life anodes are used to replicate the overall behavior of the industrial AEC.

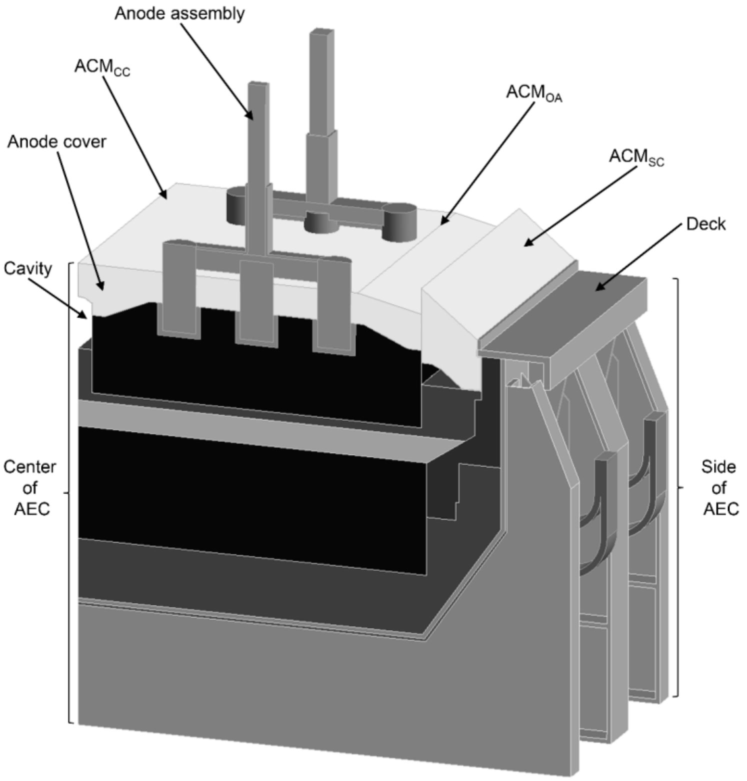

Figure 7-2 The slice geometry for an aluminum electrolysis cell, as used for the first model

The ACM and anode crust profiles on mid-life anodes were measured in industrial cells with an experimental device using the method shown in Figure 7-3A. A steel bar was positioned at each location required to measure the surfaces of ACM and anode crust. The deck was the reference point to locate the absolute height of these materials. The height of the cavity was measured by drilling a hole at the location (B) in order to validate the model prediction. The crust-cavity interface (C) is predicted by the transient model, at each analysis step, to take into account the anode crust deterioration. This boundary moves according to the heat balance and the thermal excursions occurring in AEC, which increase the local temperature and cause the melting of the anode crust.

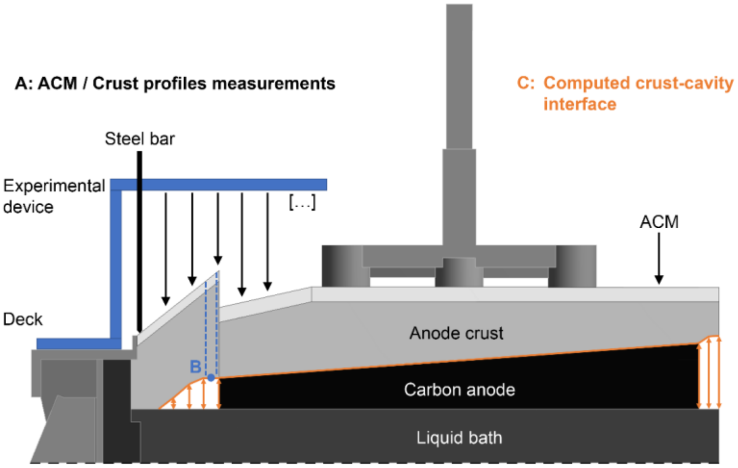

Figure 7-3 A) ACM and anode crust profiles measurements methodology in industrial cells. B) ● indicates the location where the height of the cavity was measured. C) The crust-cavity interface facing the bulk liquid bath which is calculated for each model

The anode crust in industrial cells can typically be divided into two distinct parts, the breaking point being located at the extremity of the carbon anodes, toward the side of the pot. The anode beam movement generates mechanical stresses on the anode crust resulting in the formation of the crust$_{SC}$ (see Figure 7-2), which remains attached to the side wall throughout the anode life. The shape of crust$_{SC}$ is similar to a "step" after a few days of the anode life. The crust on the anode (OA) and crust$_{CC}$ are linked to the anode and follow its movement.

The top geometry of the anode cover is set based on previous measurements of mid-life anodes in industrial AEC [Allard *et al.*, 2019b]. The angles for the top surfaces of the anode cover are given in Table 7-1. The distribution of both ACM and anode crust in the anode cover is calculated by the transient model and it depends on the corresponding transformation temperature range. Thus, the profiles of ACM and anode crust are predicted by the transient model.

Table 7-1 Geometric parameters of the anode cover of mid-life anodes

***Angle (°)**	
ACM$_{SC}$	**ACM$_{OA}$**
35	15

**Angle from the horizontal*

The bottom surface of the anode crust is complex to measure due to the local conditions: high temperature, harmful gas and corrosive bath splashes. Accordingly, the crust-cavity profile is predicted with transient modeling. This profile is time-dependent when the steady state conditions no longer apply, such as during voltage change or anode consumption. A new geometry of crust is calculated after each analysis step to consider the melting of the anode crust. The new geometric parameters of the crust bottom surface are modified automatically in the computer-aided design (CAD) tool to feed the next step.

Modeling method for the slice of AEC

The thermal balance of AEC mainly relies on the heat generation due to Joule heating effect and its dissipation to the environment. The electric current enters from the top conductors and leaves through the collector bars, but the heat generation is mainly produced in the resistive liquid bath located between the anode and the cathode. The transient heat transfer is predicted with the coupled thermal-electric model applied to the slice of AEC (Figure 7-2). This model is resolved with the finite element method and the domain is discretized into approximately 700 000 elements with midside nodes (tetrahedrons). The commercial software ANSYS Mechanical (release 18.0) was used to perform the thermal-electric calculations using an Intel Xeon E5-1650 v4 with 32 GB ECC memory.

A cavity is added in the model to consider the geometric aspects of the anode cover and to improve the heat transfer prediction. Figure 7-3C demonstrates the crust-cavity boundary, where radiation heat transfer is calculated. The cavity is integrated with a radiosity module that calculates the outgoing radiative flux for each surface (carbon anodes, liquid bath and bottom of the anode crust). This module is solved in conjunction with the thermal-electric problem. The crust-cavity interface is displaced based on the melting temperature of the chemical compounds in the anode crust. Accordingly, a moving boundary located at the bottom of the anode crust is displaced to reach the melting isotherm in the domain according to the predicted nodal temperatures. Then, the prediction of the crust-cavity profile allows to quantify the impact of operating parameters on the heat loss distribution.

The temperatures and electric fields are predicted by a step-by-step method which is automated using Python 2.7 scripting language in ANSYS Workbench. The programmed method updates the geometry and the mesh, and then applies the temperatures from the previous step to the new mesh. The detailed explanations of the modeling procedure can be found in Appendix A (see Figure 7-17). The model can be initialized from a previous steady state prediction by importing the nodal temperatures or by performing a new transient analysis. In summary, the model calculates the nodal temperatures and electric potentials for a given analysis time and export these results to the next geometry with a new crust-cavity profile. The exported nodal results contain the locations (*x*, *y*, *z*) and the temperatures (*T*) and these values are applied to the new generated mesh as initial conditions mapped with a 3D interpolation method. This procedure is repeated up to the final time of the analysis. The irreversible ACM to anode crust transformation is also integrated in the modeling algorithm by saving the previous material states of the elements in a file and by applying the values to the newly generated elements. The geometry and mesh update method described in this study is not subject to the problem of mesh distortion. However, this problem can be expected to happen with a moving mesh method, as described in [Reddy and Gartling, 2010].

Geometry for the anode life cycle modeling

The anode life cycle is modeled using the top parts of the AEC (see Figure 7-4) in order to investigate the thermal dissipation and the evolution of the anode cover. An industrial AEC contains many anodes and its thermal behavior depends on the overall top heat losses, thus the bath and ledge temperatures need to be first predicted using the previous model of the slice of AEC. A steady state analysis has been performed to get the temperature profile in the bulk liquid bath and the side ledge. These results were applied by nodal constraints in the bath of the anode life cycle model. The profiles of ACM and anode crust are also predicted with this transient model.

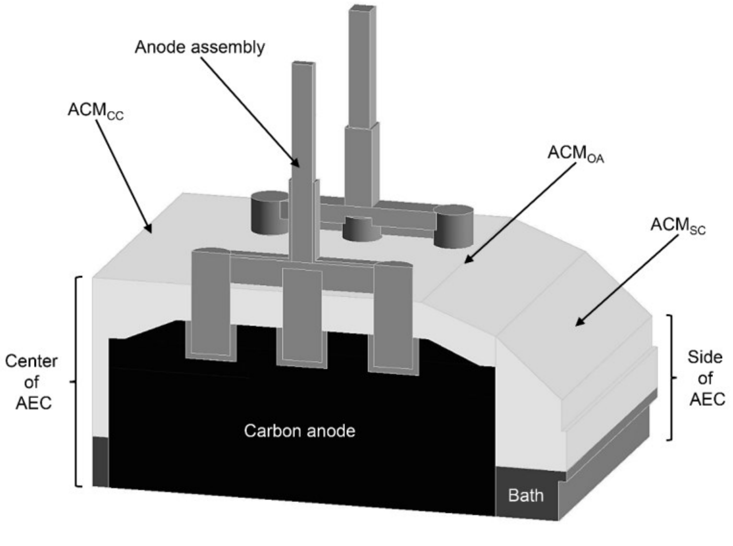

Figure 7-4 The geometry of the anode life cycle model (top parts of the AEC)

The top boundaries and materials are similar to the first model, but the main geometrical differences are the carbon anode consumption and the anode assembly displacement. The ACM and anode crust located OA and in the CC are attached to the anode and follow its motion.

Once transformed, the anode crust deteriorates and a cavity starts to grow. Accordingly, a radiosity module is also integrated in this model and the anode crust-cavity boundary is moved according to the melting isotherm. The ACM and anode crust profiles were measured with the methodology previously described in Figure 7-3A in order to set the initial ACM geometry and to ensure that the transient model represents the real evolution correctly.

Modeling method for the anode life cycle

A modeling approach is developed in order to predict the thermal-electric field for all the life cycle of the carbon anode. In the industrial process, a beam supporting all the anode assemblies is lowered to follow the carbon consumption and the operations (per example, siphoning). The parts of the anode crust, located OA and in the CC, track the anode displacement, while the crust on the SC region remains attached to the side wall. Additionally, the bottom of the anode crust melts to form the cavity. This second model aims at predicting the thermal dissipation from the geometrical variations of the anode cover and carbon content during its life cycle. The domain is discretized into approximately 600 000 elements with midside nodes (tetrahedrons).

Since the second model has a time-dependent domain and a moving boundary, a method is established to simulate these conditions in conjunction with the transient thermal-electric problem. A strategy for moving geometry, mesh update and nodal interpolation is developed and integrated in the ANSYS Mechanical software. This approach is detailed in Appendix B (see Figure 7-19). The time-dependent domain is accounted by exporting the nodal properties to a matrix and by calculating the new coordinates depending on the chosen analysis time, since the velocity of geometric displacement is known. Subsequently, the mesh is updated and the newly calculated nodal properties stored in the matrix are applied as initial conditions to the new mesh with a 3D interpolation method. In parallel, the moving boundary is treated by the same mean as described in section *Modeling method for the slice of AEC*. This step-by-step approach is programmed to automate the preprocessing, resolution and postprocessing in the ANSYS commercial software. Although this approach is currently applied to thermal-electric modeling, it can also be convenient to describe other similar physical phenomena, or to improve the capacities of other commercial software. Moreover, the moving geometry, mesh update and nodal interpolation approach does not exhibit mesh deformation due to the mesh update step. Effectively, a simple moving mesh technique would result in important mesh distortion, considering these specific domain changes, and is therefore not advisable in this work.

In order to demonstrate this modeling approach, only the top parts of the AEC have been selected in the CAD geometry. Since the anode size and its movement are time-dependent, they are modeled using the moving geometry, mesh update and nodal interpolation strategies. The irreversible phase transformation of the anode crust is also integrated in the modeling algorithm. For the moving parts, the nodal and element coordinates are displaced using matrix operations. In this simulation case, the bottom frontiers are the liquid bath and the side ledge (see Figure 7-4). Their nodal temperatures have been previously calculated with the slice model and they were applied as constraints for the anode life cycle modeling.

Assumptions for the transient modeling

In order to compute the transient thermal-electric solutions of both the slice of AEC and the anode life cycle, the following assumptions are considered: (1) ACM and anode crust behaviors are controlled by heat transfer and thermochemical processes; (2) the temperature and enthalpy of ACM → anode crust → cavity transformations are similar to already published results [Allard *et al.*, 2019a]; (3) the phase transitions inside these materials evolve to reach a state of chemical equilibrium, thus the reactions can be predicted with Gibbs energy minimization; (4) the heat transfer associated to mass transport is neglected; (5) the ACM granulometry, density and thermal conductivity are similar to the data presented in [Shen, 2006]; (6) the thermophysical properties of all materials are known; (7) the effect of the flow circulation inside the bulk liquid bath and the aluminum pad is accounted by an “augmented effective thermal conductivity” [Vidalain *et al.*, 2009]; (8) the heat transfer in the cavity is radiation dominated; (9) the surfaces in the cavity are gray and diffuse and (10) the time-variation of the electric field due to permittivity is neglected.

Governing equations

The transient heat transfer and heat generation are predicted based on a coupled thermal-electric analysis. A global system of algebraic equations is obtained with an assembly of finite elements. In this case, the finite element method solves the differential and integral equations using 3D coupled-field elements for solid and surface elements for boundary conditions. The set of algebraic equations is developed with the weighted residual statement and the Newton-Raphson method is applied to solve this nonlinear system. The preconditioned conjugate gradient (PCG) solver assembles the full stiffness matrix and it calculates the solution by iterating up to convergence. The ANSYS Mechanical solver available with APDL (ANSYS Parametric Design Language) script is used to resolve each simulation case.

The Equation 7-2 describes the governing equation for the transient heat conduction with the Joule heat generation rate per unit volume ($\dot{q}$) [Reddy and Gartling, 2010; ANSYS, 2017]:

$$\rho c_p \left(\frac{\partial T}{\partial t}\right) + \frac{\partial}{\partial x}\left(k_x \frac{\partial T}{\partial x}\right) + \frac{\partial}{\partial y}\left(k_y \frac{\partial T}{\partial y}\right) + \frac{\partial}{\partial z}\left(k_z \frac{\partial T}{\partial z}\right) = \dot{q} \tag{7-2}$$

For a transient or steady state electric analysis, the Joule heat in a conductor is described by Equation 7-3 using the centroidal values of the electric field and current density:

$$\dot{q} = \boldsymbol{J} \cdot \boldsymbol{E} \tag{7-3}$$

The electric field can be derived from:

$$\boldsymbol{E} = -\nabla V \tag{7-4}$$

The electric potential distribution is computed from the governing equation for electric conduction, in which the electrical conductivity (σ) depends on the temperature of the solid:

$$-\nabla \cdot ([\sigma]\nabla V) = 0 \tag{7-5}$$

Further information on the thermal-electric coupling is available in the ANSYS Mechanical documentation [ANSYS, 2017]. The radiosity method is applied in order to calculate the heat transfer in the cavity formed between the bottom of the crust and the top of liquid bath. A set of linear algebraic equations is used to obtain the outgoing radiative fluxes (radiosity) for each surface.

$$[A]\{q''^{,0}\} = \{D\} \tag{7-6}$$

Where:

$A_{ij} = \delta_{ij} - (1 - \varepsilon_i)F_{ij}$

$q_j''^{,0}$ = radiosity flux for surface j

$D_i = \varepsilon_i \sigma T_i^4$

Equation 7-6 is solved with the Newton-Raphson procedure for the radiosity flux $\{q''^{,0}\}$. At the surfaces facing the cavity, the boundary conditions for the heat conduction are provided by the net surface radiosity fluxes. The radiation view factors, F_{ij}, are required to solve the radiosity module. The overall view factors for each surface are calculated using the hemicube method [ANSYS, 2017; Cohen et Greenberg, 1985]. Each surface on the hemicube has an overall view factor given by:

$$F_{ij} = \frac{1}{A_i} \int_{A_i} \int_{A_j} \frac{\cos\varphi_i \cos\varphi_j}{\pi r^2} \mathrm{d}A_j \mathrm{d}A_i \tag{7-7}$$

The result is a complete set of form factors:

$$F_{ij} = \sum_{n=1}^{N} \Delta F_n \tag{7-8}$$

Where:

N = number of pixels

ΔF = delta-view factor for each pixel

Material properties

The thermophysical properties have recently been improved and implemented in the transient thermal-electric models. Table 7-2 describes the properties with a focus on the new data and the top components of the AEC. The radiation heat transfer inside the cavity is predicted with a radiosity module considering the emissivity of the anode crust, the carbon anode and the liquid bath. The bulk liquid bath and the aluminum pad are modeled with an augmented effective thermal conductivity to consider the flow circulation generated by the gas bubbles and the magnetohydrodynamics (MHD). A high ratio of advective to diffusive heat transport can be computed with the help of the Péclet number (Pe). Accordingly, the $k_{liquid\ bath}$ and the $k_{liquid\ aluminum}$ were both estimated to 10 000 W/m·K to reflect the advective heat transfer due to the movements of these liquids.

Table 7-2 Thermophysical properties of the top materials

Property	Value	Reference
ε_{ACM}	1.0	[Allard *et al.*, 2019b]
ε_{crust}	1.0	[Allard *et al.*, 2019b]
ε_{carbon}	0.95	[Touloukian and DeWitt, 1972]
$\varepsilon_{liquid\ bath}$	0.97	[Windisch *et al.*, 1992]
k_{ACM} (W/m·K)	$0.000616 \cdot T + 0.155$	[Shen, 2006]
k_{crust} (W/m·K)	$-0.000541 \cdot T + 1.386$	[Allard *et al.*, 2019a]
$k_{solid\ bath}$ (W/m·K)	1.2	-
$k_{liquid\ bath}$ (W/m·K)	10 000	-
ρ_{ACM} (kg/m^3)	1600	laboratory measurement
ρ_{crust} (kg/m^3)	2500	[Allard *et al.*, 2019a]
$c_{p,ACM}$ (J/kg·K)	Figure 7-5	chemical thermodynamic
$c_{p,crust}$ (J/kg·K)	Figure 7-5	chemical thermodynamic

**T: Temperature in °C.*

The ρ_{ACM} was simply determined in the laboratory considering the mass and the bulk volume, which were measured using a scale and a graduated cylinder. The specific heat capacity (c_p) was determined from previous quantification data of a typical ACM and the average of some anode crusts [Allard *et al.*, 2019a]. The cryolite ratio (CR), which is the molar NaF/AlF$_3$ ratio, was 1.96 for the ACM and 1.77 for the anode crust. The [Al$_2$O$_3$] for the ACM and the anode crust was 60 % and 38 % respectively. Using their corresponding compositions, the theoretical c_p of these materials was calculated by chemical equilibrium calculations by means of the FactSage 7.1 software. Furthermore, the theoretical c_p has also been validated in a previous work with differential scanning calorimetry applied on industrial samples [Allard *et al.*, 2019a]. The Figure 7-5 shows the temperature dependent c_p for the ACM and the anode crust, which also considers the enthalpy of phase transitions.

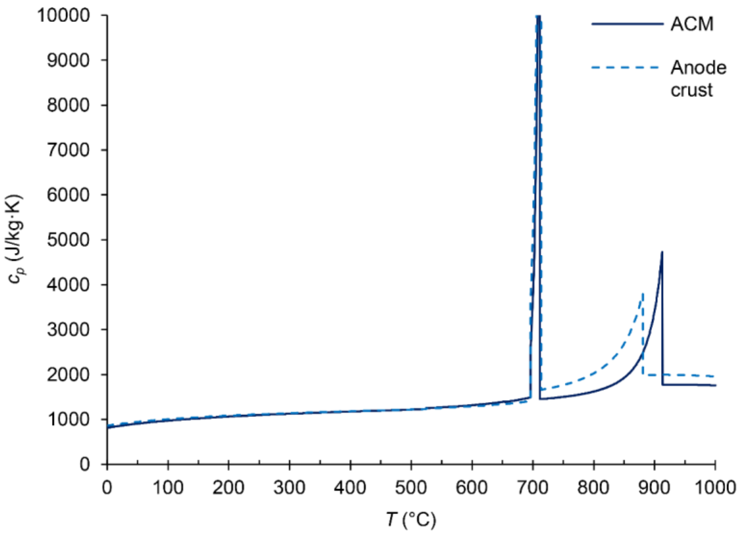

Figure 7-5 Specific heat capacity (c_p) of the ACM and anode crust of typical chemical composition

The ACM, the anode crust and the side ledge are modeled as phase change materials. The ACM transforms into anode crust from 685 °C (Equation 7-9) due to the contact with liquid or vapor fluoride species coming from the bulk liquid bath. This transformation is also favored when the liquid fraction in this material increases. Accordingly, it enhances the growth of the α-Al_2O_3 crystalline network and consolidates the particles. The liquid fraction rises quickly from 696 °C to 710 °C in ACM of typical chemical composition, according to thermodynamic equilibrium results.

$$\text{ACM} \xrightarrow{\text{fluorides}} \text{Anode crust} \qquad (685\ °\text{C to } 710\ °\text{C}) \tag{7-9}$$

For the present simulations, the ACM thermal conductivity from room temperature up to 685 °C is represented by the linear equation determined by Shen (2006). A linear transition is included in order to reach the value of the anode crust (between 685 °C and 710 °C). From 710 °C and beyond, the crust irreversible transformation is considered completed and the thermal conductivity decreases almost linearly with temperature [Allard *et al.*, 2019a].

Once the anode crust is formed, it begins to deteriorate due to high temperature and liquid bath splashes. From 935 °C, all bath phases are melted and the structure is only supported by the Al_2O_3 particles that are sintered together. The liquid bath splashes, which could have frozen at lower temperature, deteriorates the anode crust by dissolving the Al_2O_3. Consequently, the anode crust will deteriorate with these conditions and fall down in the bulk bath, thus forming the cavity. The cavity is an empty space filled with process gases in which the radiation heat transfer takes place. Equation 7-10 gives the irreversible anode crust to cavity transformation.

$$\text{Anode crust} \rightarrow \text{Cavity} \qquad (935\ ^\circ\text{C}) \qquad (7\text{-}10)$$

The ledge is formed on the side walls when liquid bath freezes due to the heat dissipated by the shell to the surroundings. The ledge is primarily composed of Na_3AlF_6 with dissolved species inside its microstructure. The melting or freezing temperature of the Na_3AlF_6 depends on chemistry of the bulk liquid bath, a phenomenon that affects the local composition at the liquid bath-ledge interface. The ledge grows or melts typically at 950 °C (Equation 7-11), a temperature that varies depending on the liquid bath composition. This reversible phase change evolves according to operating conditions and heat dissipation to the surroundings.

$$\text{Liquid bath} \leftrightarrow \text{Side ledge} \qquad (950\ ^\circ\text{C}) \qquad (7\text{-}11)$$

The irreversible transformations in the anode cover, ACM → anode crust → cavity, are considered in the transient model by exporting the material conditions after each step of simulation. The values are stored in a CSV file and read in the next step. Afterward, a material property for each element is attributed based on the previous calculations. The irreversible anode crust to cavity transformation is integrated by means of the moving boundary method previously described in section *Modeling method for the slice of AEC*.

Boundary conditions

For the thermal-electric simulations, typical thermal boundary conditions are used for the side and the bottom of the slice of AEC, while the top thermal conditions are based on previously measured data [Allard *et al.*, 2019b]. The boundary conditions are established using the average value of heat flux sensors (HFS) and T_∞, which were measured previously throughout the follow-up of three instrumented industrial anodes. The top boundaries consist of the top surfaces of the ACM and anode assemblies. These parts are facing the bottom of the superstructure and the pot hoods which are at lower temperatures. Also, the air flow coming from the potroom and entering through the gaps between the hoods cools down the top parts by convection heat transfer. The top parts are then cooled by both convection and radiation heat transfer. An "effective convection heat transfer coefficient" (h_{eff}) considering both the convection and radiation have been applied to the top boundaries of the electrolysis cell. The h_{eff} data were calculated from the heat flux measurements (q'') with Equation 7-12, knowing the surface (T_s) and gas (T_∞) temperatures.

$$q'' = h_{eff}\ (T_s - T_\infty) \tag{7-12}$$

The boundary conditions, h_{eff} and T_∞, were determined based on thermal measurements in industrial cells (method detailed in section *Measurements to validate the thermal-electric models*). T_∞ are the gas temperatures measured above the boundaries. Table 7-3 details the top boundary conditions used in the two numerical models.

Table 7-3 Boundary conditions for the top parts of the AEC

Boundary	h_{eff} (W/m^2·K)	T_∞ (°C)
Sides of anode rod	25	120
Steel yoke and stubs	40	120
Top of ACM_{OA} and ACM_{CC}	20	120
Top of ACM_{SC}	20	100

The global geometry of the AEC was cut in the center and on two sides to produce the slice shown in Figure 7-2. For each cut section, a symmetric boundary condition has been applied. Heat losses from the side and the bottom were also predicted with h_{eff} and T_∞ data calculated and measured on industrial AEC.

For the slice of AEC, the current delivered to the electrolysis cell was divided by the number of anodes and the corresponding value was applied to the top of each anode rod. An electric potential of 0 V has been applied to the top of each cathode flexible conductor. For the anode life cycle model, the electric current was measured on an instrumented anode throughout its lifetime and the corresponding value was applied on the top of each anode rod.

Measurements to validate the thermal-electric models

The transient thermal-electric model of the slice of AEC is used to determine the nodal bath temperature and to apply these values as constraints in the anode life cycle model. Additionally, the effect of a voltage increase is investigated with the slice of AEC. In order to validate this heat transfer prediction, the instrumented anode (A) was monitored during the voltage increase period. A type K thermocouple was installed on the side shell at the bath-metal interface (BMI) and another was kept in the liquid bath to evaluate the effect of the voltage increase on local temperatures. Moreover, the side ledge thicknesses were manually measured before and after this heat treatment. Another instrumented anode (B) was collecting data while the AEC operated normally, thus without noticeable events. This second dataset was used to validate the thermal-electric the anode life cycle model.

Figure 7-6 and Figure 7-7 show the locations where the typical thermal boundary conditions have been previously determined with the manual measurements of heat flux and T_∞, which were performed throughout the life of the anodes [Allard *et al.*, 2019b]. The modeling results will be validated with the thermocouples installed on the instrumented anodes A and B investigated in this study (temperatures shown in Figure 7-7).

The heat fluxes and temperatures above the ACM and on some metallic surfaces have been determined from measurements with Hukseflux HF01 sensors (HFS). The estimated accuracy of these sensors is ± 15 % and the repeatability is ± 5 % according to the product manuals [Hukseflux, 2003] The temperature was also measured by each sensor with an accuracy of approximately ± 1 % for their internally installed type K thermocouple.

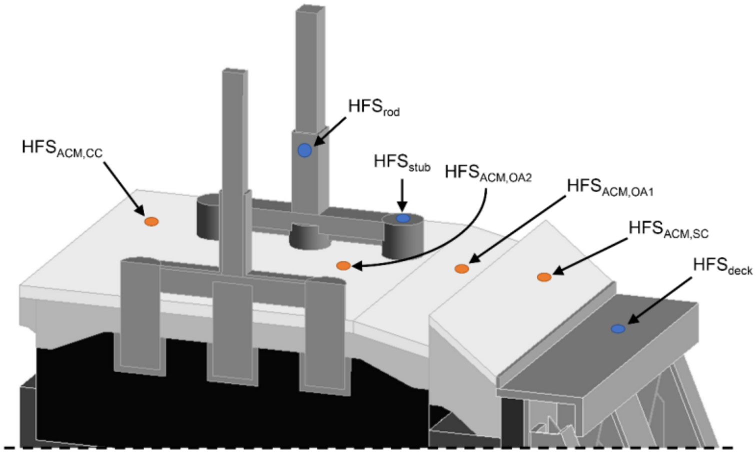

Figure 7-6 Each ● indicates the location on the ACM where a HFS was placed; ● indicates the location of a HFS set on a metallic surface

The temperatures on the anode assembly, the ACM and the anode crust were measured continuously with type K thermocouples (Omega) installed at the locations described in Figure 7-7. The thermocouples in the ACM and crust were installed before the covering of the new anode, folded in "L" shape, pointing in the opposite direction of the stubs. The ends of these thermocouples were located under the $HFS_{ACM,OA2}$, as shown in Figure 7-6. In the ACM-crust, a vertical arrangement of thermocouples was installed, with a sensor every 2.5 cm (from 0.0 cm to 10.0 cm) from the top of the carbon anode. On the anode rod, a thermocouple was soldered at each 10.0 cm. The gas temperatures (●) were measured manually with type T thermocouples at the locations shown in Figure 7-7. These gas temperatures were used to determine the boundary conditions previously presented in Table 7-3.

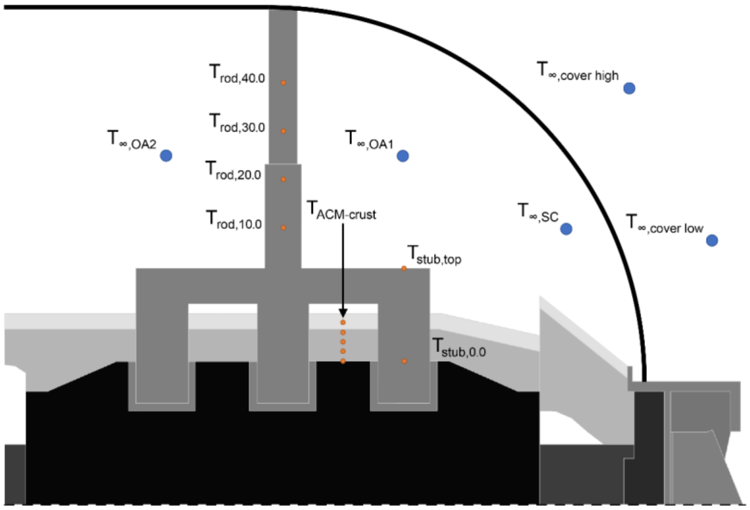

Figure 7-7 ● Thermocouples installed in the ACM, anode crust and anode assembly; ● locations where manual measurements of the gas temperatures were made

7.2.4 Results and discussion

Effect of a voltage increase investigated with the slice of AEC

The ACM → anode crust → cavity transformations throughout the anode life are irreversible, as explained in section *Material properties*. In industrial AEC, there are adverse conditions where the heat losses increase significantly for a period of time. When the AEC can be brought back to normal operation, the degradation of its anode cover subsists. In order to investigate the effect of a voltage increase and consequently a thermal excursion on heat losses, the operating voltage was increased while an instrumented anode was in the AEC to monitor the changes taking place. A 8.5 % voltage increase, calculated from the normal operating voltage, was applied for 23.0 h (0.958 day) on an industrial AEC, which was operating normally until this change. This voltage treatment was carried out by changing the operating set-point, which resulted in the increase of the anode-cathode distance (ACD). Among other things, this treatment was made in order to simulate an AEC experiencing a thermal excursion which generates the anode cover degradation and to evaluate the consequences of this event on the thermal balance.

The transient thermal-electric model of the slice of AEC was used to evaluate the effect of the voltage treatment and to determine the liquid bath and side ledge temperature profiles for the anode life cycle model (section *Anode life cycle modeling*). In order to predict the temperature and electric field during and after the voltage treatment, these cumulative steps were performed with the transient thermal-electric model:

1) A steady state was predicted with the slice of AEC and used for the initial condition ($t = 0$)
2) The voltage increase was evaluated up to $t = 0.958$ day
3) A normal voltage was applied again to assess the cell behavior from $t = 0.958$ day to $t = 3$ days

The voltage increase was simulated by means of an electrical resistivity change (vertical component only) in the liquid bath located between the anode and the liquid aluminum. The transient modeling results were validated from the instrumented anode A and the temperature from the thermocouples on the side shell and in the liquid bath.

Temperature profile

The transient modeling with the slice of AEC began with a steady state ($t = 0$) in order to simulate an industrial AEC operating at stable conditions. This simulation considered the ACM to anode crust transformation by changing the material property of each element and also integrated the anode crust melting with the moving boundary. The corresponding temperature distribution is shown in Figure 7-8.

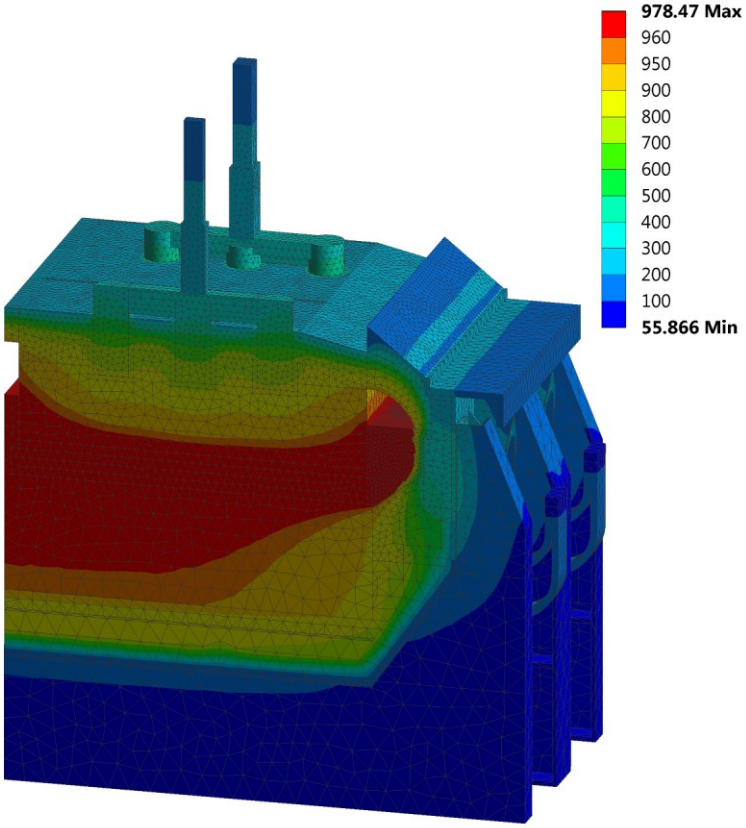

Figure 7-8 Temperature profile (°C) predicted with the slice of AEC at $t = 0$ (initial condition)

Then, the voltage increase (+8.5 %) was applied for 23 h (0.958 day) and a stabilization period of 2.042 days was evaluated. The temperature profiles for these consecutive simulations are presented in Figure 7-9. At the end of the voltage treatment, T_{max} in the liquid bath reached 998.5 °C, which is 20 °C higher than the initial condition. Considering this high temperature, the radiation heat transfer from the liquid bath is enhanced, thus causing the melting of the anode crust. The cavity boundary moved up and its size increased considerably, as observed in Figure 7-9. After 3 days, T_{max} of the liquid bath decreased to 976.1 °C, the phase change materials have stabilized in time and a new steady state was reached.

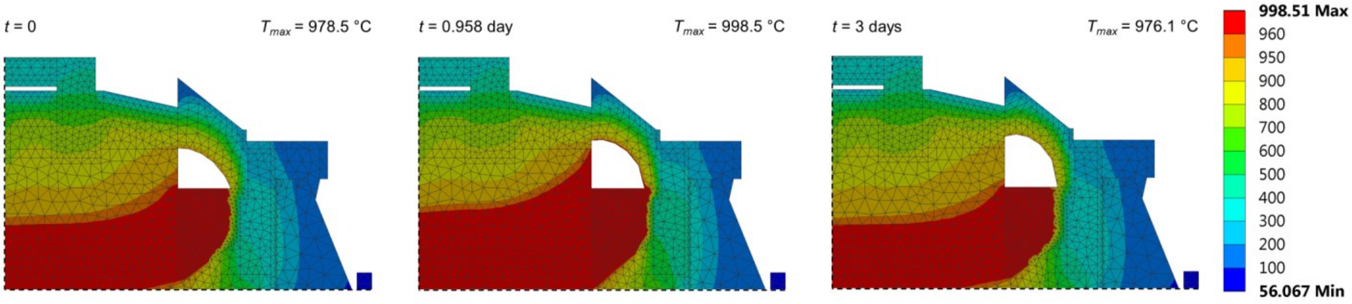

Figure 7-9 Temperature profiles (°C) predicted with the slice of AEC at $t = 0$, $t = 0.958$ day and $t = 3$ days

Effects on the side ledge, the cavity and the ACM

The effects of the voltage increase on the side ledge, the cavity size and the ACM transformation are detailed in Table 7-4. The height of the cavity$_{SC}$, taken at a location shown in Figure 7-3B, was 13.7 cm at t = 0, 17.1 cm at t = 0.958 day and 17.9 cm at t = 3 days, according to the simulation. The volume of the cavity increased by 17.5 % from its initial value, when measured immediately after the voltage treatment. After 2.042 days from the end of the voltage treatment, the cavity enlarged by 25.4 %. Since the ACM to anode crust transformation is irreversible, this material does not recover after such thermal treatment. The proportion of ACM in the anode cover, [ACM], decreased from 47.7 % to 44.1 % immediately after the voltage increase and it got to 42.3 % at t = 3 days. Furthermore, the total size of the anode cover decreased since the cavity enlarged. The side ledge, considered as a reversible phase change material, decreased by 43.9 % after 0.958 day of voltage increase. At t = 3 days, it enlarged by 17.7 % from its initial volume, which can be related to the thinner and more conductive anode cover.

Table 7-4 Effects of the voltage increase on the side ledge, the cavity and the ACM

Simulation	***t* (day)**		
	0.000	**0.958**	**3.000**
Side ledge at BMI (%)*	ref.	-60.1	36.5
Volume of side ledge (%)*	ref.	-43.9	17.7
Height of cavity$_{SC}$ (cm)	13.7	17.1	17.9
Volume of cavity in AEC (m^3)	0.610	0.717	0.765
Volume of cavity in AEC (%)*	ref.	17.5	25.4
[ACM] in the anode cover (%)	47.7	44.1	42.3

**Comparison with the initial condition (t = 0)*

Comparison with the measurements on the industrial AEC

The instrumented anode A was measured during the voltage treatment which occurred at approximately 75 % of its life. However, the anodes of the slice of AEC are at mid-life to reproduce the average behavior of an industrial cell. Hence, a difference is expected between predictions and measurements due to the different anode sizes (this effect is discussed in the section *Anode life cycle modeling*). The measured data taken in the anode crust at 0.0 cm ($T_{meas.,crust,0.0}$) and at 5.0 cm ($T_{meas.,crust,5.0}$), and the data taken on the anode stub next to the deck ($T_{meas.,stub,0.0}$ and $T_{meas.,stub,top}$) are shown in Figure 7-10A. When compared with the predicted T_{model}, the measured temperatures in the anode crust showed a larger difference than the measurements on the stub. All $T_{meas.,crust}$ and $T_{meas.,stub}$ increased when the voltage increase started (at $t = 0$) and they decreased after this treatment. The temperatures on the metallic surfaces recovered their original values after the voltage treatment, while the temperatures inside the anode crust remained higher according to the measurements. For example, $T_{meas.,crust,0.0}$ started at 797 °C and $T_{model,crust,0.0}$ at 798 °C ($t = 0$), while they reached 881 °C and 812 °C respectively at the end of the voltage treatment. In both cases, the temperatures increased. However, in industrial cells the higher temperature of the liquid bath can also enhance the rate of bath vapor production and increase the gas temperature, which may have amplified the temperature inside the industrial anode crust.

The liquid bath ($T_{meas.,bath}$) and side shell ($T_{meas.,side\ shell}$) temperatures were recorded by two thermocouples in order to evaluate the effect of the voltage increase, see Figure 7-10B. The voltage increase (+8.5 % of the AEC operating voltage) increased the temperature of the liquid bath in the industrial AEC by 29 °C from $t = 0$ to $t = 0.958$ day. In the numerical model, the temperature increased from 972 °C to 990 °C in the same time lapse. In both the measurement and the simulation, the temperature of the liquid bath recovered quickly after the voltage treatment. In one hour after the voltage increase, $T_{meas.,bath}$ decreased from 993 °C to 974 °C (-19 °C), while $T_{model,bath}$ decreased from 990 °C to 980 °C (-10 °C). After 7 h from the voltage treatment (at $t = 1.25$ day), $T_{model,bath}$ reached a slightly lower temperature (966 °C) compared to the initial state (972 °C). The $T_{model,bath}$ only regained its initial value after approximately 2 days from the voltage treatment. The $T_{meas.,side\ shell}$ and $T_{model,side\ shell}$ also increased due to the voltage increase and decreased slowly during the next 2 days. Accordingly, the $T_{model,side\ shell}$ were: 367 °C at $t = 0$, 449 °C at $t = 0.958$ day, 363 °C at $t = 2$ days and 355 °C at $t = 3$ days. From $t = 2.75$ days, the $T_{model,side\ shell}$ was stabilized at a lower temperature (355 °C) than the initial value. The voltage increase affected the anode cover by increasing its thermal conductance due to thinner anode cover and lower concentration of ACM (see Table 7-4). With a more conductive cover, the top heat dissipation is increased and the side ledge adapts to this new thermal condition. Considering a similar external environment, the side shell temperature decreases due to this condition.

The side ledge thicknesses were evaluated in the industrial AEC and the transient model. Figure 7-10C shows the length (L) of the side ledge taken at various heights (H). $L_{side\ ledge,t=0}$ is a typical side ledge profile which was determined from two measurements prior to the voltage increase, on anodes immediately next to the instrumented one. $L_{side\ ledge,t=2}$ was measured at approximately

1 day after the voltage treatment on an anode next to the instrumented one to prevent disturbing the temperature recording. This measurement is presented since it is the closest to the voltage treatment. In the industrial AEC, the local side ledge thickness decreased due to the voltage increase which increased the temperature on the side shell at BMI. The length of the side ledge was also evaluated with the numerical model at *t* = 0, 1 and 3 days, as shown in Figure 7-10D. The side ledge size decreased with increased voltage. Afterward, it enlarged to reach a larger size up upon the return to equilibrium, at *t* = 3. The temperature profile in the transient model and the side ledge evolution over time are presented in the video shown in Figure 7-18 of the Appendix A. In both the industrial measurements and the transient model, the side ledge decreased as expected with voltage increase. Moreover, a larger side ledge also implies a decrease of side heat losses due to its insulating behavior.

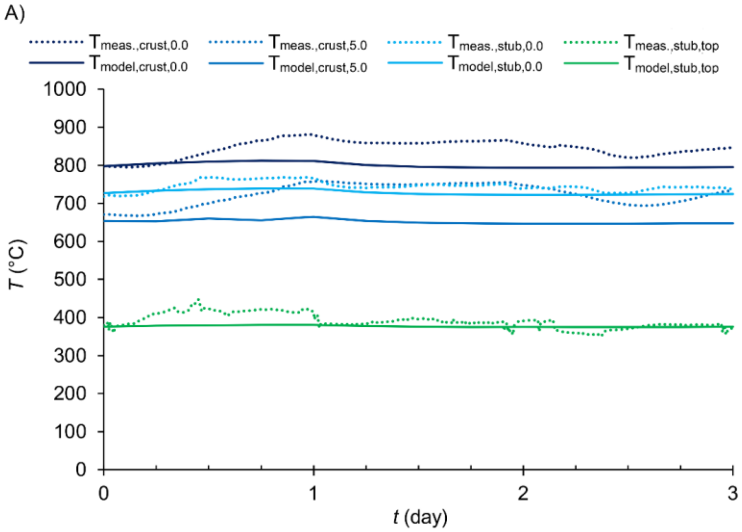

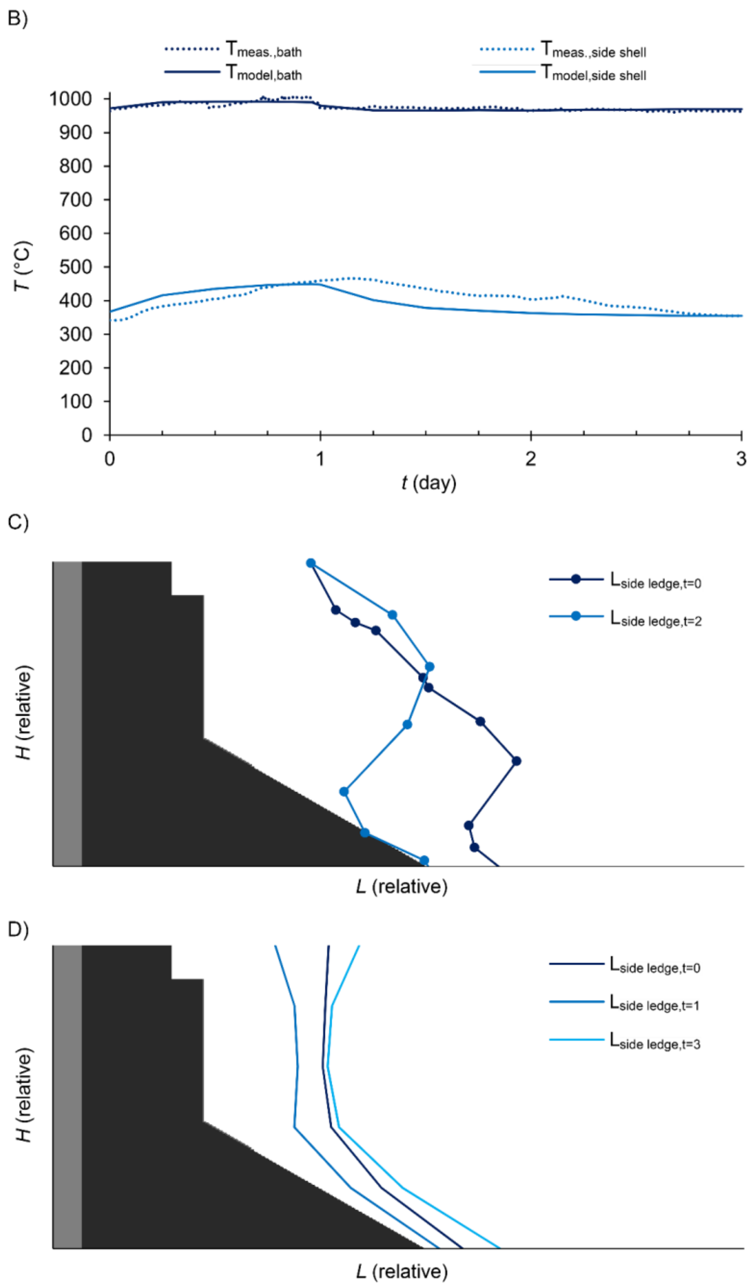

Figure 7-10 A) Temperatures taken in the anode crust and on the stub next to the deck. B) Temperatures taken in the liquid bath and on the side shell at BMI. C) Side ledge profile measured in an industrial AEC at *t* = 0 and *t* = 2 days. D) Side ledge profile predicted with the slice of AEC at *t* = 0, *t* = 1 day and *t* = 3 days

Impact of the voltage increase on the heat dissipation

Immediately before increasing the voltage (at *t* = 0), the heat losses were distributed as follows: 34.9 % from the top, 58.1 % from the side and 7.0 % from the bottom. The top heat losses include the anode assembly and the anode cover, thus all the parts dissipating heat under the pot hoods. The deck dissipates heat toward the outside of the AEC, this part is thus included in the side heat balance. Figure 7-11A demonstrates the effect of the voltage increase on the heat loss distribution when compared with the values taken at $t = 0$. After 0.958 day of increased voltage, the heat losses augmented to 36.5 % (top), 74.4 % (side), 7.2 % (bottom), representing an increase of 18.1 % from the initial heat losses. The side heat losses increased the most (+16.3 %), while the top dissipation increased by 1.6 %. Nevertheless, the top parts are mostly composed by irreversible phase change materials (ACM and anode crust), while the side ledge is a reversible phase change material. Accordingly, at $t = 3$ days, the top heat losses remained augmented at 36.3 %, but the side heat dissipation was lower than the initial value, at 56.7 % (-1.4 %). The bottom heat losses remained almost constant from $t = 0$ to $t = 3$ days.

The Figure 7-11B shows the impact of the voltage increase on the heat generation (Joule heat) from the slice of AEC, and also the thermal lag between heat generation and dissipation in this transient model. The heat dissipation responds more slowly due to both latent heat in the phase change materials and low thermal conductivities. According to the transient model, it takes about 1 day for the AEC to stabilize almost entirely from this voltage increase, while the time required to reach the stabilization is close to 2 days. After the stabilization of the thermal dissipation, the AEC ends up in a new thermal balance implying higher heat losses from the top and lower from the side. This effect is amplified with increasing ACM conversion and anode crust melting in the anode cover.

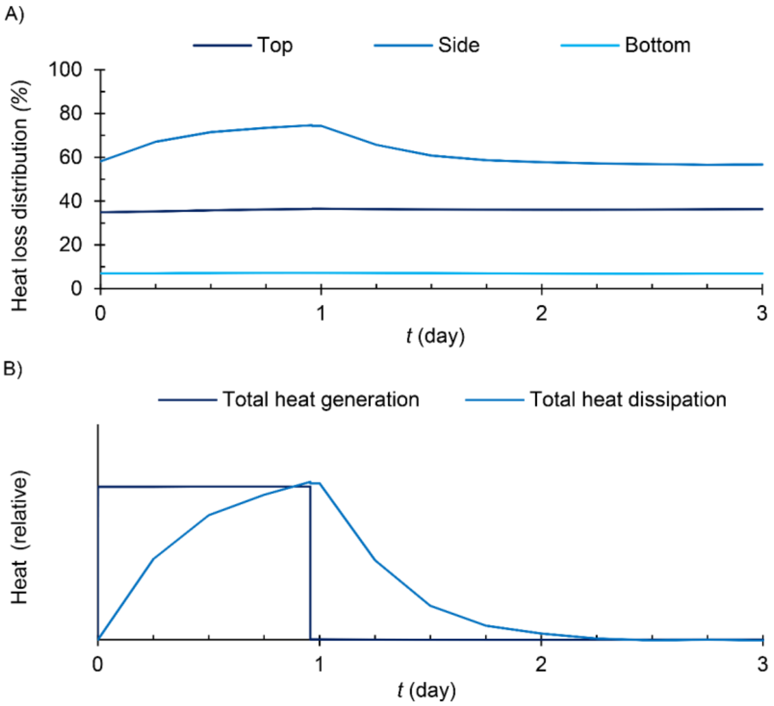

Figure 7-11 A) The heat loss distribution calculated in comparison with *t* = 0. B) Total heat generation and heat dissipation in relative scale, also in comparison with *t* = 0

Anode life cycle modeling

Temperature profile

The thermal behavior of the top parts was investigated with a transient thermal-electric model which takes into account the carbon anode consumption and the anode assembly descent to maintain ACD during the electrolysis process. The anode life cycle is modeled by applying as nodal constraints the previously calculated liquid bath and side ledge temperatures, which were obtained at steady state with the slice of AEC. This second simulation depicts the typical evolution of an anode with its cover, thus without operational disruption such as voltage increase. The anode assembly and the anode cover located both OA and in the CC were moved downward during the anode life. The ACM started at T = 30 °C (*t* = 0), it transformed into anode crust according to Equation 7-9 (between 685 °C to 710 °C) and the anode crust melted to form a cavity at 935 °C. Figure 7-12 shows the anode downward movement, the anode cover in the SC that remained fixed and the temperature variation during the anode life (at *t* = 0 %, 25 %, 50 %, 75 % and 100 % of the total anode life), where *t* = 100 % represents less than a month. Moreover, a video is added in Appendix B (see Figure 7-20) to visualize the temperatures with smaller time differences and to see the mesh updating between each analysis step. It can be observed that the mesh adapts to the moving parts with the programmed moving geometry, mesh update and nodal interpolation strategies. From $t = 75\ \%$ to $t = 100\ \%$, the ACM$_{OA}$ and crust$_{OA}$ were lowered below the cavity$_{SC}$, accordingly an open cavity was generated using the radiosity module.

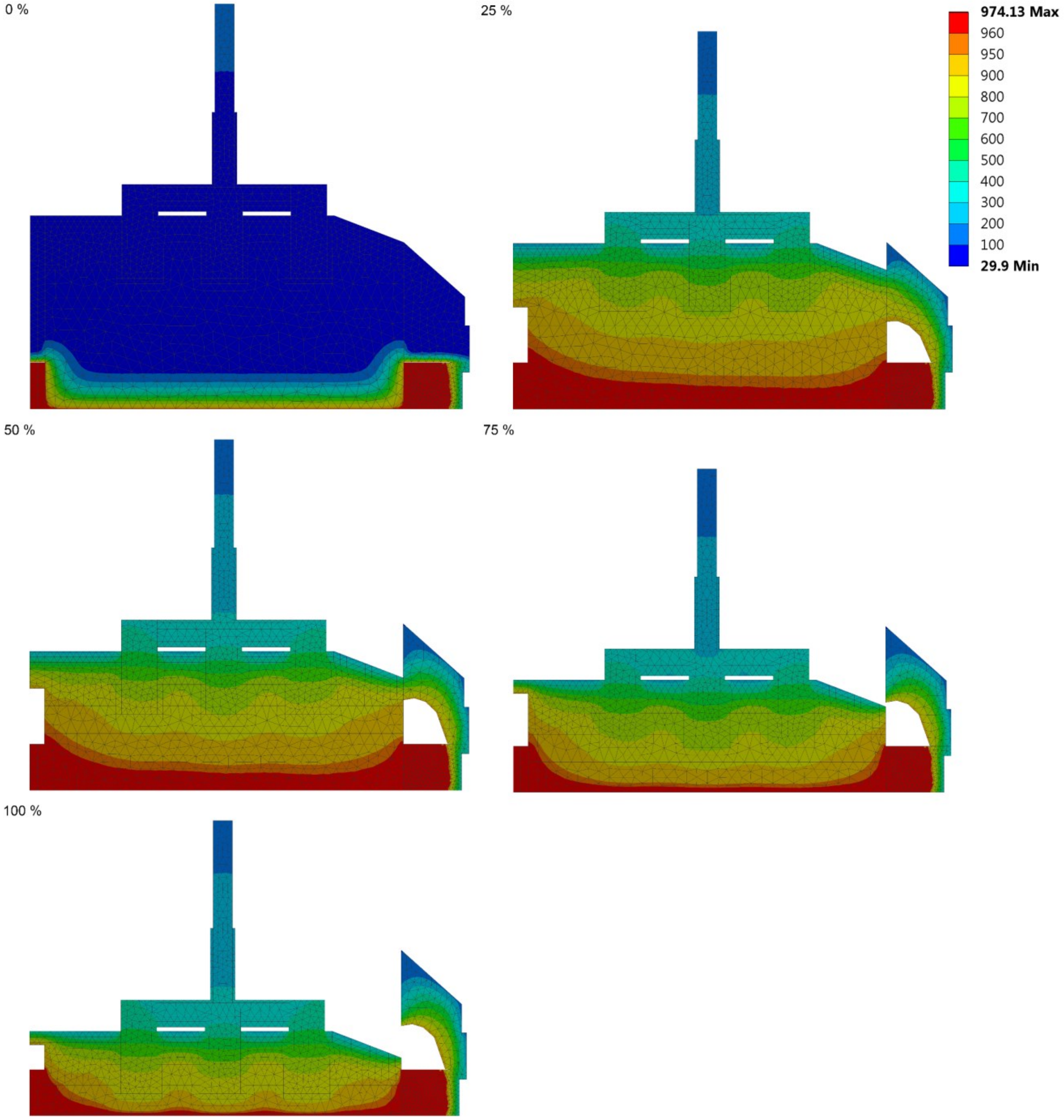

Figure 7-12 The temperature profile (°C) at 0 %, 25 %, 50 %, 75 % and 100 % of the anode lifespan, predicted using the anode life cycle model

Geometric evolution of the anode cover

The ACM and anode crust profiles were validated in industrial cells with the measurement method previously shown in Figure 7-3A, in order to built the right initial geometry and to confirm that both the anode covers OA and in the CC follow the anode displacements. Figure 7-13A shows the anode cover of the instrumented anode B with a picture taken immediately after the covering procedure. This instrumented anode operated typically, thus without any voltage treatment. In the simulations, the anode cover is designed based on the average thicknesses measured in industrial AEC. However, the leveling of the ACM in the industrial cells is not as uniform as in the model.

In this transient model, the body parts crust_{SC} and the ACM_{OA} disconnected from each other at t = 72 % of the total anode life. Accordingly, an open cavity was generated in the model, in contrast to the perfect cavity considered at $t < 72$ %. In the industrial AEC, some flames are expected to be observed, as shown in Figure 7-13B. The top boundary conditions were kept uniform during all of the anode life modeling, even though the flames are expected to increase the top T_∞.

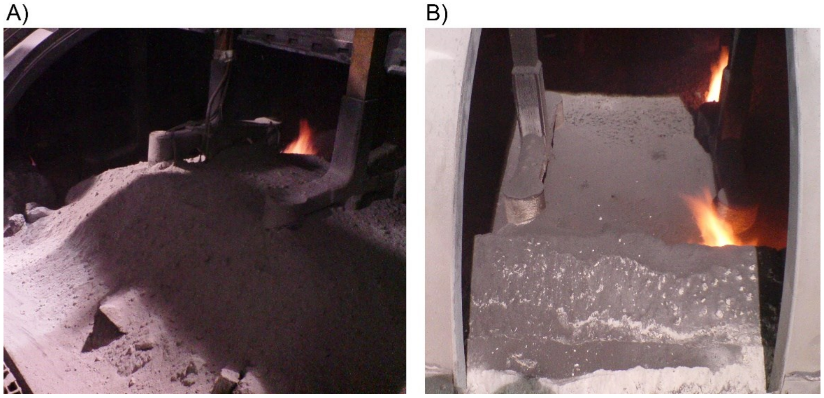

Figure 7-13 A) Instrumented anode immediately after the covering. B) Another anode at *t* = 80 % with a typical cover exhibiting flames

Comparison between the anode life cycle model and the instrumented anode B

Different temperatures were measured with thermocouples during the anode life and these results are compared with the transient prediction. Figure 7-14 gives the temperatures recorded on the anode rod (A), on the closest stub to the deck (B) and in the ACM and anode crust (C). The average temperatures measured and predicted are described in Table 7-5. The temperatures on the anode rod increased quickly between $t = 0$ to $t = 5$ % and they reached 75 % of the average test measurements after 5 % of the anode life. The temperatures on the anode rod reached the average of the test after t = 24 %. The temperature on the top of the steel stub ($T_{meas.,stub,top}$) followed the exact same trend than the anode rod: it reached 75 % of the average value also at t = 5 % and it reached its average at t = 24 %. On a longer time scale, $T_{meas.,stub,top}$ increased slowly between t = 25 % (T = 375.5 °C) and t = 75 % (T = 399.9 °C). Therefore, the temperatures of the metallic parts of the anode assembly in contact with gas located under the pot hoods increased rapidly and they remained relatively stable around the mid-life of the anode. At t = 77 %, the temperatures of these metallic parts began to raise abruptly.

The temperatures measured in the ACM and anode crust got to 75 % of their average values at t = 4 % for $T_{meas.,crust,0.0}$, at t = 7 % for $T_{meas.,crust,5.0}$ and at t = 10 % for $T_{meas.,ACM,10.0}$. In order to reach their averages, $T_{meas.,crust,0.0}$, $T_{meas.,crust,5.0}$ and $T_{meas.,ACM,10.0}$ took respectively 19 %, 43 % and 67 % of the anode life. Accordingly, the temperature rise in the anode cover was slower than the metallic parts, as expected due to their lower thermal conductivity and because of the endothermal transformation of ACM into crust. Moreover, the temperatures of the anode cover raised drastically at the end of the test (also at t = 77 %) and it contributed to increase the average temperature. This rapid temperature rise may be explained by the smaller distance between the bottom of the anode crust and the top of the bulk liquid bath in the AEC. Consequently, high temperature liquid bath may enter in contact with the anode crust and this will increase the local temperature. However, the fluid dynamic and the related heat transport are not considered in the current thermal-electric model.

In a general perspective, the anode cycle model predicted the temperatures of the anode rod, steel stub and anode cover with a mean absolute relative error (MARE) of 5.2 %, considering the absolute temperature scale (Kelvin) for the error calculations. The MARE was calculated with the average temperatures in Table 7-5 (subtracting the measured value from the predicted, dividing by the measured, taking the absolute and then calculating the mean of all the calculated absolute values). Moreover, the prediction accuracy is better at t < 77 % (calculated MARE of 2.7 % from all the dataset) and it decreases at the end of the anode life. The transient model predicted with a very high accuracy the temperature rise in the anode cover, especially from t = 0 to t = 25 % of the anode life with a calculated MARE of 1.2 %.

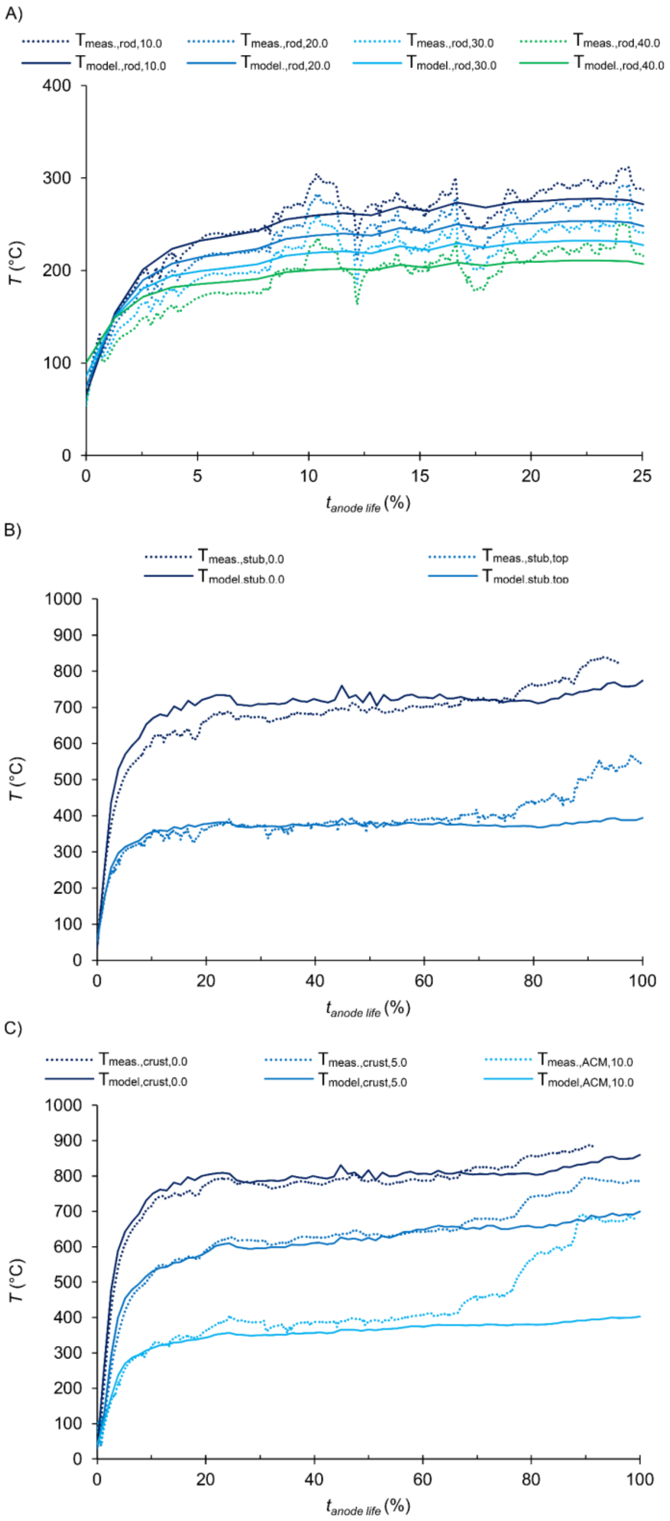

Figure 7-14 A) Temperatures on the anode rod taken at 10.0 cm, 20.0 cm, 30.0 cm, and 40.0 cm from the yoke. B) Temperatures measured at the bottom of the stub (0.0 cm) and on its top surface. C) Temperatures recorded in the ACM and anode crust at 0.0 cm, 5.0 cm and 10.0 cm from the top surface of the carbon anode. At the end of the test, only $T_{meas.,ACM,10.0}$ remained lower than the transformation temperature of ACM to anode crust

Table 7-5 Average temperatures measured on the instrumented anode and predicted with the transient model

Location	Average temperature (°C)		Error (%)
	Measurement	Simulation	
Rod at 10.0 cm	301.9	263.5	-6.7
Rod at 20.0 cm	279.5	240.9	-7.0
Rod at 30.0 cm	256.3	221.3	-6.6
Rod at 40.0 cm	231.7	202.2	-5.8
Stub at 0.0 cm	680.6	697.5	1.8
Stub top	391.5	364.1	-4.1
Anode crust at 0.0 cm	768.3	776.4	0.8
Anode crust at 5.0 cm	630.0	601.8	-3.1
ACM at 10.0 cm	429.7	351.8	-11.1

Impact of the anode consumption on the cavity size and on the top dissipation

The anode life cycle model allows to follow the evolution of the cavity and the top heat losses, which include the anode cover and the anode assembly. The height of the cavity$_{SC}$ was measured in industrial AEC at the location in Figure 7-3B. This industrial measurement was subject to large variations (standard deviation of ± 3.2 cm), since the measurements were taken on other anodes to prevent the perturbation of the instrumented anode B. According to Figure 7-15A, the height of the cavity$_{SC}$ increased up to *t* = 38 % of the anode life and then remained stable until the end, which is due to the static behavior of the crust$_{SC}$. In the case of the cavity$_{CC}$, it increased up to *t* = 15 %, stabilized until *t* = 72 % and then it decreased continuously until the end of anode life time. The height of the cavity in the CC and between the anodes decreased due to the downward movement of the anode assembly. In parallel, the crust was melting as it was closer to the bulk liquid bath.

The top heat dissipation, from the parts located under the pot hoods, was compared with the average prediction during all the anode life. Initially, the ACM and anode assembly were cooler than the pot gas, and thus these parts were heated. The top heat dissipation reached its average value at *t* = 21 %, then it oscillated due to the varying electric current of the anodes and increased up to the end of the anode life. The top heat dissipation at mid-life corresponded to 103 % of the average, thus 3 % higher. Accordingly, the investigation of mid-life anodes gives a proper approximation of the average top heat dissipation from all the anode life. Nevertheless, close to the end of the anode life, the transient model underestimated the top temperatures (as discussed in section *Comparison between the anode life cycle model and the instrumented anode B*), hence the top heat dissipation in industrial AEC is expected to be higher.

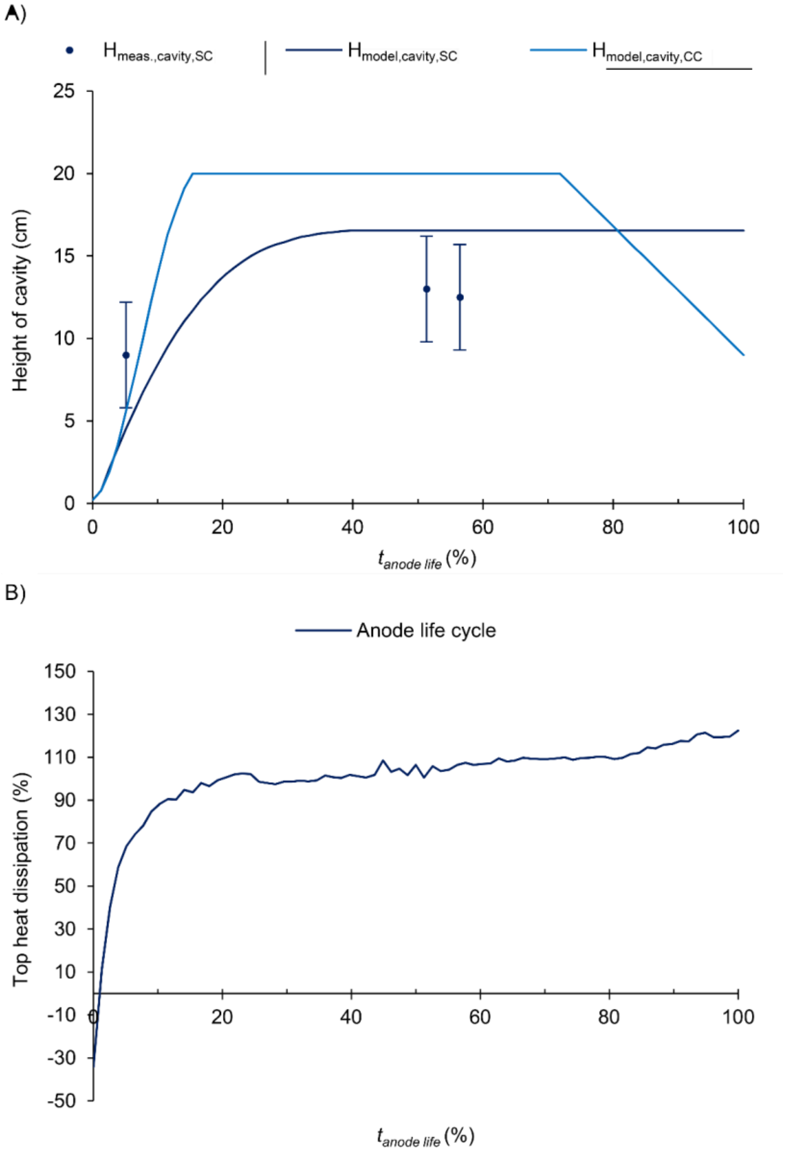

Figure 7-15 A) Height of the cavity during the anode life. B) Top heat dissipation in % of the average value over the life time

Significance of the results for the aluminum industry

Voltage increases in industrial cells

The effect of a substantial voltage increase (+8.5 % over a long period of 23 h) was quantified by both the transient slice model and the industrial measurements. The voltage treatment caused the melting of 0.107 m^3 of anode crust, thus 267.5 kg of material with high [Al_2O_3] have fallen into the bulk liquid bath, according to the prediction. This additional feeding of Al_2O_3 in the

AEC might result in sludge formation at the cathode surface, if the liquid bath does not dissolve the melted anode crust.

The voltage increase also reduced the side ledge size, consequently the side heat dissipation increased by 16.3 % from its initial value. Additionally, this treatment deteriorated the anode cover and its thermal conductance increased. Since the ACM → anode crust → cavity transformations are irreversible, the top heat dissipation remained higher even once the operating voltage was brought back to its target value. Accordingly, the side ledge, which is reversibly produced from bath phase change, adapted to the increased top heat dissipation and reached a larger size than initially.

In industrial AEC, the combination of additional Al_2O_3 on the cathode surface and the additional heat losses from the side could result in Al_2O_3 precipitation on the bottom surface of the AEC. Moreover, the voltage increase augmented the liquid bath temperature, thus favoring vapor production ($NaAlF_4$). This evaporation increases the cryolite ratio and the bulk bath liquidus. Therefore, the side ledge and ledge toe can reach a larger size than predicted due to the increased liquidus temperature of the bath under real conditions.

Anode life cycle and industrial events

The complete life of the carbon anode with its metallic parts and covering materials has been simulated for the anode lifespan. This new transient thermal-electric model predicted accurately, with a MARE of 5.2 %, the thermal behavior of the top parts. After 77 % of the anode life, the modeling could be improved by adding mass transfer phenomena such as liquid and gas motions into the anode cover. Still, this transient model has predicted accurately the temperatures in the top parts for a time scale representing more than two weeks. The anode crust properties (k, ρ, c_p) have been determined recently up to 950 °C and it helped to obtain the proper temperature profile in this material [Allard *et al.*, 2019a]. Furthermore, the transient modeling allowed to predict both the ACM to anode crust conversion and the cavity growth in function of time, two phenomena that must be considered to accurately predict the top heat dissipation of AEC.

Operating events such as voltage treatments and anode covering practices can certainly change the thermal constraints on the anode cover, thus resulting in higher ACM → anode crust → cavity transformations with additional anode crust melting and falling toward the bulk liquid bath. During the anode life, the anode crust melts and feeds the AEC with uncontrolled Al_2O_3

quantity. Accordingly, each additional thermal constraint on the anode cover must be considered for improving the industrial AEC control and operation. In summary, the heat generation and consequent heat dissipation have to be maintained stable to reduce anode cover deterioration.

General scheme of the modeling algorithm

The approach for moving geometry, mesh update and nodal interpolation was integrated in two different transient models in order to predict the thermal behavior of the AEC and the anode consumption throughout its lifespan. This modeling approach can be adapted to other finite element models that have to consider time-dependent domains, from the motion of solid bodies or moving boundaries, for example. Figure 7-16 illustrates the method with the meshes taken at two subsequent analysis steps. The downward movement due to anode consumption is remeshed for each analysis step, thereafter the previous nodal temperatures are interpolated and used as initial condition for the current step. The moving front of the anode crust melting is updated at each step and the radiation boundary adapts to the moved location in order to perform the radiosity calculations of each surface. With this method, the nodes remain connected for each analysis step and the mesh conforms to the quality criteria.

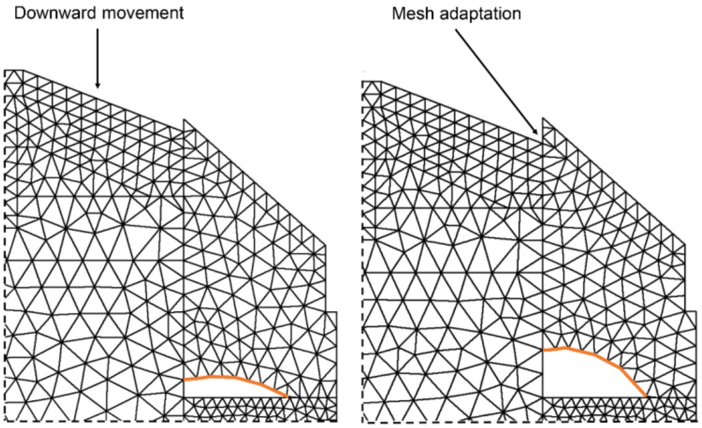

Figure 7-16 General scheme of the moving geometry, mesh update and nodal interpolation approach. The displacement of the moving boundary in orange

The approach for moving geometry, mesh update and nodal interpolation can be applied to larger scale simulations such as the complete electrolysis cell with all its components. This complex modeling case would require important computer resources, but it would allow studying parameters like the complete anode change procedure and the positioning pattern. Moreover, it should permit to get closer to the actual behavior of the industrial AEC, in which the upper parts are moving. The modeling approach is advantageous when applied to simulation cases exhibiting significant deformations or displacements.

7.2.5 Conclusions

A new modeling approach was presented and applied to the transient thermal-electric modeling of a slice of AEC and the anode life cycle. Increasing the operating voltage by 8.5 % for roughly one day affected the thermal balance of the AEC by melting the side ledge and deteriorating the anode cover, as confirmed by both modeling and industrial measurements. The top heat dissipation remained higher due to the irreversible transformations in the anode cover, even once the operating voltage was back at its target. In this occurrence, a new thermal balance has been reached and it was characterized by higher top heat losses (+1.4 % of the total dissipation) and lower side heat losses. Accordingly, the anode crust melted to form a larger cavity and the side ledge adapted to the higher top dissipation by getting thicker.

For the first time, the complete thermal-electric evolution of the anode during all its lifespan was modeled by applying strategies for moving geometry, mesh update and nodal interpolation. The anode life cycle model predicted the temperatures with a MARE of 2.7 %, when compared with the installed thermocouples on the instrumented anode (for $t < 77$ % of the anode life). The transient modeling of the temperature rise in the anode cover was particularly accurate considering the MARE of 1.2 %. Therefore, this novel modeling method combined with the recently improved transient thermal properties (k and c_p of anode crust newly determined from 100 °C to 950 °C) and also the measured boundary conditions allowed to improve the thermal prediction of the top parts of the AEC. The modeling approach allows to consider geometric displacement with high mesh quality and may be applied to other finite element models dealing with large displacements or moving boundaries.

7.2.6 Acknowledgements

This study was supported by Rio Tinto Aluminium, the “Conseil de Recherches en Sciences Naturelles et en Génie du Canada” (CRSNG) and the “Fonds de Recherche du Québec - Nature et Technologies” (FRQNT). The authors wish to thank the staff at Rio Tinto Grande-Baie smelter and Arvida Research & Development Center (ARDC), especially Mr. Jean-François Bilodeau and Mr. Sébastien Guérard from ARDC, for the support provided during the realization of this work.

7.2.7 Appendix A

A modeling method for the geometry and mesh update algorithm followed by the nodal interpolation is detailed in this appendix. This method is applied to the transient thermal-electric modeling of the industrial AEC in order to consider the melting of the anode crust by a moving boundary.

A.1 Python scripting in ANSYS Workbench

The moving geometry and mesh update algorithms are automated with a Python script interpreted by the ANSYS Workbench software. A while loop is programmed to solve each analysis step of the transient model and the results are saved automatically. The principal steps of this method are described by the scheme of Figure 7-17. A previously calculated or a new crust-cavity profile (moving boundary) is input in the parameter set to modify the geometry of the model. Accordingly, the geometry is updated using a Python command and a new mesh in the ANSYS Mechanical model is generated.

A.2 APDL scripting in ANSYS Mechanical

The coupled thermal-electric analysis is performed using Mechanical APDL solver in the ANSYS Mechanical software. APDL commands are integrated to read the load data stored in a CSV file, like the thermal and electric properties or the boundary conditions. The new properties or conditions are applied by APDL commands to the current analysis. The previously calculated temperatures are mapped to the new mesh with an interpolation function (*MOPER) (ANSYS, 2017). This function performs matrix operations by comparing arrays, which contain the previous nodal coordinates and temperatures, and also the new mesh information. A 3D interpolation is applied to get the nodal temperatures on the new mesh. In that simulation case, a similar interpolation method is used to apply the previous material conditions to the newly generated elements. This step allows to consider the irreversible phase transformation in the anode cover (ACM → anode crust). With the previous temperatures and material conditions applied to the new mesh, the transient model is solved for a specified analysis time, before starting the postprocessing. Subsequently, the temperatures in the anode crust are read and a new crust-cavity profile is calculated in order to reach the melting isotherm. The new profile is written in a CSV file to be read by Python commands in order to update the geometric parameter and so on. The nodal coordinates and temperatures are also exported to a CSV file to be read in the next iteration. The procedure in Figure 7-17 is repeated up to the final time of the analysis.

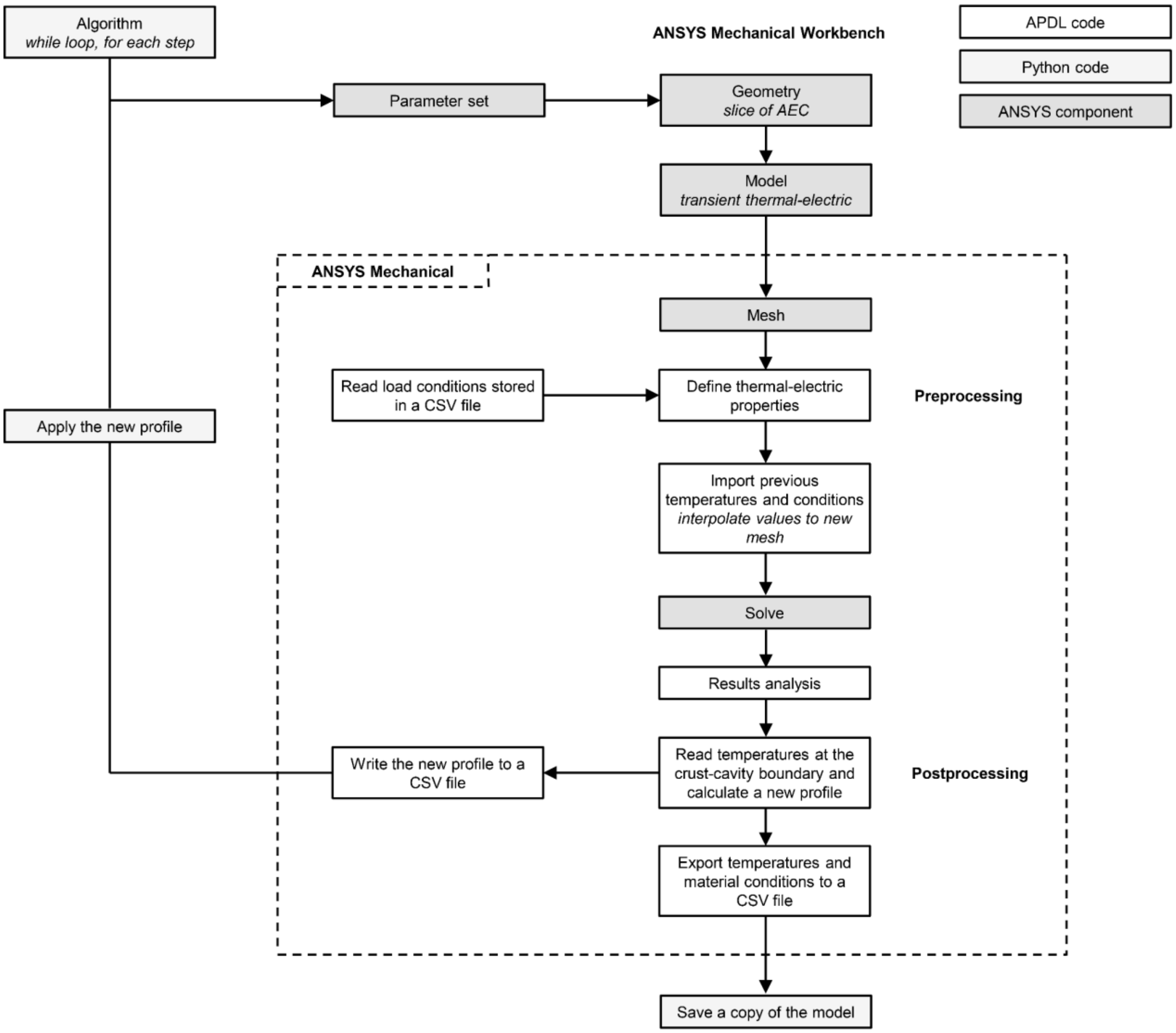

Figure 7-17 Scheme of the modeling algorithm to solve the transient thermal-electric model with geometry and mesh updates, considering the moving boundary at the crust-cavity interface

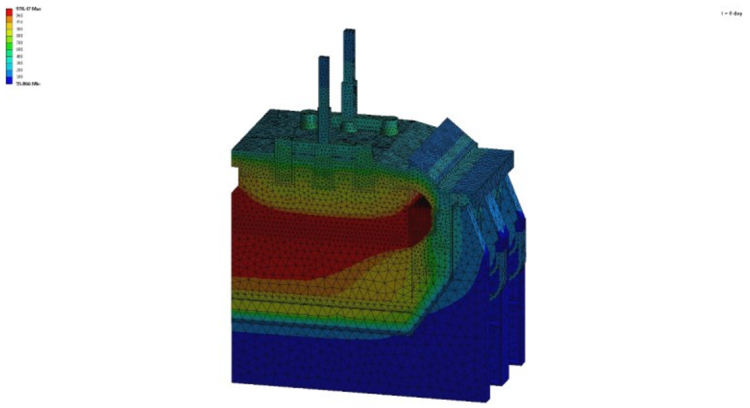

Figure 7-18 A video showing the effect of the voltage increase on the temperatures using the slice of AEC

7.2.8 Appendix B

A moving geometry, mesh update and nodal interpolation method is developed to reflect the anode consumption and its downward displacement in the AEC. The modeling approach is automated with Python scripting and the results are interpolated from one step to the next one with APDL commands. A moving interface for the melting of the anode crust is integrated in this modeling method. This second case additionally integrates an algorithm to consider the time-dependent geometry related to the anode consumption. The motion of the nodes that are located inside the moving parts is governed by the velocity of anode assembly, a downward movement in this case. The node coordinates are modified to follow the anode displacement. Since the geometry is moved and the mesh is automatically updated, the new mesh conforms to the quality criterium initially imposed. The previously calculated nodal temperatures are then applied as initial conditions before the new analysis starts. The complete scheme of resolution is detailed in Figure 7-19.

B.1 Python scripting in ANSYS Workbench

A new aspect of this second model is the displacement of the body parts with automatic updates of the CAD geometry by Python scripting. For each analysis time, a new position is calculated and applied to the moving parts. Since the anode is consumed by the process, its size is imposed before each resolution step. The python script also applies the new location of the moving boundary (anode crust melting) according to the postprocessing results.

B.2 APDL scripting in ANSYS Mechanical

In the ANSYS Mechanical interface, a new mesh is generated for each resolution step. The previously moved nodal and element properties are interpolated and then applied as initial conditions for the thermal-electric model. The boundary conditions and constraints for the analysis are imposed with APDL commands. Thereafter, the model is solved and the postprocessing is performed. During postprocessing, a new crust-cavity profile is calculated only if the anode crust has melted. The nodes in the moving geometry are selected and their coordinated are displaced using matrix operations to account for the downward movement. Consequently, the nodal temperatures and element properties are saved to CSV files to be imported in the next resolution step.

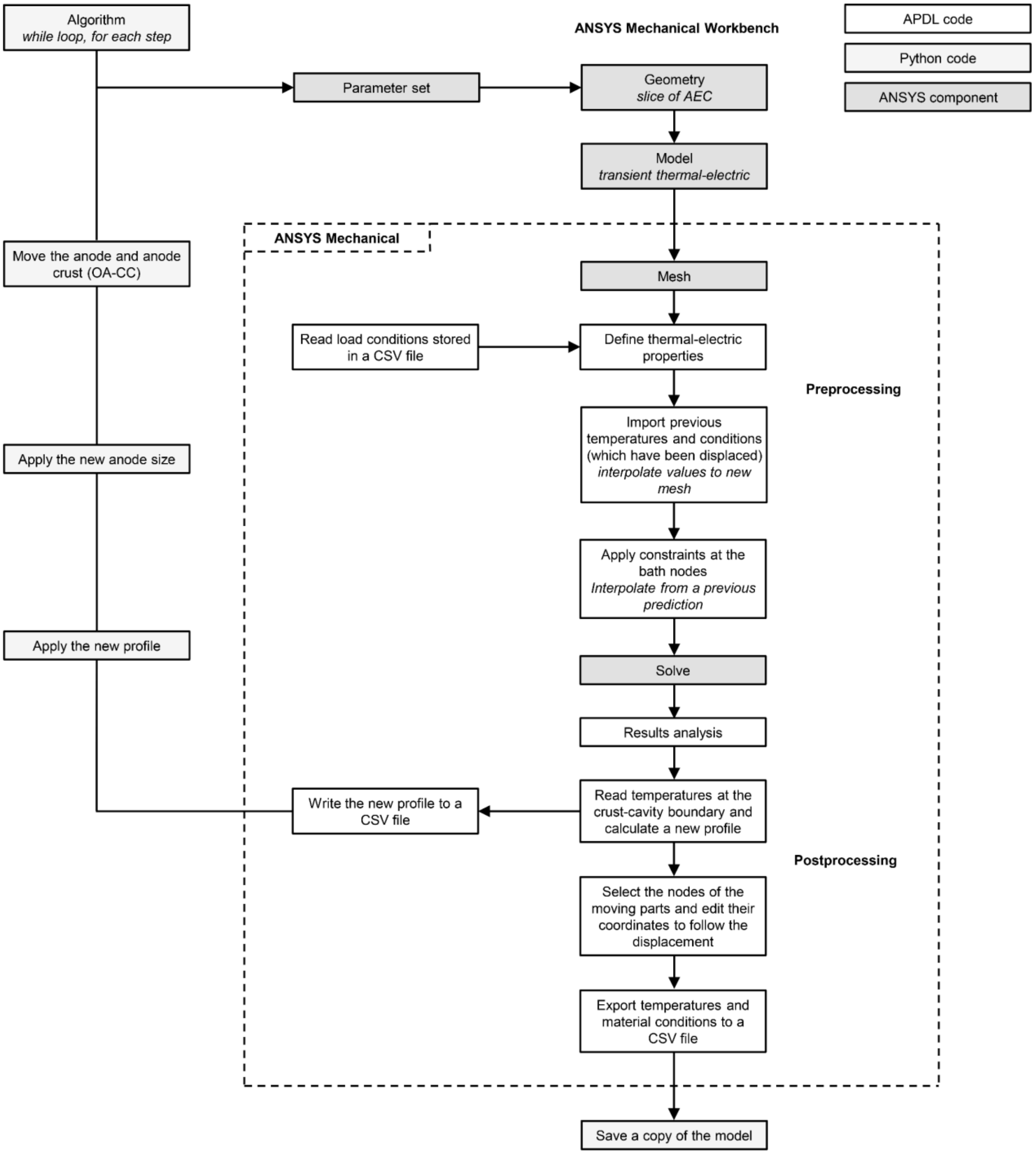

Figure 7-19 Scheme of the modeling algorithm to solve the transient thermal-electric model with moving geometry, mesh update and nodal interpolation, considering both the moving parts and the displacement of crust-cavity interface

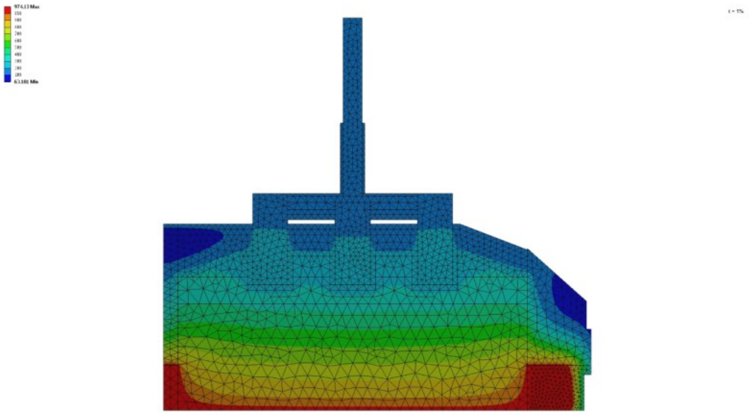

Figure 7-20 A video showing the predicted temperatures during all the anode life cycle

CHAPITRE 8 CONCLUSION

8.1 Sommaire des résultats

L’énergie produite par le procédé d’électrolyse est dissipée en majeure partie par le dessus et par le côté, deux endroits caractérisés par des matériaux complexes à changement de phase. Pour répondre à la question de recherche postulée dans l’introduction : « comment améliorer l’efficacité énergétique de la production d’aluminium en étudiant le comportement des matériaux et la dissipation thermique au-dessus des cellules d’électrolyse? », une étude méticuleuse de caractérisation chimique et thermique a été entreprise, en plus de la large étude de modélisation du transfert thermique en régime permanent et transitoire qui a été menée. Ces travaux de recherche ont été réalisés afin d’obtenir les propriétés thermiques et les conditions aux frontières de la cellule d’électrolyse dans le but de développer des outils de prédiction performants qui permettent d’améliorer la conception et l’opération des cellules d’électrolyse.

L’étude de la composition chimique a démontré par la méthode de quantification Rietveld appliquée sur les patrons de DRX que les principales phases cristallines composant la croûte d’anode industrielle sont les suivantes : $Na_5Al_3F_{14}$, Na_3AlF_6, $Na_2Ca_3Al_2F_{14}$, et Al_2O_3, bien que plus d’une dizaine de phases cristallines composent ce matériau. Le bas de la croûte d’anode, qui fait face au bain liquide, contient davantage de Na_3AlF_6 et présente un *CR* qui se rapproche du bain d’électrolyse. Le dessus de la croûte d’anode possède un *CR* plus faible et contient davantage de la phase acide chiolite ($Na_5Al_3F_{14}$). Ce phénomène s’explique par la pénétration de la vapeur provenant du bain ($NaAlF_4$) et sa réaction avec la croûte d’anode qui produit de la chiolite. Durant l’opération, la température à l’intérieur de la croûte d’anode va de ~950 °C jusqu’à ~500 °C, selon les mesures de thermocouples enregistrées en continu dans ce matériau. Les premières phases liquides apparaissent vers 685 °C, et cette température correspond à la fusion de la phase $NaAlF_4$. Sans la présence de vapeur, la croûte d’anode commence à fondre à une température de 696 °C, dû à la fusion de la phase de cryolite de calcium ($NaCaAlF_6$) et à la fusion partielle de $Na_5Al_3F_{14}$ qui s’échelonne jusqu’à 709 °C. La fin de la fusion des phases de bain électrolytique de la croûte d’anode se situe entre ~890 °C (CR = 1.8) et ~935 °C (CR = 2.2), correspondant à la température où la cryolite (Na_3AlF_6) devient totalement liquide. La croûte d’anode est dissoute par les éclaboussures de bain liquide et par la vapeur fluorée. Elle se détériore lorsque la température locale est suffisante pour que les phases de bain électrolytique demeurent à l'état liquide.

Une fois la nature chimique du matériau de recouvrement anodique et de la croûte d'anode établie, une étude de caractérisation thermochimique et microstructurale a été menée afin d'obtenir les propriétés thermiques de la croûte d'anode industrielle. Une nouvelle méthode a été développée et appliquée pour déterminer la diffusivité thermique à haute température, soit entre 700 °C et 950 °C. La diffusivité thermique de la croûte d'anode a été déterminée par *LFA* sur une plage allant de 100 °C à 950 °C. Par la suite, la capacité thermique massique expérimentale a été déterminée sur des échantillons industriels par *DSC* et elle a aussi été calculée théoriquement par équilibre chimique en connaissant la composition chimique. Avec la densité apparente mesurée, il a été déterminé que la croûte d'anode possède une conductivité thermique variant de 1.38 W/m·K à 0.89 W/m·K pour une plage de température allant de 100 °C à 950 °C. Considérant la chimie de la partie du bas de ce matériau, il y a été déterminé que la cavité qui se forme par la fonte et la dégradation de la croûte d'anode est plus propice à se former à une température d'environ 935 °C. En résumé, cette étude a présenté en détail les propriétés thermiques et thermochimiques de la croûte d'anode, des données primordiales pour améliorer la justesse de la modélisation du transfert thermique.

Le second aspect de cette thèse concerne la modélisation numérique des phénomènes thermiques et électriques se déroulant dans la cellule d'électrolyse, avec l'emphase sur l'amélioration de la justesse de prédiction de la dissipation de chaleur par le dessus. Un modèle thermique-électrique a été développé et résolu en régime permanent, en se basant une géométrie de cellule d'électrolyse de technologie P155. Les prédictions de ce modèle numérique ont été validées par des mesures de flux thermiques et de températures effectuées sur le recouvrement anodique. Le principal élément original de cet article concerne l'amélioration de la représentation géométrique du recouvrement anodique par l'introduction d'une cavité et d'un module de calculs des flux thermiques par rayonnement. En plus de se rapprocher de la physique réelle du recouvrement anodique, ce module de rayonnement a permis d'améliorer la justesse de prédiction. En effet, l'erreur de prédiction est passée de 21.8 % à 7.3 %, lorsque comparée avec des mesures de flux thermiques. Les résultats de simulation ont démontré, comme attendu, que l'augmentation de la taille de la cavité engendre l'augmentation de la dissipation thermique par le haut des cellules d'électrolyse.

Ensuite, le modèle thermique-électrique résolu par la méthode des éléments finis a été amélioré en programmant un algorithme permettant de prédire la forme et la taille de la cavité. La justesse du rayonnement thermique calculée par ce module a été améliorée par des mesures expérimentales de l'émissivité de la croûte d'anode et de l'*ACM*. Selon les mesures par thermographie infrarouge, la croûte d'anode et l'*ACM* possèdent une émissivité variant de 0.98 à 1.00, sur une plage de température allant de 50 °C à 400 °C. La valeur de la conductivité thermique de la croûte d'anode a été confirmée par des mesures de température prises dans ce matériau et par des mesures de flux thermique prises au-dessus de celui-ci. De plus, une méthode de mesure expérimentale a été mise en place pour mesurer les profils des surfaces supérieures de l'*ACM* et de la croûte d'anode dans les cellules d'électrolyse. En considérant une géométrie de recouvrement anodique améliorée (*ACM*, croûte d'anode et cavité) et les propriétés thermiques déterminées expérimentalement, le modèle a été capable de prédire la température dans la croûte d'anode avec une précision de 2.4 %, en se basant sur *MARE*. Les nombreuses campagnes de mesures thermiques sur des cellules d'électrolyse ont aussi permis d'améliorer les conditions limites générales qui ont été utilisées dans ce modèle. Avec ce modèle thermique-électrique validé, l'effet de l'épaisseur d'*ACM* ajoutée sur les anodes et l'impact d'un film de boue couvrant la surface des blocs cathodiques ont été évalués. L'augmentation de l'isolation du recouvrement anodique engendre : 1) une diminution de la dissipation par le haut, 2) la fonte de la croûte d'anode et du talus et 3) l'augmentation de la dissipation par le côté. La fonte excessive de croûte est susceptible de former de la boue, un dépôt résistif de bain liquide sursaturé en Al_2O_3, à la surface des blocs cathodiques. L'ajout d'un film de boue a provoqué une augmentation de génération d'énergie qui a conduit à la fonte de la croûte d'anode et du talus. Dans ces conditions, la fonte importante de la croûte d'anode peut engendrer la formation de la boue, qui va à son tour engendrer davantage de fonte de croûte d'anode, et ainsi de suite… Une fois la génération de chaleur revenue à la normale, il y a risque de croissance du pied de talus puisque le recouvrement anodique sera plus conducteur qu'initialement. Si le film de bain à la surface de la cathode est toujours sursaturé en Al_2O_3, le pied de talus va croître par la déposition d'Al_2O_3 (phase α) à surface de la cathode. Cette condition engendre une augmentation de la résistance électrique et des problèmes opérationnels tels que des courants électriques horizontaux et de l'instabilité électrique. Afin de diagnostiquer des cellules d'électrolyses comportant une dissipation thermique anormale, une corrélation numérique a été dérivée. En effectuant une série de mesures de flux thermique sur le dessus et sur le côté, il est donc possible de cibler des cellules d'électrolyse problématique.

$$\frac{q_{dessus}}{q_{côté}} = f\sqrt{\frac{q''_{ACM}}{q''_{caisson}}} \tag{8-1}$$

Finalement, une nouvelle approche de modélisation thermique-électrique transitoire a été développée afin de simuler l'effet d'une augmentation d'énergie ponctuelle sur le comportement de la cellule d'électrolyse et de prédire l'évolution thermique d'un ensemble anodique et de son recouvrement durant toute leur durée de vie. La nouvelle approche de modélisation considère les variations géométriques temporelles, telles que la fonte de la croûte d'anode et le mouvement de l'ensemble anodique. Comme il s'agit d'un mouvement géométrique considérable, une stratégie de déplacement de géométrie, de mise à jour du maillage et d'interpolation nodale a été mise en place. La Figure 8-1 illustre le maillage de deux étapes subséquentes dans l'analyse par éléments finis.

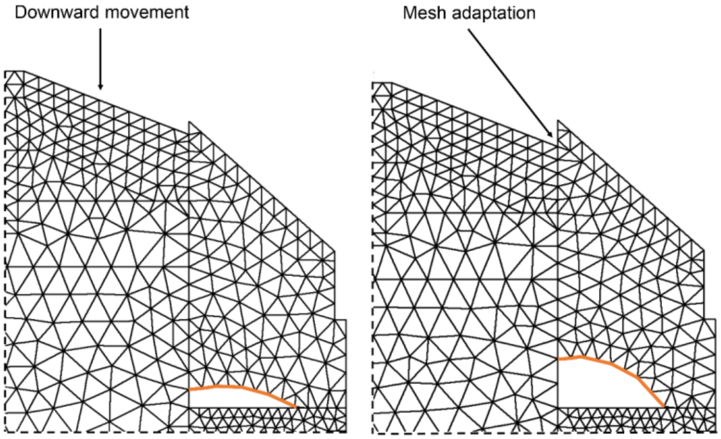

Figure 8-1 Schéma général de la stratégie de déplacement de géométrie, de mise à jour du maillage et d'interpolation nodale; le déplacement de la frontière mobile en orange [Allard *et al.*, 2019c]

En utilisant cette approche, l'impact d'une augmentation d'énergie sur le comportement transitoire de la cellule d'électrolyse a pu être évalué. Cette simulation a été validée à l'aide d'une anode instrumentée et de thermocouples placés dans le recouvrement anodique et dans le bain liquide. Dans la cellule d'électrolyse industrielle et dans la simulation, le potentiel électrique d'opération a été augmenté de 8.5 % durant 23 h, ce qui a engendré une excursion thermique majeure. Cette excursion thermique a engendré la transformation supplémentaire d'ACM en croûte d'anode et l'agrandissement de la cavité, formant ainsi un recouvrement anodique plus conducteur. Donc, l'excursion thermique a engendré un nouvel équilibre thermique caractérisé par une dissipation thermique plus importante par le haut et plus faible par le côté, occasionnant la croissance du talus sur les parois latérales. Comme les transformations dans le recouvrement anodique sont irréversibles, la cellule d'électrolyse se remettra complètement de l'excursion thermique seulement lorsque toutes ses anodes seront remplacées, ce qui peut prendre plusieurs semaines selon la technologie.

Dans un second ordre, la nouvelle stratégie a été appliquée à la modélisation thermique-électrique transitoire de l'évolution d'un ensemble anodique durant tout son cycle de vie, une première pour l'industrie de l'aluminium. Tout d'abord, la géométrie du recouvrement anodique a été mesurée durant la vie de plusieurs anodes pour déterminer les profils d'*ACM* et de croûte d'anode typique. Les toutes dernières propriétés thermiques de la croûte d'anode (k, c_p, ρ) ont été intégrées dans cette géométrie représentative. De plus, ce modèle transitoire intègre des conditions aux limites basées sur plusieurs campagnes de mesures thermiques, qui ont été exécutées durant tout le cycle de vie de trois anodes industrielles. Avec cette géométrie, ces propriétés thermiques et ces conditions aux limites, le cycle de vie de l'anode a été simulé et validé par une anode instrumentée installée dans une cellule d'électrolyse opérant de manière typique. Ce nouveau modèle transitoire a permis de prédire l'évolution de la température dans la croûte d'anode avec une précision de 1.2 % (considérant le *MARE*). De façon plus globale, ce modèle thermique-électrique a prédit la température avec une précision de 2.7 % pour 77 % de la durée de vie de l'anode, en comparant avec toutes valeurs mesurées par les thermocouples installés sur l'ensemble anodique. Finalement, ce modèle transitoire a permis de prédire pour la première fois l'évolution thermique-électrique d'un ensemble anodique durant toute la durée de sa vie dans la cellule d'électrolyse.

8.2 Contributions aux connaissances scientifiques

8.2.1 Contributions au domaine de l'aluminium

La modélisation numérique de la dissipation thermique en régime permanent et transitoire et la validation des simulations par des mesures au-dessus de cellules d'électrolyse d'aluminium a été complétée dans le cadre de ce projet de recherche. De plus, les prédictions ont été améliorées par la caractérisation chimique et thermique des matériaux composant le recouvrement anodique. La modélisation thermique-électrique en régime permanent permet de simuler l'opération typique de cellules d'électrolyse et celle en régime transitoire rend possible l'analyse d'événements influençant l'opération. Dans le cadre de ce projet de recherche, la fidélité des outils de prédiction a été améliorée par :

- Mise en place d'une géométrie de recouvrement anodique basée sur des mesures
- Détermination des propriétés thermiques (α, k *et* ε) et thermochimiques (c_p, enthalpie, T de transition de phases, ρ en fonction de T) de la croûte d'anode
  - Nouvelle méthode pour déterminer α à haute température (700 °C à 950 °C)
  - Émissivités de l'*ACM* et de la croûte d'anode déterminées expérimentalement
- Mesure des conditions limites générales au-dessus des cellules d'électrolyse
- Développement d'une nouvelle méthode de modélisation en régime permanent, considérant la cavité qui se forme sous la croûte d'anode
  - Mise en place du module de radiosité pour prédire le rayonnement thermique
  - Établissement d'une corrélation numérique simple pour le diagnostic thermique
- Mise en place d'une nouvelle stratégie de modélisation transitoire par éléments finis intégrants des variations géométriques temporelles

À l'aide de ces outils de prédiction thermique-électrique et des recommandations provenant des chapitres précédents de cette thèse, il est possible d'améliorer l'efficacité énergétique de la production d'aluminium. En autres, la conception et le contrôle des cellules d'électrolyse de différentes technologies peuvent être ajustés pour minimiser la fonte de croûte d'anode menant à la formation de boue sur les blocs cathodiques. De plus, le lien entre la dissipation thermique par le haut et par le côté a été démontré, ainsi que représenté par une corrélation numérique. Certaines contributions au domaine de la production d'aluminium primaire peuvent aussi s'appliquer de façon plus générale aux disciplines de la caractérisation chimique et thermique des matériaux inorganiques, du diagnostic thermique et de la modélisation numérique par éléments finis du transfert thermique.

8.2.2 Contributions à la discipline de la caractérisation de matériaux

Les méthodes de caractérisation chimique, telles que la DRX, l'analyse quantitative Rietveld et l'analyse élémentaire de l'oxygène, peuvent aussi s'appliquer à d'autres types d'échantillons provenant de la cellule d'électrolyse (bain d'électrolyse, talus, pied de talus, boue ou film de bain) ou encore à d'autres types de sels électrolytiques. Par exemple, ces travaux de recherche ont permis de quantifier l'Al_2O_3 amorphe présent dans les échantillons de croûte d'anode en effectuant le bilan entre les phases cristallines et l'Al_2O_3 quantifié par analyse élémentaire, une méthode qui serait aussi adéquate pour les dépôts à la cathode (pied de talus et boue).

Les propriétés thermiques ont été déterminées par *LFA* et *DSC* en mesurant la densité apparente. La quantification de la conductivité thermique de bains électrolytiques à l'état solide-liquide est une nouvelle contribution. En couplant une nouvelle méthode de détermination de la diffusivité thermique avec des calculs d'équilibre chimique (FactSage), il est possible de quantifier la conductivité thermique du bain électrolytique à haute température ($T > 700$ °C).

8.2.3 Contributions à la discipline de la modélisation numérique et validation expérimentale

Afin de prédire le comportement réel de la cellule d'électrolyse, les modèles thermiques-électriques ont été validés par des campagnes de mesures expérimentales. L'intégration de propriétés thermiques méticuleusement évaluées, la mesure de la géométrie typique et la détermination des conditions limites ont permis de minimiser l'écart entre les simulations et les mesures thermiques prises sur les cellules d'électrolyse industrielles.

Afin de résoudre un problème industriel, une nouvelle stratégie de modélisation thermique-électrique en régime transitoire a été établie. Cette stratégie permet de modifier la géométrie, de mettre à jour le maillage et d'interpoler les températures aux nœuds. L'algorithme présenté dans le Chapitre 7 permet de considérer des mouvements dans la géométrie tout en conservant la qualité de maillage, ce qui apporte une flexibilité supplémentaire pour modéliser des phénomènes physiques par la méthode des éléments finis.

8.2.4 Contributions à la société : économie et environnement

Entre autres, la recherche et développement du procédé d'électrolyse vise à améliorer le bilan environnemental et économique de l'industrie de l'aluminium. Ce projet de recherche présente des nouvelles propriétés de matériaux, méthodes de diagnostic thermique et modèles numériques permettant d'améliorer la conception et l'opération des cellules d'électrolyse. De plus, la durée de vie des équipements peut être améliorée en étudiant les contraintes thermiques locales et optimisant la stabilité thermique du procédé.

8.3 Nouvelles perspectives de recherche

Bien que cette thèse ait couvert le sujet de la caractérisation chimique et thermique du recouvrement anodique et l'aspect de la modélisation numérique de cellules d'électrolyse d'aluminium, de nouvelles perspectives méritant d'être explorées ont été générées par les travaux de recherche.

8.3.1 Caractérisation des matériaux

Les nouvelles méthodes pour déterminer les propriétés thermiques devraient être appliquées au talus, un matériau crucial pour l'opération de la cellule d'électrolyse. Selon les circonstances, ce matériau peut contenir des phases liquides à l'intérieur de la matrice de cristaux de Na_3AlF_6. La conductivité thermique du talus à l'état solide-liquide pourrait donc être déterminée par la méthode expliquée au Chapitre 4. De façon similaire, cette méthode peut être appliquée au pied de talus et à la boue, deux matériaux qui présentent très peu de données thermiques. De plus, l'émissivité des autres matériaux présents dans la cellule d'électrolyse mériterait d'être examinée de façon rigoureuse. Ces matériaux sont recouverts d'alumine, de bain électrolytique et de diverses impuretés et devraient présenter des valeurs s'écartant des valeurs typiques de la littérature. De plus, les méthodes de caractérisation chimique pourraient être améliorées afin de caractériser les traces d'impuretés dans le bain, le recouvrement anodique et le talus.

8.3.2 Modélisation thermique-électrique

La méthode des éléments finis présente l'avantage de résoudre efficacement les équations thermiques et électriques. Avec un système informatique performant, la nouvelle stratégie de modélisation transitoire par éléments finis, qui intègre des variations géométriques temporelles, pourrait permettre d'étudier l'opération d'une cellule d'électrolyse complète, en incluant les mouvements de cadres anodiques. La génération d'énergie par effet Joule et la dissipation thermique dans la cellule complète pourraient donc être simulées par cette méthode.

Toutefois, le transport de l'énergie par le mouvement de la matière n'a pas été considéré dans ces modèles thermiques-électriques. Par exemple, les flammes sortant par les fissures et les trous dans le recouvrement anodique n'ont pas été considérées dans les travaux. Une étude rigoureuse à l'aide de *computational fluid dynamics* (*CFD*) et de validation expérimentale par des capteurs de pression et de vitesse des gaz pourrait contribuer à améliorer la précision des simulations. De plus, les aspects transitoires de la fonte de croûte d'anode, de sa solubilisation dans le bain liquide et de sa déposition sur les blocs cathodiques pourraient être simulés par *CFD* afin de préciser davantage les phénomènes engendrant des problèmes d'opération.

ANNEXE A

A.1 Microtomographie aux rayons X

Afin de supporter les analyses de diffusivité thermique présentées au Chapitre 4 et d'observer la configuration microstructurale, un échantillon en forme de disque a été étudié par microtomographie aux rayons X. L'appareil Bruker Skyscan 1172 possédant une caméra 10 Mpx a été utilisé pour produire des images d'environ 4 µm/voxel, tout en fonctionnant à 70 kV et 142 µA avec un filtre Al de 0.5 mm. Les mesures, la visualisation et la reconstruction du volume 3D ont été réalisées à l'aide de la série de logiciels Skyscan.

Un volume de haute résolution a été construit à partir de l'échantillon de croûte d'anode OA-2 (pris au-dessus de l'anode). Avec le volume 3D, il est possible d'observer des particules de haute densité et des pores présents dans cet échantillon industriel. La Figure A-1 montre le volume construit à partir de l'analyse de microtomographie aux rayons X de l'échantillon OA-2.

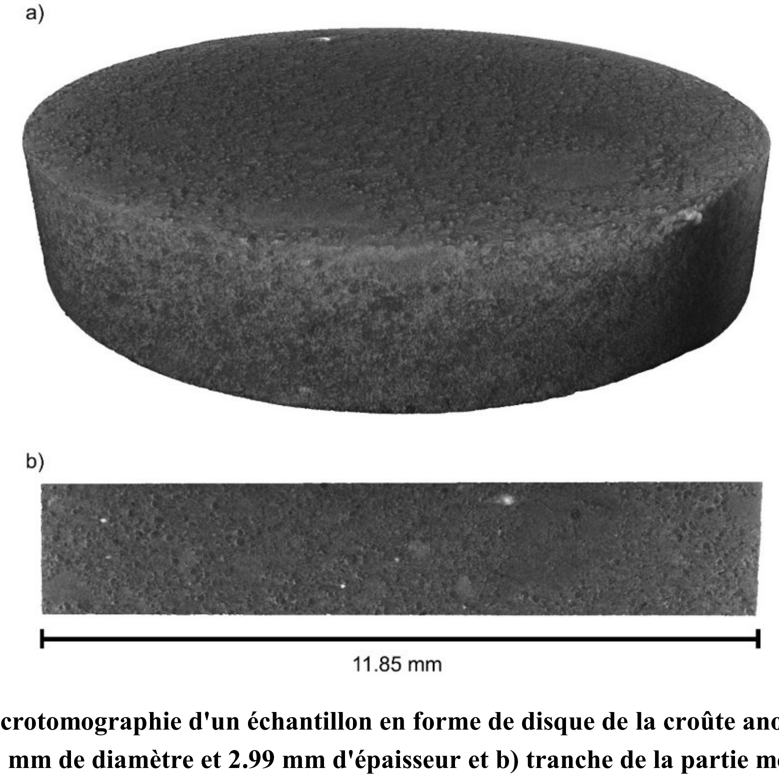

Figure A-1 Microtomographie d'un échantillon en forme de disque de la croûte anodique (OA-2): a) disque de 11.85 mm de diamètre et 2.99 mm d'épaisseur et b) tranche de la partie médiane du disque

LISTE DES RÉFÉRENCES

Abbas, H., Taylor, M.P., Farid, M. et Chen, J.J. (2009). The impact of cell ventilation on the top heat losses and fugitive emissions in an aluminium smelting cell. *TMS Light Metals*, p. 551-556.

ANSYS (2013). *ANSYS Mechanical APDL theory reference* (Guide). ANSYS, Canonsburg, États-Unis, 988 p.

ANSYS (2013). *ANSYS Fluent theory guide* (Guide). ANSYS, Canonsburg, États-Unis, 814 p.

ANSYS (2017). *ANSYS Mechanical APDL theory reference* (Guide). ANSYS, Canonsburg, États-Unis, 894 p.

Allais, B. (2013). AP technology platform for high amperage pots begins demonstration phase. *Light Metal Age*, volume 71, numéro 1, p. 42.

Allard, F., Soucy, G. et Rivoaland, L. (2014). Formation of deposits on the cathode surface of aluminum electrolysis cells. *Metallurgical and Materials Transactions B*, volume 45, numéro 6, p. 2475-2485.

Allard, F., Coulombe, M.A., Soucy, G. et Rivoaland, L. (2014). Cartography and chemical composition of the different deposits in the Hall-Heroult process. *TMS Light Metals*, p. 1233-1238.

Allard, F. (2014). *Étude des mécanismes de formation et du comportement des dépôts au pourtour de cellules d'électrolyse d'aluminium*. Mémoire de maîtrise, Université de Sherbrooke, Québec, Canada, 153 p.

Allard, F., Soucy, G., Rivoaland, L. et Désilets, M. (2015a). Thermodynamic and thermochemical investigation of the deposits formed on the cathode surface of aluminum electrolysis cells. *Journal of Thermal Analysis and Calorimetry*, volume 119, numéro 6, p. 1303-1314.

Allard, F., Désilets, M., LeBreux, M. et Blais, A. (2015b). Chemical characterization and thermodynamic investigation of anode crust used in aluminum electrolysis cells. *TMS Light Metals*, p. 565-570.

Allard, F., Désilets, M., LeBreux, M. et Blais, A. (2016). The impact of the cavity on the top heat losses in aluminum electrolysis cells. *TMS Light Metals*, p. 289-294.

Allard, F., Désilets, M., et Blais A. (2019a). Thermal, chemical and microstructural characterization of anode crust formed in aluminum electrolysis cells. *Thermochimica Acta*, volume 671, p. 89-102.

Allard, F., Désilets, M., LeBreux, M. et Blais, A. (2019b). Improved heat transfer modeling of the top of aluminum electrolysis cells. *International Journal of Heat and Mass Transfer*, en production.

Allard, F., Désilets, M., et Blais A. (2019c). A modeling approach for time-dependent geometry applied to transient heat transfer of aluminum electrolysis cells. *Metallurgical and Materials Transactions B*, en révision.

An, X.H., Cheng, J.H., Yin, H.Q., Xie, L.D. et Zhang, P. (2015). Thermal conductivity of high temperature fluoride molten salt determined by laser flash technique. *International Journal of Heat and Mass Transfer*, volume 90, p. 872-877.

Aluminium Association of Canada (2014). Canadian Primary Aluminum Production. http://www.aluminum.org/sites/default/files/css/CanadianPrimaryProduction092014.pdf (page consultée le 21 octobre 2014).

Aluminium Association of Canada (2017). Portrait of the Canadian Aluminium Industry. https://aluminium.ca/uploader/publications/portrait_alu_cdn_eng_final.pdf (page consultée le 22 juin 2018).

Apisarov, A., Dedyukhin, A., Nikolaeva, E., Tinghaev, P., Tkacheva, O., Redkin, A. et Zaikov, Y. (2011). Liquidus temperatures of cryolite melts with low cryolite ratio. *Metallurgical and Materials Transactions B*, volume 42, numéro 1, p. 236-242.

Ariana, M., Désilets, M., Proulx et P. (2014). On the analysis of ionic mass transfer in the electrolytic bath of an aluminum reduction cell. *Canadian Journal of Chemical Engineering*, volume 92, p. 1951-1964.

Association de l'aluminium du Canada (2012). Rapports de développement durable. http://ledialoguesurlaluminium.com/d%C3%A9veloppement-durable/rapports-de-d%C3%A9veloppement-durable (page consultée le 21 octobre 2014).

ASTM (2010). *ASTM E1862 - 10: Standard test methods for measuring and compensating for reflected temperature using infrared imaging radiometers* (Norme). ASTM International, West Conshohocken, États-Unis, 3 p.

ASTM (2011). *ASTM E1269 - 11: Standard test method for determining specific heat capacity by differential scanning calorimetry* (Norme). ASTM International, West Conshohocken, États-Unis, 6 p.

ASTM (2013). *ASTM E1461 - 13: Standard test method for thermal diffusivity by the flash method* (Norme). ASTM International, West Conshohocken, États-Unis, 11 p.

ASTM (2014). *ASTM E1933 - 14: Standard practice for measuring and compensating for emissivity using infrared imaging radiometers* (Norme). ASTM International, West Conshohocken, États-Unis, 3 p.

Bale, C.W., Bélisle, E., Chartrand, P., Decterov, S.A., Eriksson, G., Gheribi, A.E., Hack, K., Jung, I.H., Kang, Y.B., Melançon, J., Pelton, A.D., Petersen, S., Robelin, C., Sangster, J., Spencer, P. et Van Ende, M.A. (2016). FactSage thermochemical software and databases, 2010-2016. *Calphad: Computer Coupling of Phase Diagrams and Thermochemistry*, volume 54, p. 35-53.

Bardet, B., Foetisch, T., Renaudier, S., Rappaz, J., Flueck, M. et Picasso, M. (2016). Alumina dissolution modeling in aluminium electrolysis cell considering MHD driven convection and thermal impact. *TMS Light Metals*, p. 315-319.

Barrillon, E. (1967). Evolution thermique de la texture poreuse des cokes de petrole. *Carbon*, Volume 5, p. 167-171.

Barrillon, E. (1968). Modification de la texture du coke de petrole lors d'une desulfuration thermique. *Journal Chimie Physique*, volume 65, numéro 3, p. 428.

Beck, T.R. (1982). New directions in the aluminum industry. Electrochemistry in Industry. Springer, Boston, États-Unis, p. 331-350.

Bergman, T., Lavine, A.S., Incropera, F.P. et Dewitt, D.P. (2011). Fundamentals of heat and mass transfer, 7^{e} édition. John Wiley & Sons, Hoboken, États-Unis, 1076 p.

Bertrand, C., Marois, M.A., Désilets, M., Soucy, G. et Lacroix, M. (2013). A combined 2D inverse predictions and experimental analysis for the bank formation inside a metallurgical reactor. *International Journal of Heat and Mass Transfer*, volume 59, numéro 1, p. 58-65.

Bird, R.B., Warren, E.S. et Lightfoot, E.N. (2007). *Transport phenomena*, 2^{e} édition. John Wiley & Sons, Hoboken, États-Unis, 928 p.

Blais, M., Désilets, M. et Lacroix, M. (2013). Optimization of the cathode block shape of an aluminum electrolysis cell. *Applied Thermal Engineering*, volume 58, p. 439-446.

Blumm, J. et Opfermann, J. (2002). Improvement of the mathematical modeling of flash measurements. *High Temperatures – High Pressures*, volume 34, p. 515-521.

Bopp, A.F., Groff, G.B. et Howard, B.H. (1984). Influence of maximum temperature and heat soak times on the properties of calcined coke. *TMS Light Metals*, p. 869-882.

Brandzaeg, S.R. et Oye, H.A. (1985). High temperature calcination of anthracite, petrol coke and pitch coke. *TMS Light Metals*, p. 839-852.

Bruggeman, J.N. et Danka, D.J. (1990). Two-dimensional thermal modeling of the Hall-Heroult cell. *TMS Light Metals*, p. 203-209.

Cape, J.A. et Lehman, G.W. (1963). Temperature and finite pulse-time effects in the flash method for measuring thermal diffusivity. *Journal of Applied Physics*, volume 34, p. 1909-1913.

Cassayre, L., Palau, P., Chamelot, P. et Massot, L. (2010). Properties of low-temperature melting electrolytes for the aluminum electrolysis process: A review. *Journal of Chemical and Engineering Data*, volume 55, numéro 11, p. 4549-4560.

Chartrand, P. et Pelton, A.D. (2002). A predictive thermodynamic model for the Al-NaF-AlF_3-CaF_2-Al_2O_3 system. *TMS Light Metals*, p. 245-252.

Chessa, J., Smolinski, P. et Belytschko, T. (2002). The extended finite element method (XFEM) for solidification problems. *International Journal for Numerical Methods in Engineering*, volume 53, numéro 8, p. 1959-1977.

Clough R.W. (1960). The finite element method in plane stress analysis. *Proc. 2nd ASCE Conf. on Electronic Computation*, Pittsburg, États-Unis.

Cohen, M.F. et Greenberg, D.P. (1985). The hemi-cube: a radiosity solution for complex environments. *Computer Graphics*, volume 19, numéro 3, p. 31-40.

Coulombe, M.A., Soucy, G., Rivoaland, L. et Davies, L. (2016a). Factors leading to the formation of a resistive thin film at the bottom of aluminum electrolysis cells. *Metallurgical and Materials Transactions B*, volume 47, p. 1280-1295.

Coulombe, M.A., Soucy, G., Désilets, M. et Lombard, D. (2016b) The effect of ledge toe and thin film formation on cathode voltage drop in aluminium electrolysis cells. *Canadian Metallurgical Quarterly*, volume 55, p. 376-386.

Craig, D.F. et Brown, J.J. (1980). Phase equilibria in the system CaF_2-AlF_3. *Journal of the American Ceramic Society*, volume 60, numéro 9, p. 396-398.

Désilets, M., Marceau, D. et Fafard, M. (2003). START-Cuve: Thermo-electro-mechanical transient simulation applied to electrical preheating of a Hall-Héroult cell. *TMS Light Metals*, p. 247-254.

Dreyer, M., Samanos, B. et Vogt, F. (1996). Coke calcination levels and aluminum anode quality. *TMS Light Metals*, p. 93-100.

Dupuis, M., Bojarevics, V. et Freibergs, J. (2004). Demonstration thermo-electric and MHD mathematical models of a 500 KA aluminum electrolysis cell: Part 2. *TMS Light Metals*, p. 453-459.

Dupuis, M. et Tabsh, I. (1991). Thermo-electric coupled field analysis of aluminum reduction cells using ANSYS parametric design language. *Proceeding of the ANSYS Parametric Design Language*, volume 3, p. 80-92.

Dupuis, M. (1994). Thermo-electric analysis of the grande-baie aluminum reduction cell. *TMS Light Metals*, p. 339-342.

Dupuis, M. (1998). Computation of aluminum reduction cell energy balance using ANSYS finite element models. *TMS Light Metals*, p. 409-417.

Dupuis, M. (2000). Thermo-electric design of a 400 kA cell using mathematical models: A tutorial. *TMS Light Metals*, p. 297-302.

Dupuis, M. et Bojarevics, V. (2005). Weakly coupled thermo-electric and MHD mathematical models of an aluminium electrolysis cell. *TMS Light Metals*, p. 449-454.

Eggen, T., Rolseth, S., Rye, K. et Thonstad, J. (1992). Alumina crusting in cryolitic melts. Part I: Penetration of molten electrolyte into alumina. *TMS Light Metals*, p. 495-502.

Eick, I., Rausch, B., Chmelar, J. et Kohaupt, U. (2010). Processing of anode cover material. *TMS Light Metals*, p. 547-552.

Einarsrud, K.E., Skybakmoen, E. et Solheim, A. (2014). On the influence of MHD driven convection on cathode wear. *TMS Light Metals*, p. 485-490.

Eriksson, G. et Hack, K. (1990). ChemSage-a computer program for the calculation of complex chemical equilibria. *Metallurgical Transactions B*, volume 21, p. 1013-1023.

Fallah-Mehrjardi, A., Hayes, P.C. et Jak, E. (2014). Investigation of freeze-linings in aluminum production cells. *Metallurgical and Materials Transactions B*, volume 45, p. 1232-1247.

Feret, F.R. (2008). Breakthrough in analysis of electrolytic bath using Rietveld-XRD method. *TMS Light Metals*, p. 343-346.

Fischer, W.K. et Perruchoud, R. (1985). Influence of coke calcination parameters on petroleum coke quality. *TMS Light Metals*, p. 811-826.

Fischer, W.K. et Perruchoud, R. (1987). Determining prebaked anode properties for aluminum production. *JOM: the Journal of the Minerals, Metals & Materials Society*, volume 39, numéro 11, p. 43-45.

Fisher, W.K., Mannweiler, U., Keller, F., Perruchoud, R.C. et U. Bûhler (1995). *Anodes for the aluminium industry*. 1$^{\text{ère}}$ edition, R&D Carbon Ltd., Sierre, Suisse, 394 p.

Foosnaes, T., Grjotheim, K., Huglen, R., Kvande, H., Lillebuen, B., Mellerud, T. et Naterstad, T. (1993). *Introduction to aluminium electrolysis: Understanding the Hall-Héroult process*. 2$^{\text{e}}$ édition, Aluminium-Verlag, Düsseldorf, Allemagne, 260 p.

Fortin, H. (2009). *Modélisation du comportement thermo-électro-mécanique de l'anode de carbone utilisée dans la production primaire de l'aluminium*. Mémoire de maîtrise, Université Laval, Québec, Canada, 110 p.

Fortin, H., Kandev, N. et Fafard, M. (2012). FEM analysis of voltage drop in the anode connector induced by steel stub diameter reduction. *Finite Elements in Analysis and Design*, volume 52 p. 71-82.

Foster, P.A. (1975). Phase diagram of a portion of the system Na_3AlF_6-AlF_3-Al_2O_3. *Journal of the American Ceramic Society*, volume 58, p. 288-291.

Fraser, K., Taylor, M. et Jenkin, A. (1990). Electrolyte heat and mass transport processes in Hall-Heroult electrolysis cells. *TMS Light Metals*, p. 221-226.

Gadd, M.D., Welch, B.J. et Ackland, A.D. (2000). The effect of process operations on smelter cell top heat losses. *TMS Light Metals*, p. 231-237.

Gaertner, H., Ratvik, A.P. et Aarhaug, T.A. (2011). Particulate emissions from electrolysis cells. *TMS Light Metals*, p. 345-350.

Garbarino, R.M. et Tonti, R.T. (1993). Desulfurization and its effect on calcined coke properties. *TMS Light Metals*, p. 517-520.

Geay, P.Y., Welch, B. J. et Homsi, P. (2001). Sludge in operating aluminium smelting cells. *TMS Light Metals*, p. 541-547.

Gehlbach, R.E., Grindstaff, L.l. et Whittaker, M.P. (1976). Effect of calcination temperature on real density of high sulfur coke. *Journal of Metals*, volume 28 numéro 12, p. A31.

Gerlach, J. et Winkhaus, G. (1985). Interactions of alumina with cryolite-based melts. *TMS Light Metals*, p. 301-313.

Gheribi, A.E., Salanne, M. et Chartrand, P. (2016). Formulation of temperature-dependent thermal conductivity of NaF, β-Na_3AlF_6, $Na_5Al_3F_{14}$, and molten Na_3AlF_6 supported by equilibrium molecular dynamics and density functional theory. *Journal of Physical Chemistry C*, volume 120, p. 22873-22886.

Gheribi, A.E. et Chartrand, P. (2017). Thermal conductivity of compounds present in the side ledge in aluminium electrolysis cells. *JOM: the Journal of the Minerals, Metals & Materials Society*, volume 69, p. 2412-2417.

Gheribi, A.E., Poncsák, S., Guérard, S., Bilodeau, J.F., Kiss, L. et Chartrand, P. (2017). Thermal conductivity of the sideledge in aluminium electrolysis cells: experiments and numerical modelling. *Journal of Chemical Physics*, volume 146, p. 1-10.

Girault, G., Faure, M., Bertolo, J.M., Massambi, S. et Bertran, G. (2011). Investigation of solutions to reduce fluoride emissions from anode butts and crust cover material. *TMS Light Metals*, p. 351-356.

Groutso, T., Taylor, M. et Hudsoný, A.K. (2009). Aspects of crust formation from today's anode cover material. *TMS Light Metals*, p. 405-410.

Gudmundsson, H. (2009). Improving anode cover material quality at Nordural - Quality tools and measures. *TMS Light Metals*, p. 467-472.

Gusberti, V., Severo, D.S., Welch, B.J. et Skyllas-Kazacos, M. (2012). Modeling the mass and energy balance of different aluminium smelting cell technologies. *TMS Light Metals*, p. 929-934.

Hacini, L., Bilodeau, J. et Caratini, Y. (2014). AP60 cell start-up: Thermal electrical mechanical quarter cell model. *TMS Light Metals*, p. 673-678.

Haines, P.J. (1995). *Thermal methods of analysis: principles, applications and problems*, 1ère edition, Springer Netherlands, Pays-Bas, 286 p.

Hardin, E.E., Beilharz, C.L. et Melvin, L.L. (1993). A comprehensive review of the effect of coke structure and properties when calcined at various temperatures. *TMS Light Metals*, p. 501- 508.

Hardin, E.E., Ellis, P.J., Beilharz, C.L. et McCoy, L. (1994). A comprehensive review of the effects of calcination at various temperatures on coke structure and properties part II. *TMS Light Metals*, p. 571-581.

Haupin, W.E. (1971). Calculating thickness of containing walls frozen from melt, *TMS Light Metals*, p. 188-194.

Hatem, G., Llavona, M., Log, T., Sancho, J.P. et Ostvold, T. (1989). Thermal conductivity of some alumina powders and synthetic Hall-Heroult crusts. *TMS Light Metals*, p. 365-370.

Haugland, E., Børset, H., Gikling, H. et Høie, H. (2003). Effects of ambient temperature and ventilation on shell temperature, heat balance and side ledge of an alumina reduction cell. *TMS Light Metals*, p. 269-276.

Haupin, W.E. (1971). Calculating thickness of containing walls frozen from melt. *JOM: the Journal of the Minerals, Metals & Materials Society*, volume 23, p. 41-44.

Heintz, E.A. (1978). Crystallite growth and ordering of cokes in the pre-graphitization temperature range. *Proc. 5th London International Carbon and Graphite Conference of Society of Chemical Industry*, volume 2, p. 575-587.

Hemrick, J.G., Kistler, C.W., Wereszczak, A.A. et Ferber, M.K. (2003). Thermal conductivity of alumina measured with three techniques. *Journal of Testing and Evaluation*, volume 31, p. 438-442.

Hives, J., Thonstad, J., Sterten, A. et Fellner, P. (1996). Electrical conductivity of molten cryolite-based mixtures obtained with a tube-type cell made of pyrolytic boron nitride. *Metallurgical and Materials Transactions B*, volume 27, 255-261.

Hou, T.X., Jiao, Q., Chin, E., Crowell, W. et Celik, C. (1995). A numerical model for improving anode-stub design in aluminum smelting process. *TMS Light Metals*, p. 755-761.

Hukseflux (2003). *HF01 high temperature heat flux sensor (version 1211)* (Rapport). Hukseflux Thermal Sensors, Delft, Pays-Bas, 26 p.

Hydro-Québec (2017). Bilan de la production nette et des achats d'électricité d'Hydro-Québec (GWh). http://www.hydroquebec.com/developpement-durable/energie-environnement/tableau-bilan-production-nette-achats-hq.html (page consultée le 22 juin 2018).

International Aluminium Institute (2011). Global Aluminium Industry Sustainability Performance 2010. http://www.world-aluminium.org/media/filer_public/2013/01/15/2011_-_for_iai_website.pdf (page consultée le 21 novembre 2014).

International Aluminium Institute (2014). Primary Aluminium Production. http://www.world-aluminium.org/statistics/primary-aluminium-production/#data (page consultée le 21 octobre 2014).

International Aluminium Institute (2017). Primary Aluminium Production. http://www.world-aluminium.org/statistics/#data (page consultée le 22 juin 2018).

ISO (2000). *ISO 11713:2000 : Carbonaceous materials used in the production of aluminium - Cathode blocks and baked anodes - Determination of electrical resistivity at ambient temperature* (Norme). International Organization for Standardization, Genève, Suisse, 4 p.

Johnson, A.A. et Tezduyar, T.E., (1994). Mesh update strategies in parallel finite element computations of flow problems with moving boundaries and interfaces. *Computer Methods in Applied Mechanics and Engineering*, volume 119, p. 73-94.

Johnston, T.J. et Richards, N.E. (1983). Correlation between alumina properties and crusts. *TMS Light Metals*, p. 623-639.

Kirik, S.D. et Zaitseva, J.N. (2010). $NaAlF_4$: Preparation, crystal structure and thermal stability. *Journal of Solid State Chemistry*, volume 183, numéro 2, p. 431-436.

Kiss, I.L. et Dassylva-Raymond, V. (2008). Freeze thickness in the aluminum electrolysis cells. *TMS Light Metals*, p. 431-436.

Kjelstrup, S., Svinsas, E. et Hansen, E.M. (1998). Dissipated energy in the aluminum electrolysis. *TMS Light Metals*, p. 467-474.

Kunii, D. et Smith, J.M. (1960). Heat transfer characteristics of porous rocks. *American Institute of Chemical Engineers Journal*, volume 6, numéro 1, p. 71-78.

Kvande, H. (1983). Vapour-phase studies of NaF-AlF_3 melts. 1. The AlF_3- rich part. *High Temperatures - High Pressures*, volume 15, numéro 1, p. 51-62.

Langlois, S., Rappaz, J., Martin, O., Caratini, Y., Flueck, M., Masserey, A. et Steiner, G. (2015). 3D coupled MHD and thermo-electrical modelling applied to AP Technology pots. *TMS Light Metals*, 771-775.

LeBreux, M., Désilets, M., Blais, A. et Lacroix, M. (2014). On the prediction of the crust evolution inside aluminum electrolysis cells. *TMS Light Metals*, p. 655-660.

LeBreux, M., Désilets, M., Allard, F. et Blais, A. (2016). Modeling and measurements of anode cover behavior inside aluminum electrolysis cells. *Numerical Heat Transfer, Part A: Applications*, volume 69, numéro 2, p. 128-145.

Less, L.N. (1977). The crusting behavior of smelter aluminas. *Metallurgical Transactions B*, volume 8, numéro 1, p. 219-225.

Lewis, R.W., Nithiarasu, P. et Seetharamu, K. (2004). *Fundamentals of the finite element method for heat and fluid flow*. John Wiley & Sons, 356 p.

Liu, J., Fallah-Mehrjardi, A., Shishin, D., Jak, E., Dorreen, M. et Taylor, M. (2017). Investigation of the influence of heat balance shifts on the freeze microstructure and composition in aluminum smelting bath system: cryolite-CaF_2-AlF_3-Al_2O_3. *Metallurgical and Materials Transactions B*, volume 48, p. 3185-3195.

Liu, X., Taylor, M. et George, S. (1992). Crust formation and deterioration in industrial cells. *TMS Light Metals*, p. 489-494.

Llavona, M.A., Zapico, R., García, P., Sancho, J.P. et Verdeja, L.F. (1988). Some contributions to the study of the thermal conductivity of industrial Bayer aluminas. *TMS Light Metals*, p. 201-206.

Llavona, M.A., Verdeja, L.F., Alvarez, F., Garcia, M.P. et Sancho, J.P. (1990). Formation and characterization of aluminum electrolysis crusts. *TMS Light Metals*, p. 439-446.

Llavona, M.A., Verdeja, L.F., Zapico, R., Alvarez, F. et Sancho, J.P. (1990). Density, hardness and thermal conductivity of Hall-Heroult crusts. *TMS Light Metals*, p. 429-437.

Log, T. et Oye, H.A. (1990). A new transient hot-strip method for determination of thermal conductivity of carbon materials up to 700 °C. *TMS Light Metals*, p. 473-478.

Marceau, D., Pilote, S., Désilets, M., Bilodeau, J.F., Hacini, L. et Caratini, Y. (2011). Advanced numerical simulation of the thermo-electro-chemo-mechanical behaviour of Hall-Héroult cells under electrical preheating. *TMS Light Metals*, p. 1041-1046.

Marois, M.A., Bertrand, C., Désilets, M., Coulombe, M.A. et Lacroix, M. (2009). Comparison of two different numerical methods for predicting the formation of the side ledge in an aluminium electrolysis cell. *TMS Light Metals*, p. 563-568.

Namboothiri, S., Lavoie, P., Cotton, D. et Taylor, M.P. (2009). Controlled cooling of aluminium smelting cell sidewalls using heat exchangers supplied with air. *TMS Light Metals*, p. 317-322.

Nan, W. et Changhong, W. (2010). Numerical simulation on side heat transfer in 300kA aluminum reduction cell with graphitized cathode. *International Conference on Computer Application and System Modeling*, p. 281-284.

Oedegard, R., Roenning, S., Rolseth, S. et Thonstad, J. (1985). On alumina phase transformation and crust formation in aluminum cells. *TMS Light Metals*, p. 695-709.

Perruchoud, R.C., Weier, M.W., Fischer, W.K. et Schmidt-Hatting, W. (2001). Anode properties, cover materials and cell operation. *TMS Light Metals*, p. 695-699

Peterson, R.D. et Tabereaux, A.T. (1987). Liquidus curves for the cryolite AlF_3-CaF_2-Al_2O_3 system in aluminum cell electrolytes. *TMS Light Metals*, p. 383-388.

Pfundt, H., Vogelsang, D. et Gerling, U. (1989). Calculation of the crust profile in aluminium reduction cells by thermal computer modelling. *TMS Light Metals*, p. 371-377.

Poncsák, S., Kiss, L., St-Pierre, R., Guérard, S. et Bilodeau, J.F. (2014). Structural characterisation and thermophysical properties of the side ledge in Hall-Héroult cells. *TMS Light Metals,* p. 585-589.

Poncsák, S., Kiss, L., Belley, A., Guérard, S. et Bilodeau, J.F. (2015). Study of the structure and thermophysical properties of the side ledge in Hall-Héroult cells operating with modified bath composition. *TMS Light Metals*, p. 655-659.

Poncsák, S., Kiss, L.I., Guérard, S. et Bilodeau, J.F. (2017). Impact of the solidification rate on the chemical composition of frozen cryolite bath. *Metals*, volume 7, numéro 3, 10 p.

Powell, R.W., Ho, C.Y. et Liley, P.E. (1966). *Thermal conductivity of selected materials* (Rapport). National Standard Reference Data Series, Lafayette, États-Unis, 175 p.

Reddy, J.N. et Gartling, D.K. (2010). *The finite element method in heat transfer and fluid dynamics*, 3^e édition. CRC Press, Boca Raton, Floride, États-Unis, 524 p.

Richards, N.E. (1998). Anode covering practices. *6th Australasian Aluminium Smelting Technology Conference*, p. 143-152.

Riello, D., Zetterström, C., Parr, C., Braulio, M.A.L., Moreira, M., Gallo, J.B. et Pandolfelli, V.C. (2016). AlF_3 reaction mechanism and its influence on α-Al_2O_3 mineralization. *Ceramics International*, volume 42, p. 9804-9814.

Rio Tinto (2009). Albums photo - Usine Grande Baie. https://www.usinegrandebaie.com/albums/usine-grande-baie (page consultée le 22 juin 2018).

Rye, K. (1992). Alumina crusting in cryolitic melts part II: Bulk properties of crust. *TMS Light Metals*, p. 503-509.

Rye, K.A., Thonstad, J. et Liu, X. (1995). Heat transfer, thermal conductivity, and emissivity of Hall-Heroult top crust. *TMS Light Metals*, p. 441-449.

Safa, Y., Flueck, M. et Rappaz, J. (2009). Numerical simulation of thermal problems coupled with magnetohydrodynamic effects in aluminium cell. *Applied Mathematical Modelling*, volume 33, numéro 3, p. 1479-1492.

Schotte, W. (1960). Thermal conductivity of packed beds. *American Institute of Chemical Engineers Journal*, volume 6, numéro 1, p. 63-67.

Seger, E.J. (1975). New method of measuring electrode resistance for quality control. *TMS Light Metals*, p. 283-290.

Shen, X., Hyland, M., Welch, B., et Li, W. (2004). Temperature distribution and heat dissipation along anode rod in hall-heroult cells. *8th Australasian Aluminium Smelting Technology Conference*, p. 350-359.

Shen, X. (2006). *Top cover and energy balance in Hall-Heroult cells*. Thèse de doctorat, University of Auckland, Auckland, Nouvelle-Zélande, 263 p.

Shen, X.C., Hyland, M. et Welch, B. (2008). Top heat loss in Hall-Heroult cells. *TMS Light Metals*, p. 501-504.

Siegel, R. et Howell, J.R. (1981). *Thermal radiation heat transfer*, 2^e édition. Hemisphere Publishing Corporation, 862 p.

Skybakmoen, E., Solheim, A. et Sterten, Å. (1997). Alumina solubility in molten salt systems of interest for aluminum electrolysis and related phase diagram data. *Metallurgical and Materials Transactions B*, volume 28, numéro 1, p. 81-86.

Solheim, A., Rolseth, S., Skybakmoen, E., Støen, L., Sterten, Å. et Stoøre, T. (1996). Liquidus temperatures for primary crystallization of cryolite in molten salt systems of interest for aluminum electrolysis. *Metallurgical and Materials Transactions B*, volume 27, numéro 5, p. 739-744.

Slagtern, A., Grjotheim, K., Foosnaes, T. et Naterstad, T. (1987). Thermal expansion of carbon materials calcined at various temperatures: structure, pore volume and content of impurities. *TMS Light Metals*, p. 449-458.

Sørlie, M. et Øye, H.A. (2010). *Cathodes in aluminium electrolysis*, 3^e édition. Aluminium-Verlag, Düsseldorf, Allemagne, 662 p.

Stein, K., Tezduyar, T.E. et Benney, R. (2004). Automatic mesh update with the solid-extension mesh moving technique. *Computer Methods in Applied Mechanics and Engineering*, volume 193, p. 2019-2032.

Taylor, M. (2007). Anode cover material - Science, practice and future needs. *9th Australasian Aluminium Smelting Technology Conference*, p. 77-82.

Taylor, M.P. et Welch, B.J. (1987). Melt/freeze heat transfer measurements in cryolite-based electrolytes. *Metallurgical Transactions B*, volume 18, numéro 2, p. 391-398.

Taylor, M.P., Zhang, W.D., Wills, V. et Schmid, S. (1996). A dynamic model for the energy balance of an electrolysis cell. *Chemical Engineering Research and Design*, volume 74, numéro 8, p. 913-933.

Thonstad, J., Fellner, P., Haarberg, G.M., Hives, J., Kvande, H. et Sterten, A. (2001). *Aluminum electrolysis*, 3^e edition. Aluminium-Verlag, Düsseldorf, Allemagne, 359 p.

Tissot, P. (1994). DTA determination of liquidus temperatures and Al_2O_3 and AlF_3 content in cryolitic melts. *Thermochimica Acta*, volume 234, p. 245-254.

Touloukian, Y.S. et DeWitt, D.P. (1972). *Thermophysical properties of matter - The TPRC data series*, volume 8. Plenum Publishing Corporation, New York, États-Unis, 1890 p.

Touloukian, Y.S., Kirby, R.K., Taylor, E.R. et Lee, T.Y.R (1977). *Thermophysical properties of matter - the TPRC data series*, volume 13. Plenum Publishing Corporation, New York, États-Unis, 1800 p.

Townsend, D.W. et Boxall, L.G. (1984). Crusting behavior of smelter aluminas. *TMS Light Metals*, p. 649-665.

Tsukahara, H., Ono, N. et Fujita, K. (1982). Establishment of effective operation of prebaked anode pots. *TMS Light Metals*, p. 471-482.

Utigard, T.A. (1999). Why "best" pots operate between 955 and 970 °C. *TMS Light Metals*, p. 319-326.

Valles, A., Lenis, V. et Rao, M. (1995). Prediction of ledge profile in Hall-Heroult cells. *TMS Light Metals*, p. 309-313.

Vidalain, G., Gosselin, L. et Lacroix, M. (2009). An enhanced thermal conduction model for the prediction of convection dominated solid-liquid phase change. *International Journal of Heat and Mass Transfer*, volume 52, p. 1753-1760.

Wagner, M.H., Pauls, H., Tillmanns, H. et Wilhelmi, G. (1983). Calcination: the effect of maximum heat treatment temperature on the properties of coke. *16th biennial Conference on Carbon*, p. 583-585.

Wefers, K. et Misra, C. (1987). *Oxides and hydroxides of aluminium - Alcoa technical paper N°19* (Rapport). Aluminium Company of America, Pittsburgh, États-Unis, 92 p.

Wei, C.C., Chen, J.J.J., Welch, B.J. et Voller, V.R. (1997). Modelling of dynamic ledge heat transfer. *TMS Light Metals*, p. 309-316.

Wijayaratne, H., Hyland, M., Taylor, M., Grama, A. et Groutso, T. (2011). Effects of composition and granulometry on thermal conductivity of anode cover materials. *TMS Light Metals*, p. 399-404.

Wilkening, S., Reny, P. et Murphy, B. (2005). Anode cover material and bath level control. *TMS Light Metals*, p. 367-372.

Windisch, C.F., Brenden, B.B., Koski, O.H., Williford, R.E. (1992). *Final report on the PNL program to develop an alumina sensor* (rapport). U.S. Department of Energy - Pacific Northwest Laboratory, États-Unis, 81 p.

Xifeng, C., Yiwen, Z. et Jianhong, Y. (2014). An improved finite element model for thermal balance analysis of aluminum electrolysis cells. *TMS Light Metals*, p. 661-666.

Yang, S., Li, J., Xu, Y., Zhang, H., Lv, X. et Jia, M. (2014). A modelling of heat losses in aluminium reduction cell with slotted anodes. *TMS Light Metals*, p. 667-672.

Yang, Y., Flyland, M., Seal, C. et Wang, Z. (2014). Modelling HF generation: The role of ambient humidity. *TMS Light Metals*, p. 641-646.

Zaitseva, J.N., Yakimov, I.S. et Kirik, S.D. (2009). Thermal transformation of quaternary compounds in NaF-CaF_2-AlF_3 system. *Journal of Solid State Chemistry*, volume 182, numéro 8, p. 2246-2251.

Zhang, Q., Taylor, M.P., Chen, J.J.J., Cotton, D., Groutzo, T. et Yang, X. (2013). Composition and thermal analysis of crust formed from industrial anode cover. *TMS Light Metals*, p. 675-680.

Zhang, Q., Taylor, M.P. et Chen, J.J.J. (2014). The melting behaviour of aluminium smelter crust. *TMS Light Metals*, p. 591-596.

Zhang, Q., Taylor, M.P. et Chen, J.J.J. (2015). Computational modeling of thermochemical evolution of aluminum smelter crust. *Metallurgical and Materials Transactions B*, volume 46, p. 1520-1534.

Zhang, W., Li, H., Chen, B., Li, Q., Hou, X. et Zhang, H. (2015). CO_2 emission and mitigation potential estimations of China's primary aluminum industry. *Journal of Cleaner Production*, volume 103, p. 863-872.

Zhao, R., Gosselin, L., Fafard, M. et Ziegler, D.P. (2013a). Heat transfer in upper part of electrolytic cells: Thermal circuit and sensitivity analysis. *Applied Thermal Engineering*, volume 54, numéro 1, p. 212-225.

Zhao, R., Gosselin, L., Ousegui, A., Fafard, M. et Ziegler, D.P. (2013b). Heat transfer and airflow analysis in the upper part of electrolytic cells based on CFD. *Numerical Heat Transfer; Part A: Applications*, volume 64, numéro 4, p. 317-338.

Zhao, R., Gosselin, L., Fafard, M. et Ziegler, D.P. (2013c). Reduced ventilation of upper part of aluminum smelting pot: Potential benefits, drawbacks, and design modifications. *TMS Light Metals*, p. 805-810.

Zhao, R., Gosselin, L., Fafard, M., Tessier, J. et Ziegler, D.P. (2017). Efficiency of pot tightness in reduced pot draft conditions based on multi-length scale CFD simulations. *International Journal of Thermal Sciences*, volume 112, p. 395-407.

Živkovic, Ž., Štrbac, N. et Šesták, J. (1995). Influence of fluorides on polymorphous transformation of α-Al_2O_3 formation. *Thermochimica Acta*, volume 266, p. 293-300.

Zoric, J., Rousar, J., Thonstad, J. et Haarberg, T. (1997). Mathematical modelling of aluminium cells with prebaked anodes Part II: Current distribution and influence of sideledge. *Journal of Applied Electrochemistry*, volume 27, p. 928-938.